HELLENIC REPUBLIC
National and Kapodistrian
University of Athens
EST. 1837

National and Kapodistrian University of Athens

Physics department

Section of Astrophysics, Astronomy & Mechanics

PhD Thesis

Stability Analysis of Relativistic Magnetized Astrophysical Jets

Charalampos Sinnis

Supervisor:
Nektarios Vlahakis
Professor, National and Kapodistrian University of Athens

Athens, December 2023

Ευρωπαϊκή Ένωση
European Social Fund

Operational Programme
Human Resources Development,
Education and Lifelong Learning
Co-financed by Greece and the European Union

ΕΣΠΑ
2014-2020
ανάπτυξη - εργασία - αλληλεγγύη

HELLENIC REPUBLIC
National and Kapodistrian
University of Athens
EST. 1837

Stability Analysis of Relativistic Magnetized Astrophysical Jets

PhD Thesis
of
Charalampos Sinnis

Supervising committee
Nektarios Vlahakis, Professor, National and Kapodistrian University of Athens
Kanaris Tsinganos, Professor Emeritus, National and Kapodistrian University of Athens
Ioannis Contopoulos, Research Director, Academy of Athens

Examination committee
Theocharis Apostolatos, Professor, National and Kapodistrian University of Athens
Konstantinos-Nektarios Gourgouliatos, Associate Professor, University of Patras
Stylianos Kazantzidis, Assistant Professor, National and Kapodistrian University of Athens
Maria Petropoulou, Assistant Professor, National and Kapodistrian University of Athens

Abstract

One special trait of astrophysical jets is their enhanced structural stability, as their total length can be many times their initial radii. Although it is established from previous studies that instabilities develop along their flow, it is not fully understood how they affect the outflow properties. This thesis focuses on this specific scientific question, thus the stability properties of astrophysical jets are studied.

The term astrophysical jet involves a family of outflows that share the same formation and propagation mechanisms, i.e. an accretion disk is formed around a massive object which accretes into this central engine, leading to the creation of these cosmic outflows. The physical quantities describing the jets span over an extended value range. For example, there are jets originated from protostars (YSO jets) which are non-relativistic with total lengths of $\sim$ pc. On the contrary, there are jets originated from the accretion of matter into a supermassive black hole (AGN jets) which are relativistic and they travel distances $\sim$ kpc.

Throughout this thesis the dynamics of these outflows are described by the relativistic magnetohydrodynamic (RMHD) set of equations which consists of the equations of Maxwell coupled with three continuity equations for mass, momentum and energy and Ohm's law in the case of infinite conductivity. Finally, in order for the system to close an equation of state for the plasma is included. In order to study the stability properties of the jets the linear stability analysis methodology is utilized. This methodology requires to insert small perturbative terms in the set of equations that describe the dynamics of the outflow and expand the equations regarding terms up to the first order. The resulting linearized system of equations is essentially a boundary conditions problem. The thesis focuses on the unstable solutions of this system and their properties.

In terms of outflow configuration, the main point of interest is around mildly relativistic magnetized astrophysical jets. These jets are typical in the case of AGN outflows. They carry magnetic field usually characterized by a helical topology, and their rotation is slight or non-existent. Two main kinds of instabilities emerge from this type of jets. The first one is related to shear in the velocity profile or when two fluids with different velocity values are in contact. This is the Kelvin-Helmholtz instability. The second instability is associated with the existence of the magnetic field in the outflow, they are called current-driven instabilities. Depending on the jet configuration these two types of instability may emanate, evolve and affect the initial configuration. The effect on the outflow varies, the initial outflow may be disrupted and evolve into a new quasi-steady state or be destroyed entirely.

The thesis at hand studies the stability properties of relativistic magnetized astrophysical jets. The configurations that are probed include cylindrical outflows carrying helical magnetic fields with bulk flow velocities corresponding mainly to mildly relativistic jets. The first configuration for which the stability properties are presented is a two-component jet, most commonly known as a spine-sheath outflow. Alongside the results from the linear stability analysis, there are also numerical simulations that examine the non-linear evolution of the perturbed outflow. The results from the two different methodologies are in agreement, while the most important parameter affecting the intensity of the instabilities is magnetization. The second configuration is a single-component magnetized mildly relativistic jet. The stability profile of this specific configuration is characterized by the existence of the magnetized Kelvin-Helmholtz instability which is generalized in the relativistic regime for a cylindrical outflow geometry. The stability analysis successfully identifies the regulating parameters of the mode's behavior, while it is shown that under specific circumstances the Kelvin-Helmholtz instability of a cylindrical jet can be approximated by the corresponding results of a Cartesian counterpart.

Περίληψη

Εισαγωγικές σημειώσεις

Οι αστροφυσικοί πίδακες είναι εστιασμένες εκροές πλάσματος οι οποίες εκκινούν από μία συμπαγή πηγή. Ιστορικά η πρώτη καταγεγραμμένη αναφορά αστροφυσικού πίδακα εντοπίζεται το 1918 από τον Curtis (1918) η οποία πραγματοποιήθηκε στο παρατηρητήριο του Lick, στον ενεργό γαλαξία M87. Ο βασικός μηχανισμός δημιουργίας των πιδάκων αποτελείται από την προσρόφηση ύλης από ένα κεντρικό μαζικό αντικείμενο, με αποτέλεσμα να δημιουργείται εστιασμένη εκροή αποτελούμενη από ένα ποσοστό αυτής της ύλης. Η ποικιλομορφία αυτών των κοσμικών αντικειμένων είναι εκτεταμένη και αφορά ένα μεγάλο ποσοστό των δομικών στοιχείων που απαρτίζουν την όλη διαδικασία. Για παράδειγμα το κεντρικό σώμα στο οποίο προσπίπτει η ύλη μπορεί να είναι ένας πρωτοαστέρας, διπλά συστήματα αποτελούμενα από μία αστρική μελανή οπή και ένα συνοδό σώμα είτε έναν αστέρα νετρονίων με ένα συνοδό σώμα και μελανή οπή αστρικής ή γαλαξιακής κλίμακας. Όσον αφορά την εκροή υπάρχουν διάφορα φυσικά μεγέθη τα οποία τις κατατάσσουν σε διάφορες κατηγορίες, όπως η ταχύτητα (μη σχετικιστικές-σχετικιστικές), η πυκνότητα (ελαφρείς-βαρείς εκροές) ή την παρουσία και την ένταση μαγνητικών πεδίων. Σαν αποτέλεσμα ο παραμετρικός χώρος των φυσικών μεγεθών των πιδάκων είναι εκτεταμένος και πολυάριθμος αν και το φυσικό πλαίσιο που περιγράφει και διέπει την συμπεριφορά τους είναι το ίδιο. Κατά αυτό τον τρόπο όλα αυτά τα αντικείμενα δημιουργούν μια μεγάλη οικογένεια ροών που παρουσιάζουν επί της ουσίας ποσοτικές και όχι ποιοτικές διαφορές.

Αν και η επιστημονική κοινότητα που μελετά τα συγκεκριμένα αντικείμενα έχει να παρουσιάσει σημαντική πρόοδο πάνω στην κατανόηση των μηχανισμών που διέπουν την συμπεριφορά τους, αρκετά ερωτήματα παραμένουν ακόμα ανοιχτά για τα οποία δεν έχει επέλθει η πλήρης κατανόηση τους. Ένα από τα ανοιχτά αυτά θέματα είναι η χαρακτηριστική ευστάθεια αυτών των αντικειμένων, καθώς το συνολικό μήκος το οποίο μπορούν να φτάσουν είναι πολλαπλάσιο της ακτίνας τους. Αυτό το γεγονός έρχεται σε αντιδιαστολή με τα αποτελέσματα σχετικών πειραμάτων σε διατάξεις εργαστηριακού πλάσματος όπου παρατηρείται τόσο η ανάπτυξη ασταθειών όσο και η γρήγορη καταστροφή της σχετικής εκροής. Επιπροσθέτως, η ύπαρξη ασταθειών έχει επιβεβαιωθεί και στην περίπτωση των κοσμικών πιδάκων με τη χρήση κατάλληλων παρατηρήσεων. Με αυτό τον τρόπο το ερώτημα γίνεται σαφές: Ποιοι είναι εκείνοι οι αποσβεστικοί παράγοντες οι οποίοι επιτρέπουν στις αστροφυσικές εκροές να συνεχίζουν να διαδίδονται παρ΄ ότι οι αστάθειες υπάρχουν και επιδρούν πάνω στην ροή· Η παρούσα εργασία προσπαθεί να διαλευκάνει πιθανές φυσικές διεργασίες που έχουν σταθεροποιητική επίδραση επί των εκροών και αλληλεπιδρούν με τις διεγερμένες αστάθειες με τέτοιο τρόπο ώστε οι εκροές να διατηρούν την μακροσκοπική τους δομή.

Θεωρητικό υπόβαθρο

Η διδακτορική διατριβή επικεντρώνεται πάνω σε εκροές οι οποίες προέρχονται από τα κέντρα ενεργών γαλαξιακών πυρήνων (active galactic nuclei; AGN). Πρόκειται για πίδακες οι οποίοι προέρχονται από προσρόφηση ύλης σε μία υπερμεγέθη μελανή οπή της τάξεως των $10^8 - 10^9 M_\odot$, η ταχύτητα διάδοσής τους είναι σχετικιστική ενώ εν γένει φέρουν μαγνητικά πεδία. Στο συγκεκριμένο πλαίσιο η δυναμική των πιδάκων περιγράφεται από ένα σύνολο μη γραμμικών διαφορικών εξισώσεων, τις εξισώσεις της ιδεατής σχετικιστικής μαγνητοϋδροδυναμικής (relativistic magnetohydrodynamics; RMHD) (Vlahakis, 2023). Οι εξισώσεις αυτές αποτελούνται από τις τέσσερις εξισώσεις του Maxwell για τον ηλεκτρομαγνητισμό, τρεις εξισώσεις διατήρησης για τα ρευστά (διατήρηση μάζας, ορμής και ενέργειας), την εξίσωση του Ohm θεωρώντας άπειρη αγωγιμότητα και εν τέλει μία καταστατική εξίσωση που κλείνει το συγκεκριμένο σύστημα εξισώσεων. Το φυσικά μεγέθη του εν λόγω συστήματος εξαρτώνται τόσο από χωρικές μεταβλητές όσο και από τον χρόνο.

Τα μοντέλα των αδιατάρακτων πιδάκων που χρησιμοποιούνται είναι κυλινδρικά και αξισυμμετρικά, ουσιαστικά οι εκροές είναι συμμετρικές ως την αζιμουθιακή και την αξονική διεύθυνση, $\partial_\phi = \partial_z = 0$. Επίσης τα μοντέλα θεωρούνται πως είναι και στάσιμα, $\partial_t = 0$. Σαν αποτέλεσμα αυτών των υποθέσεων τα φυσικά μεγέθη των πιδάκων αυτών εξαρτώνται αποκλειστικά και μόνο από την κυλινδρική ακτίνα. Εδώ πρέπει να αναφερθεί ότι τα μοντέλα αυτά είναι στο εσωτερικό τους σε ισορροπία δυνάμεων και βρίσκονται σε ισορροπία πίεσης με το περιβάλλον τους, οπότε τα αδιατάρακτα μοντέλα είναι ευσταθείς λύσεις ισορροπίας του συστήματος.

Για την μελέτη των ασταθειών επιλέγεται να ακολουθηθεί η ανάλυση γραμμικής ευστάθειας (linear stability analysis) των διαφόρων μοντέλων. Η μεθοδολογία αυτή ορίζει την εισαγωγή μικρών διαταρακτικών όρων στο σύστημα εξισώσεων της RMHD, και εν συνεχεία στην ανάπτυξη τους κρατώντας όρους έως πρώτης τάξης. Οι διαταραχές αυτές λόγω των υποθέσεων που αφορούν τα μοντέλα των πιδάκων μπορούν να αναλυθούν κατά Fourier, οπότε και είναι ανάλογα ενός εκθετικού όρου που έχει την μορφή $\propto e^{i(kz+m\phi-\omega t)}$, όπου ο k είναι πραγματικός και ο m είναι ακέραιος αριθμός. Με αυτό τον τρόπο οι εξισώσεις της RMHD μετατρέπονται από μερικές διαφορικές σε ολικές διαφορικές με μεταβλητή την κυλινδρική ακτίνα και μπορούν εν γένει να λυθούν. Μία επιπλέον παραδοχή είναι πως οι αστάθειες είναι χρονοεξαρτώμενες οπότε και το ω είναι ένας μιγαδικός αριθμός. Με αυτό τον τρόπο το πλάτος των διαταραχών αποκτά την μορφή $\propto e^{\mathrm{Im}(\omega)t}e^{i(kz+m\phi-\mathrm{Re}(\omega)t)}$, όπου το πρώτο εκθετικό παρέχει την πληροφορία εάν η λύση είναι ασταθής ($\mathrm{Im}(\omega) > 0$) και αυξάνεται το πλάτος της με τον χρόνο. Ανάλογα οι υπόλοιπες λύσεις χαρακτηρίζονται ως ευσταθείς ($\mathrm{Im}(\omega) < 0$) ή οριακά ευσταθείς ($\mathrm{Im}(\omega) = 0$). Οι λύσεις που ενδιαφέρουν και μελετώνται στην παρούσα εργασία είναι μόνο οι ασταθείς.

Το σύστημα των εξισώσεων μετά την γραμμικοποίησή τους μπορεί να γραφτεί ως ένα ομογενές γραμμικό διαφορικό σύστημα (Vlahakis, 2023) το οποίο εν συνεχεία λύνεται. Επί της ουσίας πρόκειται για την επίλυση ενός προβλήματος οριακών συνθηκών. Τα σημεία ενδιαφέροντος είναι τρία. Το πρώτο είναι ο άξονας του πίδακα, στη συνέχεια η περιοχή που βρίσκεται ασυμπτωτικά μακριά από την περιοχή της εκροής και τελικά το η επιφάνεια διεπαφής του πίδακα με το περιβάλλον του. Για την περιοχή του άξονα η λύση πρέπει να είναι ομαλή, ενώ για μεγάλες αποστάσεις από τον πίδακα οι λύσεις πρέπει να είναι ομαλές και φθίνουσες. Στο όριο του πίδακα οι λύσεις πρέπει να είναι συνεχείς, η σχέση διασποράς κάθε ασταθούς τρόπου δίνεται από τις υποψήφιες λύσεις οι οποίες ικανοποιούν τις οριακές συνθήκες.

Η εφαρμογή της παραπάνω μεθοδολογίας αποτελείται από την εξεύρεση λύσεων για τον πίδακα και το περιβάλλον του ξεχωριστά και την επιτυχή εφαρμογή των οριακών συνθηκών. Όσον αφορά το περιβάλλον αυτό θεωρείται να είναι στατικό, με σταθερή πυκνότητα και ανάλογα αν είναι υδροδυναμικό ή μαγνητισμένο μπορεί να έχει μία σταθερή πίεση ή σταθερό μαγνητικό πεδίο το οποίο αποτελείται μόνο από συνιστώσα παράλληλη στον άξονα του πίδακα. Υπό τις παρούσες υποθέσεις το διαφορικό σύστημα καταλήγει σε μία διαφορική εξίσωση Bessel όπου οι λύσεις του είναι εξισώσεις Hankel πρώτου είδους. Η επιλογή της λύσης προκύπτει από την ασυμπτωτική συμπεριφορά των συγκεκριμένων συναρτήσεων. Για αποστάσεις που τείνουν στο άπειρο οι εν λόγω συναρτήσεις αναπαριστούν κύματα που απομακρύνονται από την πηγή δημιουργίας τους και έχουν μειούμενο πλάτος, οπότε η συνοριακή συνθήκη εκεί τηρείται. Επί της ουσίας με αυτή την επιλογή αποκλείεται το σενάριο να έρχονται διαταραχές από το άπειρο που να επηρεάζουν την αρχική εκροή. Για το εσωτερικό του πίδακα η εξεύρεση αναλυτικών λύσεων είναι εξαιρετικά σπάνια, για αυτό τον λόγο χρησιμοποιούνται υπολογιστικές ρουτίνες που βρίσκουν αριθμητικά τις λύσεις εκεί. Εν τέλει εάν ικανοποιείται η συνοριακή συνθήκη στην επιφάνεια διεπαφής πίδακα-περιβάλλοντος τότε πρόκειται για μία νέα ασταθή λύση του συστήματος.

Μελέτη ευστάθειας σχετικιστικού πίδακα αποτελούμενο από δύο συνιστώσες

Το πρώτο μοντέλο για το οποίο αναλύεται το προφίλ ευστάθειας του αποτελείται από δύο μέρη, η πλήρης περιγραφή του αδιατάρακτου μοντέλου πίδακα παρουσιάζεται στην εργασία "Rotation and toroidal magnetic field effects on the stability of two-component jets", Millas et al. 2017, Monthly Notices of the Royal Astronomical Society, Volume 470, Issue 1, p.592-605 (Millas et al., 2017). Στο παραπάνω πλαίσιο μελετήθηκε η γραμμική ευστάθεια του συστήματος και εν συνεχεία, τα παραχθέντα αποτελέσματα συγκρίθηκαν με αντίστοιχες τρισδιάστατες προσομοιώσεις οι οποίες πραγματοποιήθηκαν από τον Δρ. Δημήτριο Μήλλα. Αναλυτικότερα, το μοντέλο που χρησιμοποιήθηκε αποτελείται από δύο συνιστώσες, μία γρήγορη αραιή (π.χ. ηλεκτρονίων - ποζιτρονίων) κυλινδρική ροή εντοπισμένη στην περιοχή του άξονα του πίδακα, η οποία περικλείεται από μία βαρύτερη (π.χ. ηλεκτρονίων – πρωτονίων) και βραδύτερη συνιστώσα της εκροής. Τα συγκεκριμένα μοντέλα που μόλις περιγράφηκαν συναντώνται στην βιβλιογραφία ως "spine – sheath" μοντέλα πιδάκων. Ολόκληρη η εκροή περιβάλλεται από στατικό και αμαγνήτιστο μέσο με πυκνότητα συγκρίσιμη της περιοχής του άξονα.

Για την ανάλυση γραμμικής ευστάθειας η βασική παράμετρος ενδιαφέροντος ήταν η μαγνήτιση του πίδακα. Οι αρχικές ολοκληρώσεις αφορούν υδροδυναμικές λύσεις στις οποίες σταδιακά αυξάνεται η ένταση του μαγνητικού πεδίου. Ενισχύοντας την μαγνήτιση, παρατηρείται μείωση των χρονικών κλιμάκων ανάπτυξης των ασταθειών (ασταθέστερες δομές) καθώς και η ύπαρξη και ενδυνάμωση ηλεκτρομαγνητικών ασταθειών ή όπως απαντώνται στην βιβλιογραφία current-driven. Σύμφωνα με αυτό το μοτίβο οι διαταραγμένες ηλεκτρομαγνητικές δυνάμεις αρχίζουν να γίνονται συγκρίσιμες με τις αντίστοιχες αδρανειακές δυνάμεις καθώς η μαγνήτιση του πίδακα αυξάνεται. Οι λύσεις που αφορούν μικρές τιμές της μαγνήτισης κυριαρχούνται από κινητικές αστάθειες τύπου Kelvin – Helmholtz. Ανεξαρτήτως της τιμής της μαγνήτισης οι περιοχές στις οποίες οι αστάθειες φαίνονται να έχουν την μέγιστη ένταση είναι οι δύο επιφάνειες διεπαφής μεταξύ του εσωτερικού-εξωτερικού πίδακα και του εξωτερικού πίδακα με το περιβάλλον του. Αυτό σημαίνει πως η έντονη διαταραχή της αδιατάρακτης δομής αναμένεται να παρατηρείται γύρω από τις δύο συγκεκριμένες επιφάνειες.

Οι αριθμητικές προσομοιώσεις παρατηρούνται να είναι σε γενική συμφωνία με την γραμμική ανάλυση και επιβεβαιώνουν σε ικανοποιητικό βαθμό τα προβλεφθέντα αποτελέσματα της αναλυτικής μελέτης. Συγκεκριμένα, οι χρόνοι ανάπτυξης των ασταθειών ($\tau \sim 1/\mathrm{Im}(\omega)$) βρίσκονται σε μία καλή συσχέτιση μεταξύ των δύο μεθοδολογιών. Ακόμα, το είδος της αστάθειας (Kelvin – Helmholtz ή current – driven) που κυριαρχεί και ο τρόπος που αυτή εξελίσσεται, ειδικά για τους χρόνους που ισχύει η γραμμική προσέγγιση, δείχνουν να βρίσκονται σε σύγκλιση μεταξύ αναλυτικών υπολογισμών και προσομοιώσεων. Οι επιφάνειες διεπαφής όντως παρουσιάζουν εντονότερη εξέλιξη των ασταθειών στην περιοχή που αυτές βρίσκονται σε συμφωνία με την πρόβλεψη από την μελέτη γραμμικής ευστάθειας. Οι πίδακες δεν φαίνονται να καταστρέφονται εντελώς, αν και παρατηρείται μία από τις δύο συνιστώσες να επηρεάζεται περισσότερο από την άλλη. Εδώ πρέπει να σημειωθεί ότι ίσως χρειάζονται ακόμη μεγαλύτερα χρονικά διαστήματα για να παρατηρηθεί εκτεταμένη αποδιοργάνωση του πίδακα, αν και τα χρονικά διαστήματα που έχουν ήδη καλυφθεί είναι σε πρώτη προσέγγιση ικανοποιητικά.

Μελέτη γραμμικής ευστάθειας νέας αδιατάρακτη κατάστασης

Ένα από τα ζητούμενα είναι να καθιερωθεί μία νέα αδιατάρακτη κατάσταση η οποία φέρει την υπογραφή της ευθυγράμμισης και επιτάχυνσης του πίδακα στα αρχικά στάδια ύπαρξης του πίδακα. Ο πίδακας θεωρείται πως είναι κυλινδρικά αξισυμμετρικός και στάσιμος και η δυναμική του περιγράφεται από τις εξισώσεις της RMHD. Επίσης ο πίδακας είναι κρύος (μηδέν θερμική πίεση) ενώ το μαγνητικό πεδίο που φέρει έχει τόσο αζιμουθιακή όσο και πολοειδή συνιστώσα. Οι κύριες εξισώσεις που χρησιμοποιούνται είναι η ακτινική συνιστώσα της εξίσωσης ορμής και η εξίσωση ισο-περιστροφής του Ferraro (Vlahakis, 2004; Komissarov et al., 2009) η οποία συνδέει τα προφίλ των φυσικών μεγεθών με την περιστροφή κοντά στη βάση του πίδακα. Η ακτινική συμπεριφορά των φυσικών μεγεθών δεν επιδέχονται καμίας υπόθεσης εκτός από την αζιμουθιακή συνιστώσα της ταχύτητας. Η σχέση που έχει επιλεγεί για την περιγραφή της αυξάνει γραμμικά με την ακτίνα για αποστάσεις κοντά στον άξονα και φθίνει ανάλογα του αντιστρόφου της ακτίνας για αποστάσεις μακριά από τον άξονα. Η εξίσωση ορμής μετά από όλες αυτές τις παραδοχές καταλήγει σε ένα πολυώνυμο τρίτου βαθμού το οποίο έχει σε κάθε περίπτωση μία πραγματική λύση οπότε πάντα δίνει μία κατάσταση ισορροπίας.

Το μοντέλο που επιλέγεται να μελετηθεί η ευστάθεια του είναι ασθενώς περιστρεφόμενο, με σχετικιστική ταχύτητα κατά την διεύθυνση του άξονα (παράγοντας Lorentz της τάξεως 5-10) και είναι ισχυρά μαγνητισμένο κοντά στο όριο του πίδακα. Η παραμετρική μελέτη επικεντρώνεται στο λόγο πυκνοτήτων του υδροδυναμικού περιβάλλοντός του πίδακα ως προς την αντίστοιχη τιμή της πυκνότητας μετρούμενη στον άξονα της εκροής, ο λόγος αυτός συμβολίζεται με το σύμβολο η. Η επιλογή τιμών για αυτή την παράμετρο αρχικά τέθηκε να είναι 0.01 και 100, ουσιαστικά αυτό δημιουργεί έναν πίδακα ο οποίος είναι 100 φορές πυκνότερος ή αραιότερος από το περιβάλλον του αντίστοιχα. Μέσα στο φάσμα των λύσεων για $\eta = 0.01$ προκύπτει μία λύση η οποία παρουσιάζει μία γραμμική εξάρτηση μεταξύ του $\mathrm{Im}(\omega)$ και του κυματαριθμού k, η λύση παρατηρείται να σταθεροποιείται για $k \sim 0.1 - 1$ ενώ η γραμμική εξάρτηση δεν φαίνεται να έχει κάποιο άνω όριο. Ακόμα, οι τιμές που λαμβάνει το $\mathrm{Im}(\omega)$ είναι ανάλογες ή και μεγαλύτερες της μονάδας. Αυτό σημαίνει πως οι χρονικές κλίμακες ανάπτυξης της συγκεκριμένης λύσης είναι συγκρίσιμες ή και μικρότερες του χρόνου που χρειάζεται το φως να διατρέξει την ακτίνα του πίδακα (το ω μετριέται σε μονάδες ταχύτητας του φωτός ως προς την ακτίνα του πίδακα). Η συγκεκριμένη λύση δεν είναι παρούσα στις σχέσεις διασποράς για

$\eta = 100$, οπότε για πίδακες που είναι αραιότεροι του περιβάλλοντος η συγκεκριμένη αστάθεια σταθεροποιείται. Αξίζει να σημειωθεί πως για το παρόν μοντέλο ελέγχθηκαν τόσο αξισυμμετρικές διαταραχές ($m = 0$) όσο και μη αξισυμμετρικές ($m = -1, 1$) και η συγκεκριμένη λύση βρέθηκε και για τις τρεις τιμές της παραμέτρου m.

Μελέτη της γενικευμένης σχετικιστικής αστάθειας Kelvin-Helmholtz

Αρχικά τα χαρακτηριστικά αυτής της νέας αστάθειας (π.χ. γραμμικότητα $\omega - k$) και αποτελέσματα που αναφέρονται παρακάτω ταυτίζουν τη συγκεκριμένη λύση με μία αστάθεια η οποία έχει μελετηθεί εκτεταμένα στην βιβλιογραφία, την αστάθεια Kelvin-Helmholtz. Για να μελετηθεί η αστάθεια αυτή υιοθετείται μία απλοποιημένη εκδοχή του πρώτου μοντέλου για το οποίο εντοπίστηκε το οποίο δίνει μεγαλύτερη ελευθερία και ανεξαρτησία μεταξύ των φυσικών μεγεθών. Εν ολίγοις πρόκειται για ένα μοντέλο με σταθερό προφίλ για την πυκνότητα και τον παράγοντα Lorentz χωρίς περιστροφική κίνηση. Το πολοειδές μαγνητικό πεδίο είναι σταθερό κοντά στον άξονα και μειώνεται σαν την αντίστροφη ακτίνα στο τετράγωνο ενώ η αζιμουθιακή συνιστώσα αυξάνει γραμμικά με την ακτίνα κοντά στον άξονα και μειώνεται σαν αντίστροφη ακτίνα για το υπόλοιπο του πίδακα. Ως προς την καταστατική εξίσωση αυτή επιλέγεται να είναι η Taub-Matthews (Mignone &McKinney, 2007), η οποία αυτοσυνεπώς βρίσκει τις σωστές ταχύτητες ήχου για όλο το φάσμα θερμοκρασιών του πλάσματος.

Η παραμετρική μελέτη αφορά τέσσερις παραμέτρους οι οποίες είναι ο παράγοντας Lorentz, ο λόγος πυκνοτήτων περιβάλλοντος ως προς της εκροής, η ακτίνα του πυρήνα του μαγνητικού πεδίο (η ακτίνα για την οποία η αξονική συνιστώσα του μαγνητικού πεδίου παραμένει σταθερή), η μαγνήτιση του πίδακα. Ακόμη, ελέγχθηκε αν υπάρχει διαφορά στην επίδραση της αστάθειας πάνω στην διάταξη εάν το περιβάλλον είναι υδροδυναμικό ή μαγνητισμένο. Αρχικά η συγκεκριμένη λύση επιβεβαιώνεται και για το νέο μοντέλο πίδακα για ένα εύρος τιμών για το m. Παρατηρείται πως τις πιο ασταθείς λύσεις τις παρουσιάζουν αξισυμμετρικές αστάθειες με $m = 0$. Για αυτό τον λόγο η ανάλυση θα επικεντρωθεί μόνο σε λύσεις που έχουν $m = 0$.

Η παραμετρική μελέτη παρουσιάζει τιμές χρονικών κλιμάκων εξέλιξης της αστάθειας, οι οποίες είναι ξανά συγκρίσιμες με το χρόνο που απαιτείται απο το φως να διατρέξει την ακτίνα του πίδακα. Γενικά, η λύση παρουσιάζει πολύ μικρές κλίμακες ανάπτυξης όταν ο πίδακας είναι πυκνότερος του περιβάλλοντος, ισχυρά μαγνητισμένος, μετρίως σχετικιστικός και να επικρατεί η τοροειδής συνιστώσα του μαγνητικού πεδίου έναντι της πολοειδούς. Το μαγνητισμένο περιβάλλον περαιτέρω σταθεροποιεί την νέα λύση σε σύγκριση με το καθαρά υδροδυναμικό. Επίσης, αντικαταστάθηκε η πολοειδής συνιστώσα του μαγνητικού πεδίου από θερμική πίεση με παρόμοιο ακτινικό προφίλ ώστε να διατηρηθεί ίδια η κατανομή της συνολικής πίεσης, γενικά τα συμπεράσματα δεν άλλαζουν σε σχέση με τα προηγούμενα.

Ο βασικότερος παράγοντας που επηρεάζει την εξέλιξη της αστάθειας είναι η γωνία που σχηματίζει το κυματάνυσμα της αστάθειας με την διεύθυνση του μαγνητικού πεδίου. Όταν αυτή η γωνία είναι περίπου ορθογώνια τότε η τάση του μαγνητικού πεδίου δεν επηρεάζει ιδιαίτερα την εξέλιξη της αστάθειας ενώ όταν η γωνία αυτή είναι μηδενική τότε η τάση του πεδίου αποδυναμώνει και σε μερικές περιπτώσεις σταθεροποιεί την αστάθεια. Επίσης σε σχέση με την ταχύτητα της ροής, εάν αυτή εκφραστεί σε μονάδες του γρήγορου μαγνητοακουστικού κύματος τότε η αστάθεια σταθεροποιείται όταν η ροή είναι πολύ πιο γρήγορη ή αργή σε σχέση με την συγκεκριμένη ταχύτητα.

Επιπλέον η αστάθεια αυτή μπορεί να χαρακτηριστεί ως τοπική αστάθεια αφού οι λύσεις του συστήματος παρουσιάζουν τα μέγιστα τους κοντά στο όριο του πίδακα, ενώ για τις υπόλοιπες τιμές της ακτίνας οι λύσεις έχουν αμελητέα τιμή σε σχέση με την τιμή στο μέγιστο. Τα αποτελέσματα αυτά επιβεβαιώνονται και με τη χρήση της μεθοδολογίας WKBJ πάνω στο όριο του πίδακα, η οποία μπορεί να βρει τοπικές λύσεις ενός διαφορικού συστήματος. Η σύγκλιση μεταξύ της WKBJ και της πλήρους αριθμητικής μεθοδολογίας είναι παραπάνω από ικανοποιητική.

Ακόμη η μελέτη αναδεικνύει την σύνδεση της κυλινδρικής αστάθειας με το Καρτεσιανό ισοδύναμο. Όταν ένα σύνολο χαρακτηριστικών μηκών του συστήματος είναι πολύ μεγαλύτερο της ακτίνας του πίδακα τότε αποτελέσματα που προκύπτουν από Καρτεσιανή γεωμετρία του ίδιου μοντέλου συμπίπτουν με τα κυλινδρικά αποτελέσματα. Αυτό σημαίνει πως υπό τις κατάλληλες συνθήκες η Kelvin-Helmholtz αψηφά την γεωμετρία του πίδακα και συμπεριφέρεται σαν το Καρτεσιανό ισοδύναμο, οπότε και η τοπικότητα της λύσης επιβεβαιώνεται και μέσω αυτού του αποτελέσματος.

Προσομοιώσεις της σχετικιστικής Kelvin-Helmholtz

Για να ελεγχθεί η μη γραμμική εξέλιξη της προαναφερθείσας αστάθειας πραγματοποιήθηκε μια σειρά δισδιάστατων αριθμητικών προσομοιώσεων. Οι προσομοιώσεις πραγματοποιήθηκαν με την χρήση του κώδικα PLUTO (Mignone et al., 2007). Τα μοντέλα που χρησιμοποιήθηκαν στις προσομοιώσεις είναι ακριβώς τα ίδια με αυτά που χρησιμοποιήθηκαν και για την μελέτη της γραμμικής ευστάθειας.

Για τον κρύο/θερμοδυναμικό πίδακα παρατηρήθηκε συμφωνία χρονικών κλιμάκων ανάπτυξης της λύσης μεταξύ γραμμικής ανάλυσης και προσομοίωσης. Οι ιδιοσυναρτήσεις του γραμμικού ορίου παρατηρούνται και στην αριθμητική διαδικασία, ενώ η λύση αυξανομένου του χρόνου τείνει σε μία νέα ημι-ευσταθή λύση όπου κυριαρχείται από την ύπαρξη στροβίλου ο οποίος επιβιώνει για μεγάλους χρόνους ($\sim$ 100 crossing times) και ο οποίος διαμορφώνει ροή με διαφορετικά μέρη. Στον κρύο πίδακα ο στρόβιλος δεν επιβιώνει μέχρι το τέλος της προσομοίωσης, αλλά υπάρχει ένδειξη πως η αριθμητική διάχυση του κώδικα επηρεάζει εν τέλει την εξέλιξη του. Η τελική κατάσταση του πίδακα δείχνει να διατηρεί στοιχεία συγκροτημένης ροής, με μεγάλης κλίμακας μαγνητικά πεδία και δομή παρόμοια εκροών τύπου spine-sheath. Σε όλες τις προσομοιώσεις παρατηρείται διόγκωση του πίδακα και αύξηση της τιμής της ακτίνας του συνόρου του η οποία σε καμία περίπτωση δεν ξεπερνά το διπλάσιο της αρχικής τιμής.

Σε επίπεδο ροών ενέργειας παρατηρείται η μετατροπή ροής Poynting σε ροή ενέργειας μάζας. Αυτό σημαίνει πως η αστάθεια σαν μηχανισμός μετατρέπει την ροή ενέργειας που σχετίζεται με τα μαγνητικά πεδία σε ροή ενέργειας που αφορά την κινητική και την θερμική ενέργεια. Οι πίδακες ενώ αρχικά κυριαρχούνται από ροή Poynting εν τέλει καταλήγουν να κυριαρχούνται από ροή ενέργειας μάζας. Η συνολική ενέργεια των πιδάκων δεν διατηρείται καθώς οι εκροές εκπέμπουν ένα μέρος της προς το περιβάλλον τους. Παρόλα αυτά όσο μεγαλώνει ο κυματαριθμός της λύσης η εκπεμπόμενη ενέργεια μειώνεται. Ο ρυθμός μετατροπής του ενός είδους ροής στην άλλη φαίνεται να συσχετίζεται με την ύπαρξη στροβίλων στην ροή.

Σε γενικές γραμμές οι στρόβιλοι επιταχύνουν τον ρυθμό μετατροπής.

Γενίκευση της αστάθειας

Τέλος, υπήρξε προσπάθεια γενίκευσης της λύσης. Για να γίνει αυτό μεταφέρθηκε η ασυνέχεια της ταχύτητας από την επιφάνεια του πίδακα σε μία απόσταση μέσα στην εκροή. Για να μοντελοποιηθεί η μετάβαση στο προφίλ της ταχύτητας χρησιμοποιείται μία γενικευμένη λογιστική εξίσωση, επί της ουσίας πρόκειται για μία σιγμοειδή καμπύλη όπου με συνεχή τρόπο συνδέει δύο ασυμπτωτικές τιμές. Η παρούσα σχέση χρησιμοποιήθηκε τόσο για το προφίλ της ταχύτητας όσο και για το προφίλ της πυκνότητας και περιγράφει μία μετάβαση σε ένα από τα δύο μεγέθη ή και στα δύο γύρω σε μία συγκεκριμένη απόσταση από τον άξονα.

Αυτό το οποίο επιβεβαιώθηκε είναι αρχικά η ύπαρξη της υπό μελέτη αστάθειας. Η πρώτη παράμετρος που δοκιμάστηκε είναι το πλάτος που χρειάζεται για να ολοκληρωθεί η μετάβαση της ταχύτητας. Όσο μικραίνει αυτό το πλάτος και η μετάβαση πλησιάζει να γίνει ασυνεχής, τότε η συμπεριφορά της λύσης γίνεται παρόμοια με την συμπεριφορά της λύσης όταν η ασυνέχεια της ταχύτητας είναι στο όριο του πίδακα. Όσο η περιοχή αυτή μεγαλώνει, τότε η γραμμική εξάρτηση του $\mathrm{Im}(\omega)$ με τον κυματαριθμό παύει να ισχύει και οι μεγάλοι κυματαριθμοί τείνουν να σταθεροποιηθούν. Παρόλα αυτά οι χρονικές κλίμακες ανάπτυξης της αστάθειας παραμένουν συγκρίσιμες με τον χρόνο που χρειάζεται το φως να διατρέξει την ακτίνα του πίδακα. Η απόσταση που γίνεται η μετάβαση επηρεάζει ασθενώς τα αποτελέσματα.

Το προφίλ της πυκνότητας επίσης δεν επηρεάζει σε μεγάλο βαθμό τα αποτελέσματα. Αυτό το οποίο είναι σημαντικό είναι πως οι εκροές με σταθερό προφίλ πυκνότητας είναι πιο ασταθείς από τις αντίστοιχες με μεταβολή του προφίλ τους. Ακόμη, εάν το περιβάλλον είναι υδροδυναμικό ή μαγνητισμένο δεν επηρεάζει την συμπεριφορά της αστάθειας. Τα αποτελέσματα συνηγορούν στο γεγονός ότι η γωνία μεταξύ του μαγνητικού πεδίου και του κυματαριθμού είναι ίσως ο πιο σημαντικός παράγοντας και η τιμή που λαμβάνει παίζει καθοριστικό ρόλο για τον ρυθμό ανάπτυξης της αστάθειας. Για γωνίες οι ποίες είναι μικρές η αστάθεια αποδυναμώνεται, ενώ για κάθετες γωνίες συμβαίνει το αντίθετο. Το αποτέλεσμα αυτό είναι παρόμοιο με εκείνο του μοντέλου που η ασυνέχεια της ταχύτητας είναι στο όριο του πίδακα.

Contents

Chapter 1

Introduction

Astrophysical jets are collimated plasma outflows, propagating away from the vicinity of their formation region. Historically, the first jet to have been ever observed is that of the M87 galaxy in the early 20th century (Curtis, 1918). The mechanism for the creation of these objects consists of the accretion of matter into a massive central object, achieved through the formation of a disk around the central engine. Even though this mechanism seems to be universal the physical parameters observed for the central object and the subsequent jet span over a wide value range. Regarding the central objects there may be protostars in the case of Young Stellar Object jets (YSO), supermassive black holes in the case of Active Galactic Nuclei (AGNs) jets, binary systems of either neutron stars, white dwarf–star in cataclysmic variable binary systems, neutron star–black hole or more lately observed, binary system of stellar mass black holes. All of these systems create outflows with different traits, e.g. YSO jets tend to be non-relativistic with lengths of $\sim$ pc and central objects with masses $\sim M_{\odot}$, while the AGN jets are relativistic with lengths of $\sim$ kpc and central black holes with masses of $\sim 10^{8} - 10^{9} M_{\odot}$. This dissertation focuses on AGN jets and particularly their stability properties. Therefore the introduction gleans on the recent advances made on the study of these outflows regarding both observations and theoretical/numerical methodologies.

Fundamentally two main components form the extragalactic jets. First is the matter of the outflow which in most cases is an electron-positron or electron-proton plasma. Next are the magnetic fields which affect many processes occurring in the outflows through their interplay with the inertial component. These two components are involved in the multi-phase life cycle of an astrophysical jet. Initially, there is the accretion of magnetized matter into the central body which leads to the formation of the jet. The first stage for the jet evolution consists of the acceleration and collimation process, where the outflow through complex dynamical phenomena achieves certain direction, shape and flow properties such as density distribution, velocity profile etc. Next, the jet propagates away from the vicinity of the central object. This propagation transpires in different scales and through dissimilar environments. First, the jet travels into the environment of the galactic center, then through the intergalactic media and finally into the extragalactic environment. These media differ significantly in terms of physical properties, meaning that when the outflow interacts with each one of them, it is affected accordingly. Also, special focus should be given to the zones of transition from one kind of medium to another as there is a high probability that the jet is modified in these regions. Finally, the jet decelerates and stops at its termination area, whose properties and morphology heavily depend on the jet's characteristics.

All the above phases are extensively studied as they are equally complicated and affect greatly the final state of the outflow and what we observe. The stage of the jet formation is crucial, as the traits of the outflow on larger scales are defined by the accretion disk properties, the feeding procedure of the central object (in the case of AGNs a supermassive black hole) and finally the acceleration and collimation processes.

1.1 Brief summary of AGN jets observational literature

Detailed observations are valuable for someone to properly study and explore the physics of jets. They quantify the values of the various physical quantities of the jets and, therefore provide constraints to the theoretical models that attempt to explain the mechanisms behind their formation and propagation. Jets emit in a very broad range of the electromagnetic spectrum extending from radio up to γ-rays. Each component is attributed to different types of physical phenomena, for example, the radio continuum emission is associated with the synchrotron radiation of the jet particles following the field lines of the magnetic field. Therefore analyzing the whole radiation spectrum provides information about different physical processes. This section mainly focuses on observations about the structure of the jet along and perpendicular to the propagation axis, the velocity field, the structure of the magnetic field and the overall morphology of the outflow as these jet properties affect its stability behavior.

The total length of these cosmic outflows is noted to be on the scale of kpc. For example observations from radio up to x-rays for the jet of NGC 2663 reveal a total length of $\simeq 355$ kpc (Velović et al., 2022) or in the case of M87, the jet reaches a length of the scale of $\sim$ kpc (Pasetto et al., 2021). A very important observation is when a jet's shape is changed while it propagates. This is usually quantified by associating the width of the jet with the traveled distance measured from the central engine. Commonly a power law relation $w \propto r^k$ is used, with w being the jet width and r the distance from the central source. When $k = 0$ the jet is cylindrical, when $k = 0.5$ the jet is parabolic and for $k \geq 1$ the jet is hyperbolic or conical if the equality holds. The distance at which the transition occurs is equally important, as it can reveal aspects of the jet-environment interaction there.

Many recent studies have revealed that a common pattern is for the jets to have initially a parabolic or quasi-parabolic shape and eventually transitions into a conical shape. VLBI observations of NGC 315 reveal such a transition occurring at $r \simeq 0.58$ pc (Ricci et al., 2022). These transitions may not be always observed, as in the case of the NGC 2663, where the shape of the jet seems to have a constant width for its entire length, consistent with a low-density environment on Mpc scales.

Many surveys have tried to provide a definite answer around the collimation profile of jets by analyzing large samples of jetted galaxies. Kovalev et al. (2020) studied observations from MOJAVE at 15GHz, 2cm from VLBA and archival data from NRAO for a sample of low redshift AGNs. They studied the jet width profile as a function of the projected distance from the jet core. For the jets that showcase a shape transition, this usually involves a quasi-parabolic jet transcending into a conical shape. The vast majority of the sample does not show clear evidence for a shape transition. This result could be influenced by the small viewing angles or large scale factor of 8 pc mas^{-1} for a typical source of the sample and does not necessarily mean that such a transition actually does not exist. This also leads to carefully consider the parameter of the proximity of the sources. Pushkarev et al. (2017) probed the shapes and opening angles of AGN jets using radio observations at 15GHz and 22cm from VLBA. Using a single power law BL Lacs and quasars have a conical shape as the median $k = 1$, the galaxies are close to parabolic shapes with median $k = 0.68$. The difference could be attributed to the proximity of the latter cosmic objects and their larger viewing angles. In the survey it is noted that regarding sources with known physical parameters the calculated median length ~ 6 kpc. In general, a large number of sources in the sample present intrinsic opening angles between $0^{\circ}.1$ and $1^{\circ}.3$, this indicates a very high degree of collimation. Boccardi et al. (2021) note that mostly radio galaxies present parabolic expansion, contrary to BL Lacs where the profiles are mainly conical. Yet, once more it is noted that the collimation zone may not be resolved properly, thus leading to this difference.

The transition in the shape of the outflows can provide valuable information for the status of the flow or the surrounding medium. In some cases the distance where the shape transition is observed can be associated with a change in the configuration of the surrounding medium. For example Nakahara et al. (2020) observe and study the width profile of the NGC 1052 radio galaxy. The galaxy hosts a two sided jet which showcases a transition at $\sim 10^4$ gravitational radii. Both jets are initially cylindrical and transit to a conical structure. The transition site coincides with the distance at which the high density ionized region in the center of the galaxy is terminated. Regarding NGC 315 the jet transforms from a parabolic to a conical shape at $\sim 5{\cdot}10^3$ gravitational radii. The transition does not coincide with the Bondi radius of the central object, but a plausible scenario is that an ADAF disk having an outer radius $\sim 10^3$ gravitational radii confines the jet up until that point, after this distance the jet becomes conical. Another scenario assumes changes in the pressure profile of the environment leading to changes in the collimation profile of the outflow (Boccardi et al., 2021).

Nonetheless, there are also observations in which there can be no association of the jet collimation profile with the surrounding medium. In their survey Kovalev et al. (2020) comment that for the majority of their sample the distance at which the transition occurs is observed at $10^5 - 10^6$ gravitational radii. Due to the fact that the status of the environment at these distances from the central object is similar for these sources, the transition is probably situated in the vicinity where the magnetic and plasma energy fluxes become equal. This means that the transitions can also be triggered by modulations of a jet's internal properties and not only on a change of an external factor. An intrinsic process can also be attributed to trigger the jet shape transition of the NGC 4261 radio galaxy.

The jet is observed to have a parabolic shape that evolves into a conical counterpart. The transition occurs at $\sim 10^4$ gravitational radii, while the Bondi radius is estimated to be at $\approx 7 \cdot 10^5$ gravitational radii (Nakahara et al., 2018). Also, it has been suggested that the more powerful a jet is the farther from the central engine the transition occurs (Boccardi et al., 2021).

Nonetheless, the collimation process and the resulting jet profile may be more complex. For example Casadio et al. (2021) studies the acceleration and collimation zone (ACZ) of the BL Lac jet. This study also notes that the higher the energy of the jet the farther the ACZ extends. In general, the jet is conical from ~ 0.9 pc up to ~ 30 pc. There is a zone of rapid expansion followed by a second collimation zone. This intermediate stage can be accredited to a possible modulation in the status of the environment or an alteration in the intrinsic properties of the jet. The jet expands freely after the Bondi radius, as a result under-pressure is created into the outflow and the jet recollimates. Therefore, if the resolution of the observations suffices the whole process of collimation may be multi-phase and more complex than a single smooth collimation stage.

In general, an important factor affecting the collimation of the outflows is the possible acceleration that the same jet zone may undergo. In Pushkarev et al. (2017) they note that sources undergoing accelerated motion experience enhanced collimation rate, their median exponent of the power law is calculated to be $k = 0.73$. On the other hand non-accelerated sources present $k = 0.91$. A large number of sources is accelerated in the parabolic region of the outflow. Regarding NGC 315 the shape of the jet is initially parabolic and transcends into a conical counterpart, during this parabolic phase the the jet experiences the acceleration and during the conical phase the velocity seems to be constant (Ricci et al., 2022). Park et al. (2021) also analyze VLBA observations of NGC 315, alongside archival data from HSA and VLA. Once more they note that the jet transforms into a conical shape from a parabolic one at $\sim 10^5$ gravitational radii. The observations indicate acceleration for the parabolic component of the outflow, after the transition the jet decelerates. Both studies assume that the acceleration probably occurs due to Poynting flux conversion into kinetic energy flux. Interestingly, the jet undergoes a second acceleration phase at kpc scale, the final velocity value is calculated to be $\approx 0.85c$.

Distant objects seems to also exhibit similar behavior. Okino et al. (2022) analyze radio observations for quasar 3C273. The data are radio observations at 86GHz from GMVA, 15/22/43 GHz from HSA and 1.7 GHz from VLBA. The jet is initially parabolic and transcends into a conical/hyperbolic flow at $\sim 10^6 - 10^7$ gravitational radii. This distance does not coincide with the sphere of gravitational radius of the super-massive black hole. The jet is accelerated to relativistic velocities before the break of the jet shape. Lister et al. (2021) conducted a survey on a sample of 449 AGNs observed from 1994 until 2009 from VLBA at 15.4 GHz. Most notably 60% of the sample show traces of acceleration and non-radial motion. Therefore, these processes are not rare but are observed for numerous sources.

The jet acceleration should not be regarded as a smooth single phase process. Sources which are sufficiently resolved provide detailed observations indicating the complexity of this mechanism. For example, in the case of NGC 315 the jet obtains terminal value of

$\beta \equiv V/c \sim 0.9$ around ~ 0.6 pc, suggesting fast acceleration on sub-pc scale. Interestingly, the jet seems to decelerate at ~ 10 pc down to $\beta \sim 0.4$ and at larger scales of $\sim$ kpc the velocity of the outflow increases again to $\beta \sim 1$ (Ricci et al., 2022).

Another jet which has been extensively studied is the jet of the M87 galaxy. Mertens &Lobanov (2016) analyzed the velocity field of the M87 regarding scales of 100-1000 gravitational radii. The analysis suggests that the outflow exhibits stratified structure perpendicular to the axis of the jet. The jet becomes conical at kpc scales and it has become kinetically dominated already at few parsecs from central engine. Park et al. (2019) also focuses on the kinematic properties of M87 in the collimation zone based on observations made by KAVA on scales $\lesssim 20$ mas. At ≈ 0.5 mas velocity is $\approx 0.3c$, while at ≈ 20 mas the corresponding value is $\approx 2.7c$. The velocity field is found to be quite disperse. Below 1 mas the velocity is subluminal and its value increases with distance. The jet accelerates in the collimation zone and the authors discuss that the probable scenario is the magnetic acceleration mechanism. There is a chance that the velocity profile is stratified at $\lesssim 20$ mas.

The observations suggest that jets which show such complicated internal structures may be composed by more than a single flow component. For example, regarding the M87 the first component is a slow subluminal flow wrapped around a fast relativistic counterpart Mertens &Lobanov (2016). The same model of a two component outflow for the jet of the M87 is also suggested by Park et al. (2019). These two component structures are widely known as the spine-sheath model where a fast inner core is surrounded by a slower and denser counterpart in general. These two components may vary significantly in terms of physical properties and may affect the observations, depending on the component that dominates the emission of the jet. For example in Paraschos et al. (2022) there is a 2 decade review of 3C84 using observations at the radio frequencies. Observations at different wavelengths reveal different components of the outflow, consequently when they are combined a stratified jet structure is uncovered for both the Lorentz factor and the collimation profile respectively. The authors also suggest that the acceleration for this source is probably driven by the conversion of the Poynting flux into kinetic energy flux.

The internal structure of jets can also be probed by observations on the magnetic field carried by the outflows. This information can be extracted by analyzing the polarization of their emission. Pushkarev et al. (2023) conducted a polarization sensitive multi epoch survey from MOJAVE at 15 GHz including archival results from NRAO, totaling 436 sources. 5.3% show no signs of polarization where among the polarized sources the radio galaxies are the least polarized. A key result is that the analysis of the linear polarization component reveals magnetic field structures that maintain their large-scale structure as the separation from the central core increases. The polarization maps alongside the EVPA patterns suggest the existence of helical magnetic fields which show signs of shear interaction with their ambient medium for parsec-scale AGN jets.

The existence of helical magnetic field is also confirmed by other studies, in many cases this magnetic field topology is associated with spine-sheath configurations. Pushkarev et al. (2005) observe signs of spine-sheath structure in the polarization pattern of four AGN jets (3 BL Lac and one blazar objects). The magnetic field orientation observed is the element that supports this claim, as it is transverse near the jets' central ridge line and is roughly longitudinal at the edges of the jets. This pattern is detected at some distance from the base of the flow. Similarly, Gabuzda et al. (2014b) finds evidence of polarization that indicates towards a spine-sheath configuration of 8 AGNs. The orientation of the magnetic field of the outer jet is longitudinal with respect to the line of sight direction, while the inner counterpart has transverse orientation. The RM gradients support the existence of a helical magnetic field. Also, evidence of persisting RM gradient profiles is provided by the works of Contopoulos et al. (2009); Gabuzda et al. (2012); Christodoulou et al. (2016), in which the magnetic field creation and subsequent topology is explained by the model of the cosmic battery (Contopoulos &Kazanas, 1998). In a similar work in Lisakov et al. (2021) the jet from 3C273 presents persistent RM gradients of slices downstream the core (up to 500pc deprojected). There is evidence of an oversize sheath wrapped around a narrow single jet. The sheath seems to be disconnected from the jet and has no significant variability.

Nonetheless, there have been observations of small-scale field structures, hinting towards turbulent flow patterns. Gabuzda et al. (2014a) note that the RM gradients in the jet of 3C380 suggest the existence of a helical magnetic field. At 0.7 arcsec from core there is a conical shock where the field seems to become randomized and no systematic RM gradients are observed beyond this point. While this fact antagonizes the helical structure of the magnetic field, the spine-sheath scenario facilitates the co-existence of well-ordered and turbulent flow components in the same outflow. Kravchenko et al. (2017) focuses on 20 AGN jets showing both significant polarization and RM gradients. The authors note that the jets, per se, carry a well-ordered magnetic field (poloidal or toroidal) while sheaths have no preferred magnetic field orientation. Nonetheless, both ordered and random structures for the magnetic field of the sheaths are noted.

Finally, Laing (2015) provides details on kinematics and dynamics of kpc-scale jets in radio galaxies associated to their polarization properties from SKA1-MID results. Laing (2015) notes that in kpc scales jets on average are highly relativistic and intrinsically symmetric. The analysis categorizes the jets using the Fanaroff-Riley dichotomy (Fanaroff &Riley, 1974). FRI jets expand and recollimate to conical flows at distances $r_0 \simeq 2 - 15$ kpc from the nucleus. At $\approx 0.1 r_0$ a high emissivity region with $\sim 0.8c$ and uniform transverse profile emerges. From $\approx 0.2 r_0$ until $\approx 0.6 r_0$ the flows decelerate, the majority of the deceleration occurs near the boundary of the jet. The magnetic field is longitudinal near the AGN and mostly toroidal after the recollimation. FRII jets are either mildly relativistic ($\beta \approx 0.5 - 0.7; \gamma \approx 1.2 - 1.4$) or have two components with a relativistic spine surrounded by a much slower sheath which dominates the jet emission.

In summary, extragalactic jets display total lengths on the scale of $\sim$ kpc. An important number of sources present a change in their shape, most commonly from a parabolic to a conical configuration. These transitions occur at distances that may be associated with analogous changes in the status of the environment such as the Bondi radius or the distance of the gravitational effect of the galaxy. On the other hand, there are various sources that can not be associated with any relevant distance, therefore internal processes of the jet are assumed to influence the shape transition. The parabolic section of the outflows is usually linked to their acceleration, hence this section of the jets is also referred to as the acceleration and collimation zone. Observations of the structural complexity of the ACZ lead to the scenario of observing multi-component outflows, widely known in the literature as spine-sheath jets. There is evidence based on observations of polarization maps and the subsequent RM gradients that the outflows carry large scale helical magnetic fields. Nonetheless, this type of observation is not universal and there are counter examples of jets that do not show strong evidence of linear polarization or significant RM gradients. This indicates that possibly the large-scale structure is not valid, and that the field has become randomized. In the case of multiple component jets there is the possibility that well-ordered and small-scale magnetic fields may co-exist. This is achieved if one of the flow components is ordered while the other is a turbulent, randomized counterpart.

1.2 Theoretical modeling of jets

The observations discussed in section 1.1 are the test that the various models need to explain and replicate. There are different phenomena at different length scales that are utilized in order to formulate the models. Also there are different theoretical frameworks and different methodologies regarding the various stages of the jet formation and evolution.

1.2.1 Black hole matter accretion- Jet launching region

The first stage involves the accretion of matter into the black hole and the formation of the outflows. Theoretically the mechanism for the creation of jets requires a magnetized disk threaded by a poloidal magnetic field which accretes into the central engine. The rotation of the disk/central object creates a toroidal component which enables the formation of the outflow. For example in the literature this magnetic launching scenario was analyzed in the seminal publications of Blandford &Znajek (1977) and Blandford &Payne (1982). Similarly, Sauty &Tsinganos (1994) study the jet launching using meridionally self-similar models and Chantry et al. (2018) expand these models by including general relativity.

The scales that are relevant to this phase of a jet's evolution are of the order of the gravitational radius. At these scales and near the central object the effects described by the general theory of relativity are not negligible. One of the most successful ways to study the evolution of these systems is through the utilization of general relativistic magnetohydrodynamics (GRMHD) numerical codes. GRMHD schemes can evolve self-consistently the system and provide important results that can be compared with the theoretical models and the existing observations. A summary of the most recent results regarding GRMHD simulations is provided.

In most cases the initial configuration requires to place a torus of magnetized plasma in hydrostatic equilibrium at some specific distance from the central engine, usually in the range of a few tens of the gravitational radius. Alternatively an already formed disk can be initialized by specifying its configuration and properties. One of the key elements in the initialization process is the choice for the initial magnetic field configuration. For a torus, in most cases, the magnetic field is defined via the toroidal component of a vector potential, thus the magnetic field lies purely on the poloidal plane. A similar choice is usually made in the case of an already existing disk, where only a poloidal component for the magnetic field is considered.

The distribution of the magnetic field seems to be an important parameter. As an example Dihingia et al. (2021) studies the accretion process of thin magnetized disks in a modified Kerr-Schild metric for an axisymmetric flow. Initially the magneto-rotational instability (MRI) transports angular momentum and drives turbulence. The disks are threaded by a poloidal magnetic field and is characterized by the inclination of the field lines relative to the equatorial plane. The toroidal component of the magnetic field is created by the rotation and the subsequent winding of the poloidal magnetic field. As the inclination increases (field lines become more vertical) the disk becomes less magnetized. In the limit of very weak and vertical magnetic field the BZ (Blandford-Znajek; BZ) jet is not well developed. In general a multiple component outflow is formed, i.e. the rotation of the black hole drives the outflow and three regions are noticed, a low density funnel near the rotation axis followed by a disk-wind at the off equatorial part of the domain and finally the high density accretion disk near the equatorial plane. The topology of the magnetic field directly affects the jet properties. The wind density is associated with the inclination of the magnetic field in the disk, the higher the inclination the sparser the wind and the magnetic flux that it carries. The inner funnel is always less dense than the wind and has a parabolic shape while when the field is more inclined the funnel is more turbulent and vice versa. The higher the initial magnetization the faster the jet becomes at long distances away from the BH. The disk-wind has velocities of the order of $0.1 - 0.2c$ and its field lines become mainly azimuthal.

In the case of initializing simulation box without a preexisting disk, the torii carry a magnetic field aligned with the poloidal surface (e.g. see Tchekhovskoy et al., 2011; Mościbrodzka et al., 2016; Chashkina et al., 2021). The topology of the magnetic field inside the torus is indicated as an important factor. Chashkina et al. (2021) notes that initial configurations with no alternate polarities is the most efficient, as any possible phenomenon that can disrupt the accretion process (for example sites of magnetic reconnection in the disk) are minimized. Once again in these works the MRI amplifies and enables the accretion into the central object. In most cases and especially in 2D simulations, the disk becomes magnetically arrested (MAD) meaning that the accumulation of magnetic flux near the event horizon disrupts the accretion process. This is manifested through fluctuations in the accretion rate of mass/magnetic flux into the central engine or subsequently with fluctuations in the output of the outflow. The above phenomenon is mediated and the accretion rates become smoother when the simulation are 3D. This is due the freedom the plasma has to also move in the toroidal direction and overcome any flux barrier which in three dimensions is not homogeneous around the entire disk circumference (Chashkina et al., 2021; Chatterjee et al., 2019).

The magnetization of the disk near the launching region can also be characterized as the energy reservoir of the resulting jet. Near the jet base the disk is highly magnetized, this builds up the energy of the jet for the magnetic acceleration mechanism to be efficient. The conversion of the Poynting flux into mass energy flux is a crucial and viable mechanism for the jet to accelerate (Chatterjee et al., 2019; Tchekhovskoy et al., 2010). In order for the jets to sustain this acceleration, the poloidal field lines must show differential bunching; that is, the number of field lines must decrease with increasing distance from the axis (Tchekhovskoy et al., 2009; Dihingia et al., 2021), this result has also been discussed in works studying models of magnetic acceleration of AGN jets (e.g. see Komissarov et al., 2009, and references therein). This bunching leads to spine-sheath configuration for the outflows. Most importantly, the magnetic field topology may vary between these two components, especially in the case where one component may carry a well-ordered field and the other may show signs of turbulence. This last result is linked to the observations and serves as a possible mechanism for observing different topologies at different separation levels from the core.

Another important parameter for the formation of the outflow is the spin of the central engine. In Curd &Narayan (2023) the asymptotic behavior of the velocity field is associated with the black hole spin. For a highly relativistic outflow a spinning black hole is required, while a non-spinning counterpart provides a mildly relativistic jet. Similar results are also observed in Nakamura et al. (2018). Moreover, Nakamura et al. (2018) note that as spin value increases the poloidal magnetic field lines bunch towards the jet axis, therefore self-collimation mechanism of magnetic nozzle effect becomes important. The energy extraction from the central engine requires high spin parameters (Tchekhovskoy et al., 2011; Mościbrodzka et al., 2016). In addition these works indicate that the spin value also affects the magnetization, the shape and the topology of the magnetic field of the outflow.

Another important parameter is the mass loading of the outflow, especially in the case of a two component jet. The sheath is usually noted to show higher mass loading rates than the spine, this result explains the different traits noticed for the two components (spine is light and fast while the sheath is dense and slower). Along the central object spin and the shape of the magnetic field line (magnetic nozzle effect) the mass loading rates can also modify the velocity profile of the outflow, with higher rates leading to slower flows (Huang et al., 2020).

As was mentioned previously, all these mechanisms refer to length scales in the scale of the gravitational radius. Ideally, someone would like to simulate the launching of the jet self-consistently and watch its evolution until its termination point. This kind of work has not been done up until recently as they are computationally demanding and require a hefty amount of storage capacity. Nonetheless, as the resources that are available evolve such works begin to appear in the literature. For example in Lalakos et al. (2022) the Event Horizon scales are bridged with the Bondi radius scale using 3D GRMHD simulations. The Bondi radius is set to be 10^3 times the gravitational radius. The gas density is uniform for distances greater than the Bondi radius, and there is a cavity for distances smaller than this. Initially, the magnetic field is parallel to the axis of the black hole rotation and the accretion is matter dominated. The main result is that the emerging outflow overpowers the environment's pressure and is not disrupted when its energy is sufficiently high. This leads to outflows that can preserve their alignment along the polar axis, whereas weaker jets can be reflected more easily. At asymptotic timescales the accretion becomes magnetically arrested, meaning that only a small portion of the matter is accreted into the BH ($\sim 2\%$), the rest escapes through the outflow. The jet, in its initial phase, is cylindrical and later on becomes parabolic. No shape transition is noted at the Bondi radius.

To summarize, the GRMHD codes probe the accretion process and the eventual launching of the jet. The magnetic field configuration of the initial torus or disk is an important factor. It can affect the accretion rate of the matter and the accretion rate of the magnetic flux into the central engine, which in turn affects the properties of the outflow. Moreover the spin of the central engine is also a key parameter, high spin values are required in order to extract energy from the central engine. When the generated outflows consist of two components, an inner funnel (spine) surrounded by a disk wind (sheath) are observed. The funnel density is lower and the velocity higher in comparison to the sheath. The acceleration involves the conversion of Poynting flux into mass energy flux. Therefore the magnetization of the jet near its base is crucial, as the higher the magnetization the higher the asymptotic Lorentz factor can be. An important element for the magnetic acceleration mechanism is the bunching of the magnetic field lines on the poloidal plane. This mechanism requires the field lines to accumulate near the jet's axis and become sparser towards the jet's boundary. This acts as a magnetic nozzle effect and accelerates the flow even more. This result is in accordance to theoretical models on the acceleration of MHD outflows and the application on various types of collimated flows (e.g. see Li et al., 1992; Contopoulos, 1994; Vlahakis &Königl, 2001, 2003a,b; Vlahakis, 2004; Komissarov et al., 2009).

Finally, an alternate approach to study the accretion process and the launching of the jet has been available through the evolution of the computational methodologies. Particle-in-cell (PIC) simulations probe these processes by assuming the matter to consist of individual particles that interact with each other respecting the electromagnetic forces and any collisional processes. This way the evolution of the system depends only on the interactions of the particles and disregards any assumptions that any other theoretical framework makes, such as the MHD. For example this kind of studies can be found in Parfrey et al. (2019), Kin et al. (2023).

1.2.2 Propagation of jets through astrophysical environments

The first stage in an outflow life cycle is the accretion process, and its subsequent launching in the vicinity of the central engine. The observations clearly indicate that these cosmic flows extend to distances up to the scale of kpc. This means that the jets need to travel through vast spaces characterized by different physical traits. This propagation may affect and accordingly modify the characteristics of a traveling jet.

Apart from theoretical calculations the use of numerical schemes are very efficient in order to study the propagation of extragalactic jets through their respective surrounding media. In most cases an outflow is set to travel through various kind of environments, which are modeled using actual observational data.

For the jet propagation mainly two scenarios are prevalent in the literature. Either it occurs in a pre-existing empty funnel or in a symmetric ambient medium relative to the launching area. In the first case the funnel walls define the shape of the jet (Barniol Duran et al., 2017; Bromberg &Tchekhovskoy, 2016). Usually these outflows are axisymmetric, the evolution of the jet inside this funnel does not show strong evidence of deceleration and it can travel to large distances with ease as the resistance and the feedback from the environment are minimized. These funnels can be created by intermittent jet launching, or when merger ejecta move prior to the jet, for example this could be the case of a supernova explosion when two neutron stars merge. The shock wave is capable of creating this kind of sparse environments, therefore the jet that follows after the merging event can propagate through a funnel-type environment.

The jets that have to propagate through an ambient medium are usually referred to as headed jets throughout the literature. Essentially the jet needs to drill through the environment and naturally this process takes place on the head of the jet. The results of various simulations regarding the processes at this portion of the outflow may vary greatly. In the case of three dimensional simulations the head can wobble, this leads to higher drilling efficiency, smaller rates of deceleration for the jet head and higher propagation rate for the entire outflow Perucho et al. (2019). This drilling process and the wobbling is fueled by three dimensional asymmetries on the jet head or three dimensional instabilities occurring there. In some cases the phenomena associated with the drilling process may lead to possible bending of the jet head Mukherjee et al. (2020). This means that two dimensional simulations can not replicate these results and usually show less efficient jet propagation with more stable jet heads.

This part of the jet is a very dynamical component of the outflow. Due to the drilling process there are also shocks that form there. The shock and/or the instabilities heat up considerably material that passes through this region and creates a backflow that engulfs the jet. This new component is more commonly refereed to as the jet cocoon, and essentially is an overpressured hot plasma component in contact with the main jet. This cocoon is an extremely important element of the entire configuration. Firstly, it provides pressure support to the jet and helps it to collimate (Gottlieb et al., 2021a; Barniol Duran et al., 2017; Pavan et al., 2023; Urrutia et al., 2023). Through the jet head momentum or energy from the jet can be transferred towards the cocoon or the environment (Rossi et al., 2020; Bromberg &Tchekhovskoy, 2016). The aforementioned shock is able to transform magnetic or kinetic jet energy into thermal energy of the cocoon, while the efficiency of the conversion is affected by the wobbling of the jet head (Barniol Duran et al., 2017; Perucho et al., 2019). The jet head in most case decelerates, this deceleration is mainly driven by internal or cocoon-driven instabilities (Perucho et al., 2019) alongside the baryon loading of the outflow (Gottlieb et al., 2021a).

Apart from the jet head, internal shocks can also form in the propagating jets through recollimation of the outflows. Recollimation patterns are a chracteristic of an overpressurized configuration. Such a jet expands radially until the pressure becomes smaller than the corresponding pressure of the environment. The surrounding medium pushes the jet back until the two competing pressures are matched. At that point the jet recollimates and a shock is usually formed, thus as the flow passes through this shock it heats up and its pressure increases possibly leading to a new recollimation cycle Fromm et al. (2018); Massaglia et al. (2016); Urrutia et al. (2023); Matsumoto et al. (2021). These shocks may be viewed as bright spots inside the flow, and also may introduce a certain level of variability Pavan et al. (2023); Mukherjee et al. (2020). This process may repeat several times, thus the outflow shape exhibits a diamond-like pattern. Jets in pressure balance with their environments do not exhibit similar behavior.

The jet propagation is heavily influenced by the magnetic field carried by the outflow. For purely hydrodynamic outflows the initial laminar flow turns into turbulence after crossing a shock, as for example in the case of an outflow that has been recolimmated (e.g. see Massaglia et al., 2016; Matsumoto et al., 2021; Yates-Jones et al., 2021). Weak magnetic fields helps the jet to remain collimated at great distances from the central object (Massaglia et al., 2019). These weak fields are in the range of $\sigma \sim 0.01$, where σ is the magnetization and it is defined as the Poynting flux over the mass kinetic energy flux. Jets having even smaller σ behave similarly to the the purely hydrodynamic counterparts.

As it is mentioned above, slightly magnetized configurations exhibit enhanced stability and propagation properties. First, the turbulence is suppressed and even the instabilities are weakened when the magnetization value is appropriate (Massaglia et al., 2019; Matsumoto et al., 2021). When the magnetization decreases the dissipated energy stored in the cocoon increases and the material of the interface between the jet and the cocoon is mixed more intensely (Gottlieb et al., 2020). Moreover simulation results show that as the magnetization increases the baryon loading in the jet head halts due to the presence of magnetic pressure (Gottlieb et al., 2021b). Some studies also suggest that the magnetization of the environment may be beneficial for the jet's integrity even when the jet is purely hydrodynamic. In this case, as the magnetization of the environment increases the Lorentz factor of the jet increases and the number of recollimation shocks decrease, the jet may also become magnetized through the interaction with the surrounding medium (García-García et al., 2023). It is noted that the topology of the magnetic field of the jet in most cases becomes helical, even when the injected magnetic field may be purely azimuthal or poloidal (e.g. see Mukherjee et al., 2020; Soares et al., 2023). It should be highlighted that any further increase in the value of the magnetization start to have a negative effect on the stability profile of the jet. This is due to the kink type instabilities, usually current-driven instabilities, that tend to disrupt the overall linear shape of the jet. This disruption includes disposition of the axis, bending of the whole outflow and in some cases destruction of the outflow (e.g. see Massaglia et al., 2022; Soares et al., 2023). Therefore, the beneficial existence of the magnetic field needs to be constrained by limiting the magnetization value in the proper value range. Nonetheless, the mechanisms involved in the phenomena discussed above are not fully understood. The existence of magnetic fields in some cases may enhance the stability profile of the outflows but does not fully suppresses the effect that various kind of instabilities may have on the wide variety of configurations. In most cases the severe destabilization of the initial outflow eventually occurs.

The magnetization is not the only parameter that affects the propagation of the outflows. The power of the jet and its opening angle also influence the propagation of the outflows. In general the higher the power of the jet the more stable it becomes. This means that the jet propagates farther (Massaglia et al., 2022), it is less prone to instabilities (Barniol Duran et al., 2017; Mukherjee et al., 2020; Tchekhovskoy &Bromberg, 2016) and fro mainly hydrodynamic flows the number of recollimation shocks decrease as the power increases (Mandal et al., 2022). Decrease in the value of the opening angle enhance the propagation and the overall stability of the jets in general.

The really interesting point is that the interplay of these three parameters is seemingly the crucial factor shaping the jet properties. More powerful jets or narrower jets require smaller magnetization value in order for the flow to remain intact. Low power jets or wider jets require stronger magnetic fields for enhanced stability properties (Gottlieb et al., 2021a,b). In low power jets high magnetization may lead to sharp bends due to kink modes, while as the power increases less bending is observed and the collimation of the jets becomes enhanced for increasing magnetization values. Enhanced stability in high power jets is also provided by relativistic effects such as time dilation (Bromberg &Tchekhovskoy, 2016). These effects are able to suppress various kind of instabilities (Mukherjee et al., 2020). Finally, the FR dichotomy of extragalactic jets is associated with the jet power value, simulations of high powered jets are more frequently observed as FRII outflows while low powered jets as FRI counterparts (Massaglia et al., 2016; Tchekhovskoy &Bromberg, 2016). Nonetheless there are also other parameters, apart from the jet power, that possibly affect the type of a jet. Such example is the density of the jet, as low density jets tend to form FRI type of outflows (Massaglia et al., 2016).

The configuration of the environment, especially the density profile, can greatly affect the collimation and propagation properties of the outflow. The simulations confirm that steep changes in the density profile of the environment ensue modifications in the shape of the outflow (Barniol Duran et al., 2017). As the density of the environment increases the jet propagation is inhibited (Massaglia et al., 2022), the Lorentz factor of the jet decreases, while the energy and the density values of the cocoon are increased (Perucho et al., 2022).

To summarize, the propagation of the outflows through the ambient medium of the host galaxy or the intergalactic medium radically affects their properties. Regarding the jet environment the value and the spatial distribution of the density profile are the most important parameters. The denser the environment the greater the inhibition of the propagation rate is. Discontinuities in the density profile may create transitions in the shape of the jet or possibly ensue instabilities or asymmetries to the flow. The shock residing at the jet head shocks material both of the environment and the outflow and creates a surrounding cocoon full of thermal gas. This cocoon helps the collimation process of the jet while extracted energy from the jet is absorbed by the cocoon in the form of internal gas energy. The magnetic field possibly carried by the jet enhance its stability and aid it to propagate farther compared to purely hydrodynamic counterparts. This scenario is valid as long as the jets are slightly or moderately magnetized. In the case where the magnetization increases even further the configurations are disrupted due to kink modes introduced by current-driven instabilities. Apart from the magnetization, there are also other parameters affecting the jet properties. The studies note that the power carried by the jet and the opening angle at the injection site are also important. The more powerful a jet is the more stable it becomes. Enhanced stability is also observed as the outflows become narrower. The interplay of these three quantities is noted to be important regarding the behavior of the propagating outflow.

1.3 Instabilities of astrophysical jets

Instabilities are ubiquitous during the whole life cycle of an astrophysical jet. As it is mentioned in sections 1.2.1 and 1.2.2 the role of instabilities is of utmost importance in order for the jets to form and propagate through their respective environments. For example during the launching of the jet the magneto-rotational instability enables the accretion of matter and magnetic flux into the central engine. During the propagation phase the accumulation of magnetic flux near the jet head triggers kink instabilities, resulting to the propagation efficiency to be affected. The simulations also suggest that on the interface of the jet and the pressurized cocoon various kind of instabilities emanate and evolve.

In general instabilities that act upon an outflow tend to change its properties and transform the initial configuration into a new one. The outcome of this transformation may range greatly in terms of the structural integrity of the initial jet. For example a new altered quasi-steady/steady state outflow may arise or the initial flow can be totally disrupted. Apart from the large-scale structure of the jet the instabilities may influence many aspects of the configurations. For instance they can alter the energy distribution of the outflow or introduce shocks and various other features such as blobs into the flow.

There are two main methodologies one can utilize in order to study the various kind of instabilities. The first one, which is also introduced in section 1.2.2, involves numerical algorithms which evolve the configurations self-consistently. This can be achieved by introducing small perturbations in the unperturbed outflow state and then the numerical algorithm provides the onset and the evolution of the instabilities. Apart from the numerical schemes there are also semi-analytical methodologies such as the linear stability analysis. This method requires to introduce small perturbative terms into the equations describing the dynamics of the configuration and then generate either analytical or semi-analytical solutions which describe the evolution of the perturbed system. Thorough presentation of the linear stability analysis is provided in chapter 2.

There are various kind of instabilities that are associated with astrophysical jets. Among the many types there are two specific instabilities that are prominent in astrophysical jets and have been studied extensively in the literature. The first one arises when there are strong shear layers in the velocity profile of the outflow or two fluids with different velocities are in contact, this is the Kelvin-Helmholtz instability (KHI). The second one is associated with the existence of magnetic fields in the outflow, they are called current-driven instabilities (CDIs). Below there is a brief overview for the Kelvin-Helmholtz and the current-driven instability. In general these two instabilities are expected to affect mildly relativistic configurations carrying magnetic fields with weak to no rotation and a quasi-cylindrical or cylindrical geometry. This thesis focuses on this kind of configurations, therefore the interest is focused on the KHI and the CDI.

Begelman (1998) and Das &Begelman (2019) note that CDIs are driven by the current, which is parallel to the total magnetic field. Currents that are perpendicular to the total magnetic field are categorized as pressure driven, similar to those that are affected by the gradient of the thermal pressure. They also mention that current-driven effects are dominant when the poloidal magnetic field prevails over the toroidal counterpart.

The interplay between the components of the magnetic field is important regarding the evolution of the instability. Appl et al. (2000) highlighted that for a force-free column the CDI growth rates strongly depend on the pitch value of the magnetic field measured on the axis of the jet when the poloidal magnetic field is dominant. The shear of the pitch profile across the jet is important when the magnetic field is mainly azimuthal, highly sheared profiles reduce the instability growth rate. The same conclusion about the shearing of the magnetic field profile is also validated by Begelman (1998), Das &Begelman (2019) where strong gradients of the poloidal magnetic field tend to stabilize the CD modes. Moreover the same study highlights that the strength of the poloidal field also affects the locality of the modes, i.e. a strong poloidal component may transform localized solutions to global counterparts. Finally, the growth rate positively correlates with the magnetization of the outflow (Bodo et al., 2022).

In similar fashion Bodo et al. (2013) note that for a jet with a non-zero axial velocity field a purely longitudinal magnetic field does not trigger CDIs, while highly sheared counterparts have a stabilizing effect on the configurations. Moreover when the profile of the poloidal component of the magnetic field is constant the kink solutions tend to mainly affect the boundary of the jet. These surface solutions present dispersion relations proportional to the wavevector, similarly to the KH modes (Sobacchi &Lyubarsky, 2018). In the static case surfaces on which $\boldsymbol{k} \cdot \boldsymbol{B} = 0$ holds nurture CDIs, as the magnetic tension is absent there. This relation can provide a proper estimation for the triggering wavelength value of the mode. Lastly, Sobacchi et al. (2017) note that the kink solutions are also strongly correlated with the Lorentz factor, the higher the value of the Lorentz factor the more stable the jet becomes.

Apart from the magnetic field profile, non-constant profiles of other quantities may also regulate the behavior of the CDIs. For example, Mizuno et al. (2011) study a force-free sub-Alfvénic jet with helical magnetic field which shows sheared profile for both the velocity and the magnetic field. It is established that the ratio consisting of the width of the velocity shear over the radius of the magnetic field core affect the evolution of the kink mode. As this ratio increases so does the instability e-folding time, therefore the solution needs larger time intervals to grow. Also Singh et al. (2016) notice that radially decreasing density profiles enhances the instability growth rate. On the other hand, increasing density profile leads to more stable counterparts and favor fast and smooth large scale flows.

The non-linear evolution of the CDI includes a variety of phenomena such as energy dissipation and bending of the outflow/plasma column among others. Bromberg et al. (2019) note that the kink mode acting on force-free jets transform these configurations into jets attaining a minimal energy state. The electromagnetic energy dissipates into internal energy of the gas, this dissipation occurs mainly on current sheets and more prominently through magnetic reconnection events. Interestingly the pitch of the magnetic field affects the rate of dissipation. The process stops when the jet is in a new minimal energy state compared to the initial configuration.

The non-linear evolution of a force-free jet in Bodo et al. (2022) shows the emergence of turbulence in various parts of the jet, and the decrease in the electromagnetic energy carried by the jet which transforms mainly into the thermal counterpart. Higher magnetization

Figure 1.1: Kelvin-Helmholtz instability acting on a cloud formation in the sky above the city of Athens. The picture was taken from the premises of the National and Kapodistrian University of Athens.

leads to stronger current sheets in the non-linear phase. It should be noted that the existence of a poloidal magnetic field in the environment suppresses the evolution of the mixing and leads to more stabilized configurations. Mizuno et al. (2012) note that a poloidal magnetic field component without a strongly sheared profile suppresses the non-linear evolution of the kink mode, while the coupling of different wavelengths is crucial for the survivability of the jet in the non-linear phase, especially for rotating jets.

O'Neill et al. (2012) probe a force-free configuration in comparison to configurations which include pressure and rotation. The force-free constant pitch column saturates in the non-linear regime while the counterparts having thermal pressure lead to much more turbulent configurations. The rotation seems to hinder a little bit the deformation of the pressure carrying jets, nonetheless their evolution is more or less similar. In every configuration magnetic energy transforms into kinetic energy, then dissipation transforms these components into thermal energy. The existence of a poloidal component for the magnetic field saturates the CDI, while the plasma temperature does not affect its development.

Regarding the KHI the fundamental quantity is the velocity difference on the boundary of the two media. In terms of a moving flow against a static environment, it has been noted that extremely large differences in the velocity shear tend to stabilize the KH mode (Ferrari et al., 1978, 1980; Osmanov et al., 2008). In the case of ultra-relativistic outflows the same result applies, thus jets with high Lorentz factors are more stable than mildly relativistic counterparts (Ferrari et al., 1981).

Bodo et al. (2004) derived an analytical expression for the dispersion relation of the KH mode in the relativistic regime of a fully hydrodynamic configuration. The two media have opposite velocities and equal density values. Most importantly, the KH mode is stabilized when the relativistic Mach number surpasses a specific threshold, which equals to $\sqrt{2}$. This threshold is modified by the angle the mode's wavevector forms with the velocity field. Essentially, the results of the classic Newtonian configurations are generalized to the relativistic regime. Thus it is established that whenever the velocity difference of the two media becomes sufficiently large the KHI is stabilized.

The presence of magnetic fields is crucial for the development of the KH mode. A magnetic field that is parallel to both the velocity field and the wavevector tends to stabilize the KH mode (Ferrari et al., 1980, 1981). Osmanov et al. (2008) also confirm that the direction of the wavevector is critical for the resulting growth rate of the mode. When its direction is parallel to the magnetic field then higher velocity contrasts and strengthened magnetic fields stabilize the mode. It should be noted that increasing the velocity difference between the two flows eventually stabilizes the mode in both non-relativistic and relativistic regime regardless of the magnetic field strength or the wavevector direction.

In this fashion Chow et al. (2022) probe a planar vortex-sheet interface where a magnetized moving flow is in contact with a hydrodynamic static medium. It should be highlighted that the magnetic field has two components, one parallel to the velocity field and one that is perpendicular to the surface of the interface. In Chow et al. (2023) they set in contact two flows that are symmetrical with respect to the separation surface. Once more, the angle of the wavevector and the magnetic field is important. When this angle becomes almost orthogonal then the tension of the magnetic field is minimized and the instability is strengthened.

Berlok &Pfrommer (2019a) and Berlok &Pfrommer (2019b) probe the properties of the KHI in Cartesian and cylindrical geometries when shear is added in the velocity and density profile respectively. They note that when the region of the velocity shear increases then KH mode stabilizes regarding small wavelengths. Similar transitions of the density profile moderately weaken the KH mode. The KHI is stabilized when simultaneously the flow is subsonic or supersonic and the magnetic field is strengthened. If the same occurs when the velocity is trans-sonic the KHI is enhanced. The hydrodynamic configurations present higher mixing rates than the magnetized counterparts. This last result is also supported in Borse et al. (2021) where the existence of a helical magnetic field can damp the effects of the KHI, especially the evolution of the emerging vortices on the surface of the outflow. From a technical standpoint 3D simulations show increased rate of dissipation and mixing as the azimuthal motions caused by the KHI are not affected by the tension of the magnetic field (parallel to the velocity field) contrary to the 2D counterparts.

It should be noted that the two modes, KHI and CDI, are able to coexist and may affect at the same time the unperturbed outflows. For example, Cohn (1983) probe a non-relativistic magnetized jet surrounded by a magnetized environment. In the case of supersonic flows the velocity discontinuity drives the instabilities and small wavelengths are the most unstable. The instabilities associated to the magnetic field are dominant when the velocity of the jet becomes sufficiently small. For these cases denser jets tend to be more unstable.

Under certain circumstances the modes can not be distinguished from one to the other (Bodo et al., 2013). Nonetheless, there are ways to identify each solution, for example the KHI is insensitive to the sign of azimuthal wavenumber (Bodo et al., 2019). Therefore, the dispersion relation that does not change when the sign of the azimuthal wavenumber is modified hints towards the KHI. Kim et al. (2015) probe jets without current sheets on the boundary surface of the jet in the non-relativistic regime. In Kim et al. (2016) the same configuration is studied when the velocity profile is sheared. For both papers the jets show enhanced stability when they are current sheet free on the boundary in comparison to jets with current sheets on their surface. Also the velocity shear further enhances the stability of these jets. In Kim et al. (2017) and Kim et al. (2018) they repeat the study of this current sheet free configuration in the relativistic regime. The main finding is that the relativistic counterparts are more stable than the Newtonian counterparts while the non-existence of current sheets on the boundary still enhances the stability of these jets.

Briefly the magnetic field is important for both kind of instabilities. Especially the provided tension by the field can drastically change the development of the instabilities discussed above. For the CDIs the strength and the shear of the poloidal component of the magnetic field is also an important factor. Apart from these the density ratio of jet over the density of the environment and the shear of the density profile also affect the CDI. For the KHI the most important parameter is the velocity jump on the boundary surface of the two media. In the case of the magnetized Kelvin-Helmholtz the angle of the wavevector and the magnetic field seems to be a key factor regarding the instability evolution. An important result highlighted throughout the literature review is that for both kind of instabilities the relativistic outflows tend to be universally more stable than the non-relativistic counterparts.

Chapter 2

Theoretical framework

2.1 RMHD set of equations

Throughout this chapter the theoretical framework and the necessary tools in order to conduct linear stability analysis on cosmic outflows is established. The outflows of interest are assumed to consist of fully ionized, quasi-neutral, collisionless plasma. The outflows are assumed to be magnetized, i.e. carry electric and magnetic fields. The bulk velocity field is assumed to be relativistic. Throughout this thesis the system of equations describing the dynamics of these cosmic jets is the ideal relativistic magnetohydrodynamics set of equations, commonly abbreviated as RMHD (e.g. see Vlahakis 2023). This set consists of mass, momentum and energy continuity equations alongside Maxwell's and Ohm's laws.

$$\frac{\partial}{\partial t}\left(\gamma\rho_0\right) = -\nabla\cdot\left(\gamma\rho_0\boldsymbol{V}\right) , \tag{2.1}$$

$$\gamma\rho_0\left(\frac{\partial}{\partial t}+\boldsymbol{V}\cdot\nabla\right)\left(\xi\gamma\boldsymbol{V}\right) = -\nabla P + J^0\boldsymbol{E} + \boldsymbol{J}\times\boldsymbol{B}\,, \tag{2.2}$$

$$\left(\frac{\partial}{\partial t}+\boldsymbol{V}\cdot\nabla\right)\xi = \frac{1}{\rho_0}\left(\frac{\partial}{\partial t}+\boldsymbol{V}\cdot\nabla\right)P\,, \tag{2.3}$$

$$\nabla\cdot\boldsymbol{B} = 0\,, \tag{2.4}$$

$$\nabla\cdot\boldsymbol{E} = J^0\,, \tag{2.5}$$

$$\nabla\times\boldsymbol{E} = -\frac{\partial\boldsymbol{B}}{\partial t}\,, \tag{2.6}$$

$$\nabla\times\boldsymbol{B} = \boldsymbol{J} - \frac{\partial\boldsymbol{E}}{\partial t}\,, \tag{2.7}$$

$$\boldsymbol{E} = -\boldsymbol{V}\times\boldsymbol{B}\,. \tag{2.8}$$

$\boldsymbol{B}$, $\boldsymbol{E}$, $\boldsymbol{J}$ and J^0 are the magnetic field, electric field, current density and charge density respectively. The Heaviside-Lorentz unit system is adopted, hence magnetic and electric fields are over $\sqrt{4\pi}$. Also, $\boldsymbol{J}$, J^0 are multiplied with $\sqrt{4\pi}/c$ and $\sqrt{4\pi}$ respectively.

$\boldsymbol{V}$ is the outflow velocity field over c, $\gamma = \left(1 - \boldsymbol{V}^2\right)^{-1/2}$ is the Lorentz factor and ρ_0 is the rest mass density times c^2. P is the gas pressure and ξ is the specific enthalpy over c^2. Equation (2.8) is derived by Ohm's law when the conductivity is assumed to be infinite.

In order to close the system of equations (2.1)-(2.8), an equation of state is utilized, provided in the general form by $\xi = \xi(\Theta)$, where $\Theta = P/\rho_0$. The theory of relativistic perfect gases provide the relation between ξ and Θ (Synge, 1957):

$$\xi\left(\Theta\right) = \frac{K_3\left(1/\Theta\right)}{K_2\left(1/\Theta\right)}\,, \tag{2.9}$$

where $K_2,\ K_3$ are 2nd and 3rd degree modified Bessel functions of the second kind. Equation (2.9) under specific assumptions can be approximated by alternative formulas. In this thesis two common expressions are used. First one is the ideal eos (equation of state), which is widely employed in the literature. The relation is provided by:

$$\xi = 1 + \frac{\Gamma}{\Gamma - 1}\Theta\,, \tag{2.10}$$

where Γ is the constant polytropic index. The index value depends on the value of Θ. So, when the gas is relativistically hot, $\Theta \gg 1 \Rightarrow \Gamma = 4/3$, whereas when the gas tends to be near-cold/cold $\Theta \to 0 \Rightarrow \Gamma = 5/3$. In this case the sound velocity is given by

$$\begin{aligned} c_s^2 &= \frac{\Gamma P}{\rho_0 \xi} \xRightarrow{(2.10)} \\ c_s^2 &= \frac{(\Gamma - 1)(\xi - 1)}{\xi}\,. \end{aligned} \tag{2.11}$$

The drawback in equations (2.10),(2.11) is that when the temperature of a jet varies greatly and transcends between the two regimes, then the constant Γ approximation is not sufficient. A proper correction is provided by another approximation of equation (2.9), usually referred to as the Taub-Matthews eos and the corresponding formula is given by (Mignone &McKinney, 2007):

$$\xi\left(\Theta\right) = \frac{5}{2}\Theta + \sqrt{\frac{9}{4}\Theta^2 + 1}\,. \tag{2.12}$$

The advantage of (2.12) is that for both $\Theta \gg 1$ & $\Theta \ll 1$ the Taub-Matthews equation yields equation (2.10) with the correct Γ value. Equation (2.12) inherently provides ξ and c_s for Θ values that can not be assigned to neither of the two extreme cases. The corresponding sound speed is given by:

$$c_s^2 = \frac{\Theta}{\xi}\,\frac{d\xi/d\Theta}{d\xi/d\Theta - 1}\,. \tag{2.13}$$

2.1.1 Unperturbed outflow state

The aim of the linear stability analysis is to introduce small perturbations into a jet configuration and observe the evolution of the various instabilities that arise and modify the initial state of the outflow. The outflows are assumed initially to be cylindrical, steady-state ($\partial_t = 0$) and every quantity depends solely on the radius ϖ, which is translated to $\partial_\phi = \partial_z = 0$. The assumed coordinate system is cylindrical where ϖ, ϕ and z are the cylindrical radius, the azimuth and the axial coordinate respectively. The radial components for both the velocity and the magnetic field are always assumed to be zero, $B_\varpi = V_\varpi = 0$. The most general forms for the velocity and the magnetic field are given by $\boldsymbol{V} = V_z\hat{z} + V_\phi\hat{\phi}$ and $\boldsymbol{B} = B_z\hat{z} + B_\phi\hat{\phi}$ respectively. In order to filter any other dynamical phenomena the initial jet setup needs to be dynamically stable and in force balance with the surrounding medium. This is achieved when the unperturbed physical quantities obey the radial component of the momentum equation (2.2):

$$\frac{B_\phi^2 - E^2}{\varpi} - \xi\rho_0\frac{\gamma^2 V_\phi^2}{\varpi} + \frac{d\Pi}{d\varpi} = 0\,. \tag{2.14}$$

The first term is related to the magnetic field tension, the second one is the centrifugal term and finally the third one is related to the force exerted by the total pressure. The total pressure is denoted with Π and the quantity is provided by:

$$\Pi = \frac{B^2 - E^2}{2} + P\,. \tag{2.15}$$

In order to establish a new unperturbed state, a common strategy is to choose the profiles for every quantity apart from one and then solve equation (2.14) with regards to the remaining quantity. For example, in Bodo et al. (2013, 2019) where a cold jet is assumed ($\xi = 1$), equation (2.14) is solved with regards to V_ϕ while every other quantities' profile is defined by the authors. In the following chapters a variety of unperturbed models and their derivation is presented.

2.2 Linear Stability Analysis

2.2.1 Linearization

In order to study the stability properties of the outflows in the linear regime, equations (2.1)-(2.8) and the equation that closes the system need to be perturbed. This is achieved by inserting small perturbations for every physical quantity

$$Q(\varpi,\ \phi,\ z,\ t) = Q_0(\varpi) + \delta Q(\varpi,\ \phi,\ z,\ t)\,, \tag{2.16}$$

where Q_0 and δQ are the unperturbed quantities and the small perturbations respectively.

Since the zeroth order quantities depend only on the radius, the perturbations can be analyzed into Fourier parts, $\delta Q(\varpi,\ \phi,\ z,\ t) = Q_1(\varpi)\exp[i(-\omega t + kz + m\phi)]$ where $|Q_1| \ll |Q_0|$.

If it is assumed that the growth of the instabilities is time-dependent then the temporal approach is adopted, so $\omega = \mathrm{Re}(\omega) + i\mathrm{Im}(\omega)$ is complex, while k is real and m is integer. Modes with $\mathrm{Im}(\omega) > 0$ are unstable and modes with $\mathrm{Im}(\omega) \leq 0$ are characterized as stable. The equality $\mathrm{Im}(\omega) = 0$ corresponds to marginally stable solutions. This can be seen by inserting ω into equation (2.16) which takes the form $\delta Q = Q_1 \exp[\mathrm{Im}(\omega)t]\exp[i\,(-\mathrm{Re}(\omega)t + kz + m\phi)]$. The time dependent amplitude is the product $Q_1\exp[\mathrm{Im}(\omega)t]$, so in the case of unstable modes the complex amplitude grows exponentially in the linear regime.

The linearization process is quite demanding and tedious. The final form of the linearized system consists of ten equations, which are analytically presented in Vlahakis (2023). A useful overview of the full system is presented by equation (2.17). This form of the system is achieved after the proper algebra has been applied to the initial linearized set of equations

$$\frac{d}{d\varpi}\begin{pmatrix} y_1 \\ y_2 \end{pmatrix} + \frac{1}{\mathcal{D}}\begin{pmatrix} \mathcal{F}_{11} & \mathcal{F}_{12} \\ \mathcal{F}_{21} & \mathcal{F}_{22} \end{pmatrix}\begin{pmatrix} y_1 \\ y_2 \end{pmatrix} = 0\,, \tag{2.17}$$

where $y_1 = i\frac{\varpi V_{1\varpi}}{\omega_0}$, $y_2 = \Pi_1 + \frac{y_1}{\varpi}\frac{d\Pi_0}{d\varpi}$ and $\omega_0 = \omega - kV_z - mV_\phi/\varpi$. y_1 is associated to the Lagrangian displacement, a physical quantity that measures the deviation of the flow's field lines with respect to their initial position. y_2 is associated to the total pressure perturbation. These two variables are the unknowns of the system, while the $\mathcal{F}$ & $\mathcal{D}$ coefficients (functions of ϖ) consist of unperturbed quantities, their respective derivatives and factors related to the Fourier transform. See appendix A for a brief but more detailed overview of the linearization process.

2.2.2 Boundary conditions

The problem at hand is a boundary conditions problem. In order to find the unstable modes, boundary conditions have to be imposed to the solutions of system (2.17). There are three points of interest in the computational box. The first one is the axis of the jet, where the solutions are required to remain finite. The exact same condition also holds for very long distances from the jet, so as $\varpi \to \infty$ the solutions need to vanish. From this point on-wards jet's radius is denoted with ϖ_j.

The final point of interest is the boundary surface of the jet. As the environment and the jet have most likely different configurations, this means that the solutions are going to be different for the two media. The physically acceptable solutions are the functions which are continuous on the perturbed boundary surface of the jet. This statement is expressed with:

$$y_1\big|_{\varpi\to\varpi_j^-} = y_1\big|_{\varpi\to\varpi_j^+}\,, \tag{2.18}$$

$$y_2\big|_{\varpi\to\varpi_j^-} = y_2\big|_{\varpi\to\varpi_j^+}\,. \tag{2.19}$$

2.2.3 Numerical procedure

The computational domain consists of two distinct areas. The first one is the jet $\varpi \leq \varpi_j$ and the second one is the surrounding medium $\varpi > \varpi_j$. The environment is considered to be static, with a constant profile for its density. The pressure can be either thermal or magnetic and the corresponding profile is also assumed to be constant. In the case of a magnetized environment the magnetic field has only a z-component. Under these assumptions (2.17) yields a Bessel differential equation provided by (2.20)

$$\varpi^2\Pi_1'' + \varpi\Pi_1' + \left(\lambda^2\varpi^2 - m^2\right)\Pi_1 = 0\,, \tag{2.20}$$

where λ is given by:

$$\lambda^2 = \frac{\left(1+U_A^2\right)\left[\left(\omega_{co}/k_{coz}\right)^2 - U_A^2/\left(1+U_A^2\right)\right]\left[\left(\omega_{co}/k_{coz}\right)^2 - c_s^2\right]}{\left(c_s^2+U_A^2\right)\left[\left(\omega_{co}/k_{coz}\right)^2 - U_A^2c_s^2/\left(c_s^2+U_A^2\right)\right]}k_{coz}^2\,, \tag{2.21}$$

with $U_A^2 = (B^2 - E^2)/(\rho_0\xi)$ being the Alfvén four velocity, $\omega_{co} = \gamma(\omega - kV_z)$ and $k_{coz} = \gamma(k - \omega V_z)$ are ω and k in the co-moving reference frame respectively. Due to the fact that the environment can be either purely hydrodynamic or magnetized λ^2 greatly simplifies to $\lambda^2 = (\omega_{co}/c_s)^2 - k_{coz}^2$ or $\lambda^2 = (\omega_{co}/\upsilon_A)^2 - k_{coz}^2$ respectively. $\upsilon_A^2 = U_A^2/(1+U_A^2)$ is the Alfvén three velocity.

The solution of (2.20) is a Hankel function of the first kind (e.g. see Hardee, 2007), $H_m^{(1)}\left(\lambda\varpi\right) = J_m\left(\lambda\varpi\right) + iY_m\left(\lambda\varpi\right)$ with J_m and Y_m Bessel equations of first and second kind respectively. The choice of $H_m^{(1)}$ is based on the asymptotic behavior of the function for $\varpi \gg \varpi_j$, as it represents a wave propagating away from the jet with diminishing amplitude $H_m^{(1)} \propto \varpi^{-1/2}\exp(i\lambda\varpi)$. It is required that there are no perturbations originating from large distances away from the jet, which are able to affect the configuration. It should be noted that $\mathrm{Im}(\lambda) > 0$ for the function to diminish at infinity.

The system for the jet's interior (2.17) is perplexed, making the effort to find analytic solutions very demanding. Nearly every configuration is treated numerically, so a shooting method is utilized to find the unstable modes. The integration starts from a point in the proximity of the axis and ends on the boundary of the jet, where the boundary conditions (2.18) and (2.19) are applied between the numerical solution and the analytical expression of the environment.

Technically, the boundary conditions (2.18) and (2.19) consist of four components as the eigenfunctions are complex functions of the radius. Thus, the numerical procedure must match $[\![\mathrm{Re}(y_1)]\!]$, $[\![\mathrm{Im}(y_1)]\!]$, $[\![\mathrm{Re}(y_2)]\!]$, $[\![\mathrm{Im}(y_2)]\!]$, where $[\![\cdot]\!]$ denotes the jump on the discontinuity surface for the quantity in the brackets. As the differential system (2.17) is linear, there is the option to multiply the solutions with a complex constant. This eases the numerical procedure as two of the four boundary conditions can always be fulfilled. Suppose that for $\varpi \geq \varpi_j$ the solution is $y_{01}(\varpi)$, $y_{02}(\varpi)$ and for $\varpi < \varpi_j$ the numerical integration provides y_1, y_2. If $y_2(\varpi = \varpi_J^-) = c+id$ and $y_{02}(\varpi_j) = f+ig$ then by modifying the solutions for $\varpi \geq \varpi_j$,

$$y_1 = \frac{cg + df + i\,(dg - cf)}{g^2 + f^2} y_{01}, \;\; y_2 = \frac{cg + df + i\,(dg - cf)}{g^2 + f^2} y_{02}\,, \tag{2.22}$$

both $[\![\mathrm{Re}(y_2)]\!] = 0$, $[\![\mathrm{Im}(y_2)]\!] = 0$ are automatically satisfied. The other two conditions which are yet to satisfied can be written as

$$\begin{aligned} Re\left[y_1(\varpi = \varpi_j^-)\right] &= \frac{cg + df}{g^2 + f^2} Re\left[y_{01}(\varpi = \varpi_j)\right] - \frac{dg - cf}{g^2 + f^2} Im\left[y_{01}(\varpi = \varpi_j)\right]\,, \\ Im\left[y_1(\varpi = \varpi_j^-)\right] &= \frac{cg + df}{g^2 + f^2} Im\left[y_{01}(\varpi = \varpi_j)\right] + \frac{dg - cf}{g^2 + f^2} Re\left[y_{01}(\varpi = \varpi_j)\right]\,. \end{aligned}$$

At this point the solution algorithm is complete. The implementation of the algorithm into a numerical code has been fulfilled by professor N. Vlahakis. In general, the program utilizes a shooting method in order to produce the dispersion relation of each mode. There are two main modules, the first one traces the solutions for a specific k value, which is then used as an initial guess for the iterative module which generates the dispersion relation. The code accepts as input the profile of the jet's physical quantities , the values of k, m and the setup of the environment. The solutions for the environment are analytical as was shown previously, hence for $\varpi \geq \varpi_j$ there is no need for numerical integration. Next, the ω-plane in which the first module searches for possible solutions needs to be defined. In order to trace the possible solutions on the plane, the difference of the eigenfunctions on the boundary of the jet is usually plotted.

Figure 2.1 depicts the ω-plane for specific values of k, m. Horizontal axis shows $\mathrm{Re}(\omega)$ and vertical axis $\mathrm{Im}(\omega)$ respectively. The quantities are normalized for the jet's radius light crossing time. The lines are contour plots of the difference between the eigenfunctions on the boundary of the jet. The value of the contour is set to zero, hence every time the orange and green lines cross, a possible solution is pinpointed. As an example, in figure 2.2 the eigenfunctions of a solution for a jet without current sheet on the boundary of the outflow (Sinnis, 2016) are plotted along the radial direction. Note the continuity of the functions at $\varpi = \varpi_j$, as well as the diminishing amplitude for the solutions as $\varpi \to \infty$.

The second module carries out the iterative process which generates the dispersion relation for each mode. The initial guess provided by the previous step is given as input, and then the program numerically integrates the solutions from the axis until the boundary

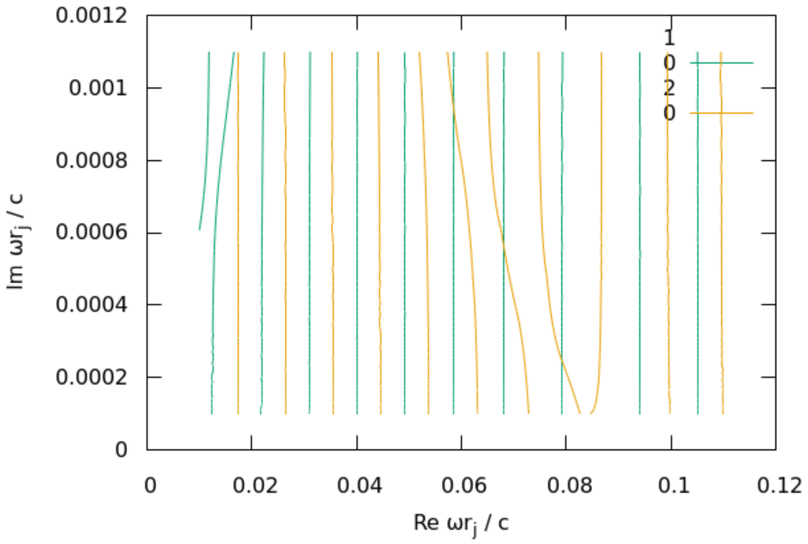

Figure 2.1: Plot of ω-plane, horizontal axis is Re(ω) and vertical axis is Im(ω), in jet's radius light crossing time for a specific k value . Orange and green lines are contour plots of real and imaginary parts of $[\![y_1]\!]$ respectively. The value of every line in the ω plane is zero.

of the jet, where the boundary conditions are applied. If the match on the boundary surface is accomplished, the routine keeps this solution as the new initial guess and reiterates for a new slightly different k value.

Section 2.2 briefly showcases the steps and the outline of the underlying mathematical processes needed for someone to conduct linear stability analysis on a cylindrically symmetric outflow. For a more detailed and extensive analysis on the expressions, their derivation, and the boundary conditions on the rotation axis, see Vlahakis (2023).

2.3 WKBJ approximation

As was demonstrated in section 2.2, the numerical methodology provides the eigenfunctions of the linearized system of equations for both the jet and the environment entire cross section. Due to this fact these solutions are also referred as global solutions. Someone, however, could be interested to probe the local properties of the system at some specific radius. This can be done by applying the WKBJ approximation on system 2.17. At this point, it should be noted that instead of the differential system 2.17, the solutions can be obtained by expressing one eigenfunction in terms of the other and solve a second degree differential equation with respect to the independent eigenfunction. Such an example is provided by equations (2.23) and (2.24). The eigenfunction y_1 is found by solving the differential equation:

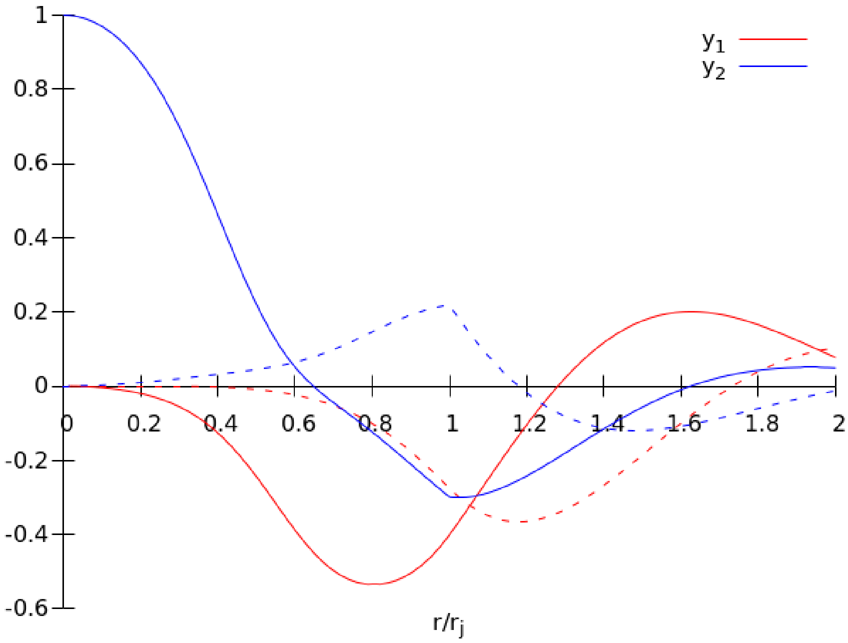

Figure 2.2: Eigenfunctions' plot across the outflow. Solid lines represent real parts of the eigenfunctions and dashed lines the imaginary counterparts.

$$y_1'' + \left[\frac{\mathcal{F}_{11}+\mathcal{F}_{22}}{\mathcal{D}} + \frac{\mathcal{F}_{12}}{\mathcal{D}}\left(\frac{\mathcal{D}}{\mathcal{F}_{12}}\right)'\right] y_1' + \left[\frac{\mathcal{F}_{11}\mathcal{F}_{22}-\mathcal{F}_{12}\mathcal{F}_{21}}{\mathcal{D}^2} + \frac{\mathcal{F}_{12}}{\mathcal{D}}\left(\frac{\mathcal{F}_{11}}{\mathcal{F}_{12}}\right)'\right] y_1 = 0\,, \tag{2.23}$$

while the corresponding y_2 is given by:

$$y_2 = -\frac{\mathcal{D}y_1' + \mathcal{F}_{11}y_1}{\mathcal{F}_{12}}\,, \tag{2.24}$$

for details on the derivation of equations (2.23) and (2.24) refer to Vlahakis (2023).

WKBJ assumes that $y_1 \propto \exp(ik_\varpi \varpi)$ and requires $||k_\varpi||\varpi \gg 1$, k_ϖ is assumed to be complex. Essentially by demanding $||k_\varpi||\varpi \gg 1$, the eigenfunction y_1 rapidly varies across the jet in comparison with the physical quantities of the background.

The coefficients of differential equation (2.23) consist of $\mathcal{F}_{ij}/\mathcal{D}$, $i,j=\{1,2\}$ and their respective derivatives. Hence, it is required to know the expression of the $\mathcal{F}$ factors in order to be able to solve equation (2.23) and find y_2 by using (2.24). The analysis below assumes that the jet does not rotate and has constant velocity in the z-direction, i.e. $V_\phi = 0$ and constant V_z. The expressions for $\mathcal{F}$ variables are given by:

$$
\begin{aligned}
\mathcal{F}_{11} = {}& \frac{\gamma\rho^3\xi^3}{\varpi^2} U_{A\phi}\omega_{co}^2 \Big\{ U_{A\phi}(1+U_A^2)\omega_{co}^4 - \big[U_{A\phi}(\boldsymbol{k_{co}}\cdot\boldsymbol{U_A})^2 c_s^2 \\
& + (U_A^2+c_s^2)(2k_{co\phi}\boldsymbol{k_{co}}\cdot\boldsymbol{U_A} - U_{A\phi}k_{co}^2)\big]\omega_{co}^2 + (\boldsymbol{k_{co}}\cdot\boldsymbol{U_A})^2 \\
& (2k_{co\phi}\boldsymbol{k_{co}}\cdot\boldsymbol{U_A} - U_{A\phi}k_{co}^2)c_s^2 \Big\}, && (2.25)\\
\mathcal{F}_{12} = {}& -\gamma\xi^2\rho^2\omega_{co}^2 \Big\{ (1+U_A^2)\omega_{co}^4 - \big[k_{co}^2(c_s^2+U_A^2) + (\boldsymbol{k_{co}}\cdot\boldsymbol{U_A})^2 c_s^2\big]\omega_{co}^2 + \\
& k_{co}^2(\boldsymbol{k_{co}}\cdot\boldsymbol{U_A})^2 c_s^2 \Big\}, && (2.26)\\
\mathcal{F}_{21} = {}& \big[(\boldsymbol{k_{co}}\cdot\boldsymbol{U_A})^2 - (1+U_A^2)\omega_{co}^2\big] \frac{\xi\rho}{\varpi}\mathcal{D} + \frac{\gamma\xi^4\rho^4}{\varpi^4} U_{A\phi}^2\omega_{co}^2 \\
& \Big\{ (\boldsymbol{k_{co}}\cdot\boldsymbol{U_A})^2 c_s^2 \left[4k_{coz}U_{Az}(\boldsymbol{k_{co}}\cdot\boldsymbol{U_A}) + U_{A\phi}^2 k_{co}^2\right] - \\
& \big[4(\boldsymbol{k_{co}}\cdot\boldsymbol{U_A})(c_s^2+U_A^2)k_{coz}U_{Az} + U_{A\phi}^2 k_{co}^2(c_s^2+U_A^2) + \\
& U_{A\phi}^2 c_s^2(\boldsymbol{k_{co}}\cdot\boldsymbol{U_A})^2\big]\omega_{co}^2 + U_{A\phi}^2(1+U_A)^2\omega_{co}^4 \Big\}, && (2.27)\\
\mathcal{F}_{22} = {}& -\mathcal{F}_{11}\,. && (2.28)
\end{aligned}
$$

Finally, $\mathcal{D}$ is provided by:

$$
\mathcal{D} = -\frac{\gamma\xi^3\rho^3}{\varpi}\omega_{co}^2\left[(1+U_A^2)\omega_{co}^2 - (\boldsymbol{k_{co}}\cdot\boldsymbol{U_A})^2\right]\left[(c_s^2+U_A^2)\omega_{co}^2 - c_s^2(\boldsymbol{k_{co}}\cdot\boldsymbol{U_A})^2\right], \qquad (2.29)
$$

where $\boldsymbol{k_{co}} = \gamma\,(k-\omega V_z)\,\hat{z} + \frac{m}{\varpi}\hat{\phi}$. Next, if $y_1 \propto \exp(ik_\varpi\varpi)$ is inserted into (2.23) then the equation transforms into:

$$
k_\varpi^2 - i\frac{\mathcal{F}_{12}}{\mathcal{D}}\left(\frac{\mathcal{D}}{\mathcal{F}_{12}}\right)' k_\varpi - \left[\frac{\mathcal{F}_{11}\mathcal{F}_{22} - \mathcal{F}_{12}\mathcal{F}_{21}}{\mathcal{D}^2} + \frac{\mathcal{F}_{12}}{\mathcal{D}}\left(\frac{\mathcal{F}_{11}}{\mathcal{F}_{12}}\right)'\right] = 0\,. \qquad (2.30)
$$

Equation (2.30) is a quadratic equation with respect to k_ϖ. The solutions are provided by:

$$
k_\varpi = \frac{-B \pm \sqrt{B^2-4AC}}{2A}, \qquad (2.31)
$$

where $A=1$, $B = -i\frac{\mathcal{F}_{12}}{\mathcal{D}}(\frac{\mathcal{D}}{\mathcal{F}_{12}})'$ and $C = -\left[\frac{\mathcal{F}_{11}\mathcal{F}_{22} - \mathcal{F}_{12}\mathcal{F}_{21}}{\mathcal{D}^2} + \frac{\mathcal{F}_{12}}{\mathcal{D}}\left(\frac{\mathcal{F}_{11}}{\mathcal{F}_{12}}\right)'\right]$. Equation (2.31) provides the value of the radial wavenumber k_ϖ. The value of k_ϖ defines the properties of the approximated eigenfunction. This can be seen as $k_\varpi = \mathrm{Re}(k_\varpi) + i\mathrm{Im}(k_\varpi) \Rightarrow$

$y_1 \propto e^{i\mathrm{Re}(k_\varpi)\varpi} e^{-\mathrm{Im}(k_\varpi)\varpi}$. The first factor is an oscillating term while the second factor is an exponential growth term with respect to the radius. For $\mathrm{Im}(k_\varpi) < 0$ the eigenfunction increases exponentially as the radius increases, while for $\mathrm{Im}(k_\varpi) > 0$ the solution diminishes as the radius increases. When $\mathrm{Im}(k_\varpi) = 0$ then the solution has a non radius-dependent amplitude across the jet. Moreover, if $\mathrm{Re}(k_\varpi) = 0$ the solution is non-oscillatory along the $\hat{\varpi}$ direction, but shows an exponential increase or decay accordingly to the value of $\mathrm{Im}(k_\varpi)$. Thus, the different roots of equation (2.31) may be associated with solutions which present different traits. For a detailed analysis of the WKBJ approximation applied on the RMHD set of equations see section 4 of Vlahakis (2023).

2.4 Linear stability analysis in Cartesian geometry

The linear stability analysis can also be conducted for different type of outflow geometries. In section 2.2 the analysis presented assumes cylindrical geometry. Linear stability analysis in Cartesian geometry also provides insightful and important results regarding astrophysical outflows. As an example, if the wavelengths of the instabilities invoked by the fluids in contact are significantly smaller than the rest of the characteristic length scales of the system, then the results of the Cartesian geometry can be an efficient and accurate approximation of the corresponding results in cylindrical geometry.

It is assumed that two fluids are in contact, their interface coincides with the $y - z$ plane, therefore the $\hat{x}$ direction is perpendicular to the respective contact surface of the two media. The first fluid is considered to be the "jet", so it is assumed to be a magnetized relativistic fluid. The unperturbed velocity field is of the form $\boldsymbol{V} = V_y\hat{y} + V_z\hat{z}$ and the respective unperturbed magnetic field of the form $\boldsymbol{B} = B_y\hat{y} + B_z\hat{z}$, so throughout this section $B_x = V_x = 0$. The second fluid is considered to be the "environment", thus it is a static fluid that can, in general, include both a thermal pressure component and magnetic fields. Also, for the environment B_x and V_x are also assumed to be zero. Every unperturbed physical quantity either in the "jet" or in the "environment" is considered to be constant. Also, the configuration is stationary, i.e. $\partial_t = 0$. Finally, the two media are initially in pressure balance.

2.4.1 Linearization in Cartesian geometry

To linearize the system of the RMHD set of equations (see section 2.1) the quantities are needed to be perturbed as showcased below:

$$Q(x, y, z, t) = Q_0 + \delta Q(x, y, z, t)\,. \tag{2.32}$$

The perturbation can be analyzed into Fourier parts $\delta Q = Q_1 \exp[i(-\omega t + \boldsymbol{k}\cdot\boldsymbol{r})]$, where $\boldsymbol{k}\cdot\boldsymbol{r} = k_x x + k_y y + k_z z$, Q_0 is the unperturbed quantity and Q_1 is the complex amplitude of the perturbation. This kind of analysis of the perturbation into Fourier parts is doable as the zeroth-order quantities are constant and do not depend on t or any spatial variable.

This means that the differential equations become algebraic if the perturbation are inserted into the system. The terms involving differential operators are transformed into algebraic terms following:

$$\begin{aligned}
&\nabla \cdot \delta \boldsymbol{Q} = i\boldsymbol{k} \cdot \delta \boldsymbol{Q}\,, \\
&\nabla \times \delta \boldsymbol{Q} = i\boldsymbol{k} \times \delta \boldsymbol{Q}\,, \\
&\nabla \delta \Phi = i\boldsymbol{k} \delta \Phi\,, \\
&\frac{\partial \delta \boldsymbol{Q}}{\partial t} = -i\omega \delta \boldsymbol{Q},\ \frac{\partial \delta \Phi}{\partial t} = -i\omega \delta \Phi\,, \\
&(\boldsymbol{D} \cdot \nabla)\delta \boldsymbol{Q} = i(\boldsymbol{k} \cdot \boldsymbol{D})\delta \boldsymbol{Q},\ (\boldsymbol{D} \cdot \nabla)\delta \Phi = i(\boldsymbol{k} \cdot \boldsymbol{D})\delta \Phi\,.
\end{aligned}$$

$\delta \boldsymbol{Q}$, $\delta \Phi$ are random perturbations of a vector and a scalar quantity respectively. Also, $\boldsymbol{D}$ is a random vector of the Cartesian space.

The linearization of the Lorentz factor yields:

$$\gamma_1 = \gamma_0^3 (\boldsymbol{V}_0 \cdot \boldsymbol{V}_1)\,. \tag{2.33}$$

The linearization of the three conservation equations yields:

$$(2.1) \Rightarrow \gamma_1 \rho_{00} + \gamma \rho_{01} = \gamma \rho_{00} \frac{\boldsymbol{k} \cdot \boldsymbol{V}_1}{\omega_0}\,, \tag{2.34}$$

$$(2.3) \Rightarrow \xi_1 = \frac{P_1}{\rho_{00}} \tag{2.35}$$

$$(2.2) \Rightarrow -i\omega \left(\xi_1 \gamma_0 \boldsymbol{V}_0 + \xi_0 \gamma_1 \boldsymbol{V}_0 + \xi_0 \gamma_0 \boldsymbol{V}_1\right) = -i\boldsymbol{k} P_1 + J_1^0 \boldsymbol{E}_0 + \boldsymbol{J}_1 \times \boldsymbol{B}_0\,. \tag{2.36}$$

where $\omega_0 \equiv \omega - \boldsymbol{k} \cdot \boldsymbol{V}$. The linearization of the Maxwell's equations yields:

$$(2.4) \Rightarrow i\boldsymbol{k} \cdot \boldsymbol{B}_1 = 0\,, \tag{2.37}$$

$$(2.5) \Rightarrow i\boldsymbol{k} \cdot \boldsymbol{E}_1 = J_1^0\,, \tag{2.38}$$

$$(2.6) \Rightarrow \boldsymbol{k} \times \boldsymbol{E}_1 = i\omega \boldsymbol{B}_1\,, \tag{2.39}$$

$$(2.7) \Rightarrow i\omega \boldsymbol{E}_1 + i\boldsymbol{k} \times \boldsymbol{B}_1 = \boldsymbol{J}_1\,. \tag{2.40}$$

It should be noted that equation (2.37) is fulfilled automatically by equation (2.39). The linearization of the ideal Ohm's law yields:

$$(2.8) \Rightarrow \boldsymbol{E_1} = -\boldsymbol{V} \times \boldsymbol{B_1} - \boldsymbol{V_1} \times \boldsymbol{B}\,. \tag{2.41}$$

Also, equation (2.13) is used to relate the the perturbations of the quantities with the speed of sound. An alternative formula to equation (2.13) is given by:

$$\begin{aligned}
&c_s^2 = \frac{\Theta/\xi}{1 - d\Theta/d\xi} \Leftrightarrow \\
&\frac{d\Theta}{dt} = \left(1 - \frac{\Theta}{\xi c_s^2}\right)\frac{d\xi}{dt} \Leftrightarrow \\
&\frac{1}{\rho_{00}}\frac{dP}{dt} - \frac{P}{\rho_{00}^2}\frac{d\rho_{00}}{dt} = \left(1 - \frac{\Theta_0}{\xi_0 c_s^2}\right)\frac{d\xi_0}{dt}\,.
\end{aligned} \tag{2.42}$$

where $d/dt \equiv (\partial/\partial t + \boldsymbol{V}\cdot\nabla)$. The linearization of equation (2.42) yields:

$$\begin{aligned}
&\frac{P_1}{\rho_{01}} - \frac{P}{\rho_{00}^2}\rho_{01} = \left(1 - \frac{\Theta_0}{c_s^2\xi_0}\right)\xi_1 \overset{(2.36)}{\Longrightarrow} \\
&P_1 = c_s^2\xi\rho_{01}\,.
\end{aligned} \tag{2.43}$$

Then equation (2.36) combined with equation (2.43) yields:

$$\xi_1 = \frac{c_s^2\xi_0}{\rho_{00}}\rho_{01} \tag{2.44}$$

There are numerous ways to treat the above linearized system of equations. It is opted to express every perturbed quantity in terms of the perturbed velocity field. If the expression for γ_1 is inserted into (2.34) the latter becomes:

$$\rho_{01} = \rho_{00}\frac{\boldsymbol{k}\cdot\boldsymbol{V}_1}{\omega_0} - \gamma_0^2\rho_{00}(\boldsymbol{V}_0\cdot\boldsymbol{V}_1)\,. \tag{2.45}$$

Equation (2.45) provides the relation of the perturbed density with $\boldsymbol{V}_1$. Immediately, if equations (2.43) and (2.44) are combined with equation (2.45), then the expressions for P_1 and ξ_1 with the perturbed velocity field are provided. Equation (2.39) using (2.41) yields:

$$\boldsymbol{B}_1 = \frac{(\boldsymbol{k}\cdot\boldsymbol{V}_1)\boldsymbol{B} - (\boldsymbol{k}\cdot\boldsymbol{B})\boldsymbol{V}_1}{\omega_0}\,. \tag{2.46}$$

The final two relations involve the expressions for J_1^0 and $\boldsymbol{J}_1$. These formulas are given by:

$$J_1^0 = i\left\{\frac{1}{\omega_0}(\boldsymbol{k}\cdot\boldsymbol{V}_1)(\boldsymbol{k}\cdot\boldsymbol{E}_0) - (\boldsymbol{k}\times\boldsymbol{V}_1)\cdot\left[\frac{1}{\omega_0}(\boldsymbol{k}\cdot\boldsymbol{B}_0)\boldsymbol{V}_0 - \boldsymbol{B}_0\right]\right\}\,, \tag{2.47}$$

$$\boldsymbol{J}_1 = \frac{i\omega}{\omega_0}\left[(\boldsymbol{k}\cdot\boldsymbol{V}_1)(\boldsymbol{E}_0 + \boldsymbol{k}\times\boldsymbol{B}_0) - (\boldsymbol{k}\cdot\boldsymbol{B}_0)(\boldsymbol{V}_0\times\boldsymbol{V}_1 + \boldsymbol{k}\times\boldsymbol{V}_1)\right] - i\omega\boldsymbol{V}_1\times\boldsymbol{B}_0\,. \tag{2.48}$$

The three components of the linearized momentum equation can be expressed via $\boldsymbol{V}_1$. In order to proceed with the linearization process, from the y and z components of the momentum equation both V_{1y} and V_{1z} can be expressed in relation to V_{1x}. In order to simplify the calculations, the system can be solved in the co-moving frame of reference and then transport back to the observer's frame.

$$\frac{V_{1y,co}}{k_{x,co}V_{1x,co}} = \frac{\omega_{co}^2\left[c_s^2 U_{Ay}(\boldsymbol{k}_{co}\cdot\boldsymbol{U}_A) + c_s^2 k_{y,co} - U_{Az}(\boldsymbol{k}_{co}\times\boldsymbol{U}_A)_x\right] - c_s^2 k_{y,co}(\boldsymbol{k}_{co}\cdot\boldsymbol{U}_A)^2}{\omega_{co}^4(1+U_A^2) - \omega_{co}^2\left[c_s^2(\boldsymbol{k}_{co}\cdot\boldsymbol{U}_A)^2 + (c_s^2+U_A^2)(k_{y,co}^2+k_{z,co}^2)\right] + c_s^2(k_{y,co}^2+k_{z,co}^2)(\boldsymbol{k}_{co}\cdot\boldsymbol{U}_A)^2}\,, \tag{2.49}$$

$$\frac{V_{1z,co}}{k_{x,co}V_{1x,co}} = \frac{\omega_{co}^2\left[c_s^2 U_{Az}(\boldsymbol{k}_{co}\cdot\boldsymbol{U}_A) + c_s^2 k_{z,co} - U_{Ay}(\boldsymbol{k}_{co}\times\boldsymbol{U}_A)_x\right] - c_s^2 k_{z,co}(\boldsymbol{k}_{co}\cdot\boldsymbol{U}_A)^2}{\omega_{co}^4(1+U_A^2) - \omega_{co}^2\left[c_s^2(\boldsymbol{k}_{co}\cdot\boldsymbol{U}_A)^2 + (c_s^2+U_A^2)(k_{y,co}^2+k_{z,co}^2)\right] + c_s^2(k_{y,co}^2+k_{z,co}^2)(\boldsymbol{k}_{co}\cdot\boldsymbol{U}_A)^2}\,, \tag{2.50}$$

where $\boldsymbol{k} = k_x\hat{x}+k_y\hat{y}+k_z\hat{z}$, $\boldsymbol{k}_{co} = \boldsymbol{k}+(\frac{\gamma_0}{\gamma_0+1}\boldsymbol{k}\cdot\boldsymbol{V}_0-\omega)\gamma_0\boldsymbol{V}_0$, $\boldsymbol{B}_{0,co} = \frac{\boldsymbol{B}_0}{\gamma_0}+\frac{\gamma_0}{\gamma_0+1}(\boldsymbol{B}_0\cdot\boldsymbol{V}_0)\boldsymbol{V}_0$ and $\boldsymbol{U}_A = \frac{\boldsymbol{B}_{0,co}}{\sqrt{\xi_0\rho_{00}}}$. The x component of the momentum equation using (2.49), (2.50) yields:

$$\left(\omega_{co}^2 - \frac{(\boldsymbol{U}_A\cdot\boldsymbol{k}_{co})^2}{1+U_A^2}\right)\left(\frac{\omega_{co}^4}{k_{co}^4} - \frac{\omega_{co}^2}{k_{co}^2}\frac{U_A^2+c_s^2+c_s^2(\boldsymbol{U}_A\cdot\boldsymbol{k}_{co})^2/k_{co}^2}{1+U_A^2} + \frac{c_s^2(\boldsymbol{U}_A\cdot\boldsymbol{k}_{co})^2}{k_{co}^2(1+U_A^2)}\right) = 0\,, \tag{2.51}$$

the first parenthesis provides the dispersion relation for the Alfvén waves. The second parenthesis provides the dispersion relation for the fast/slow magnetosonic waves. For an alternative derivation of equation (2.51) and the corresponding expressions in the observer's frame the reader can refer to Appendix C in Vlahakis &Königl (2003a). The Alfvén waves generate stable solutions (e.g. see Osmanov et al. 2008), therefore only the fast/slow magnetosonic dispersion waves contribute to the unstable modes.

The perturbations for the density and the thermal pressure in dependence solely on V_{x1} are given by:

$$\frac{\rho_{01,co}}{k_{x,co}V_{1x,co}} = \frac{\rho_{00}\omega_{co}[\omega_{co}^2(1+U_A^2) - (\boldsymbol{k}_{co}\cdot\boldsymbol{U}_A)^2]}{\omega_{co}^4(1+U_A^2) - \omega_{co}^2\left[c_s^2(\boldsymbol{k}_{co}\cdot\boldsymbol{U}_A)^2 + (c_s^2+U_A^2)(k_{y,co}^2+k_{z,co}^2)\right] + c_s^2(k_{y,co}^2+k_{z,co}^2)(\boldsymbol{k}_{co}\cdot\boldsymbol{U}_A)^2}\,, \tag{2.52}$$

$$\frac{P_{1,co}}{k_{x,co}V_{1x,co}} = \frac{c_s^2\xi_0\rho_{00}\omega_{co}[\omega_{co}^2(1+U_A^2) - (\boldsymbol{k}_{co})^2\cdot\boldsymbol{U}_A]}{\omega_{co}^4(1+U_A^2) - \omega_{co}^2\left[c_s^2(\boldsymbol{k}_{co}\cdot\boldsymbol{U}_A)^2 + (c_s^2+U_A^2)(k_{y,co}^2+k_{z,co}^2)\right] + c_s^2(k_{y,co}^2+k_{z,co}^2)(\boldsymbol{k}_{co}\cdot\boldsymbol{U}_A)^2}\,. \tag{2.53}$$

The three components of the magnetic field:

$$\frac{B_{1x,co}}{V_{1x,co}} = -\frac{\boldsymbol{B}_{co}\cdot\boldsymbol{k}_{co}}{\omega_{co}}\,, \tag{2.54}$$

$$\frac{B_{1y,co}}{k_{x,co}V_{1x,co}} = \frac{NB_{1y,co}}{DNB_{1y,co}}\,, \tag{2.55}$$

$$\frac{B_{1z,co}}{k_{x,co}V_{1x,co}} = \frac{NB_{1z,co}}{DNB_{1z,co}}\,. \tag{2.56}$$

where

$$\begin{aligned}
NB_{1y,co} &= \sqrt{\xi_0\rho_{00}}\{\omega_{co}^4 U_{Ay}(1+U_A^2) - \omega_{co}^2(\boldsymbol{U}_A\cdot\boldsymbol{k}_{co})[k_{y,co}U_A^2 + c_s^2(k_{y,co} + U_{Ay}(\boldsymbol{U}_A\cdot\boldsymbol{k}_{co}))] \\
&\quad + c_s^2 k_{y,co}(\boldsymbol{U}_A\cdot\boldsymbol{k}_{co})^3\}\,, \\
NB_{1z,co} &= \sqrt{\xi_0\rho_{00}}\{\omega_{co}^4 U_{Az}(1+U_A^2) - \omega_{co}^2(\boldsymbol{U}_A\cdot\boldsymbol{k}_{co})[k_{z,co}U_A^2 + c_s^2(k_{z,co} + U_{Az}(\boldsymbol{U}_A\cdot\boldsymbol{k}_{co}))] \\
&\quad + c_s^2 k_{z,co}(\boldsymbol{U}_A\cdot\boldsymbol{k}_{co})^3\}\,, \\
DNB_{1y,co} &= DNB_{1z,co} = \omega_{co}\{\omega_{co}^4(1+U_A^2) - \omega_{co}^2[c_s^2(\boldsymbol{k}_{co}\cdot\boldsymbol{U}_A)^2 + (c_s^2+U_A^2)(k_{y,co}^2+k_{z,co}^2) \\
&\quad + c_s^2(k_{y,co}^2+k_{z,co}^2)(\boldsymbol{k}_{co}\cdot\boldsymbol{U}_A)^2]\}\,.
\end{aligned}$$

The corresponding perturbations for the electric field:

$$\frac{E_{1x,co}}{k_{x,co}V_{1x,co}} = \frac{\sqrt{\xi_0\rho_{00}}[\omega_{co}^2(c_s^2+U_A^2) - (\boldsymbol{k}_{co}\cdot\boldsymbol{U}_A)^2 c_s^2](\boldsymbol{U}_A\times\boldsymbol{k}_{co})_x}{\omega_{co}^4(1+U_A^2) - \omega_{co}^2\left[c_s^2(\boldsymbol{k}_{co}\cdot\boldsymbol{U}_A)^2 + (c_s^2+U_A^2)(k_{y,co}^2+k_{z,co}^2)\right] + c_s^2(k_{y,co}^2+k_{z,co}^2)(\boldsymbol{k}_{co}\cdot\boldsymbol{U}_A)^2}\,, \tag{2.57}$$

$$\frac{E_{1y,co}}{V_{1x,co}} = B_{z,co}\,, \tag{2.58}$$

$$\frac{E_{1z,co}}{V_{1x,co}} = -B_{y,co}\,. \tag{2.59}$$

Where $(\boldsymbol{a}\times\boldsymbol{b})_x$ is the x-component of the cross product between two random vector quantities $\boldsymbol{a}$ and $\boldsymbol{b}$. Finally, the expression for J_1^0 and $\boldsymbol{J}_1$ are provided by:

$$\frac{J_{1,co}^0}{iV_{1x,co}} = \frac{\xi_0\rho_{00}(\boldsymbol{k}_{co}\times\boldsymbol{B}_{co})_x\{\omega_{co}^4(1+U_A^2) - \omega_{co}^2[(\boldsymbol{k}_{co}\cdot\boldsymbol{U}_A)^2 c_s^2 + (c_s^2+U_A^2)k^2 + c_s^2(\boldsymbol{k}_{co}\cdot\boldsymbol{U}_A)^2 k^2]\}}{\omega_{co}^4(1+U_A^2) - \omega_{co}^2\left[c_s^2(\boldsymbol{k}_{co}\cdot\boldsymbol{U}_A)^2 + (c_s^2+U_A^2)(k_{y,co}^2+k_{z,co}^2)\right] + c_s^2(k_{y,co}^2+k_{z,co}^2)(\boldsymbol{k}_{co}\cdot\boldsymbol{U}_A)^2}\,, \tag{2.60}$$

$$\frac{J_{1x,co}}{k_{x,co}V_{1x,co}} = \frac{i\xi\rho_{00}(c_s^2-1)(\boldsymbol{k}_{co}\times\boldsymbol{B}_{co})_x}{\omega_{co}^4(1+U_A^2) - \omega_{co}^2[c_s^2(\boldsymbol{k}_{co}\cdot\boldsymbol{U}_A)^2 + (c_s^2+U_A^2)(k_{y,co}^2+k_{z,co}^2) + c_s^2(k_{y,co}^2+k_{z,co}^2)(\boldsymbol{k}_{co}\cdot\boldsymbol{U}_A)^2]}\,. \tag{2.61}$$

For $J_{1y,co}$ and $J_{1z,co}$ the expressions are lengthy, so the nominator for the y component is given by:

$$\sqrt{\xi_0\rho_{00}}\{\omega_{co}^6(1+U_A^2)U_{Az} - \omega_{co}^4[U_{Az}c_s^2[(\boldsymbol{U}_A\cdot\boldsymbol{k}_{co})^2 + U_A^2(k_{y,co}^2 + k_{z,co}^2)]+$$
$$U_{Az}k_{co}^2(1+U_A^2) + (1+U_A^2)k_{y,co}(\boldsymbol{k}_{co}\times\boldsymbol{B}_{co})_x] + \omega_{co}^2[(\boldsymbol{U}_A\cdot\boldsymbol{k}_{co})[k_{z,co}k_{co}^2(c_s^2+U_A^2) + c_s^2k_{z,co}(\boldsymbol{U}_A\cdot\boldsymbol{k}_{co})^2+$$
$$U_{Az}c_s^2k_{co}^2(\boldsymbol{k}_{co}\cdot\boldsymbol{U}_A)] - c_s^2k_{z,co}(\boldsymbol{U}_A\cdot\boldsymbol{k}_{co})^3k_{co}^2]\}k_{1x,co}V_{1x,co} \tag{2.62}$$

The nominator of the z component is the same as equation (2.62) if the subscripts y and z are interchanged. The denominator is common for both quantities and is exactly the same as the denominator of $J_{1,co}^0$.

2.4.2 Boundary conditions

In the Cartesian geometry there is only one surface of interest, on this surface the solutions from the "jet" and the "environment" must fulfill the boundary conditions. Unlike the cylindrical counterpart, in the planar configuration there is no axis of symmetry or rotation. This means that the analysis of the expressions near the axis of the jet (e.g. see section 3.1 in Vlahakis 2023) is not applicable to a Cartesian configuration. Both eigenfunctions must be outgoing with respect to the boundary surface and with diminishing amplitude as $|x|$ increases, i.e. there can not exist any in-going perturbations from the infinity.

On the boundary surface the eigenfunctions must be continuous. The first eigenfunctions is the Lagrangian displacement, which is defined as:

$$y_1 = iV_{1x}/\omega_0\,, \tag{2.63}$$

and the second one is the total pressure perturbation which is given by:

$$\begin{aligned} y_2 &= \Pi_0 + \Pi_1 \Rightarrow \\ y_2 &= \Pi_0 + P_1 + \boldsymbol{B}_0\cdot\boldsymbol{B}_1 - \boldsymbol{E}_0\cdot\boldsymbol{E}_1\,. \end{aligned} \tag{2.64}$$

This form of y_2 arises from the fact that the unperturbed physical quantities are constant valued. Also, from the pressure equilibrium of the unperturbed configurations the unperturbed total pressure is a continuous quantity, $[\![\Pi_0]\!] = 0$. Subsequently, the continuity of y_2 on the boundary surface is simply the continuity of the perturbed total pressure, $[\![\Pi_1]\!] = 0$.

2.4.3 Numerical procedure

The expressions for the various physical quantities in section 2.4.1 are analytical. They depend on the unperturbed physical quantities, ω and $\boldsymbol{k}$. This provides the opportunity to derive analytical dispersion relations, and specify exactly the parameters that affect the unstable modes. Similarly to section 2.2.3, there are two fluids with different properties in general. For both components the expression for the total pressure perturbation is required, which is provided by equation (2.65):

$$\frac{\Pi_1}{k_x V_{1x,co}} = \xi_0 \rho_{00} \frac{N\Pi_1}{DN\Pi_1}\,, \tag{2.65}$$

where

$$\begin{aligned}
N\Pi_1 &= \omega_{co}^4 (c_s^2 + U_A^2)(1 + U_A^2) - \omega_{co}^2 [U_A^2 + c_s^2 + c_s^2(1 + U_A^2)](\boldsymbol{U}_A \cdot \boldsymbol{k}_{co})^2 + c_s^2 (\boldsymbol{U}_A \cdot \boldsymbol{k}_{co})^4\,,\\
DN\Pi_1 &= \omega_{co}\{\omega_{co}^4 (1 + U_A^2) - \omega_{co}^2 [c_s^2 (\boldsymbol{k}_{co} \cdot \boldsymbol{U}_A)^2 + (c_s^2 + U_A^2)(k_{y,co}^2 + k_{z,co}^2) +\\
&\quad c_s^2 (k_{y,co}^2 + k_{z,co}^2)(\boldsymbol{k}_{co} \cdot \boldsymbol{U}_A)^2]\}\,.
\end{aligned}$$

The final element in order to be able to find the dispersion relation is to define the value of the normal wavevector to the boundary surface, k_x. This can be achieved by utilizing from equation (2.51) the dispersion relation of the fast/slow magnetosonic waves. If this relation is solved with respect to k_x^2:

$$\begin{aligned}
k_{co}^2 &= \frac{(1 + U_A^2)\omega_{co}^4 - (\boldsymbol{k}_{co} \cdot \boldsymbol{U}_A)^2 c_s^2 \omega_{co}^2}{\omega_{co}^2 (c_s^2 + U_A^2) - c_s^2 (\boldsymbol{k}_{co} \cdot \boldsymbol{U}_A)^2} \Rightarrow\\
k_x^2 &= \frac{(1 + U_A^2)\omega_{co}^4 - (\boldsymbol{k}_{co} \cdot \boldsymbol{U}_A)^2 c_s^2 \omega_{co}^2}{\omega_{co}^2 (c_s^2 + U_A^2) - c_s^2 (\boldsymbol{k}_{co} \cdot \boldsymbol{U}_A)^2} - (k_{y,co}^2 + k_{z,co}^2)\,.
\end{aligned} \tag{2.66}$$

All the prerequisites in order to be able to generate the dispersion relation are completed. Equation (2.66) showcases that k_x is complex. The required behavior of the solutions at infinity, which was discussed in section 2.4.2 can be fulfilled by imposing $\mathrm{Im}(k_x) > 0$ for $x > 0$ and $\mathrm{Im}(k_x) < 0$ for $x < 0$.

The respective configurations of the "jet" and the "environment" modify accordingly the eigenfunctions, the perturbations of the physical quantities and the expression of k_x. When applying the boundary conditions, instead of using the complex constant as was shown in section 2.2.3, the ratio of y_2/y_1 can be used. When following this approach the complex constant vanishes and the boundary condition is simply $[\![y_2/y_1]\!] = 0$. For configurations in planar geometry the utilization of the ratio when applying the boundary conditions is favored.

2.4.4 Cold jet - Hydrodynamic environment example

As an example, the derivation for the dispersion relation for a cold jet which is in contact with a hydrodynamic environment follows. The jet is cold ($c_s = 0$) and the velocity field is assumed to only have a z-component. The environment is static ($\boldsymbol{V}_{0,e} = 0$) and unmagnetized ($\boldsymbol{B}_{0,e} = 0$), subscript "e" denotes the quantities of the environment. For this particular example the propagation for the waves is assumed to be along the z-direction, meaning that $k_y = 0$. Next, the expressions for the ratio of the eigenfunctions y_2/y_1 must be determined. Regarding the environment the expression for k_x^2 simplifies to:

$$k_{x,e}^2 = \frac{\omega^2}{c_{s,e}^2} - k_z^2\,. \tag{2.67}$$

For $\Pi_{1,e}$ the magnetic field terms vanish. The expression for the eigenfunction is given by:

$$\begin{aligned}
\Pi_{1,e} &= \frac{\xi_e \rho_{00,e}}{\omega} \frac{\omega^2}{\sqrt{\omega^2/c_{se}^2 - k_z^2}} V_{1x} \Rightarrow \\
\Pi_{1,e} &= \xi_e \rho_{00,e} \frac{\omega}{k_{x,e}} V_{x1}\,.
\end{aligned} \tag{2.68}$$

The eigenfunctions ratio is given by:

$$\frac{y_{2,e}}{y_{1,e}} = -i\xi_{0,e}\rho_{00,e}\frac{\omega^2}{k_{x,e}}\,. \tag{2.69}$$

For the jet the expression for k_x^2 is provided by:

$$k_x^2 = \frac{(1+U_A^2)\omega^2}{U_A^2} - k_{y,co}^2 - k_{z,co}^2\,. \tag{2.70}$$

The expression for the eigenfunctions ratio regarding the interior of the jet can be derived for a non-zero value for k_y and then simplify the expression by setting $k_y = 0$. The total pressure perturbation is provided by:

$$\begin{aligned}
\Pi_1 &= \frac{\rho_{00}}{\omega_{co}} U_A^2 \frac{\omega_{co}^2(1+U_A^2) - (\boldsymbol{U}_A \cdot \boldsymbol{k}_{co})^2}{\omega_{co}^2(1+U_A^2) - U_A^2(k_{y,co}^2 + k_{z,co}^2)} k_x V_{1x,co} \Rightarrow \\
\Pi_1 &= \frac{\rho_{00}}{\omega_{co}} U_A^2 \frac{\omega_{co}^2(1+U_A^2) - (\boldsymbol{U}_A \cdot \boldsymbol{k}_{co})^2}{U_A^2 k_x^2} k_x V_{1x,co} \xrightarrow{\omega_{co}^2 = k_{co}^2 U_A^2} \\
\Pi_1 &= \frac{\rho_{00}}{\omega_{co}} \frac{U_A^2 k_{co}^2 - (\boldsymbol{U}_A \cdot \boldsymbol{k}_{co})^2}{k_x} V_{1x,co} \Rightarrow \\
\Pi_1 &= \frac{\rho_{00}}{\omega_{co}} U_A^2 \frac{(\boldsymbol{k}_{co} \times \boldsymbol{U}_A/U_A)^2}{k_x} V_{1x,co}\,.
\end{aligned} \tag{2.71}$$

From the pressure equilibrium form the unperturbed configuration, the product $\rho_{00}U_A^2$ can be expressed in terms of the physical quantities of the environment.

$$
\begin{aligned}
&[\![\Pi_0]\!] = 0 \Rightarrow \\
&\frac{B_0^2 - E_0^2}{2} = P_{0,e} \Rightarrow \\
&\rho_{00}\frac{U_A^2}{2} = \Theta_{0,e}\rho_{00,e} \Rightarrow \\
&\rho_{00}U_A^2 = 2\Theta_{0,e}\rho_{00,e}\,.
\end{aligned}
$$

Finally, the total pressure perturbation becomes:

$$
\Pi_1 = \frac{2\Theta_{0,e}\rho_{00,e}}{\omega_{co}}\frac{(\boldsymbol{k}_{co} \times \boldsymbol{U}_A/U_A)^2}{k_x}V_{1x,co}\,. \tag{2.72}
$$

The eigenfunctions ratio for the jet is provided by:

$$
\frac{y_2}{y_1} = -2i\Theta_{0,e}\rho_{00,e}\frac{(\boldsymbol{k}_{co} \times \boldsymbol{U}_A/U_A)^2}{k_x}\,. \tag{2.73}
$$

The dispersion relation is derived by equaling (2.69) and (2.73).

$$
\begin{aligned}
&[\![y_2/y_1]\!] = 0 \Rightarrow \\
&-2i\Theta_{0,e}\rho_{00,e}\frac{(\boldsymbol{k}_{co} \times \boldsymbol{U}_A/U_A)^2}{k_x} = -i\xi_{0,e}\rho_{00,e}\frac{\omega^2}{k_{x,e}} \Rightarrow \\
&\frac{(\boldsymbol{k}_{co} \times \boldsymbol{U}_A/U_A)^2}{k_x} = \frac{\xi_{0,e}}{2\Theta_{0,e}}\frac{\omega^2}{k_{x,e}}\,.
\end{aligned} \tag{2.74}
$$

The dispersion relation corresponding to the configuration given in this section is equation (2.74). The relation is compact and quite simple, nonetheless it is arduous to find analytically the relation $\omega = \omega(\boldsymbol{k})$. This difficulty roots in the fact that ω exists in k_x, $k_{x,e}$ and $\boldsymbol{k}_{co}$, thus it is very laborious to express ω in terms of $\boldsymbol{k}$ explicitly. In most cases, the roots of the dispersion relation are still found numerically. Nonetheless, equation (2.74) provides a detailed overview over the physical quantities from which the stability properties of the configuration depend on.

The analysis above is utilized in the thesis to validate if the results provided by the linear analysis of a Cartesian configuration is able to successfully approximate the results of a corresponding cylindrical configuration.

Chapter 3

Linear stability analysis of a relativistic two component magnetized jet

3.1 Jet modeling

The stability analysis focuses on a two-component cylindrical outflow surrounded by a static, unmagnetized external medium. The analysis presented throughout this chapter has been published in the article Sinnis et al. (2023). The simulations and the respective analysis in section 3.3 was conducted by Dr. Dimitrios Millas.

For the modeling of the flow, parameters appropriate for an AGN jet are adopted. This description is the same as in Meliani &Keppens (2009); Millas et al. (2017), with a slightly modified toroidal velocity and magnetic field component.

The jet has a radius ϖ_j and consists of two parts, an inner one $\varpi \leq \varpi_{in}$ and an outer $\varpi_{in} < \varpi < \varpi_j$. Both parts have constant poloidal velocity corresponding to a Lorentz factor of $\gamma_{z,in} \simeq 30$ and $\gamma_{z,out} \simeq 3$ respectively (equation 3.1).

$$V_z(\varpi) = \begin{cases} v_{zin}, & \varpi \leq \varpi_{in} \\ v_{zout}, & \varpi_{in} < \varpi < \varpi_j \end{cases} \tag{3.1}$$

The toroidal velocity and magnetic field components are given in equations 3.2 and 3.3 for both jet regions.

$$V_\phi(\varpi) = \begin{cases} v_{\phi in}\left(\dfrac{\varpi}{\varpi_{in}}\right)^{\alpha_{in}/2}, & \varpi \leq \varpi_{in} \\ v_{\phi out}\left(\dfrac{\varpi}{\varpi_{in}}\right)^{\alpha_{out}/2}, & \varpi_{in} < \varpi < \varpi_j \end{cases} \tag{3.2}$$

$$B_\phi(\varpi) = \begin{cases} b_{\phi in}\left(\dfrac{\varpi}{\varpi_{in}}\right)^{\alpha_{in}/2}, & \varpi \leq \varpi_{in} \\ b_{\phi out}\left(\dfrac{\varpi}{\varpi_{in}}\right)^{\alpha_{out}/2}, & \varpi_{in} < \varpi < \varpi_j \end{cases} \tag{3.3}$$

The exponents $\alpha_{in} = 2$ and $\alpha_{out} = -2$ determine the behavior of the toroidal components: a linear increase up to the inner radius, followed by a $1/\varpi$ decay. The toroidal velocity profile is continuous at $\varpi = \varpi_{in}$, choosing $v_{\phi in} = v_{\phi out} = 0.01$; the same holds for the magnetic field, where $b_{\phi in}$ is determined by the magnetization parameter:[1]

$$\sigma = \frac{B_\phi^2}{\gamma^2 \rho_0} \tag{3.4}$$

at $\varpi = \varpi_{in}^-$. The quantities are expressed in Heaviside–Lorentz units. A piecewise constant density profile (equation 3.5) is used; the ratio of the components is arbitrarily defined via the kinetic luminosity of the jet.

$$\rho_0(\varpi) = \begin{cases} \rho_{0,in}, & \varpi \leq \varpi_{in} \\ \rho_{0,out}, & \varpi_{in} < \varpi < \varpi_j \\ \rho_{0,med}, & \varpi > \varpi_j \end{cases} \tag{3.5}$$

First the number density of the external medium to $n_{med} = 10^{-2}$ cm^{-3} is fixed. For a kinetic luminosity of $\sim 10^{46}$ ergs/s and for the inner part contributing to 1% of the flux, the values for the comoving density are $\rho_{0,in} = 6.9\ \rho_{0,med}$ and $\rho_{0,out} = 1.2 \times 10^4\ \rho_{0,med}$.

The pressure distribution is calculated via an initial total force balance in the radial direction. The effective polytropic index is $\Gamma_{eff,in} \simeq 4/3$ for the inner jet and the external medium and $\Gamma_{eff,out} \simeq 5/3$ for the outer jet. In the simulations, a Taub approximation is used[2] for the energy equation (Mignone &McKinney, 2007), having a smooth transition from $\Gamma_{eff} = 4/3$ in the relativistic temperature regime to $\Gamma_{eff} = 5/3$ in the non-relativistic ones.

---

[1] Notice that the definition of σ as in Millas et al. (2017) is followed; not to be confused with other definitions existing in the literature.

[2] The specific enthalpy ξ is given by $(\xi - p/\rho)(\xi - 4p/\rho) = 1$. The effective polytropic index is defined as $\Gamma_{eff} = \dfrac{d\ln p}{d\ln \rho}$.

Finally, an initial pressure equilibrium between the inner and the outer jet is assumed and also between the outer jet and the environment by appropriately calculating the initial thermal pressure profile.

3.2 Linear stability

3.2.1 Method

The methodology for the linear stability analysis conducted on the configuration presented in 3.1 is analyzed in section 2.2. There is only one difference that should be highlighted. Apart from the boundary of the jet at $\varpi = \varpi_j$, there is also another tangential discontinuity surface situated at $\varpi = \varpi_{in}$. This implies that for the interior of the jet there are two separate regions (inner and outer jet) for which the differential system (2.17) is numerically integrated.

Also, there are two surfaces at which the boundary conditions are going to be applied. The first one is the boundary of the jet, as was discussed in 2.2.2. The second one is the inner jet radius ϖ_{in}. On this surface the eigenfunctions of the system need to be continuous, similarly to the jet's boundary. Alongside equations (2.18) and (2.18), simultaneously equations (3.6) and (3.7) must be fulfilled.

$$y_1|_{\varpi=\varpi_{in}^-} = y_1|_{\varpi=\varpi_{in}^+} \, , \tag{3.6}$$

$$y_2|_{\varpi=\varpi_{in}^-} = y_2|_{\varpi=\varpi_{in}^+} \, , \, . \tag{3.7}$$

3.2.2 Results

The stability properties for the specific cases of the unperturbed state analyzed in section 3.1 are studied. Configurations with magnetizations (σ) equal to 0.01, 0.1, 1 and 10 are probed, and the study focuses on modes having maximum $\mathrm{Im}(\omega)$. These modes are the fastest growing, and naturally they are expected to have the most significant impact on the jet structure. As for m cases with $m = 0, \ \pm 1$ are considered, known in literature as pinch and kink modes respectively. Especially $m = \pm 1$ cases are very interesting and important, as they exhibit displacement of the jet's axis, possibly leading to severe implications for the structural integrity of the outflow.

Dispersion relation

The first case has low magnetization, $\sigma = 0.01$, and the resulting dispersion relation is shown in Fig. 3.1. Essentially, such low values for σ mean that a hydrodynamic jet is analyzed. In this case the perturbations will manifest mainly due to kinetic mechanisms (dominant at the interfaces) rather than being magnetically driven.

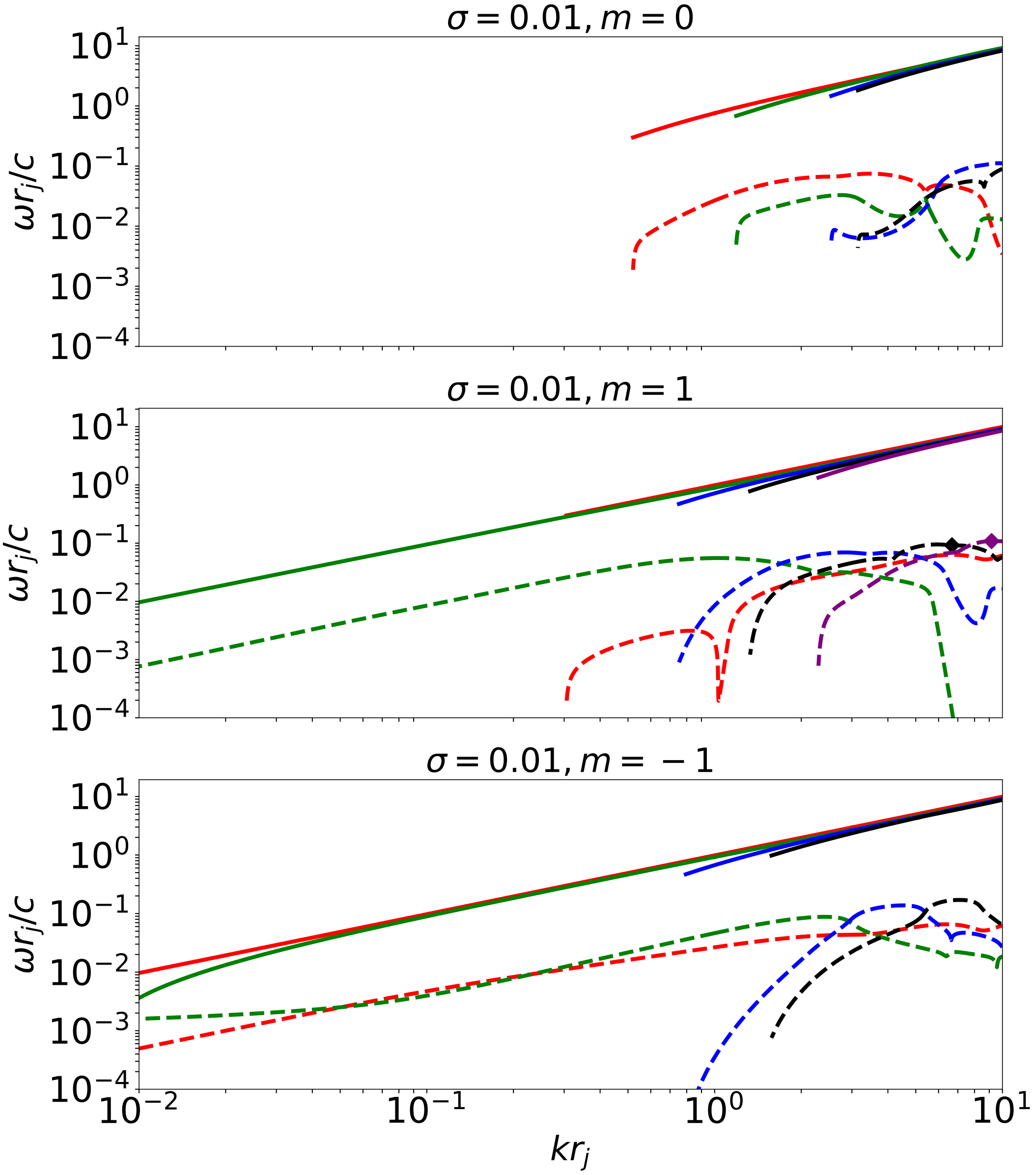

Figure 3.1: Dispersion plots for $\sigma = 0.01$ jet configuration. The figures show the real and imaginary parts of ω (in units of c/ϖ_j) as functions of the wavenumber k (in units of ϖ_j). Different colors refer to different oscillation modes. Solid lines are $\mathrm{Re}(\omega)$ while dashed lines represent $\mathrm{Im}(\omega)$. The specific solutions are indicated by different colors in order to be able to distinguish them. The rule is that among the solutions which are of interest, the mode having the highest values for $\mathrm{Re}(\omega)$ is depicted by red, the next one by green then blue, black, purple. From top to bottom the results correspond to $m = 0,\ m = 1,$ and $m = -1$ respectively. The red diamond represents the first solution that was analyzed in sections 3.2.2 & 3.2.2, while purple diamond the second one respectively.

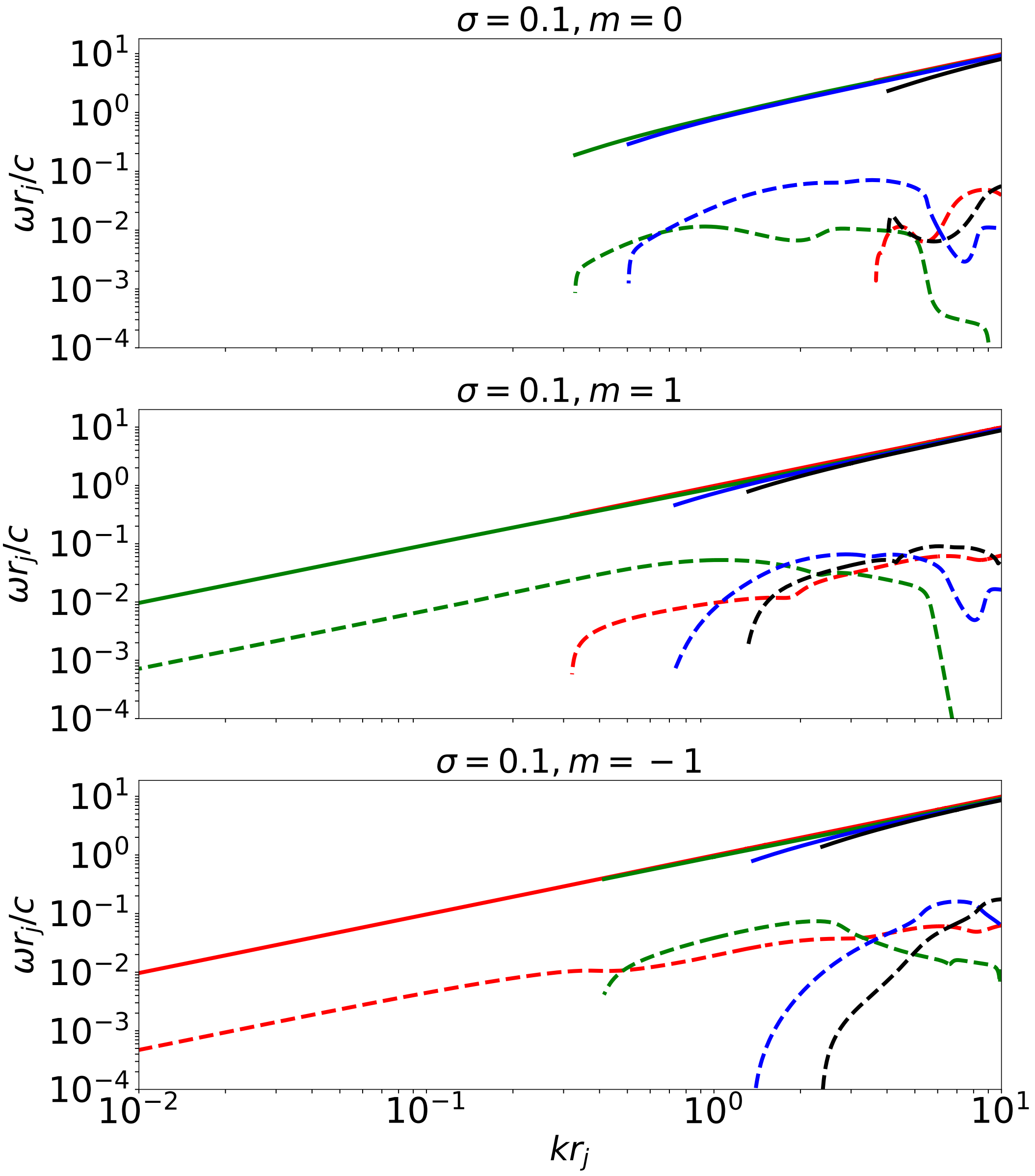

Figure 3.2: Similar to Fig. 3.1 for $\sigma = 0.1$.

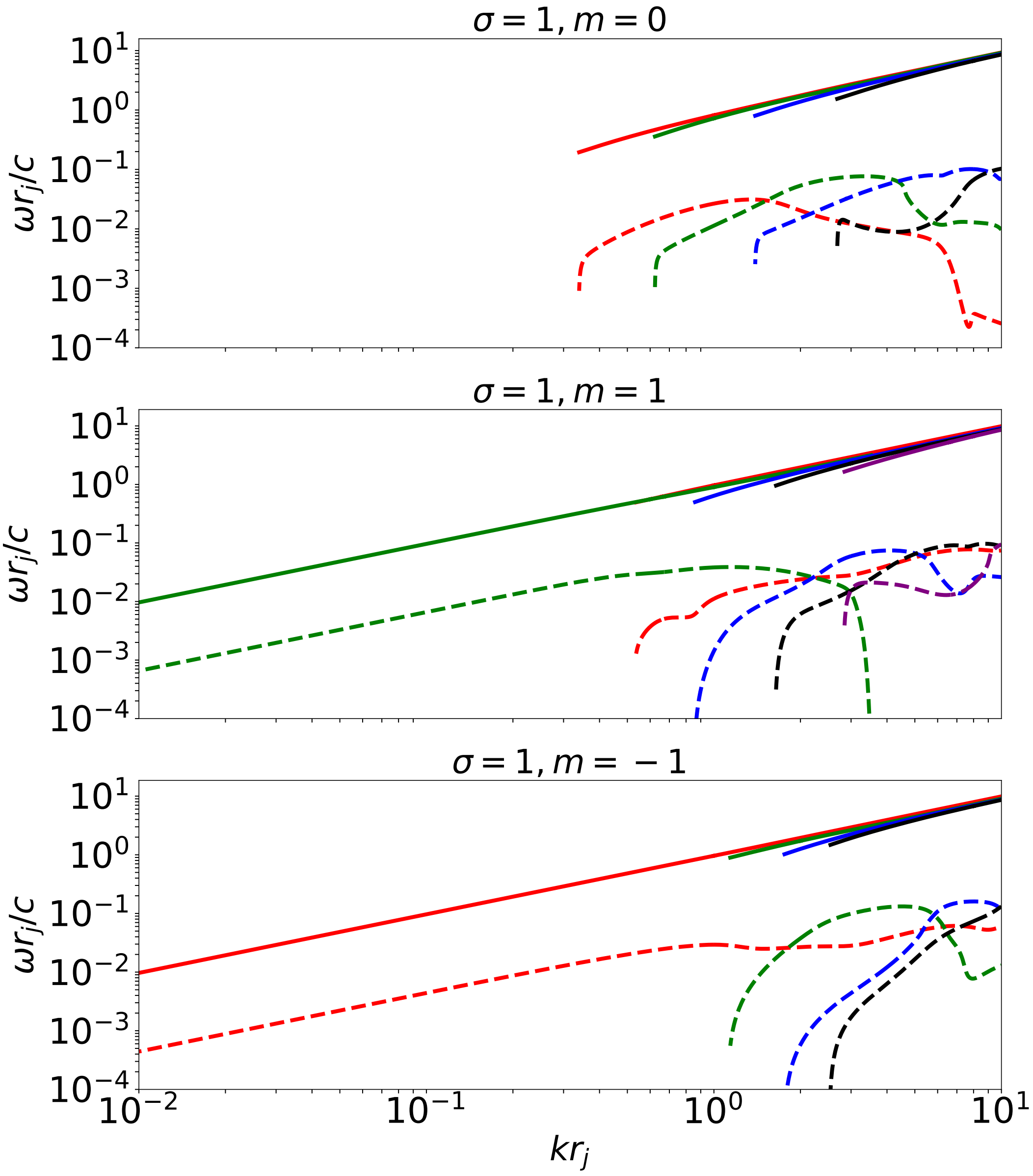

Figure 3.3: Similar to Fig. 3.1 for $\sigma = 1$.

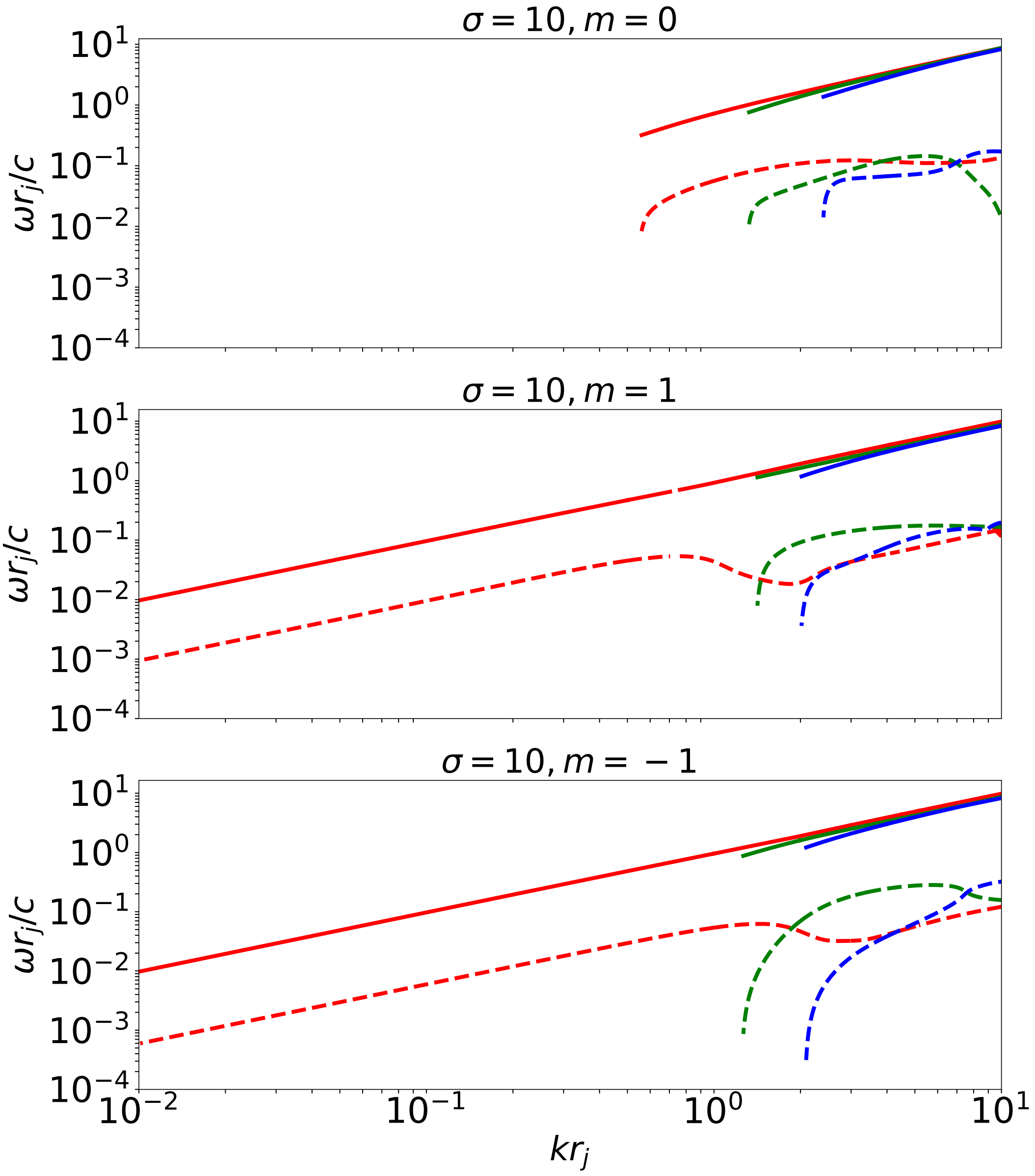

Figure 3.4: Similar to Fig. 3.1 for $\sigma = 10$.

For every m the maximum $\mathrm{Im}(\omega)$ components are of the same order, having similar numerical values. This means that the time periods needed for the perturbations to become significant with respect to the unperturbed quantities is comparable for all m. The maximums are located at $k \gtrsim 8$ (always the wavenumber is given in units of $1/\varpi_j$).

The main difference is that for the pinch mode, $m = 0$, the dispersion curves do not cover the whole range of k, while the opposite is exhibited for both kink modes $m = \pm 1$. For $m = -1$ we see a single curve spanning over the whole k interval, while, for $m = +1$ we find different modes creating an equivalent effect. Thus, kink mode perturbations excite both large and small wavelengths while $m = 0$ case is restricted only to large k.

Moving on to $\sigma = 0.1$ quite similar plots (Fig. 3.2) are noticed. Pinch mode showcase a cut-off around $k \sim 0.6 - 0.8$, $m = 1$ curves cover the whole k range and accumulate their maximums for $k > 3$ creating a plateau with approximately constant $\mathrm{Im}(\omega)$ modes. Also, $m = -1$ have a mode spanning over the whole k range and their maximums are also for large k. In general, both figures 3.1 & 3.2 have many traits in common, even though the magnetization has a tenfold increase.

Moving to a more magnetized structure in Fig. 3.3 results for $\sigma = 1$ are provided, a case practically corresponding to an equipartition between electromagnetic and rest energy densities carried by the jet. Comparing with the previous results for less magnetized jets the dispersion plots are observed to behave, vaguely speaking, in the same fashion. The numerical values for $\mathrm{Im}(\omega)$ are of the same order with the ones provided in the low σ cases. So, even though the magnetic energy density increased a hundredfold times, the stability profile of the jet remains quite unchanged. This implies that current–driven instabilities still may not be the main contributor as a physical mechanism. So, at first glance a rather consistent state regarding jet stability properties have been observed for increasing magnetization from 0.01 up to 1.

The last case is the most magnetized with $\sigma = 10$. As can be seen in Fig. 3.4, this configuration is the most unstable. Every m case has higher $\mathrm{Im}(\omega)$ values compared to any previous case. So, further increase in magnetization over $\sigma = 1$ significantly decreases the perturbations' characteristic growth timescale $\tau \sim 1/\mathrm{Im}(\omega)$. Also, in $m = 1$ plot the emergence of a mode stretching over the entire domain of k is noted, likewise in the previous $m = -1$ plots.

To give a better understanding on how the maximum growth rates correlate with magnetization, in Fig. 3.5 the maximum imaginary part of ω versus σ is plotted. As can be seen $\sigma = 0.01$ and $\sigma = 0.1$ are almost identical, reaching the same maximum for $\mathrm{Im}(\omega)$ components. The $\sigma = 1$ case seems to have slightly smaller values than the previous two cases, pretty consistent with the trend set by the previous two cases nonetheless. Lastly, the highly magnetized state is by far the most unstable, as the absolute maximum for $\mathrm{Im}(\omega)$ is almost doubled compared to the lower magnetization counterparts.

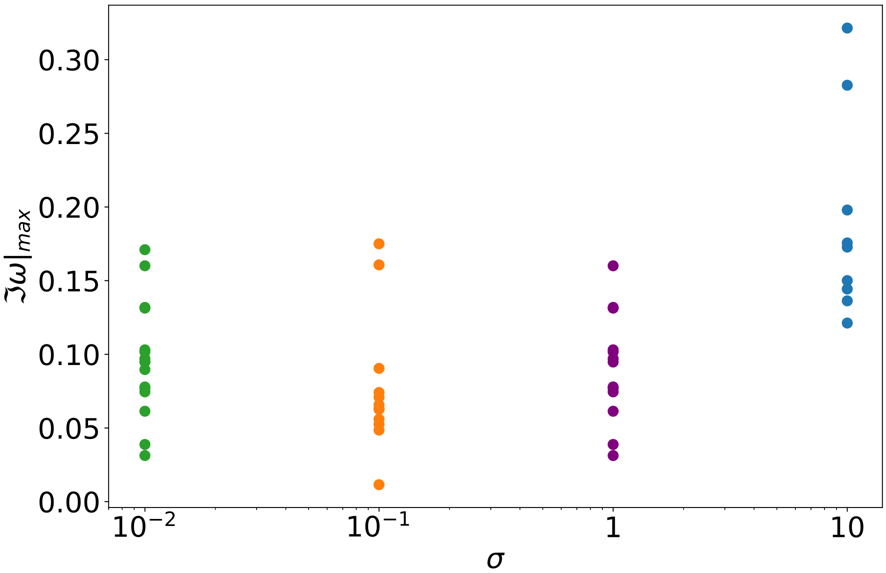

Figure 3.5: Plot for maximum $\mathrm{Im}(\omega)$ (in units of c/ϖ_j) versus σ. For each magnetization the maximum values for $\mathrm{Im}(\omega)$ are shown for every oscillation mode that have been found and for every m case considered.

Perturbations of physical quantities

In this section the analysis attempts to determine if there are substantial differences in the distribution of perturbed physical quantities with radius among the different configurations that have been explored. Results for cases with $\sigma = 0.01$ and $\sigma = 10$ are presented, the least and most magnetized cases considered, respectively. Also, for the azimuthal wavenumber the analysis focuses on the most dangerous case in terms of displacement of the jet axis, choosing $m = 1$.

In the dispersion plots the Fourier parameters corresponding to the most unstable modes are found, i.e. the value of k for which the $\mathrm{Im}(\omega)$ is the highest for every mode. The perturbed quantities presented are the density and the three components of the magnetic field. To begin with $\sigma = 0.01$ plots, which are shown in Fig. 3.6. Note that this solution is the one represented by a purple diamond drawn on the corresponding branch in Fig. 3.1.

There are several features on these curves worth discussing. To begin with, unequal amplitudes for the quantities plotted between the inner and the outer part of the jet can be seen (the density perturbation is non zero for $\varpi < \varpi_j/3$, but much smaller than in the outer part of the jet). The spine seems to be less active in terms of instability intensity than the sheath.

Furthermore, in the outer region it is noticed that the absolute values of the density perturbations acquire their maximum values as $\varpi \to \varpi_j$, meaning that as time passes,

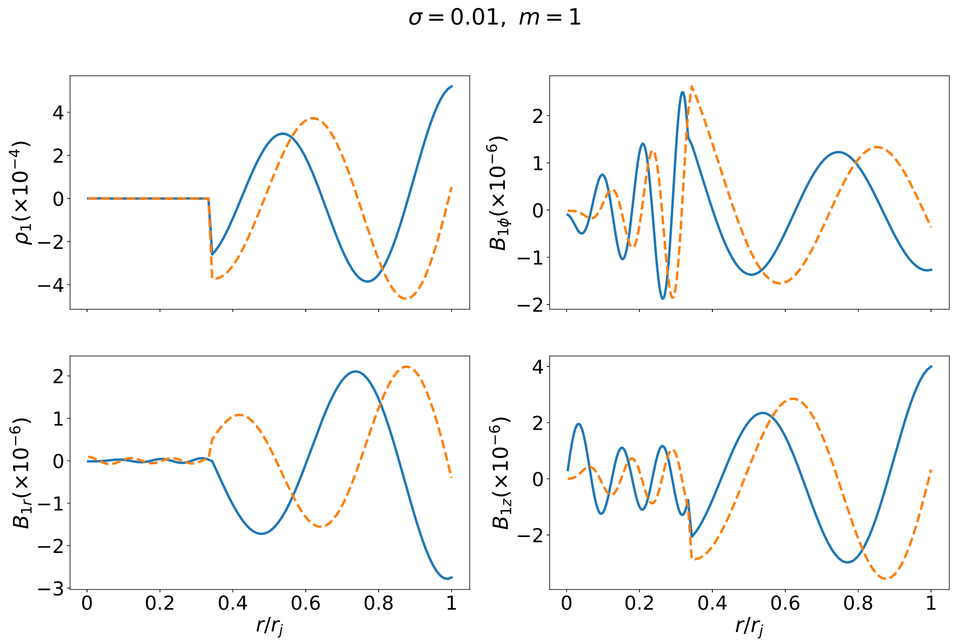

Figure 3.6: Plots for perturbations of various quantities versus ϖ. Solid lines represent the real part of the eigenfunctions and the dashed lines the imaginary counterpart. Top left plot is density perturbation and top right is the toroidal component of magnetic field perturbation. Bottom left and right the magnetic field's perturbations in radial and z direction are shown respectively. Once again, up to $\varpi/\varpi_j = 1/3$ corresponds to the jet's core and for $1/3 < \varpi/\varpi_j \leq 1$ to the jet's sheath.

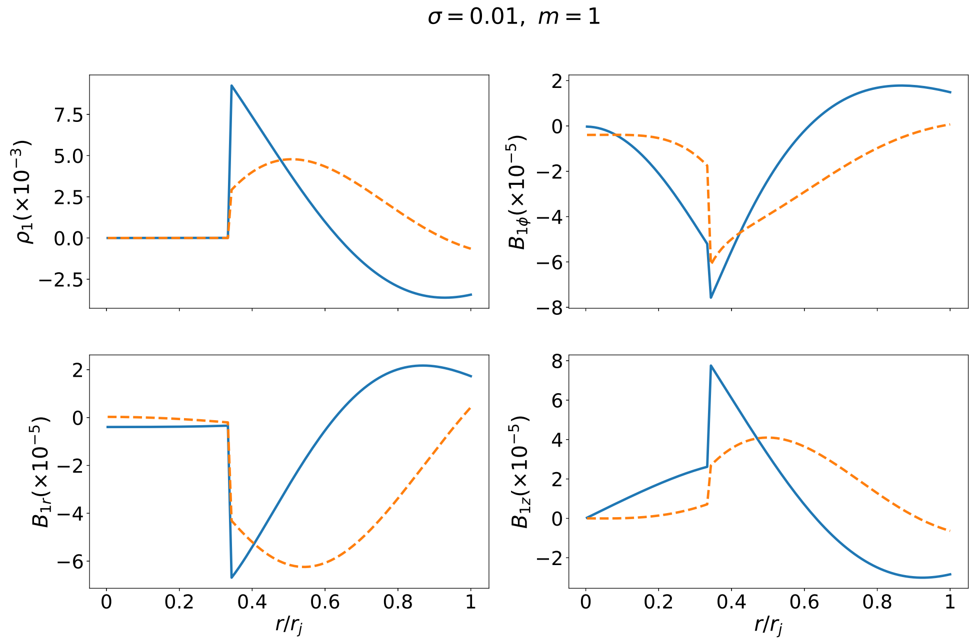

Figure 3.7: Plots for the same physical quantities' perturbations versus ϖ as in Fig. 3.6, for the second case with $\sigma = 0.01$.

the regions near the jet boundary will be significant for the stability of the structure and possibly will be the first to be disrupted. (Both the real and the imaginary parts of the quantities' support these conclusion as there are not important differences to their respective distributions over the radius of the jet.)

Next a second case for $\sigma = 0.01$ is analyzed, the one having maximum $\mathrm{Im}(\omega)$ in another solution branch, shown with the red diamond marker in Fig. 3.1. As can be seen in Fig. 3.7, even though the solutions originate from exactly the same unperturbed jet equilibrium, different branches incubate different solutions in terms of evolution and characteristics. It is evident that the eigenfunctions are either located at $\varpi \approx \varpi_j$ or have a maximum at $\varpi \approx 0.5\varpi_j$.

Obviously, there are differences between the real and imaginary part of the solutions. The real part for every quantity is largest at $\varpi \simeq \varpi_{in}$. The $\varpi < \varpi_{in}$ area shows less fluctuations compared to the outer part of the jet. The imaginary part of the quantities' also showcase activity in the sheath. They are less localized than the real counterpart but have an evident maxima at $\varpi \sim 0.5\varpi_j$, apart from $B_{1\phi}$ which is similar to the real counterpart. Both the solid and the dashed lines are discontinuous on the inner boundary of the outflow.

In general, the activity of this mode is expected to manifest mainly in the vicinity of the inner boundary of the jet and up to distances of $\sim 0.5\varpi_j$. In essence, the solution resides in the outer section of the outflow, the sheath. Also, the majority of the distributions exhibit discontinuities at $\varpi = \varpi_{in}$, a trait which was inconspicuous in Fig. 3.6.

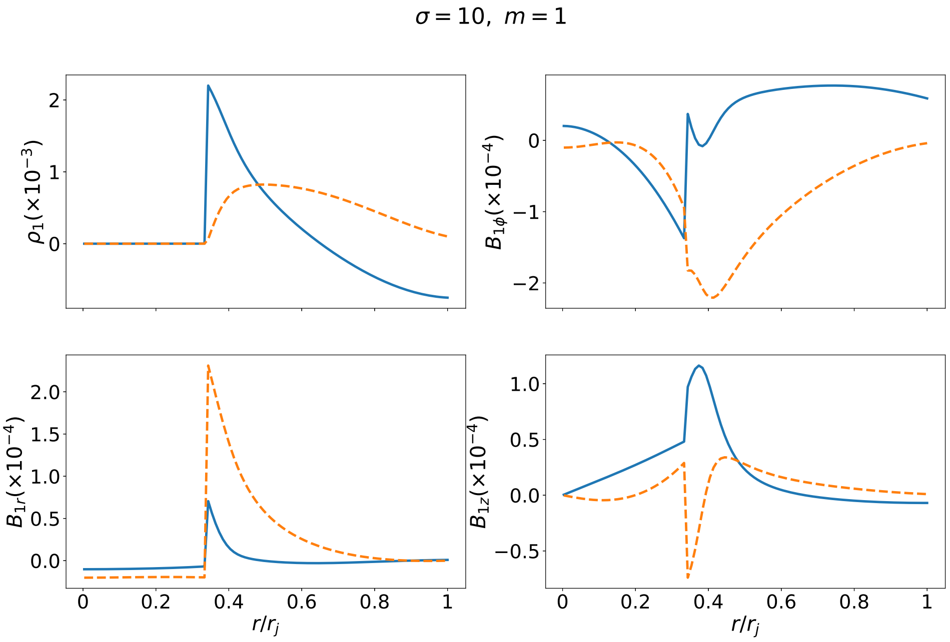

Figure 3.8: Plots for physical quantities' perturbations versus ϖ, for high magnetization configuration with $\sigma = 10$.

Although no particular kind of eigenfunctions is expected to dominate since their values of $\mathrm{Im}(\omega)$ are similar between the two cases analyzed, the instabilities mainly affect the outer part of the jet and the internal boundary surface. The two most unstable modes do not affect the inner jet component. Probably, the instabilities have a kinetic character, mainly due to the fact that the magnetization is very small. The regions most involved in the destabilization process are the two interfaces separating inner and outer jet, and the outer jet and the environment, respectively.

The final case corresponds to the high magnetization configuration ($\sigma = 10$) exhibited in Fig. 3.4 as a red diamond on the right edge of the middle box. Obviously, this distribution is different from the first case of $\sigma = 0.01$ (Fig. 3.6) but very similar to the second one (Fig. 3.7). The perturbations become largest at $\varpi \approx \varpi_{in}$, the interface between spine and sheath areas. This means that the instabilities should exhibit maximum activity around this specific distance. So, perturbations affect mostly internal areas of the flow.

The perturbations exhibit significant discontinuities at $\varpi \approx \varpi_{in}$. Specifically, considering magnetic fields, both real and imaginary parts are discontinuous at this interface. The density is discontinuous regarding only the real part, whereas the imaginary part is continuous.

Also, it is useful in the process of studying the eigenfunctions to plot the total pressure perturbation for the jet-environment system, similarly to Payne &Cohn (1985) in which a purely hydrodynamic flow was studied. As a reminder, the relation for the quantity is given by:

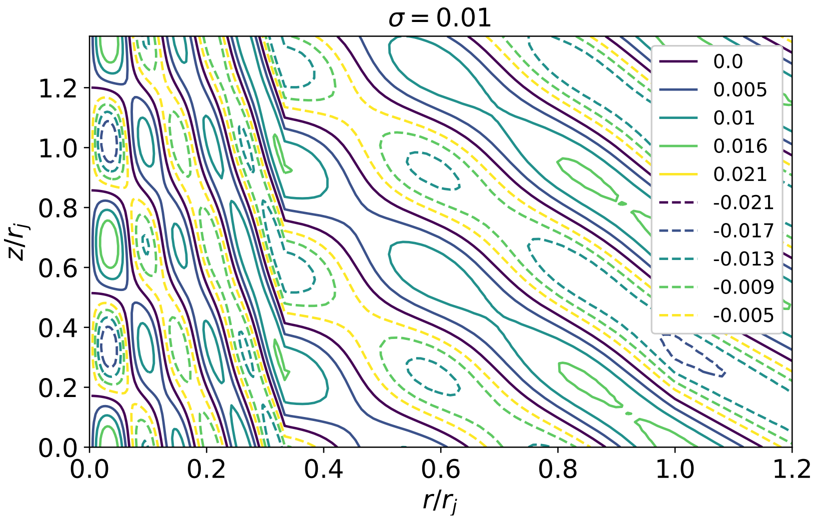

Figure 3.9: The perturbation of the total pressure in the xz plane for the solution with $\sigma = 0.01$ and $k = 9.16$.

$$\delta\Pi = \delta P + \boldsymbol{B} \cdot \delta\boldsymbol{B} - \boldsymbol{E} \cdot \delta\boldsymbol{E} \tag{3.8}$$

where δP is the thermal pressure perturbation, $\boldsymbol{E}$ the electric field and $\delta\boldsymbol{E}$ its perturbation. In Figs. 3.9 & 3.10 the total pressure perturbation is presented on the xz plane (for $\phi = 0$). The solid lines represent the parts of the jet where the perturbation increases the total pressure, while the dashed counterparts are areas with decreasing pressure. The plots show both the whole jet ($\varpi/\varpi_j \leq 1$) and part of the environment ($1 < \varpi/\varpi_j \leq 1.2$).

Figure 3.9 showcases the solution with $\sigma = 0.01$ and Fig. 3.10 the solution with $\sigma = 10$. The quasi–periodic dependence in the radial direction is observed (as in Figs. 3.6 & 3.8) where the zero-valued nodes are located between the transitions from solid to dashed lines and vice versa. In these two plots there can also be observed the wave propagation in both the radial and z direction. These figures highlight the different excitation of the two solutions, i.e. in Fig. 3.9 the whole domain is perturbed with interchanging over/under pressure areas for the jet and the environment. In Fig. 3.10 this pattern is centered around the inner boundary surface ($\varpi/\varpi_j = 1/3$) while the propagation of the mode towards the environment is diminished.

Next, the radial component of the Lagrangian displacement versus the radius is plotted (Fig. 3.11, 3.12 & 3.13) for every case discussed previously. The first case for $\sigma = 0.01$ is plotted in (Fig. 3.11). Both components of the Lagrangian displacement exhibit small amplitudes in the core region, followed by larger values at the sheath. This means that, in terms of movement, the jet's core is fairly stable and will need more time in order to be disrupted from it's initial cylindrical shape compared to the rest of the jet.

For the second case (Fig. 3.12) the maximum of ξ_{Lagr} for the real part of the quantity is located at $\varpi \simeq \varpi_j/2$. Both the axis and the surface of the jet display slight move-

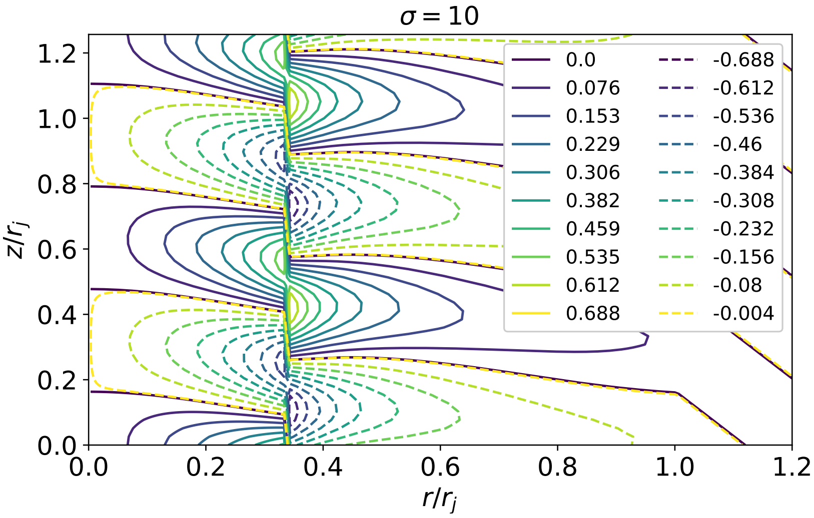

Figure 3.10: Similarly to Fig. 3.9 for $\sigma = 10$, $k = 10$.

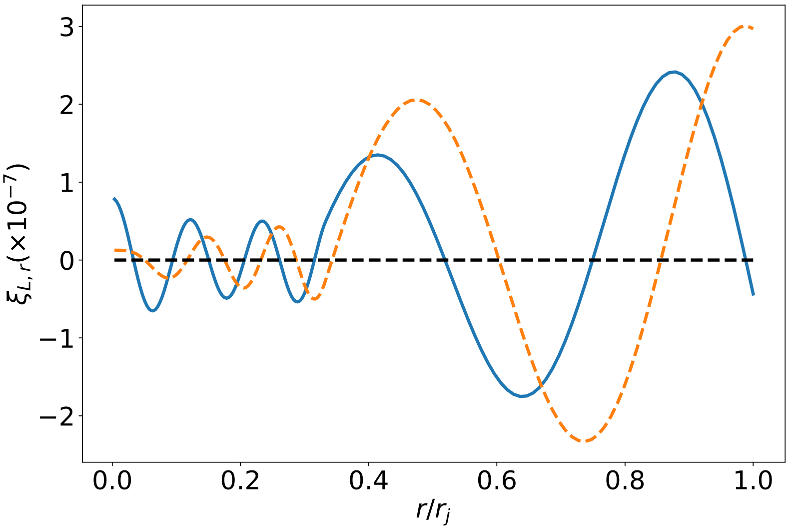

Figure 3.11: Plot for radial component of Lagrangian displacement. This is the low magnetization case with $\sigma = 0.01$. Black dashed line indicates zero displacement for the perturbed configuration.

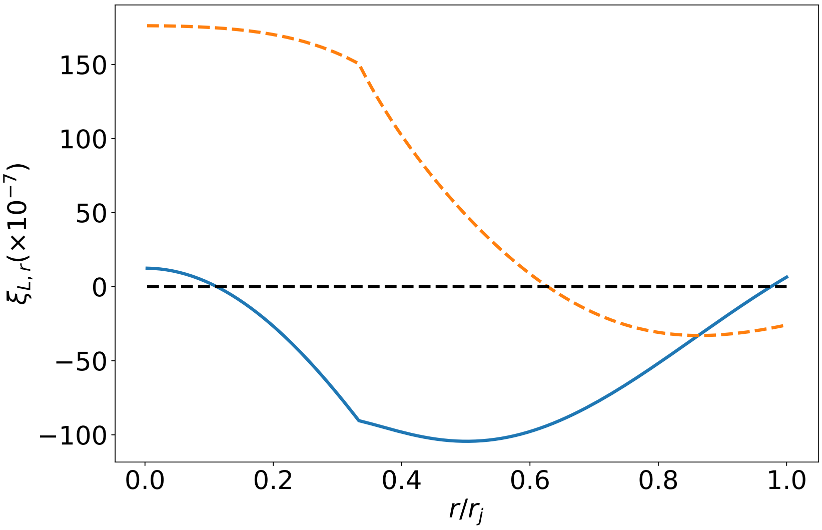

Figure 3.12: Similarly to Fig. 3.11, but for the second case having $\sigma = 0.01$.

ment, especially when compared to the maximum of the curve. So, the jet is expected to have maximum displacement at $\varpi \sim \varpi_j/2$ (surely not on the internal boundary surface, although both interfaces are displaced as well). The imaginary counterpart is negligible on the boundary of the jet and increases towards the axis. Contrary to the real part, the quantity maximizes on the axis, meaning that regarding this component the maximum movement of the flow lines resides in the inner part of the jet.

For $\sigma = 10$ (Fig. 3.13), the displacement at $\varpi \approx \varpi_j$ is small, indicating that jet's boundary will not get displaced from its initial position. On the other hand, towards the jet's axis the displacement of the flow becomes prominent, reaching maximum movement for a small region adjacent to the axis. This analysis is valid for both components of the Lagrangian displacement.

The similarity between the second case of $\sigma = 0.01$ and $\sigma = 10$ is apparent for both the perturbed physical quantities and the Lagrangian displacement. This could indicate that the mode relies on the same physical mechanism, even though the magnetization is increased 1000 times. In essence, the magnetization defined through equation (3.4) follows the definition of Millas et al. (2017) and compares the electromagnetic energy density with the rest energy density of the plasma. If one compares electromagnetic and plasma energy densities the enthalpy should be included in the plasma part. The ratio of electromagnetic to plasma energy densities is then $\sigma_\xi = \sigma/\xi$, where ξ is the specific enthalpy. This leads to both cases $\sigma = 0.01$ and $\sigma = 10$ having $\sigma_\xi < 1$ (the actual values corresponding to the maxima of σ_ξ in each case are $\sigma_\xi \sim 5 \cdot 10^{-4}$ and $\sigma_\xi \sim 0.5$, respectively). Even when the highest magnetization σ is considered, eventually the configuration is not strongly magnetized because $\sigma_\xi < 1$. Based on this fact it is logical to assume that the modes are generated by kinetic type mechanisms and is not likely to be current-driven.

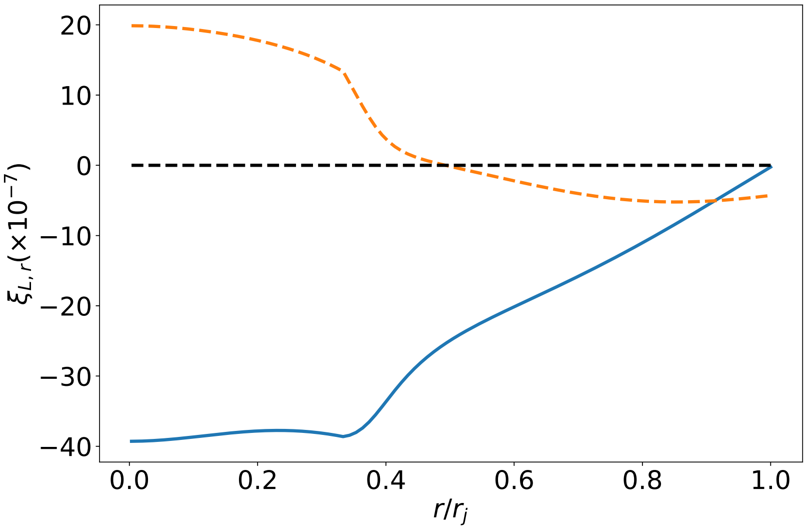

Figure 3.13: Similarly to Fig. 3.11, but for the case having $\sigma = 10$.

In every solution that was analyzed the values of y_2 are much greater that y_1, implying that the instabilities are related to the total pressure perturbation which constitutes of both the thermal and the magnetic components.

Analyzing every other mode included on the dispersion relation plots (apart from the cases that have already been discussed), the conclusions remain the same. The two regions of interest are the two boundary surfaces, in the sense that the maxima of the distributions of the displacement and the perturbed physical quantities are located on these surfaces. This result is consistent with the expectation that low magnetization configurations are more unstable on the interfaces where the velocity is discontinuous.

Perturbed forces

Additional valuable pieces of information for the nature of the instabilities can be obtained by looking into the perturbed forces and their spatial distribution across the jet. Focusing on the radial component of the linearized momentum equation and listing the various terms, we have the perturbed thermal pressure gradient (eq. 3.9), the force related to inertial shearing effects across the jet (eq. 3.10), and the radial projection of the perturbation of the Lorentz force (eq. 3.11). We omit the terms involving the toroidal components of velocity, either zeroth or first order ($\propto V_\phi^2$ or $\propto V_\phi V_{1\phi}$) because they are insignificant compared to the rest of the terms, as V_ϕ has a very small value.

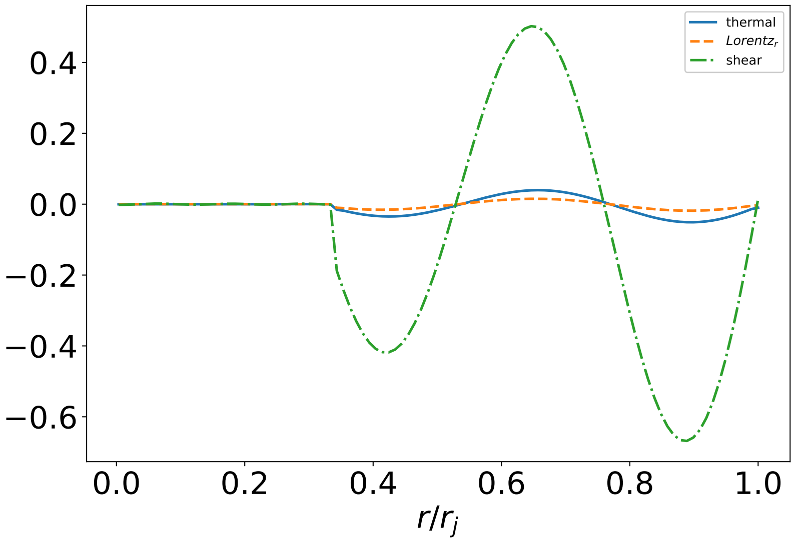

Figure 3.14: Plot of radial components of perturbed force densities across the jet over $\xi\gamma$. Solid line represents thermal pressure gradient, while dashed line Lorentz force and dash-dotted line the shearing component of inertial forces acting upon the plasma of the jet.

$$\delta f_{th} = -\nabla \delta p \tag{3.9}$$
$$\delta f_{sh} = i\gamma^2 \xi \rho \left(mV_\phi/\varpi + kV_z\right) \delta V_\varpi \tag{3.10}$$
$$\delta f_L = \frac{1}{c}\left(\delta \boldsymbol{J} \times \boldsymbol{B} + \boldsymbol{J} \times \delta \boldsymbol{B}\right) \cdot \hat{\boldsymbol{\varpi}} \tag{3.11}$$

The forces are calculated over $\xi\gamma$ regarding the cases analyzed in the previous subsection (3.2.2). For the weakly magnetized configuration depicted in Fig. 3.14 & 3.15 the prominent type of force is inertial. Second in order is the pressure gradient force and the weakest is the Lorentz force. The relative contribution for each force is consistent with the low magnetization. Basically the same trends regarding the specifics of the distributions as in 3.2.2 are noticed.

In Fig. 3.16,the same kind of forces acted on the jet with $\sigma = 10$ can be observed. The Lorentz force becomes important. Obviously the pressure gradient is the weakest (practically negligible). The shearing forces come second reaching roughly 40% of the Lorentz force. Thus, for the highest σ a marginal dominance of the Lorentz force over the other is observed. The electromagnetic perturbed forces in this case are aiding in the destabilization process, contrary to the previous cases.

One last point of discussion is why different prominent forces between the second case of low σ and the high σ case are noticed, although the eigenfunctions behave quite similarly. The answer lies in the way the perturbed forces are calculated. When a term

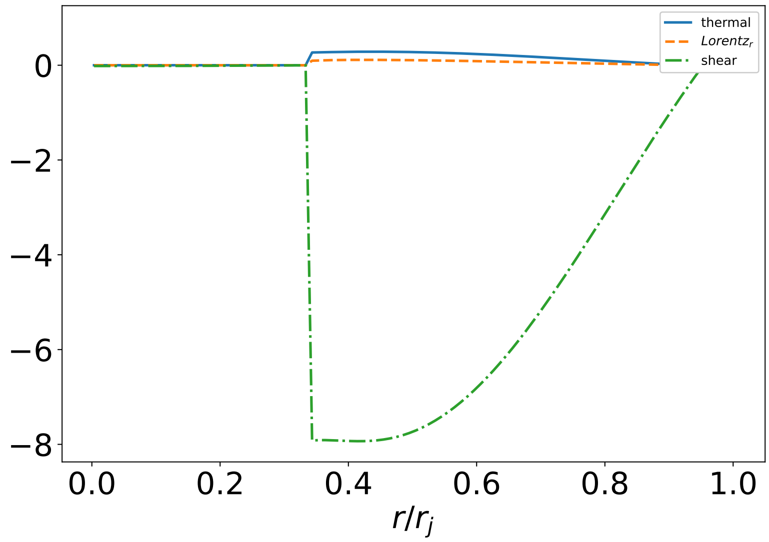

Figure 3.15: Similarly to Fig. 3.14 for the second case of $\sigma = 0.01$.

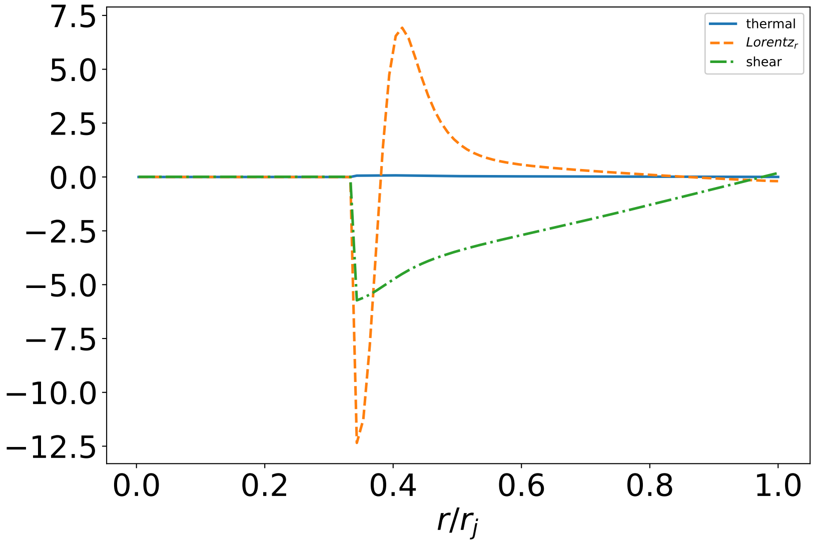

Figure 3.16: Similarly to Fig. 3.14 for $\sigma = 10$.

of the momentum equation is linearized, the resulting function depends on both first and zeroth order physical quantities. Therefore, while the eigenfunctions may be quite similar, the resulting force is substantially affected by the unperturbed physical quantities. This leads to different results, suggesting different physical mechanisms involved in each case. This is also true for the calculation of the perturbed forces and the Lagrangian displacement from y_1, y_2.

3.3 Numerical simulations

To check the validity of the analytical predictions mentioned in the previous section, a series of numerical simulations using the relativistic MHD `PLUTO` code (Mignone et al., 2007, 2012) were performed.

The default choices (unless stated otherwise) for the computational domain and its resolution are as follows: on the x, y plane the domain is -0.29 pc$\leq x, y \leq 0.29$ pc with a resolution of 356×356. Along the z axis we select $0 \leq z \leq 5\lambda$, where λ is the wavelength corresponding to the selected k. The full computational domain is thus determined by the wavelength λ of each perturbation and in principle is different for each case. It is opted to extend the length of the box along the z axis up to 5λ in order to be able to capture other potential instabilities. The resolution along the z axis is selected accordingly in each run so that always almost identical scales $\delta z \simeq 0.0018$ pc are resolved. The boundary conditions on the x, y plane are open (outflow) and periodic along z.

A third order Runge-Kutta scheme is employed for time advancing with a third order limiter (Čada &Torrilhon, 2009); an hll solver is used in all runs and reconstruction is performed using the 4-velocity. To easily detect any displacement of the interface between the jet components, a passive tracer around $r = r_{in}$ is injected. The passive tracer is a scalar quantity whose value is determined by a simple advection equation, as described in Mignone et al. (2012).

The simulations are initialized using the eigenfunctions of the theoretical study, multiplied by an arbitrary constant c_o. For every case, the time t_i at which the instability is expected to significantly modify the jet dynamics can be estimated, using the approximate formula $c_o e^{\mathrm{Im}(\omega) t_i} \simeq 1$.

3.3.1 Cases with $\sigma = 0.01$

First cases with very low magnetizations ($\sigma = 0.01$) and different wavenumbers in the perturbations are examined. Furthermore, for each case different values for the amplitude of the perturbations are used. The time difference of the evolution of instabilities between the various cases can be calculated (approximately) analytically and can be estimated via simulations as well.

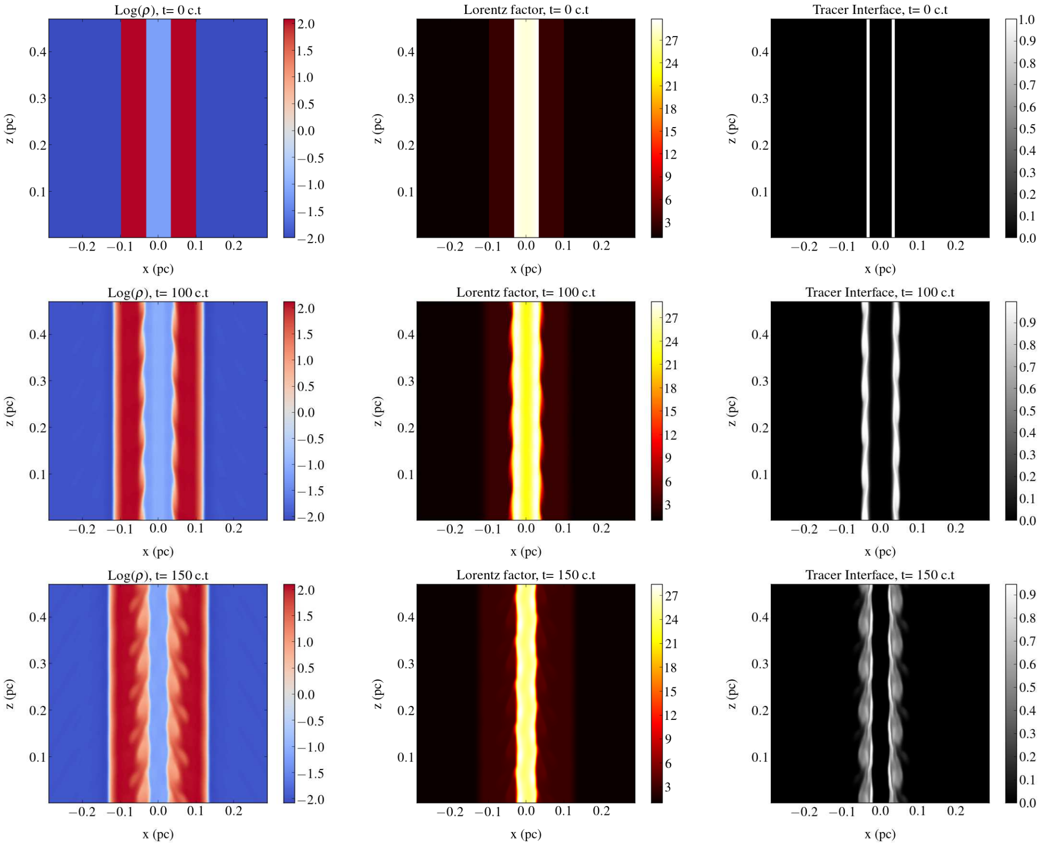

Figure 3.17: Evolution of a jet with initial $\sigma = 0.01$, perturbation with $k \simeq 6.68$ and $c_o = 10^{-3}$. Shown here: density in log scale (left), Lorentz factor (middle) and the passive tracer (right) at t=0,100 and 150 radial light crossing times. The jet is clearly unstable at $\sim 150 c.t.$, with the instability starting around 100c.t.

Case 1a: $k \simeq 6.68$

First perturbations with wavenumber of $k = 6.68$ are introduced. In order to be able to verify the $|Q_1| \ll |Q_0|$ condition there is the the freedom of multiplying the eigenfunctions with a numerical constant, called here c_o. The linearized system makes this option available, so for every simulation in this section the constant $c_o = 10^{-3}$ has been included. The instability for this setup is estimated to develop approximately at $t \sim 110$ radial (light) crossing times (c.t.). In the following plots (Fig. 3.17, maps of the density (in log scale), the Lorentz factor and of the passive tracer introduced in the interface between the two jet components are presented.

A displacement of the jet axis after $t \simeq 100$c.t. is observed, very close to the theoretical prediction. At the same time, the outer interface (between the jet and the external medium) remains quite stable.

A useful test that allows to follow the evolution of the instability is the behaviour of a perturbed quantity with time, e.g. $\frac{\delta\rho}{\rho_{0,0}}$, where $\delta\rho = \rho(t) - \rho_{0,0}$ and $\rho_{0,0}$ is the initial density.

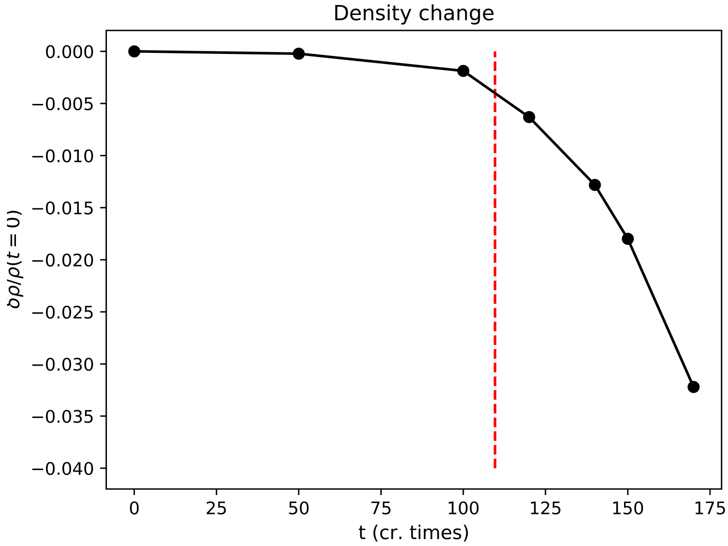

Figure 3.18: Evolution of $\frac{\delta\rho}{\rho_{0,0}}$. The change in the density is small during the linear phase and becomes significant after ~ 100 crossing times. The vertical line marks the expected time the configuration enters the nonlinear regime based on the analytical calculation of $\mathrm{Im}(\omega)$ (at this time $c_0 e^{\mathrm{Im}(\omega)t} = 1$).

This quantity is integrated in the entire jet. The change is expected to be close to zero before the development of the instability (~ 100 crossing times, given by the theoretical prediction). The result is shown in Fig. 3.18, where it is observed that the change in the density is significant after approximately 100 crossing times.

Case 1b: $k \simeq 9.16$

For this case a different kind of perturbation is utilized, with $k = 9.16$, while keeping the same values of σ and c_o. The instability is expected to develop around $t \sim 60$ crossing times near the interface between the outer jet and the external medium. The Lagrangian displacement for this case was presented previously in Fig. 3.11 and shows that the instability in this case is expected to develop near the outer jet boundary. The evolution of the jet is shown in Fig. 3.19.

It appears that the instability develops somehow later than the theoretically predicted time. However, if the behavior of the interface between the sheath and the surrounding medium is carefully examined, it can be found that the time estimate is verified. The passive tracer introduced at the interface between the sheath and the environment shows the development of instability around $t \simeq 50$c.t. (see Fig. 3.20, with an adapted color bar to enhance the outer part). At the same time, the passive tracer inserted in the interface between the inner and outer jet is very stable. The unstable pattern of the inner jet which we observe at later times (Fig. 3.19, third row) develops after the initial displacement of the outer interface.

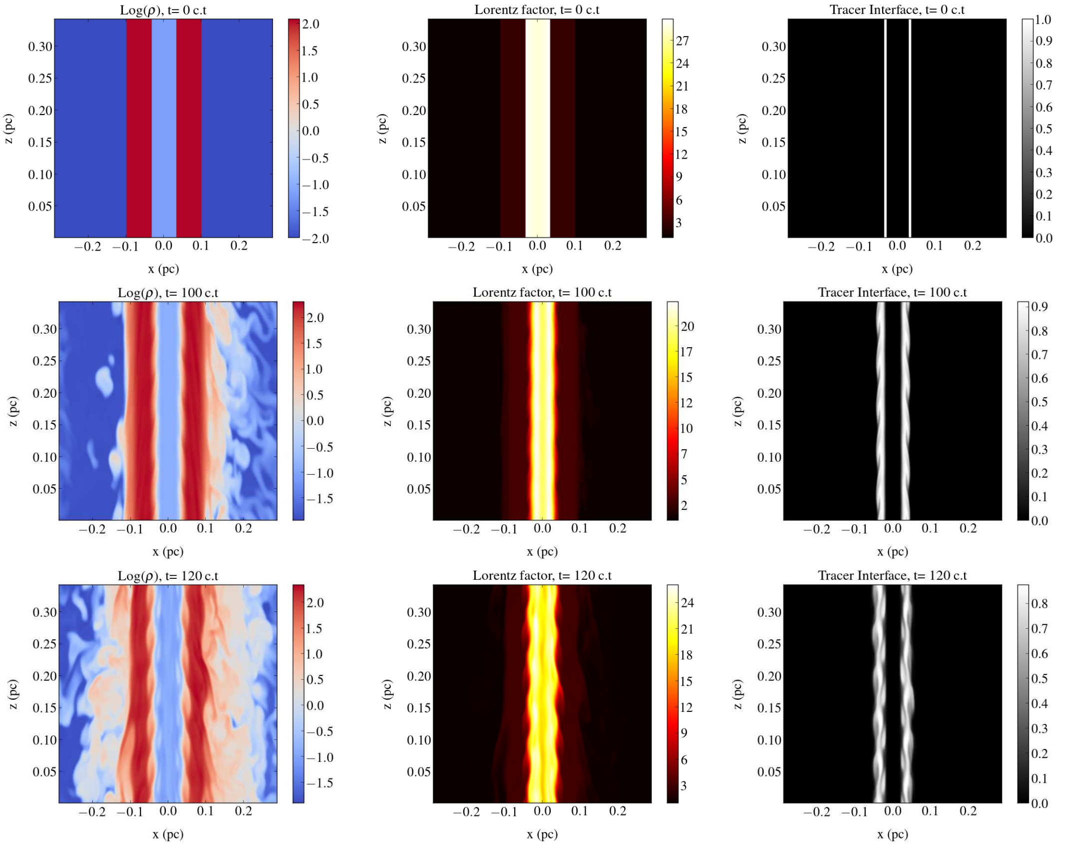

Figure 3.19: Evolution of a jet with initial $\sigma = 0.01$, perturbation with $k \simeq 9.16$ and $c_o = 10^{-3}$. Shown here: density in log scale (left), Lorentz factor (middle) and the passive tracer in the *outer* jet (right) at t=0, 100 and 120 radial light crossing times. The jet is clearly unstable at $\sim 120c.t.$. Notice now that the instability starts from the interface between the outer jet and the environment.

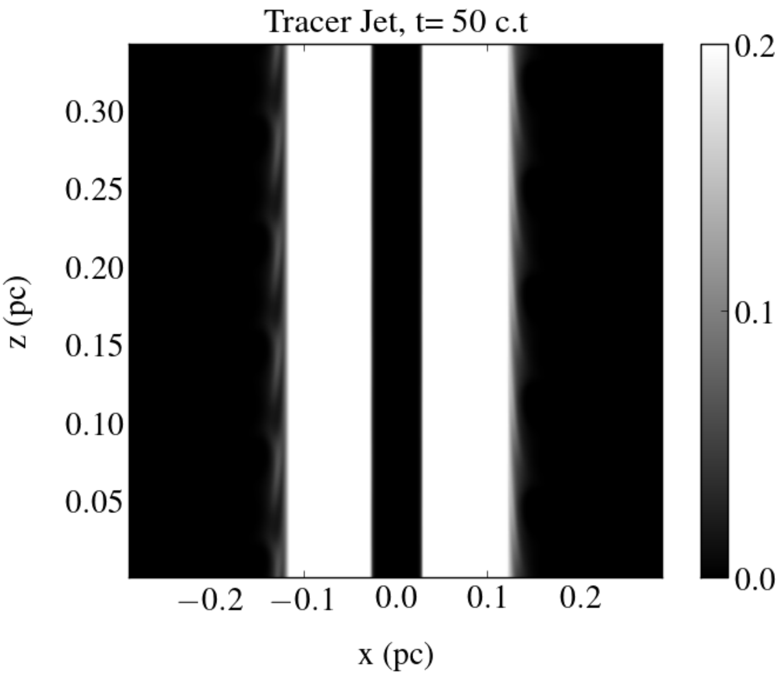

Figure 3.20: Tracer at the interface of the sheath with the environment. Notice now that the instability starts from the interface between the outer jet and the environment rather than the spine.

If the criterion of the density change is used again, it is found that it becomes unstable significantly later compared to the estimation for the development of the instability (in agreement with the density maps of Fig. 3.19). In this case (see Fig. 3.21), the change is larger in the initial stages (compared to the simulation with $k = 6.68$), as there is strong diffusion towards the environment. We remind here that the estimation of the time when the instability starts to develop uses an arbitrary constant; this predicts quite accurately the order of magnitude but does not exclude an offset.

3.3.2 Case 2: $\sigma = 1$ $k \simeq 9.99$

The magnetization is increased by an additional factor of 10. The thermal pressure for $p_o = 2.5$ and $b_{z,in} = 2.1$ is kept positive for every value of ϖ. The instability is expected to develop again near the interface of the two jet components, at an estimated time of $t \sim 70$ crossing times.

Although it is observed (Fig. 3.22) that the inner jet becomes eventually unstable, this happens at a later time. Moreover, the outer jet strongly interacts with the environment and significant diffusion is noticed. Kelvin–Helmholtz type instabilities might naturally come to mind, but if it is indeed the reason needs to be further investigated.

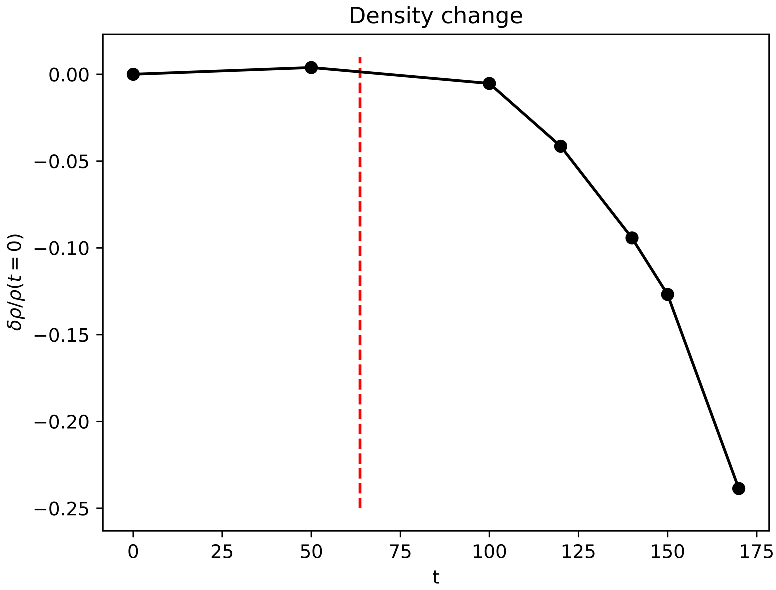

Figure 3.21: Similarly to Fig. 18 for the simulation with $\sigma = 0.01$ and $k = 9.16$.

3.3.3 Case 3: $\sigma = 10$ $k = 10$

Finally, the case with the largest value of σ is examined. To ensure again that the thermal pressure is positive throughout the domain, parameters p_o and $b_{z,in}$ are assigned to values $p_o = 8.275$ and $b_{z,in} = 8$. As mentioned in more detail in the discussion section, this may not be the optimal choice of constants as it can potentially increase diffusion. The instability is expected to develop around $t \sim 45$ crossing times.

The development of the instabilities agree generally with the predicted time. Especially if one looks at the radial magnetic field or the radial velocity, where the deviation from the equilibrium values (both zero) are more easily noted. The instabilities appear, as expected closer to the inner boundary and once more the displacement of the jet axis is noticed as the instabilities develop.

The evolution of $\frac{\delta\rho}{\rho_o}$ is presented in Fig. 3.25. The comparison with the density maps given in Fig. 3.23 is not trivial here, as the instability seems to develop later than the approximate prediction. Ideally, more frequent snapshots of the evolution are required to determine the time when the jet becomes unstable using the $\frac{\delta\rho}{\rho_{0,0}}$ criterion. This emphasizes that the estimate is reliable as an order of magnitude, but the exact time can differ depending on the value of c_o.

3.4 Discussion

In this chapter the stability of two-component relativistic magnetized jets was investigated both analytically and numerically, extending previous studies by including magnetic field

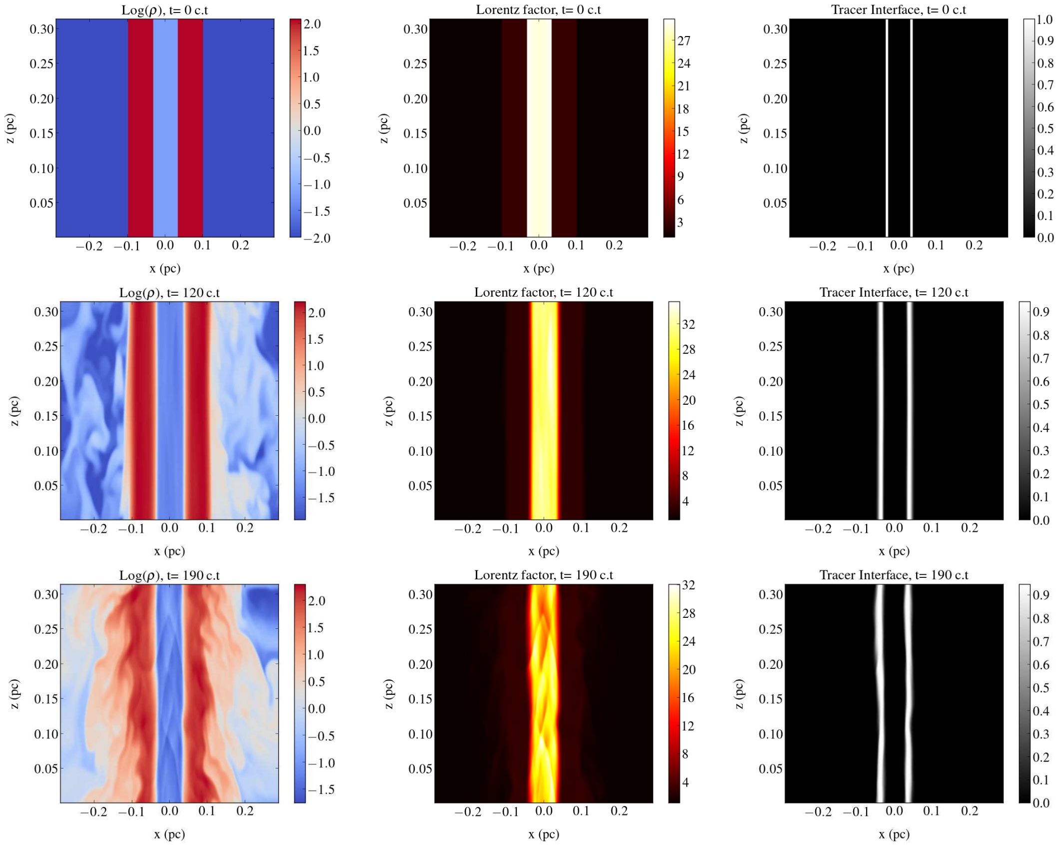

Figure 3.22: Evolution of a jet with initial $\sigma = 1$ and perturbation with $k \simeq 9.99$. Shown here: density in log scale (left), Lorentz factor (middle) and the passive tracer (right) at t=0,120 and 190 radial light crossing times.

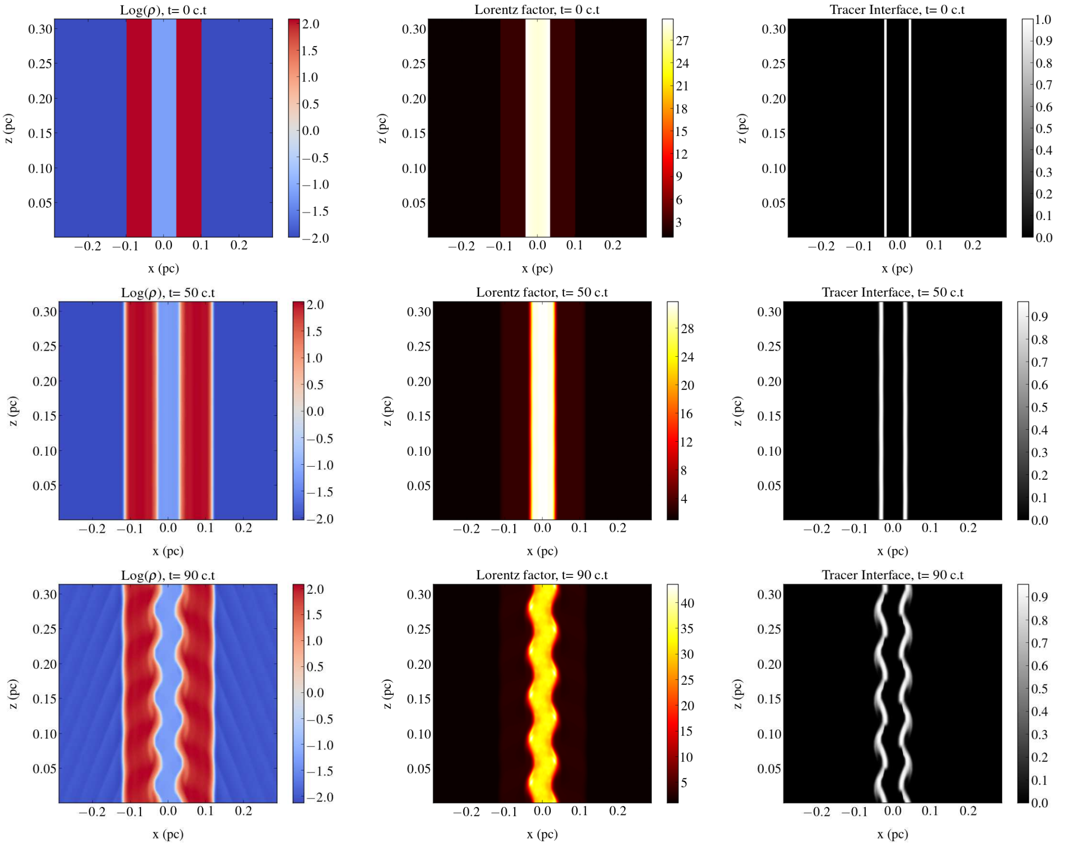

Figure 3.23: Evolution of a jet with initial $\sigma = 10$ and perturbation with $k = 10$. Shown here: density in log scale (left), Lorentz factor (middle column) and the passive tracer (right) at t=0,50 and 90 radial light crossing times.

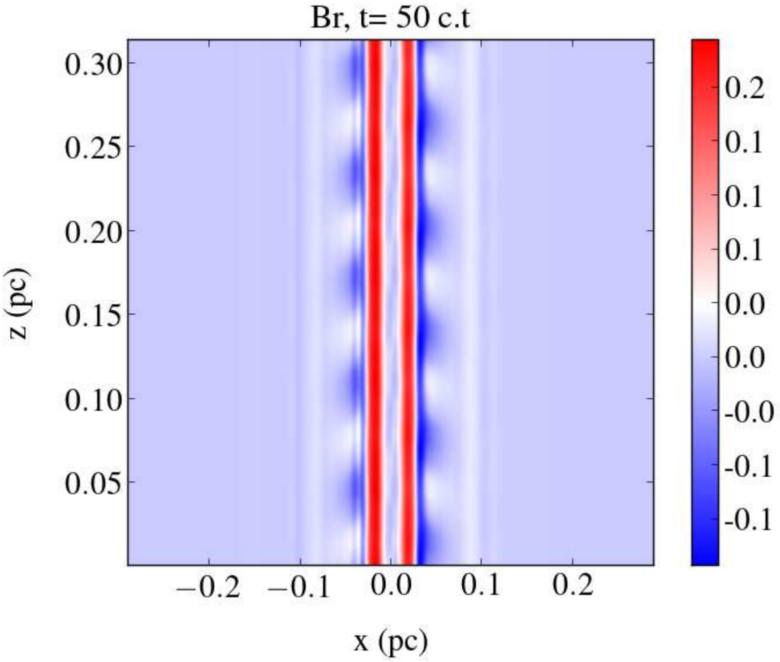

Figure 3.24: The development of the instability seen in the case with $\sigma = 10$ via the radial component of the magnetic field at t=50 radial light crossing times.

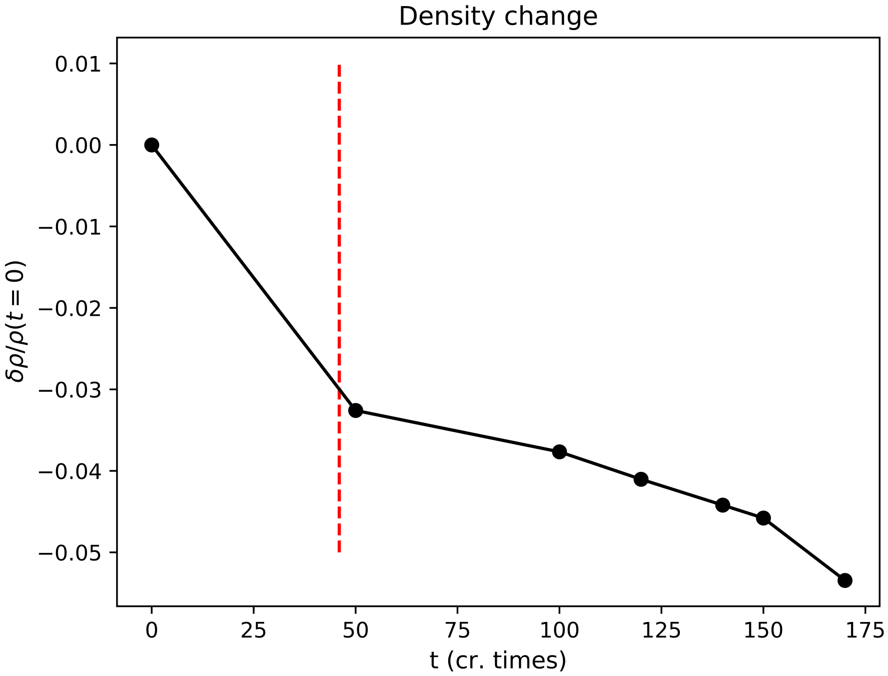

Figure 3.25: Similarly to Fig. 18 for the simulation with $\sigma = 10$ and $k = 10$.

and z-dependence. All cases include differential rotation between the two jet components and a non-uniform, radial profile for all the physical quantities (density, velocity, magnetic field, pressure). The analysis mostly focuses on low magnetization values (kinetic dominated jets), since all jets profiles tested here lead to high enthalpy. Numerical simulations of these two-component jets were performed, where the non-linear evolution of instabilities with analytical predictions were compared.

The main result is that the linear approximation is verified by the independent numerical simulations in a good extent. There was a quite good confirmation by the simulations in the predicted timescales. Apart from $\sigma = 1$ case, every other prediction linear approximation made was verified by the simulations. Also, the evolution suggested for each different solution was also verified.

The instabilities that were analyzed seem to behave quite similarly, even though the magnetization increases up to 10^4 times. The maxima of the $\mathrm{Im}(\omega)$ of the modes remain the same, apart from the $\sigma = 10$ case where an evident increase in these values is observed. Except for the imaginary part of ω, while analyzing the perturbed physical quantities and the Lagrangian displacement it was observed that two specific areas of the outflow that the majority of the destabilization process takes place. These are the two surfaces dividing the configuration into inner-outer jet and outer jet-environment respectively.

An accumulation of the maxima of the distribution of these specific quantities were noted, meaning that the initial configuration in terms of change of the profile of the physical quantities and displacement is going to be mostly affected. There was not found any correlation of specific modes with increasing magnetization. This was also verified by modes that are not present in the main analysis but follow this derived trend.

The perturbed forces for $\sigma = 0.01$ are inertial in nature while for $\sigma = 10$ the inertial and Lorentz forces are comparable in strength. In every case considered the maximum of these distributions are located at the same two surfaces mentioned above. The fact that the Lorentz force is not clearly dominant for such high magnetization value lies in the relativistic correction to equation (3.4), which divides the current formula by specific enthalpy. This results to smaller values for the parameter, which do not exceed $\sigma_\xi \lesssim 0.5$. In general, the instabilities seem to be of kinetic nature.

The need to study using as much information that can be extracted from the analysis in order to make conclusions as safe as possible for the physical mechanisms causing the disturbances should be emphasized. This can be seen by the similar eigenfunctions that the second case of low magnetization and the highest magnetization case have. This issue originates from the fact that the unperturbed physical quantities affect substantially the perturbed quantities that were examined.

In all cases examined here the evolution of *kink* modes was observed, which are included in the initial perturbations via the choice of the azimuthal wavenumber $m = 1$. This is evident especially via the displacement of the jet axis at the latest stages of the simulations, e.g. in Figures 3.17, monitored via a passive tracer injected at the interface of the two components.

However, in all cases, the rapid development of modes with $m = 4$ was noticed as well, which can be attributed to the use of Cartesian grid. This fact has already been reported in various similar studies (Meliani &Keppens, 2009; Porth, 2013). To avoid completely the effect of the Cartesian grid, combined with any boundary effects, one must use a larger box in the radial direction. However, this increases the requirements in terms of computing time or resources and the detailed study is beyond the scope of this work. The testing was limited to the use of two different domains ($-0.21 < x, y < 0.21$ pc and $-0.29 < x, y < 0.29$ pc), using the second domain size for the actual production runs. The overall evolution of the simulation is not drastically affected by the box size as long as it is larger than 2 jet radii; however, some boundary effects can be avoided, especially in the high σ cases, when using bigger domain.

The instabilities appear to develop mostly near the interface between the inner and the outer jet. This is, in general, consistent with the theoretical study and depends on the profile of the perturbations. However, the case with $k = 9.16$ is a notable exception, where the Lagrangian displacement has a larger amplitude near the outer jet. This leads to an unstable outer jet, a fact captured also in the simulations.

In all runs, and up to a certain extent, control over the growth time of instabilities is maintained via the arbitrary constant c_o in each perturbation. It was verified that the time difference in the development of instabilities due to different values of c_o are indeed observed in the simulations and are in good agreement with the analytical predictions.

The differences in the observed times and predicted times of the development of instabilities in the case with $\sigma = 1$ is not trivial to explain. It might be associated with the numerical diffusion, though it does not apply to the case with stronger magnetic field values ($\sigma = 10$). Another alternative is the introduction of noise during the numerical fitting of the eigenfunctions that are later used as initial perturbations. This process can introduce small, artificial discontinuities that may eventually cause a deviation from the full analytical solution.

To check the validity of the simulations from a more technical perspective, the simulations were also tested in lower resolution, 200^3, where the same overall evolution was noticed but with coarsened details. It must be highlighted, however, that for even lower resolution, the diffusion can be important and quench the instabilities. The reference cases (runs with $\sigma = 0.01$) were, in turn, tested in higher resolution, 400^3, with no significant differences as well. Last, all cases are also tested with a tvdlf solver, where no major difference was observed.

In agreement with the results of Meliani &Keppens (2009); Millas et al. (2017), the instabilities cause deceleration of the jet. The trend of less prominent deceleration, quantified by the average Lorentz factor of the inner jet, with increasing magnetization is also retrieved in all cases presented here (for instabilities that develop in the inner or the outer interface alike).

The next steps are to examine jets with a more realistic pressure profile, in particular modifying the constant p_o to achieve higher values of magnetization while reducing the enthalpy, to model relativistically cold jets as well. This will allow to explore a different category of jets (Poynting dominated flows) which, in principle, will behave differently when perturbed.

Another aim is to examine different magnetic field and density profiles in order to avoid steep transitions between different regions in the computational domain. This is particularly important for high σ cases, as the conditions we imposed here for $\sigma = 10$ lead to a considerable gap in the magnetic pressure between the outer jet and the environment.

Finally, a parametric study is needed in order to model the power ratio between the jet components, something related to the Fanaroff-Riley dichotomy. This can be a complementary study on jet stability.

Chapter 4

Cylindrical jet configurations based on acceleration and collimation processes

4.1 Derivation of unperturbed jet configuration

In this chapter the aim is to derive the behavior of the physical quantities for outflows which are assumed to be cylindrical and the dynamics dictated by the ideal relativistic magnetohydrodynamics (RMHD) set of equations (see for example Vlahakis 2023). Similarly to chapters 2 and 3 the imposed symmetry on the system leads to the dependence of the physical quantities solely on the radius, $\partial_\phi = \partial_z = 0$, while the system is also assumed to be stationary, $\partial_t = 0$. The plasma resistivity is zero and finally the outflow is considered to be cold, meaning that the thermal pressure of the jet is zero, $P = 0$ or equivalently the specific enthalpy equals one, $\xi \equiv 1 + \frac{\Gamma}{\Gamma - 1}\frac{p}{\rho} = 1$ (Γ is the polytropic index). The magnetic and electric fields have absorbed $\sqrt{4\pi}$ and we assume that the speed of light and jet's radius are equal to unity ($c = \varpi_j = 1$).

The main task is to derive profiles which are in accordance with the acceleration and collimation processes taking place at the early stages of the outflow, in the vicinity of the central engine. In order to do so, the radial component of the momentum equation (force balance) needs to be solved,

$$\frac{B_\phi^2 - E^2}{\varpi} - \rho_0 \frac{\gamma^2 V_\phi^2}{\varpi} + \frac{1}{2}\frac{d(B^2 - E^2)}{d\varpi} = 0\,, \tag{4.1}$$

where γ is the Lorentz factor, ρ_0 the proper density, $\mathbf{V}$ the velocity, $\boldsymbol{B}$ & $\boldsymbol{E}$ the magnetic and electric field respectively. Equation (4.1) is the simplified version of equation (2.14) assuming zero thermal pressure. The magnetic field consists of two components $\boldsymbol{B} = B_\phi\hat{\phi} + B_z\hat{z}$, the toroidal and z-component. The electric field is derived by Ohm's law,

$\boldsymbol{E} = -\boldsymbol{V} \times \boldsymbol{B}$. If the squared co-moving magnetic field is defined as F equation (4.1) may be formulated as:

$$\frac{F - B_z^2}{\varpi} - \rho_0 \frac{\gamma^2 V_\phi^2}{\varpi} + \frac{d(F/2)}{d\varpi} = 0 \,. \tag{4.2}$$

The Ferraro's law is also required:

$$\begin{aligned} \Omega &= \frac{V_\phi}{\varpi} - \frac{V_z}{\varpi} \frac{B_\phi}{B_z} \xRightarrow{\chi = \Omega\varpi} \\ \chi &= V_\phi - V_z \frac{B_\phi}{B_z} \,, \end{aligned} \tag{4.3}$$

where Ω is the angular velocity of the field lines and $\chi = \Omega\varpi$ the radius measured in light cylinder length units. This equation connects the physical quantities' profiles with the rotation at the base (Vlahakis, 2004; Komissarov et al., 2009). Among the physical quantities a desired behavior is only imposed on the velocity toroidal component

$$V_\phi = \frac{\lambda\chi}{1 + \lambda\chi^2} \,, \tag{4.4}$$

where λ is a constant regulating the maximum value of $V_\phi|_{max} = \sqrt{\lambda}/2$. This choice for V_ϕ ensures that for distances near the axis $\chi \ll 1$ the profile is linear with respect to the radius, $V_\phi \sim \chi$ and for distances $\chi \gg 1/\sqrt{\lambda}$ drops as the inverse of the radius $V_\phi \sim 1/\chi$. This is the only assumption for any physical quantity that is required for the rest of the solution. If equation (4.3) and the definition of the electric field are combined, then E can be written as $E = -\chi B_z$. So, when (4.4) is inserted into equation (4.3) and is squared the equation yields:

$$\begin{aligned} &\left(\frac{V_z}{B_z}\right)^2 \left[F + B_z^2(\chi^2 - 1)\right] = (\chi - V_\phi)^2 \Leftrightarrow \\ &\left(\frac{V_z}{B_z}\right)^2 \left[F + B_z^2(\chi^2 - 1)\right] = \chi^2 \left(1 - \frac{\lambda}{1 + \lambda\chi^2}\right)^2 \,, \end{aligned} \tag{4.5}$$

where the toroidal component of the magnetic field is expressed through F, $B_\phi^2 = F + B_z^2(\chi^2 - 1)$. If V_z is replaced with $V_z^2 = 1 - V_\phi^2 - \dfrac{1}{\gamma^2}$ then (4.5) becomes:

$$\left(1 - \frac{1}{\gamma^2} - \frac{\lambda\chi^2}{1 + \lambda\chi^2}\right)^2 \left[\frac{F}{B_z^2} + (\chi^2 - 1)\right] = \chi^2 \left(1 - \frac{\lambda}{1 + \lambda\chi^2}\right)^2 \,. \tag{4.6}$$

The unknown of (4.6) is χ, so obviously the above equation is polynomial with respect to the variable. In order to bring the equation to a comprehensive form (4.6) is algebraically manipulated into:

$$\chi^6\left(\frac{\lambda}{\gamma}\right)^2+\chi^4\lambda\left[\frac{2-\lambda}{\gamma^2}-\lambda\frac{F}{B_z^2}\left(1-\frac{1}{\gamma^2}\right)\right]$$
$$+\chi^2\left[\lambda\frac{F}{B_z^2}\left(\lambda-2+\frac{2}{\gamma^2}\right)+\frac{1-2\lambda}{\gamma^2}\right]+\left(1-\frac{1}{\gamma^2}\right)\left(1-\frac{F}{B_z^2}\right)=0\,. \quad (4.7)$$

Clearly this form of the equation is much easier to handle. One crucial element is that there are only even powers of χ, meaning that the equation can be reduced to a 3rd degree polynomial of χ^2. This is really important as any 3rd degree polynomial is always solvable, hence enables to have a proper solution in all cases. Furthermore, since this cubic equation has real coefficients, there is always at least one real solution.

4.2 Outflow modelling

The goal is to produce new jet models as described in the previous section. The only assumption made thus far is only for V_ϕ (4.4) in order to formulate the equation providing the radial profile of χ. Observing (4.7) there are also other quantities and parameters which must be specified in order to be able to fully solve the equation numerically.

Hence, there is also the need to define the behavior for $F,\ B_z,\ \gamma$ as functions of radius and specify the value for the parameter λ. The focus is on configurations having a fast central component, engulfed by a slower one, with different in general densities. In terms of asymptotic dependence on the radius the desired behaviors are:

$$F, B_z \propto \begin{cases} constant, & \varpi \ll \varpi_j \\ 1/\varpi^2, & \varpi \to \varpi_j \end{cases} \qquad \gamma \propto \begin{cases} constant, & \varpi \ll \varpi_j \\ constant, & \varpi \to \varpi_j \end{cases}$$

The functions chosen that fulfil the above requirements are:

$$F=\frac{B_0^2}{1+\Delta y^2}\,, \quad B_z=\frac{B_0}{1+y^2}\,, \quad \gamma=\gamma_b+\frac{\gamma_a-\gamma_b}{1+Ky^2}\,, \qquad (4.8)$$

where $B_0,\ K,\ \Delta,\ \gamma_a$ and γ_b are constants. Particularly, γ_a and γ_b are the values of the Lorentz factor on the axis and the boundary surface of the jet. y is normalised distance given by $y=\varpi/\varpi_0$. The new unit length, ϖ_0, can be calculated by (4.7) for $\varpi\to 0$ and is given by:

$$\varpi_0=\sqrt{\frac{(2-\Delta)(1-1/\gamma^2)}{(\lambda-1)^2-(1-1/\gamma^2)}\frac{1}{\Omega_0}}\,, \qquad (4.9)$$

where Ω_0 is the value of Ω on the axis of the jet. Density distribution is given by (4.2) solved with respect to ρ_0. The toroidal component of the magnetic field is provided by $B_\phi=-\sqrt{F+B_z^2(\chi^2-1)}$. Finally, new unperturbed models can be produced for any choice of parameter values. One particular set of parameters is analyzed including $\gamma_a = 10,\ \gamma_b = 5,\ \Omega_0 = 100,\ K = 10,\ B_0 = 1,\ \Delta = 0.99$ and $\lambda = 10^{-4}$.

The above selection results to $V_\phi|_{max} = 0.01$ so that rotation of the plasma is not important, $V_\phi \ll V_z$. The outlook of the model is summarized in Fig. 4.1. The solution gives a constant profile for Ω near the axis and then drops to much smaller values near the boundary of the outflow. As a result ρ_0 is constant near the axis going to its' maximum value at $\varpi \sim 0.1\varpi_j$ and then drops up until jet's radius attaining a value $\rho_0|_{\varpi_j} \sim 10^{-4}$.

The magnetization (σ) is defined as the electromagnetic energy density flow over the kinetic energy density flow, or in the limit where $V_\phi \ll V_z \Rightarrow \sigma \simeq B_\phi^2/(\gamma^2\rho_0\xi) \xrightarrow{\text{cold jet}} B_\phi^2/(\gamma^2\rho_0)$. The jet is kinetically dominated up to $\varpi \lesssim 0.1\varpi_j$ while for larger distances until the jet's boundary magnetization increases reaching a maximum value of $\sigma|_{max} \simeq 12$, corresponding to a magnetically dominated part of the jet. This trend is heavily affected by the decrease in the proper density in the outer region of the outflow.

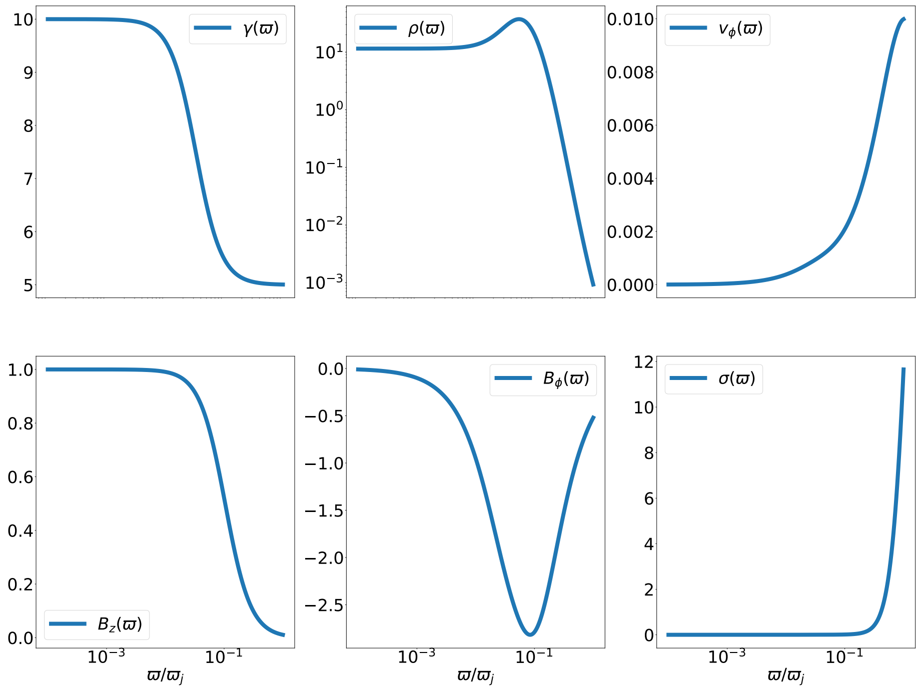

Figure 4.1: Plot of the unperturbed jet model generated for the parameters values in section 4.2. From left to right for the top row Lorentz factor, proper density and $\Omega\backslash\chi$ are presented, middle row V_ϕ, B_ϕ and magnetization (σ) and bottom row B_z respectively.

4.3 Linear stability analysis

The methodology to conduct linear stability analysis on a cylindrical outflow is presented in section 2.2. The methodology is applied to the model of section 4.2. In figure 4.2 the corresponding dispersion relation for the model is presented. The density ratio η which is the density of the environment over the density on the axis of the jet is set to $\eta = 100$. The general characteristics of the three different dispersion plots are similar. The maximum values for $\mathrm{Im}(\omega)$ are obtained for $k \lesssim 10$. This is achieved by numerous modes being well localized around a specific k. These modes begin at $k \sim 0.1$ and are present up to $k \simeq 10$. The trend of these localized solutions continues also for $k > 10$. The values of $\mathrm{Im}(\omega)$ through the various modes increase and reach an upper maximum which is approximately $\mathrm{Im}(\omega)|_{max} \simeq 0.2$ for all three plots.

As for the solutions which are present over a big range of k, for $m = 0$ the values of $\mathrm{Im}(\omega)$ (red colored mode) is below 10^{-4}, a fairly stable mode compared to the others. For $m = \pm 1$ two components are observed, one that peaks at small k and the other at high k. The trend is also the same, so the high k solutions are more unstable compared to their small wavenumber counterparts, but more stable compared to the localized modes for $k \simeq 8 - 10$.

The prevailing type of instability (maximum $\mathrm{Im}(\omega)$) should be the same for either $m = 0, \pm 1$ since the k values for which they manifest and the corresponding $\mathrm{Im}(\omega)$ are similar. For these solutions the observed growth rates are comparable to the corresponding values found in the literature, $\mathrm{Im}(\omega)|_{max} \sim 0.1$. The modes spanning across the dispersion plot range ($m = \pm 1$) are most probably of electromagnetic nature, as the value of m affects both the shape and the values of $\mathrm{Im}(\omega)$. The axisymmetric case does not showcase a mode similar to the one mentioned above. The localized modes which behave similarly for every dispersion plot hints towards a kinetic instability, most probably Kelvin-Helmholtz due to the difference in the velocity along the jet axis at the boundary of the outflow. Instabilities based on the rotation of the jet are deemed as improbable due to the really small value of V_ϕ.

In figure 4.3 the dispersion relations for the configuration described in section 4.2 but for $\eta = 0.01$ are presented. Beginning with the axisymmetric modes, the first observation is that the existence of the localized modes persist. They can be located for $k \sim 10$ at the right end of the plot. The green colored solution could be of the same type and it spans over $k \gtrsim 0.5$. The red colored solutions is more wide and cover a significant portion of the domain. This mode possibly is not of the same type as the localized counterparts. Nonetheless, this solution is effectively unstable for $0.1 \lesssim k \lesssim 10$.

Among those modes there is also another one which is depicted in blue color. The mode presents a cut-off $k \approx 0.35$ and then the imaginary part of ω increases monotonically with k up to $k = 10$. The characteristic for the blue dashed line is the linear relation between the two quantities, thus $\mathrm{Im}(\omega) \propto k$. Also, the value of the $\mathrm{Im}(\omega)$ reaches a maximum of $\approx 1.75 > 1$. This value for $\mathrm{Im}(\omega)$ ensues growth time scales which are comparable to the time the light needs to travel the jet's radius, this is a very rapidly growing mode. If the $\mathrm{Im}(\omega)$ value between the blue and the green mode are compared at the wavenumber

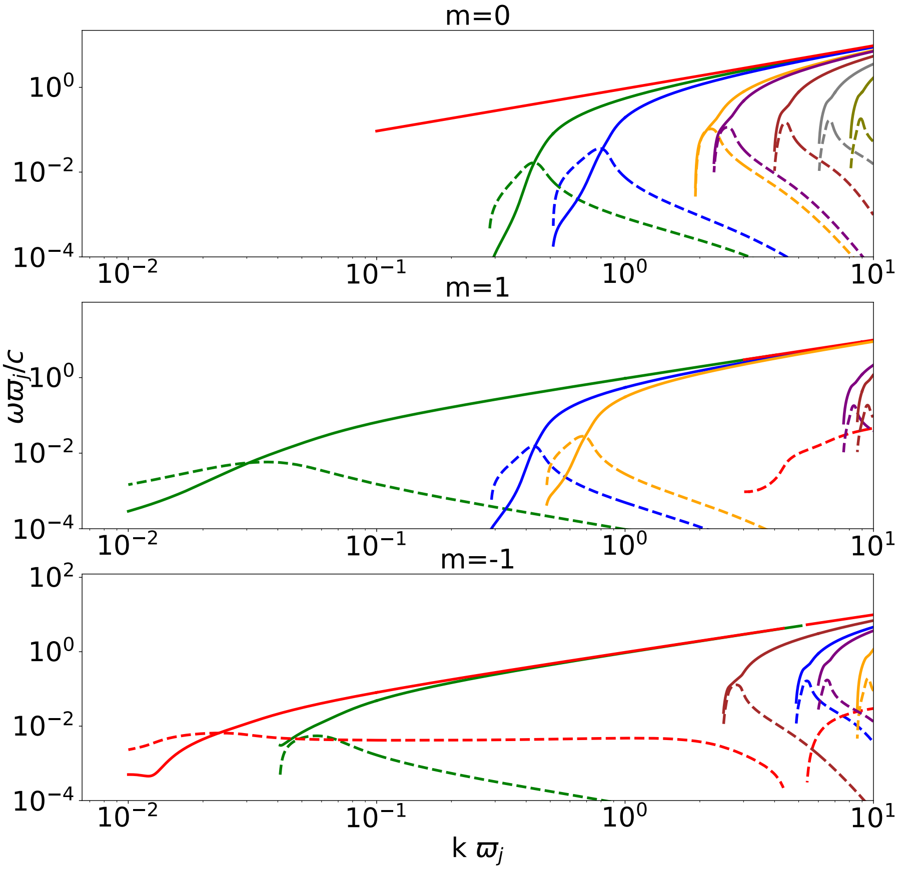

Figure 4.2: Dispersion plots for the model of section 4.2. Plots from top to bottom are for $m = 0, 1, -1$ respectively. Solid lines represent real part of ω while dashed lines are the imaginary counterpart. Different modes are represented with different colors. The modes of interest have maximum $\mathrm{Im}(\omega)$ at every k of the domain range as they are the modes which will have the smallest growth timescales and make their impact first on the jet configuration. The unit of ω is the inverse of the jet radius light-crossing time and the unit of k is the inverse of the jet radius.

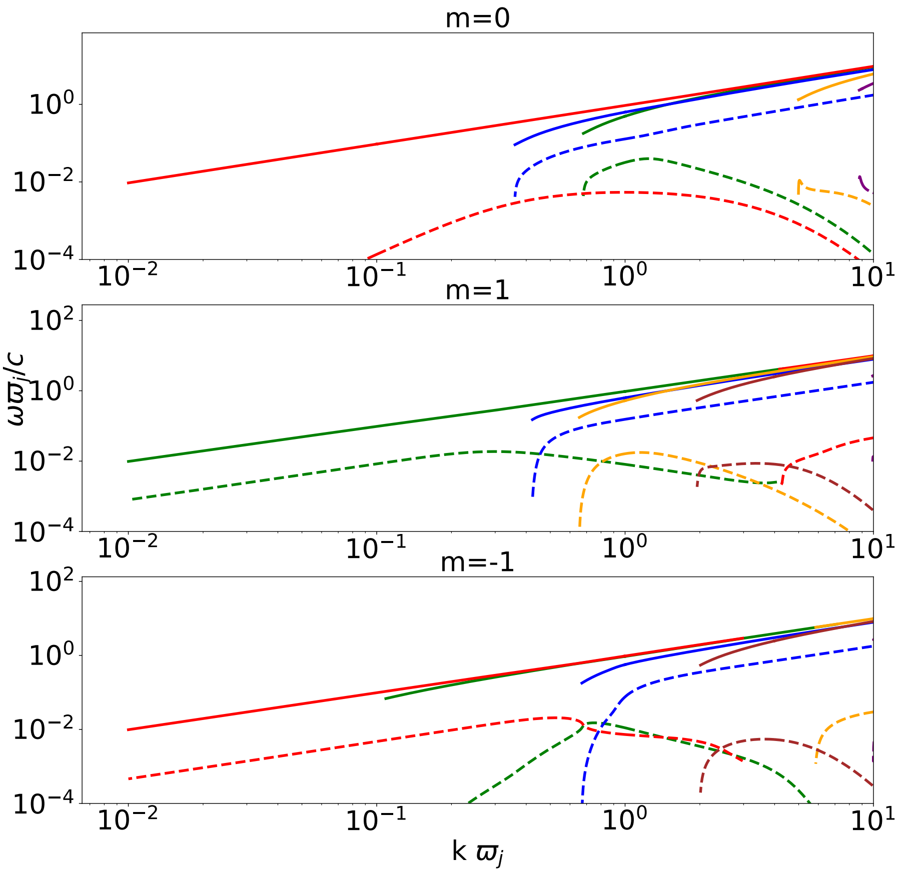

Figure 4.3: Similar to Fig. 4.2 for a configuration having $\eta = 0.01$.

for which the green mode maxes out, the linear solution's Im(ω) is approximately ×4 the corresponding value of the green mode.

The non-axisymmetric solutions ($m = \pm 1$) present similar results. The localized modes seem to have become much less concentrated around a specific wavenumber. There are two solutions which almost span over the entire domain (green and red colored modes for $m = 1,\ -1$ respectively). The blue colored modes, which showcase the Im(ω) $\propto k$ are also present for $m = \pm 1$. This means that this specific solution is weakly dependent on the value of m, at least for the three values that are included in these figures. The maximum Im(ω) is similar across the three plots, and the value of the wavenumber regarding the cut-off is the same for $m = 0, 1$ and slightly higher for $m = -1$. This blue mode dominates over every other mode for the wavelengths that the blue mode co-exists with the rest.

If this new solution is disregarded the conclusions drawn from figure 4.2 also apply for the configuration with $\eta = 100$. Therefore, this new solution depends on the value of the

η parameter. As the environment becomes denser the instability seems to weaken. The linearity of the mode alongside the high values for the $\mathrm{Im}(\omega)$ assign an extra importance to this specific mode. Such a rapidly growing instability is possible to outpace any other mode and affect the configuration even before the rest of the modes have begun to emerge. Already, the ratio of the environment's density value over the jet's counterpart on the axis seems to be an important factor. For this reason the next chapter focuses on the study of this specific mode and its properties.

Chapter 5

Linear stability analysis of relativistic magnetized jets The Kelvin-Helmholtz mode

This chapter focuses on the stability properties of the blue colored modes shown in figure 4.3. The model presented in 4.2 is not suitable to be used for this task, as the change in a single parameter value may affect numerous profiles of other physical quantities. This means that it is difficult to isolate and measure the effect on the specific solution by the change of a single parameter value. For this reason, this chapter adopts a new, simplified version of the model presented in chapter 4.

5.1 Unperturbed state of the jet

The dynamics of the outflow are described by the ideal relativistic magnetohydrodynamic (RMHD) set of equations (see, e.g. Vlahakis, 2004). The initial configurations are assumed to be steady–state ($\partial_t = 0$), cold (i.e. zero thermal pressure, $P = 0$), and cylindrically symmetric ($\partial_\phi = \partial_z = 0$), meaning that every physical quantity depends solely on the cylindrical radius, ϖ. The units system and formulation of the RMHD set of equations adopts the Heaviside-Lorentz system as presented in section 2, or as in Vlahakis (2023), hereafter V23. The units of length, time and velocity are the radius of the jet ϖ_j, the jet's radius light crossing time ϖ_j/c and the speed of light c respectively. The jet is required to be in force balance across its radius. Thus the physical quantities of the system must obey the radial component of the momentum equation (2.14).

In the case of a cold jet $P = 0$ and $\xi = 1$. Generally, both the magnetic and the velocity fields consist of two components $\boldsymbol{B} = \boldsymbol{B}_z + \boldsymbol{B}_\phi$ & $\boldsymbol{V} = \boldsymbol{V}_z + \boldsymbol{V}_\phi$. Specifically, the configurations of interest do not rotate ($V_\phi = 0$ & $V_z = \sqrt{1 - 1/\gamma^2}$) so the second term of (2.14) vanishes. This gives a complete freedom of choice for the radial distribution of the density.

Case	ρ_0	η	γ	σ	ϖ_0	ω
F	1	10	2	1	0.1	1.34+0.68i
F5	1	10	5	1	0.1	2.44+0.31i

Table 5.1: The parameters for the fiducial cases examined. The unit for density is arbitrary. The values of ω correspond to $k = \pi$. As a reminder $\eta = \rho_e/\rho_0$, where ρ_e is the density of the environment, The magnetization is defined in equation (5.3), and ϖ_0 controls the distribution of the magnetic field given by equations (5.1), (5.2).

The Lorentz factor and the density profile are chosen to be constant. For the magnetic field components the following relations are adopted (as in Mizuno et al., 2012):

$$B_z(\varpi) = \frac{B_0}{1 + (\varpi/\varpi_0)^2}\,, \tag{5.1}$$

$$B_\phi(\varpi) = -\frac{B_0\gamma}{1 + (\varpi/\varpi_0)^2}\frac{\varpi}{\varpi_0}\,, \tag{5.2}$$

where B_0 is constant and represents the value of B_z on the axis of the jet and ϖ_0 represents the jet's magnetic core. The magnetic field for the fiducial case (case F in Table 5.1) is plotted in Fig. 5.1 (middle & bottom panels). Also in Fig. 5.1, the top plot shows the magnetization which is defined in general by:

$$\sigma = \frac{B^2 - E^2}{\rho_0\xi}\,. \tag{5.3}$$

Equation (5.3) is used to find the value of B_0 given ρ_0 and the value of σ measured on the boundary of the jet. Also, the Matthews–Taub equation of state is adopted.

The jet is assumed to be surrounded by a static environment. This creates a top-hat profile for the jet-environment system as the jet has a constant velocity up to jet's radius which drops to 0 for the environment. The pressure of the environment can be hydrodynamic or can only have magnetic field and zero thermal pressure (cold environment). In the case of the magnetized environment the magnetic field is along the z-direction. Also a constant value for both the density and pressure/magnetic field profile is assumed. The environment is in pressure balance with the jet.

5.2 Linear Stability Analysis - Results

5.2.1 Parametric study of Kelvin–Helmholtz mode

Fiducial case

The methodology utilized to conduct linear stability analysis is described in section 2.2. The blue colored mode of figure 4.3 is also verified for the model described in section

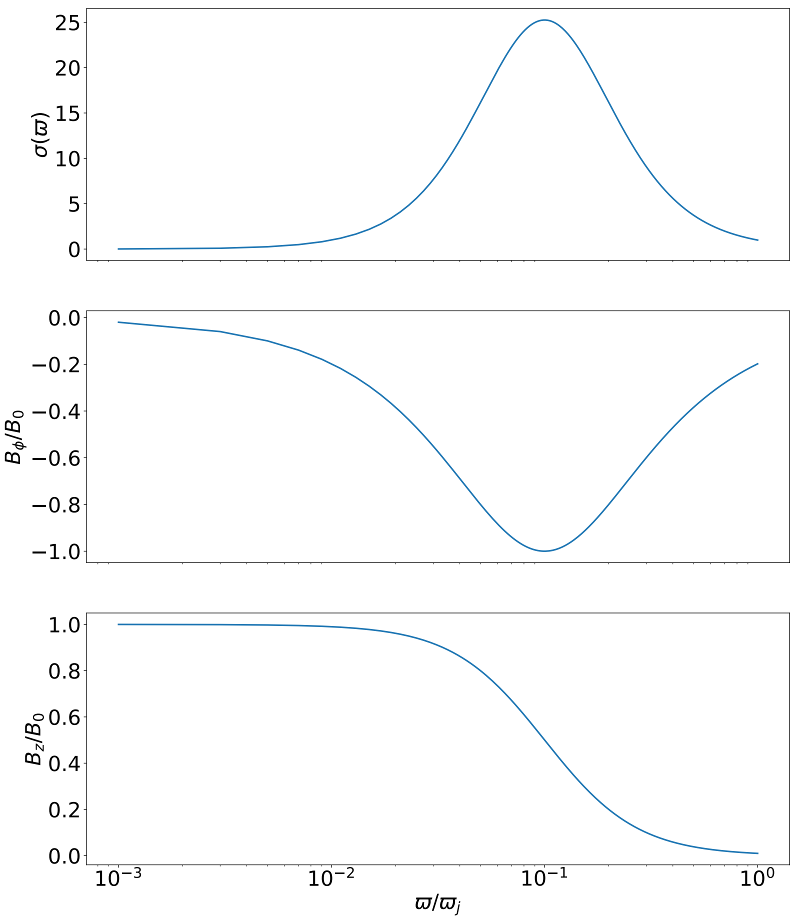

Figure 5.1: Plots for the quantities corresponding to the fiducial case. The top plot is the magnetization, middle and bottom plots are the toroidal and poloidal component of the magnetic field respectively.

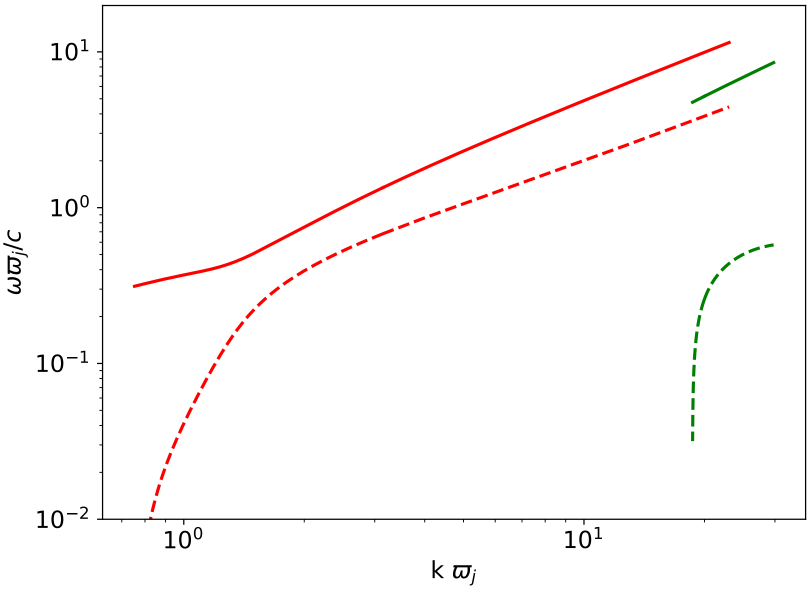

Figure 5.2: Dispersion relation plot for KH mode (red colored solution). Solid line represents Re(ω) while dashed line Im(ω). This dispersion plot correspond to case F and the environment is hydrodynamic.

5.1. The dispersion relation of the configuration for $m = 0$ can be viewed in Fig. 5.2, where it is reminded that the units for ω, k are c/ϖ_j, $1/\varpi_j$ respectively. Solid and dashed line represent the real and imaginary part of ω respectively and the specific solution mentioned earlier is in red color. The dashed line values are Im(ω) $\gtrsim 1$ for $k \gtrsim 10$ meaning that the instability growth timescales are comparable to the light crossing time of jet's radius. Additionally, the analysis in the present section reveals a number of traits for this specific solution, such as mode's locality and linear dependence of Im(ω) on k among others. These traits link to an established and well-studied instability in the literature, the Kelvin–Helmholtz instability. In essence a generalized relativistic equivalent in a cylindrical configuration is analyzed. For brevity's sake the Kelvin-Helmholtz mode is denoted as KH from this point on wards for this chapter.

The mode shows a linear relation of Im(ω) with k (Im(ω) $\propto k$) for $k \gtrsim 2$. This proportionality does not hold as k decreases, so the linearity stops at $k \sim 2$ and the mode becomes stable through a cut-off at $k \sim 1$. It should be noted that every other mode has Im(ω) values which are much smaller compared to the KH solution. Such a solution is the green-colored mode in Fig. 5.2. The mode starts at $k \sim 20$ and the Im(ω) ~ 0.3 for $k \sim 30$. At this wavenumber the dashed color line has value ~ 4, hence the KH mode is much more unstable compared to the green-colored mode. Also, there are other solutions which can be found for even higher wavenumbers but their respective Im(ω) are not comparable with the KH mode's equivalent. KH instability will surely be the first to emanate and disrupt the initial configuration, outpacing every other mode.

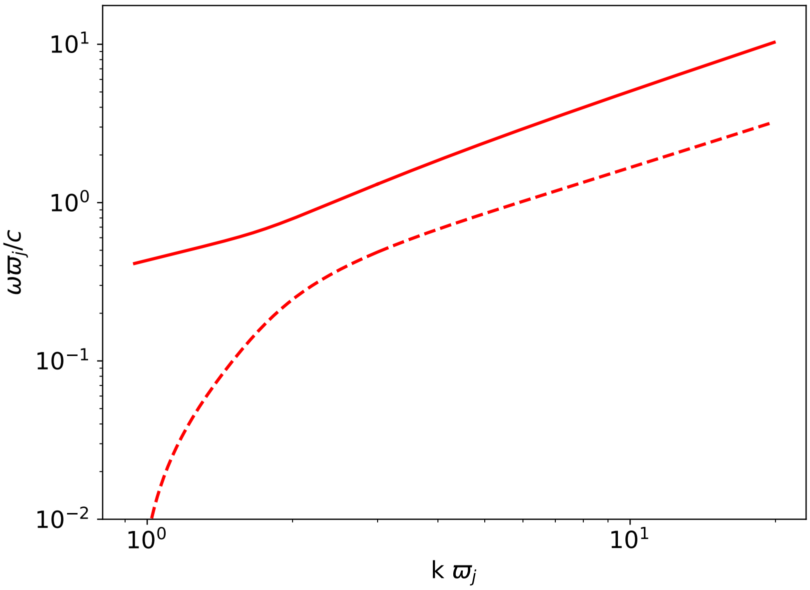

Figure 5.3: Dispersion relation plot for KH mode (red colored solution) for case F when the environment of the jet is magnetized. Solid line represents $\mathrm{Re}(\omega)$ while dashed line $\mathrm{Im}(\omega)$.

In Fig. 5.3 the dispersion relation of the KH mode when the environment of the jet is magnetized is plotted. The dispersion relation is quite similar to the respective one in Fig. 5.2. The imaginary part is proportional to the wavenumber for $k \gtrsim 2$ and $\mathrm{Im}(\omega) \gtrsim 1$ for $k \gtrsim 10$. The linearity stops for $k \sim 2$ and the mode stabilizes via a cut-off at $k \simeq 1$. The next solution is found for $k \gg 20$ and has $\mathrm{Im}(\omega) \ll \mathrm{Im}(\omega)_{\mathrm{KH}}$ so it is not included in Fig. 5.3. In both Figs. 5.2 & 5.3 other solutions apart from the KH mode are sparse. The instability profile of the jet is KH mode dominated.

Apart from $m = 0$ the KH mode was also found for $m \neq 0$. It was opted to check four other cases with $m = \pm 1,\ \pm 3$. In Fig. 5.4 $\mathrm{Im}(\omega)/\sqrt{k^2 + m^2}$ for the KH mode versus the corresponding m is plotted while $k = \pi$. For $m \pm 3$ the mode attains smaller $\mathrm{Im}(\omega)$ values than the rest of the cases. For $m = -3$, $\mathrm{Im}(\omega) \approx 0.05$ and for $m = 3$, $\mathrm{Im}(\omega) \approx 0.14$. Then for $m = 0,\ \pm 1$, the $\mathrm{Im}(\omega)$ values are really close and approximately equal to 0.21. It is noted that $m = 0$ is, by a small margin, the most unstable followed by $m = 1$ and $m = -1$ respectively. As m increases the $\mathrm{Im}(\omega)$ decreases, the mechanism for this behavior is discussed in section 5.3.

This linearity of $\mathrm{Im}(\omega)$ gives the chance to study the mode without having to plot the solution for multiple wavenumbers. The results are easily generalized just by calculating the difference in the value of $\mathrm{Im}(\omega)$ in relation to the change in k, so the analysis focuses on this component.

In this section the parametric stability analysis is presented. Initially, the fiducial

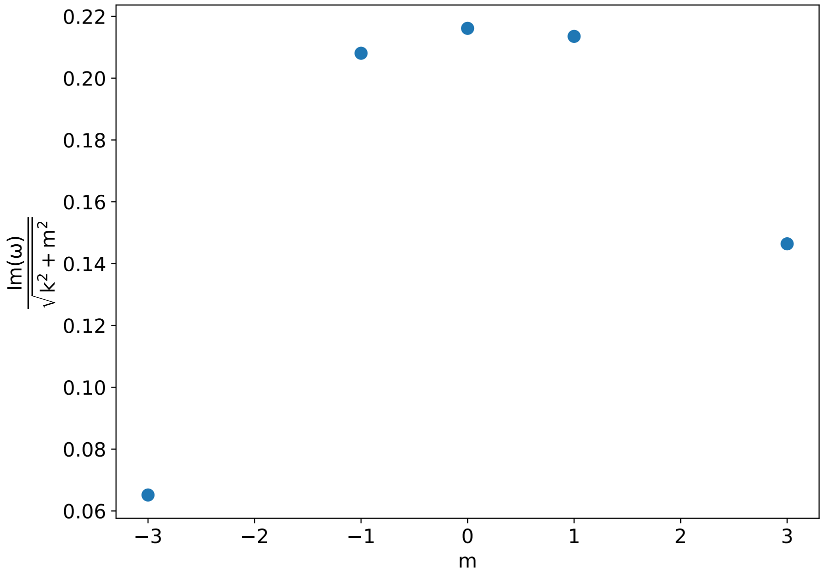

Figure 5.4: $\mathrm{Im}(\omega)/\sqrt{k^2+m^2}$ for KH modes regarding case F having $m = 0,\ \pm 1,\ \pm 3$ versus m for $k = \pi$.

configuration is probed, which is denoted as case "F" and the configuration is described in section 5.1. The density profile is constant and the parameter values are shown in Table 5.1. Parameter η is the ratio of environment's rest mass density over the jet's rest mass density, $\eta = \rho_e/\rho_0$.

This study focuses only on the axisymmetric mode, as it is the most unstable. For the parametric study that follows the wavenumber is fixed to $k = \pi$, corresponding to wavelength equal to jet's diameter.

Dependence of KH mode on the density ratio (η)

The first parameter under consideration is the density rest mass ratio, η. Both purely thermal and magnetized environments are discussed, the corresponding results are depicted in Figs. 5.5 & 5.6 respectively. The parameter spans over a wide value range from sparse environments ($\eta = 10^{-2}$) up to very dense counterparts ($\eta = 10^2 - 10^3$).

In Fig. 5.5 $\mathrm{Im}(\omega)$ versus η is observed for the thermal environment. For $\eta \leq 1$ a plateau of constant $\mathrm{Im}(\omega) \simeq 0.7$ is formed, while from $\eta \simeq 1$ up to $\eta \simeq 10$ a small increase in the value is noted. For higher ratio values the $\mathrm{Im}(\omega)$ decreases, and for $\eta \sim 10^3$ $\mathrm{Im}(\omega)$ has dropped down to ~ 0.4. Hence, the increase in the environment's density in general stabilizes the mode, while for a wide range of the parameter value ($\eta \leq 1$) the mode seems to not be affected by any change in η.

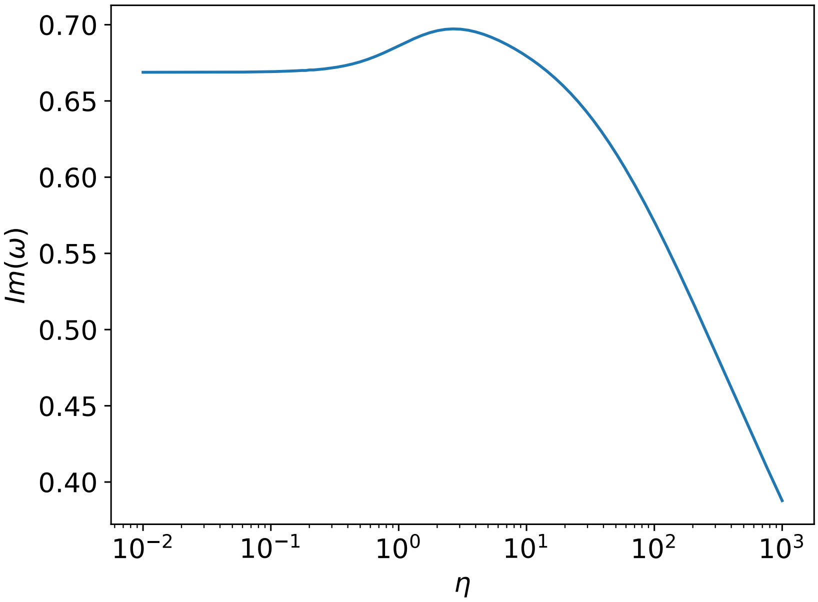

Figure 5.5: Plot of Im(ω) versus density ratio η for case F and a jet with hydrodynamic environment.

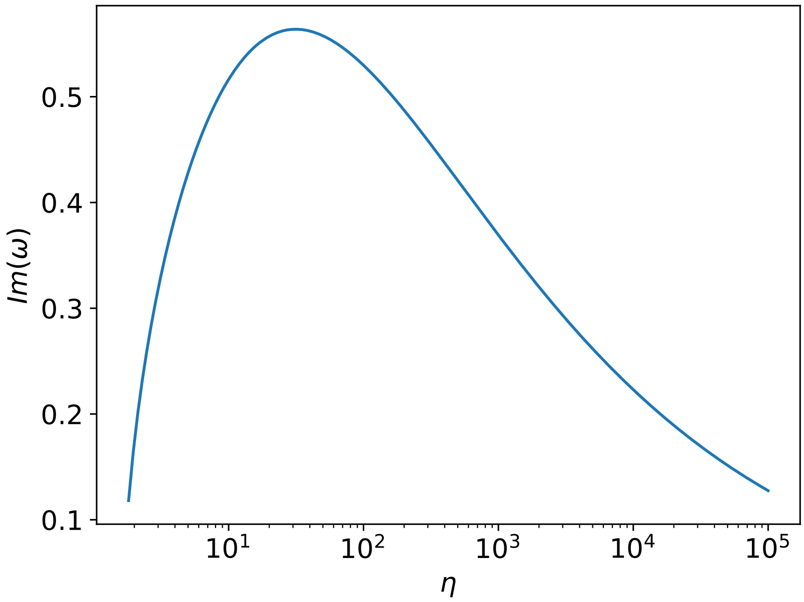

Figure 5.6: Similar to Fig. 5.5 for for case F and a magnetized environment.

In Fig. 5.6 $\mathrm{Im}(\omega)$ versus η is plotted in the case of a jet with a magnetized environment. Initially, a cutoff is noted at $\eta \sim 1$, then the $\mathrm{Im}(\omega)$ increases monotonically up until its maximum value $\mathrm{Im}(\omega) \simeq 0.6$ for $\eta \sim 30$. After this maximum a decrease starts towards higher η. The maximum $\mathrm{Im}(\omega)$ for the magnetized environment is smaller compared to the thermal equivalent.

Plots 5.5 and 5.6 suggest different mode behavior regarding the pressure providing mechanism of the environment, with the magnetized one being more stable than the thermal counterpart. When the environment is magnetized the KH mode is stabilized for $\eta \lesssim 1$. The thermal environment solution spans over a greater η range and has higher maximum $\mathrm{Im}(\omega)$. Clearly, the two different kind of environments lead to different results, setting the physics of the medium supporting the jet as an important factor. In general, denser environments stabilize the mode either by entirely eliminating it or sufficiently reducing the $\mathrm{Im}(\omega)$.

Dependence of KH mode on the magnetization (σ)

Moving on, the effect of the magnetization of the jet on the growth rate is studied. The magnetization value is calculated for $\varpi = \varpi_j$, along every other quantity which is radius dependent. The reason for making this choice is extensively discussed in sections 5.2.5 and 5.2.4. At this point it suffices to state that it has been observed that only the conditions of the region around the jet's boundary are important for the KH mode. First, Fig. 5.7 is examined, for which the environment is hydrodynamic. Clearly, the increase in the magnetization leads to increase in $\mathrm{Im}(\omega)$. For $\sigma \ll 1$ and $\sigma \gg 1$ the $\mathrm{Im}(\omega)$ becomes approximately constant. For $\sigma \ll 1$, $\mathrm{Im}(\omega) \to 0$ while for $\mathrm{Im}(\omega) \gg 1$, $\mathrm{Im}(\omega) \simeq 0.8$. The transition between these two extremes occurs at $\sigma \sim 1$.

In Fig. 5.8 $\mathrm{Im}(\omega)$ versus σ is presented for a magnetized environment. When $\sigma \ll 1$, $\mathrm{Im}(\omega) \to 0$ similarly to Fig. 5.7. As magnetization increases the imaginary part of ω also increases and reaches its maximum, $\mathrm{Im}(\omega) \simeq 0.5$, at $\sigma \simeq 1$. Immediately after this maximum a steep descent follows and the instability effectively vanishes at $\sigma \simeq 4$. Essentially, the KH mode is active only for a specific range of σ, contrary to the hydrodynamic counterpart for which this range is much more extended towards the higher σ values.

Also, the maximum $\mathrm{Im}(\omega)$ between the two cases is different, as the thermodynamic environment shows higher $\mathrm{Im}(\omega)$ values compared to the magnetized equivalent. In general, the magnetized environment seems to weaken the instability strength and even stabilize the mode entirely for the highly magnetized jets.

Dependence of KH mode on the Lorentz factor (γ)

In this section the relation of $\mathrm{Im}(\omega)$ with the Lorentz factor is explored. In Fig. 5.9 & 5.10 the plots of $\mathrm{Im}(\omega)$ versus γ for thermal and magnetized environment are presented respectively. Specifically, instead of γ the $\mathrm{Im}(\omega)$ is plotted versus the proper jet velocity, $\gamma v = \sqrt{\gamma^2 - 1}$.

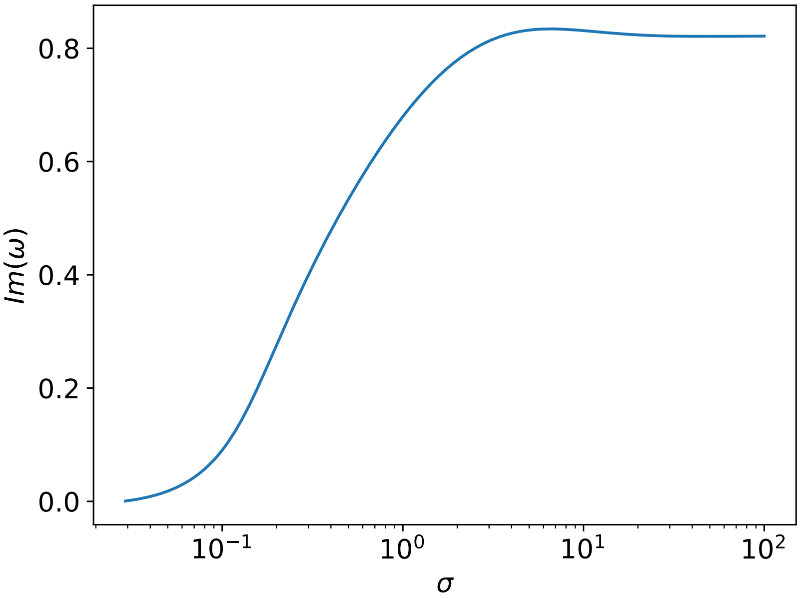

Figure 5.7: Plot of Im(ω) versus magnetization σ for case F and a jet with hydrodynamic environment.

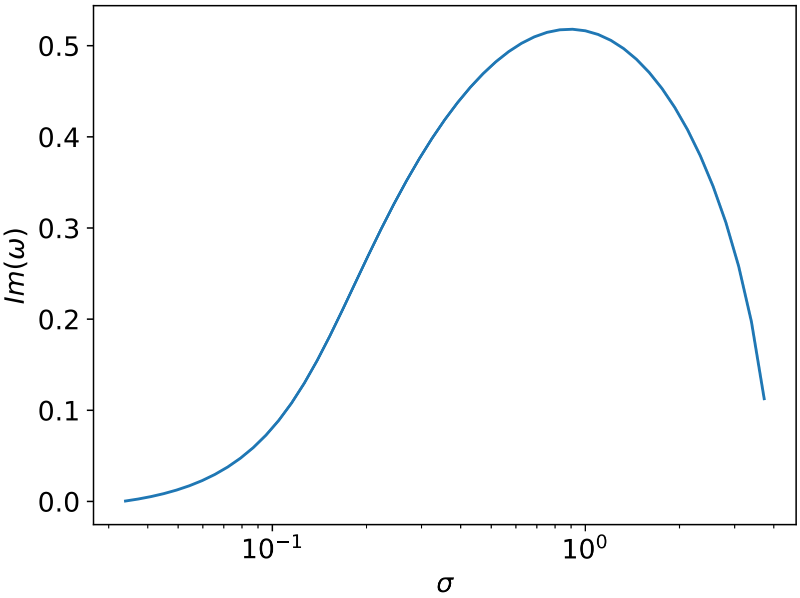

Figure 5.8: Similar to Fig. 5.7 for case F and a magnetized environment.

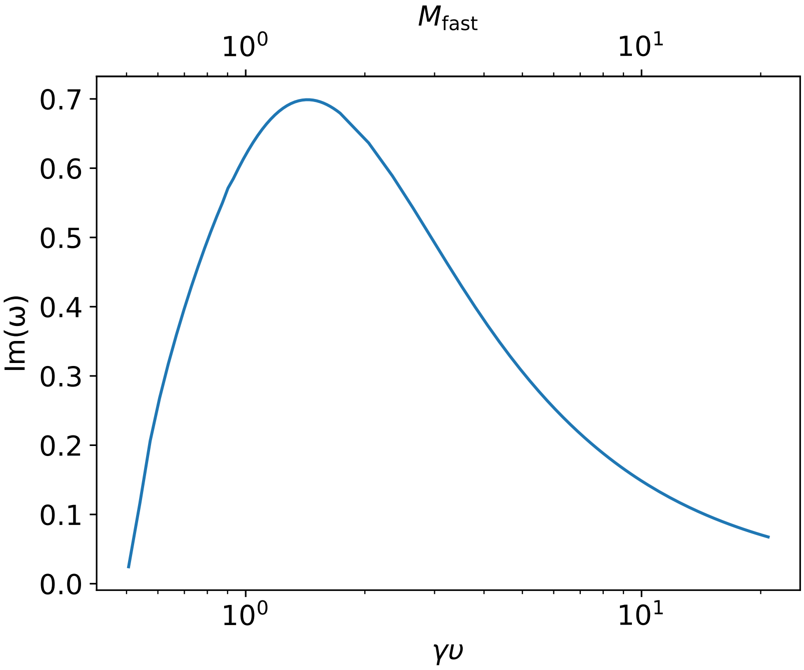

Figure 5.9: Plot of $\mathrm{Im}(\omega)$ versus outflow's proper velocity $\gamma\upsilon$ for case F. Jet's environment is hydrodynamic. The plot incorporates a secondary axis on the top edge of the plot box. The axis shows the proper fast magnetosonic Mach number.

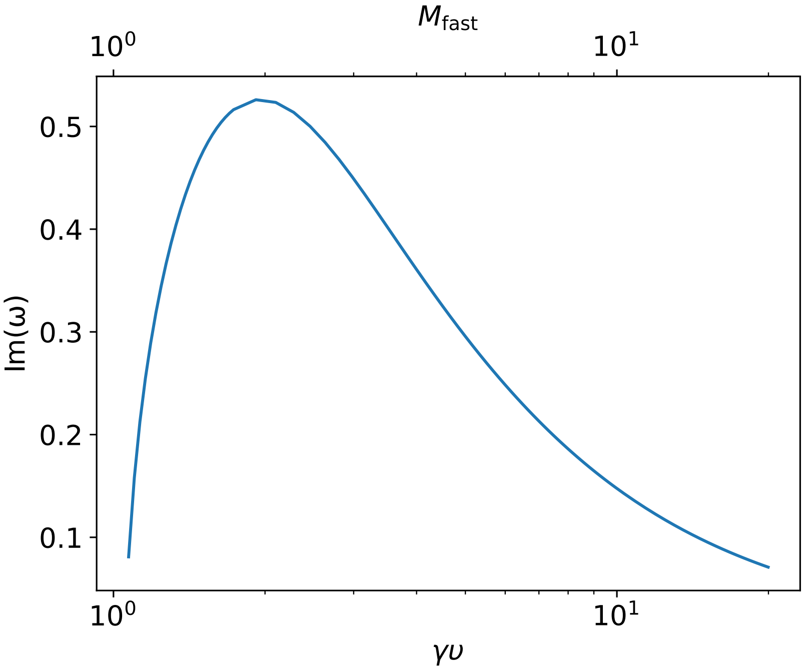

Figure 5.10: Similar to Fig. 5.9 for case F and a magnetized environment.

Starting with the hydrodynamic environment (Fig. 5.9), the first remark is that the KH mode is active for a specific velocity range. The mode disappears for $\gamma v \lesssim 0.5$ and its maximum is located near this cut-off with $\mathrm{Im}(\omega) \sim 0.7$ for $\gamma v \sim 1$. After the maximum, the $\mathrm{Im}(\omega)$ decreases with increasing γ, attaining value of $\mathrm{Im}(\omega) \sim 0.2$ for $\gamma v \simeq 10$. This way the effective range for the instability is set between $\gamma v \gtrsim 0.5$ and roughly $\gamma v \lesssim 10-15$. The axis on the top of the plot box shows the proper fast magnetosonic Mach number. The relation providing this Mach number is given by $M_{fast} = \gamma v/(\gamma_f v_f)$, where $\gamma_f = (1 - v_f^2)^{-1/2}$. It can be shown that for a cold jet $\gamma_f v_f = \sqrt{\sigma}$ (cf Appendix C of Vlahakis &Königl, 2003a). For the fiducial setup $\gamma_f v_f = 1$, hence the two horizontal axes are identical. We see that the instability hinders for ultra–fast magnetosonic velocities, with its maximum being close to $M_{\mathrm{fast}} \sim 1$. In general, the KH mode is inefficient for both ultra–relativistic and non–relativistic configurations.

In Fig. 5.10 the configuration with the magnetized environment is shown. Once more, the mode lies in a specific range regarding the γ value. Similar to Fig. 5.9 for $\gamma v \simeq 10$ the $\mathrm{Im}(\omega) \simeq 0.2$. The maximum is located at $\gamma v \sim 2$ and has a value of $\mathrm{Im}(\omega) \sim 0.5$. As the flow velocity further decreases, a cut–off is formed, where the mode stabilizes at $\gamma v \simeq 1$. Hence, jets with $\gamma v \lesssim 1 \Rightarrow \gamma \lesssim 1.4$ are not affected by the KH mode when the environment is magnetized. The mode becomes most unstable for $M_{fast} \approx 2$ and vanishes for ultra-fast magnetosonic velocities.

The magnetized environment affects negatively the KH mode, similar to sections 5.2.1 & 5.2.1. It decreases both the value of the maximum $\mathrm{Im}(\omega)$ and the γ range for which the jet is being affected by the mode.

Dependence of KH mode on the magnetic field components ratio (ϖ_0)

The next parameter to take into consideration is ϖ_0. As can be seen in equation (5.4) , ϖ_0 is directly associated with the ratio of magnetic field's components in the co–moving reference frame

$$\frac{B_z}{|B_{\phi,co}|} = \frac{\varpi_0}{\varpi} \,. \tag{5.4}$$

In the central source frame the ratio equals $\varpi_0/(\varpi\gamma)$. Changing the value of ϖ_0 affects which component of the jet is dominant over the other. In order to understand more clearly the effect ϖ_0 has on $B_z/|B_\phi|$ we keep the z-component of the magnetic field constant and vary only the toroidal counterpart. This way the effect B_ϕ has on the KH mode can be isolated. This is done by fixing the value of $B_z|_{\varpi\simeq\varpi_j}$ to the one corresponding to the fiducial case F. Then, the variation in ϖ_0 only changes the value of the toroidal magnetic field.

Fig. 5.11 presents the $\mathrm{Im}(\omega)$ versus ϖ_0 for the hydrodynamic environment. For $\varpi_0 \ll 1$, the $\mathrm{Im}(\omega)$ has an approximately constant value ≈ 0.8. As ϖ_0 increases the $\mathrm{Im}(\omega)$ decreases, especially after $\varpi_0 \approx 0.1$. At this particular value a cut-off is formed, leading to the subsequent mode stabilization ($\mathrm{Im}(\omega) \to 0$).

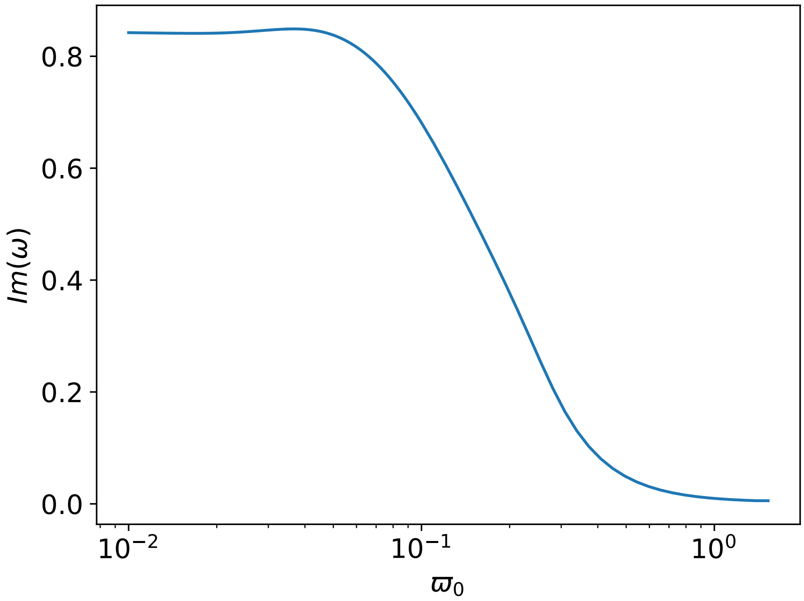

Figure 5.11: Plot of Im(ω) versus magnetic field components ratio ϖ_0 for case F. Jet's environment is hydrodynamic.

In Fig 5.12 the environment is magnetized. The two plots are quite different. For $\varpi_0 \approx 0.05$ the inhibition of the mode through a cut-off is noted. The growth rate becomes maximum for $\varpi_0 \approx 0.1$ with $\mathrm{Im}(\omega) \approx 0.5$ and then decreases as ϖ_0 further increases. For both Fig. 5.11 and 5.12 the instability has already been stabilized when ϖ_0 becomes equal to 1. The hydrodynamic environment case has larger maximum Im(ω) compared to the magnetized counterpart. Essentially, for both scenarios it seems that when $B_z/\left|B_\phi\right| \geq 1$ the KH mode is stabilized.

5.2.2 Jet configuration with a thermal pressure component

The results of section 5.2.1 suggest that B_z is an important regulator for the behavior of the Kelvin-Helmholtz mode. Roughly, when $B_z/\left|B_\phi\right| \to 1$ the mode becomes completely stabilized. In order to test if the value of the B_z is the main stabilizing factor, a modified case F is formulated. The component of the magnetic pressure originating from B_z is replaced with an equivalent thermal pressure component, while the rest of the configuration remains unaltered

$$P(\varpi) \equiv \frac{B_z^2}{2} = \frac{B_0^2}{2\left[1+(\varpi/\varpi_0)^2\right]^2}\,. \tag{5.5}$$

Essentially, with this change the jet's total pressure distribution is preserved. For this

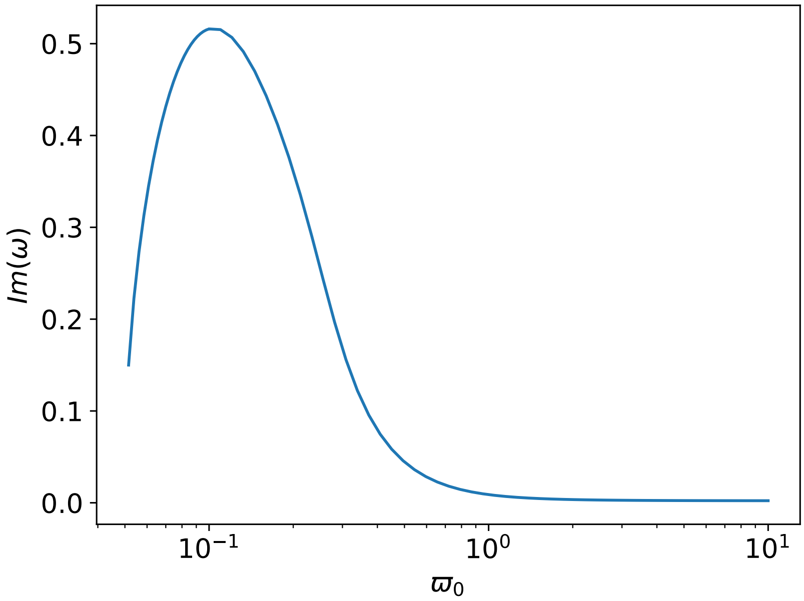

Figure 5.12: Similar to Fig. 5.11 for case F and a magnetized environment.

section only a hydrodynamic environment is considered. The KH mode was also confirmed for this configuration. This result further expands the outflows which produce this specific solution, including jets with thermal pressure components.

In Fig. 5.13 Im(ω) versus ϖ_0 is plotted. For $\varpi_0 \ll 1$ the mode has a constant value of Im$(\omega) \approx 0.8$. As ϖ_0 increases Im(ω) does not experiences any substantial change until $\varpi_0 \sim 0.1$. For this value the Im(ω) sharply decreases until the mode is essentially stabilized. The transition has already completed for $\varpi_0 \approx 1$. The differences with Fig. 5.11 are subtle, hence the two cases present almost the same behavior.

Furthermore, ϖ_0 can be associated with the ratio of the thermal pressure over the magnetized counterpart, $P/(\frac{B_\phi^2 - E^2}{2})$, known in the literature as plasma β. The relation is provided by:

$$\beta \equiv \frac{2P}{B_\phi^2 - E^2} = (\frac{\varpi_0}{\varpi})^2 , \tag{5.6}$$

which is exactly equal to ϖ_0^2 on the boundary of the jet. This means that the mode is present for a really wide range of β values. Beginning from negligible thermal pressure over to thermally dominated configurations the KH solution is found. The mode initiates from roughly $P/(\frac{B_\phi^2 - E^2}{2}) \sim 10^{-6}$ up to $P/(\frac{B_\phi^2 - E^2}{2}) \sim 1$.

In Fig. 5.14 Im(ω) versus η is plotted. The figure is essentially the same with Fig. 5.5.

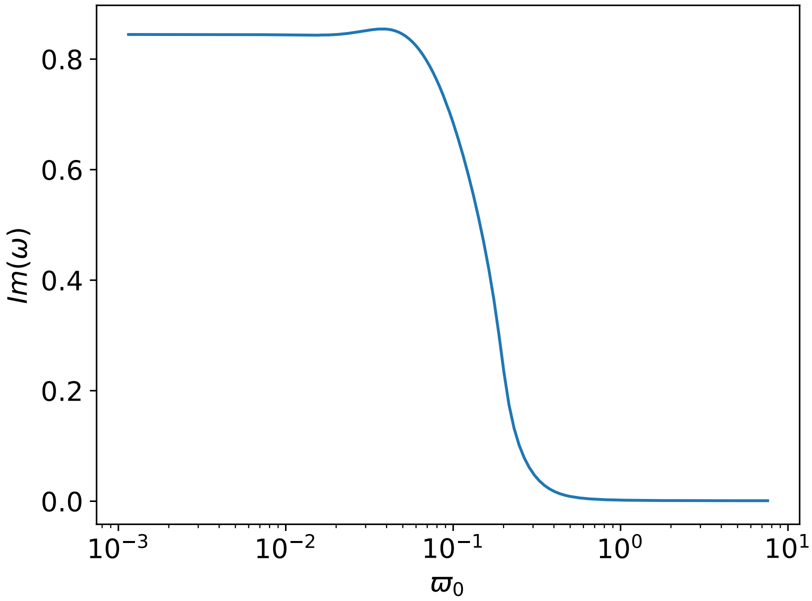

Figure 5.13: Plot of Im(ω) versus ϖ_0 for a jet with a thermal pressure component.

This means that the dependence of the mode on η disregards the existence of the B_z component.

In Fig. 5.15 Im(ω) versus the Lorentz factor is plotted. This result is almost identical to Fig. 5.9. The mode's strength declines as γ increases, and experiences a cut–off around $\gamma v \approx 0.5$. The maximum is located at $\gamma v \sim 1$ and has a value of $\mathrm{Im}(\omega) \approx 0.7$. Similar to the solution's behavior regarding η, the mode's dependence on the Lorentz factor does not seem to be affected by the presence of the thermal pressure component.

In Fig. 5.16 Im(ω) versus the magnetization is observed. The profile of Im(ω) stays unaltered compared to Fig. 5.7. It should be highlighted that from 5.5 a change in the value of σ, also affects plasma β, as P also changes. Nonetheless, there is a transition between two constant values at $\sigma \approx 1$. For $\sigma \gg 1$, $\mathrm{Im}(\omega) \approx 0.8$ while for $\sigma \ll 1$ $\mathrm{Im}(\omega) \to 0$. It should be noted that the difference in the values on the horizontal axis between Figures 5.7 and 5.16 is due to the value of the specific enthalpy which is not equal to 1 when the jet includes a thermal pressure component.

Overall, the configurations with and without B_z behave similarly. The profiles of Im(ω) versus the various quantities between sections 5.2.1 and 5.2.2 are similar. This deduction implies that the presence of the thermal pressure is not a key factor for the behavior of the mode and the mechanisms that inhibit or enhance the instability.

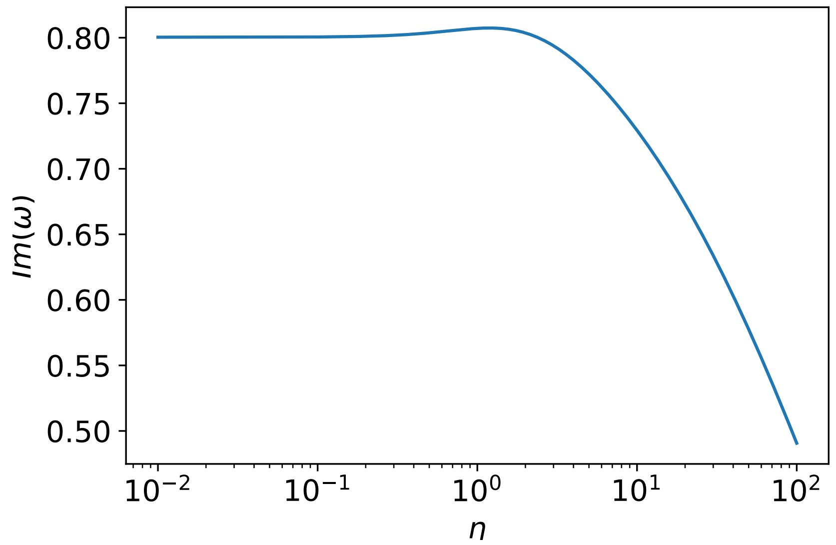

Figure 5.14: Plot of Im(ω) versus η for a jet with a thermal pressure component.

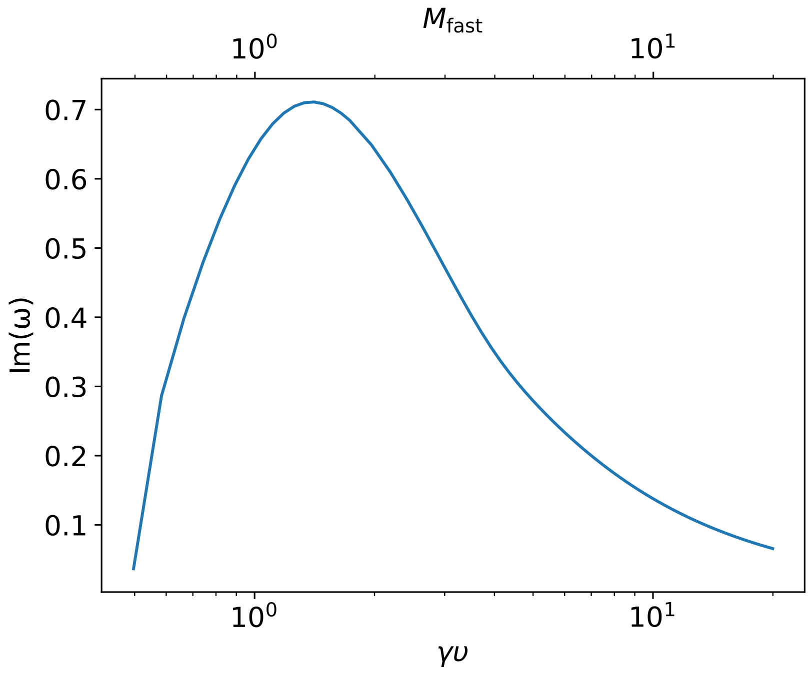

Figure 5.15: Plot of Im(ω) versus the Lorentz factor for a jet with a thermal pressure component.

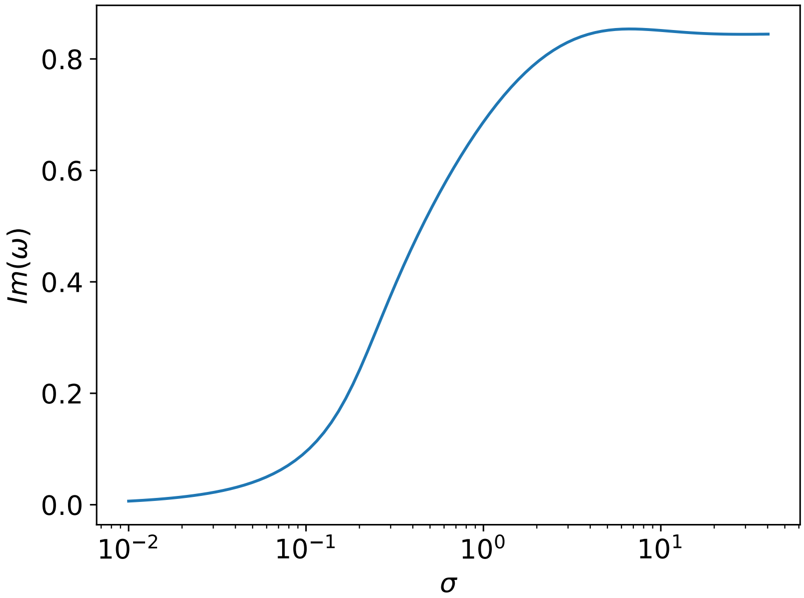

Figure 5.16: Plot of $\mathrm{Im}(\omega)$ versus σ for a jet with a thermal pressure component.

5.2.3 Alternative configuration, $\gamma = 5$

In this section an alternate configuration to case F is discussed. The setup is identical to the previous case, apart from Lorentz factor which is set to $\gamma = 5$. The new configuration is denoted as F5 and its parameters fiducial values are also summarized in Table 5.1 including the corresponding ω when $k = \pi$. In Fig. 5.17 the dispersion relation for this modified setup is presented. The KH is represented by the red lines. The $\mathrm{Im}(\omega)$ clearly increases with k, but does not showcase a strict linear dependence on it. There are also numerous solutions whose $\mathrm{Im}(\omega)$ become comparable to KH's $\mathrm{Im}(\omega)$ value as k increases. Some of them are $\propto k$ (yellow and brown colored solutions) but as the blue colored mode ceases to be linear for large enough k, it is possible that the rest of the modes behave similarly.

It should be noted that the physical mechanism of these new modes could be different to that of the KH solution. This was probed via a multiple η test, where we increased the density ratio to $\eta = 100$. This resulted to the elimination of the KH mode but didn't affect any of the other modes at all. This trait is typical of current-driven instabilities (Appl et al., 2000) and these solutions could be linked to this type of instability.

Following the structure of section 5.2.1 the parametric study of the stability analysis for F5 configuration regarding η, σ, and ϖ_0 for both hydrodynamic and magnetized environment is presented.

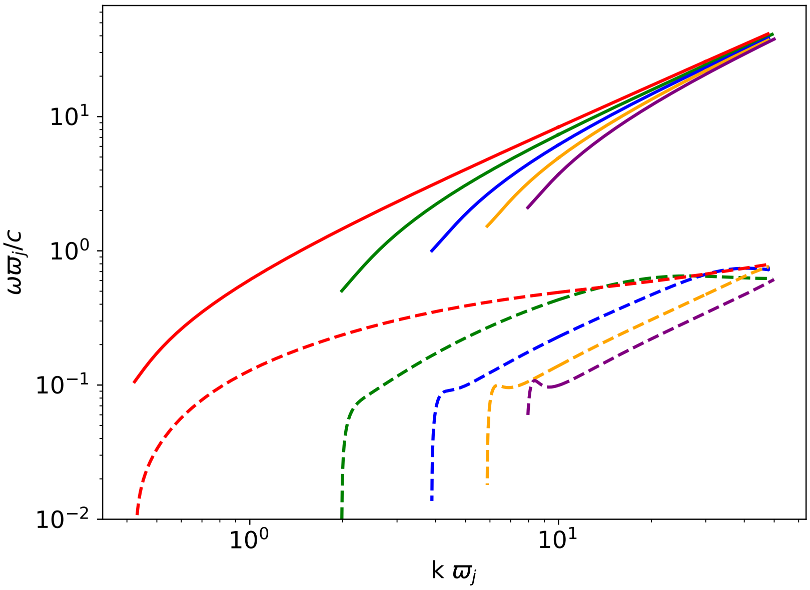

Figure 5.17: Dispersion relation plot for KH mode (red colored solution) for the alternative configuration (case F5), for which the Lorentz factor $\gamma = 5$.

Alternative configuration–
Dependence of KH mode on density ratio (η)

Beginning with the density ratio, in Fig. 5.18 and 5.19 the Im(ω) versus η for hydrodynamic and magnetized environment have been drawn respectively. Both plots resemble Fig. 5.5 and 5.6, except for a few details. In general, smaller Im(ω) values are observed across the whole η range. This could already be expected by the result of Im(ω) versus γ in section 5.2.1, where for $\gamma = 5 \Rightarrow \gamma \upsilon \simeq 5$ the Im(ω) is substantially smaller than the corresponding value for $\gamma \sim 2$.

In Fig. 5.18 a constant valued plateau for $\eta \ll 1$ is observed. As η increases, the Im(ω) also increases starting from $\eta \approx 1$ up to $\eta \approx 20$, where its maximum is reached. The amount of total increase in Im(ω) is substantial, whereas this trend in case F is almost unobservable. Then as η further increases the mode begins to weaken and shows stabilizing behavior for $\eta \gg 1$.

The figure for the magnetized environment, Fig. 5.19, seems to be almost identical to Fig. 5.6. Apart from the smaller Im(ω) values, the distribution in Fig. 5.19 has its maximum slightly shifted towards smaller η. The mode is stabilized at $\eta \approx 0.2$, which is just a little less than the respective value in case F.

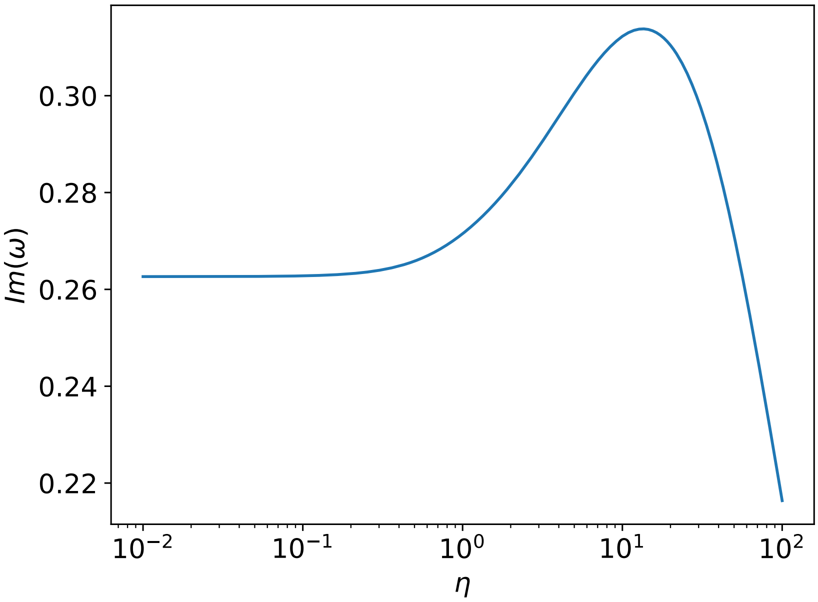

Figure 5.18: Plot of Im(ω) versus density ratio η for the alternative configuration F5. The environment is hydrodynamic.

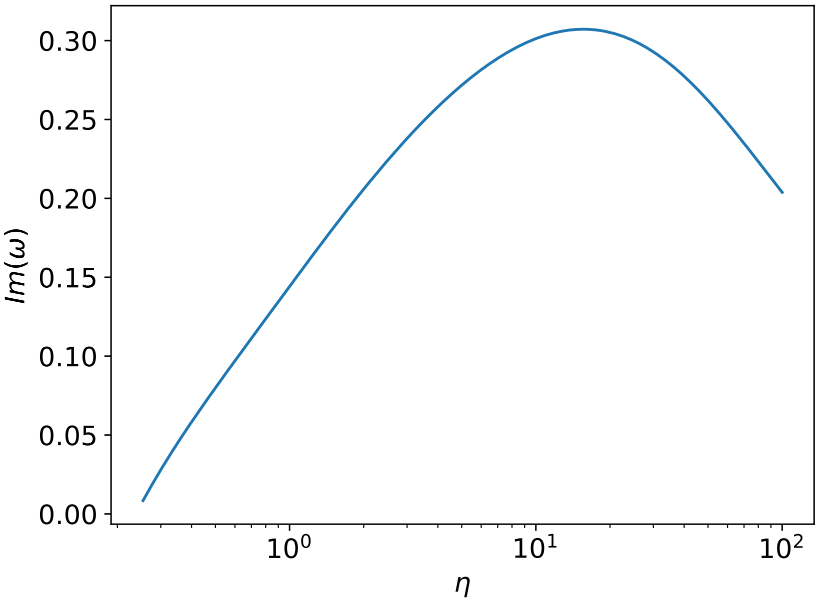

Figure 5.19: Similar to Fig. 5.18 for case F5 and a magnetized environment.

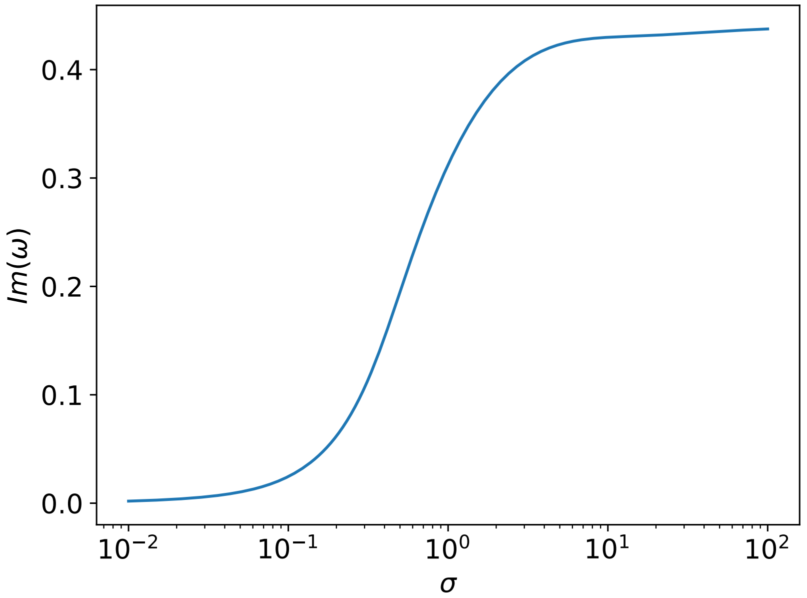

Figure 5.20: Plot of Im(ω) versus magnetization σ for the alternative configuration F5. The environment is hydrodynamic.

Alternative configuration– Dependence of KH mode on magnetization (σ)

Like section 5.2.1, the dependence of KH mode with the value of the magnetization at $\varpi \approx \varpi_j$ is probed. In Fig. 5.20 the Im(ω) versus σ for the hydrodynamic environment is plotted. Figures 5.7 and 5.20 are similar, presenting two constant Im(ω) for $\sigma \ll 1$ and $\sigma \gg 1$ respectively. The instability is favored by highly magnetized configurations, while as σ decreases the mode fades out. The transition between the two plateaus, similarly to Fig. 5.7, occurs at $\sigma \sim 1$.

Fig. 5.21 presents results corresponding to the magnetized environment. The mode is stabilized for both $\sigma \ll 1$ and $\sigma \gtrsim 20$. The decrease for $\sigma \gtrsim 3$ is quite steep. The maximum is located at $\sigma \approx 3$, slightly higher than the corresponding value in Fig. 5.8. The Im(ω) values, in general, are smaller compared to the ones in Fig. 5.8. Overall, the results regarding magnetization are in line with the results of section 5.2.1.

Alternative configuration – Dependence of KH mode on magnetic field components ratio (ϖ_0)

Finally, the results for Im(ω) versus ϖ_0 for both hydrodynamic and magnetized environment are presented. Fig. 5.22 depicts results for the hydrodynamic environment. Likewise Fig. 5.11, the mode is favored by small ϖ_0, specifically $\varpi_0 \lesssim 0.1$. While ϖ_0 decreases

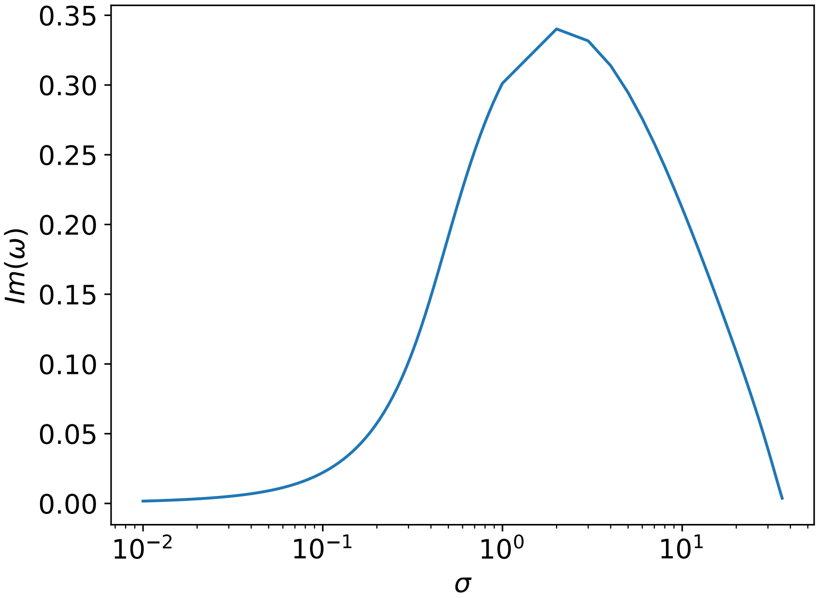

Figure 5.21: Similar to Fig. 5.20 for case F5 and a magnetized environment.

further below 0.1, the mode showcases a slight $\mathrm{Im}(\omega)$ increase. This trait is not present in Fig. 5.11. For $\varpi_0 \gtrsim 0.1$, the $\mathrm{Im}(\omega)$ decreases rapidly until $\varpi_0 \approx 1$, where the $\mathrm{Im}(\omega)$ becomes negligible.

Fig. 5.23 shows $\mathrm{Im}(\omega)$ versus ϖ_0 for the magnetized environment. Similar to the hydrodynamic counterpart, Fig. 5.23 and 5.12 present substantial similarities. The mode is stabilized for $\varpi_0 \ll 1$ and $\varpi_0 \gg 1$, while the maximum is located at $\varpi_0 \approx 0.1$, with the $\mathrm{Im}(\omega) \approx 0.35$. The maximum $\mathrm{Im}(\omega)$ is smaller than the corresponding value of case F. The mode is effectively stabilized for $\varpi_0 \approx 10^{-2}$ through a steep descent.

5.2.4 Eigenfunctions

The eigenfunctions for the fiducial case (case F) are depicted in Fig. 5.24. The top panel depicts y_1 and the bottom panel y_2 for $k = \pi$. Both the real and the imaginary component for each eigenfunction are shown. Beginning with y_1 it is observed that both the real and the imaginary part have their respective maxima in the vicinity of jet's boundary surface. This indicates that the jet's flow lines are going to be displaced mainly at $\varpi \approx \varpi_j$ area. Lagrangian displacement diminishes for both $\varpi \to 0$ and $\varpi \to \infty$.

For y_2 different traits are showcased compared to y_1. Both components tend to present their global maxima near the axis of the jet. As radius increases the eigenfunction's components decrease in value, but after a closer inspection it is noted that both real and imaginary parts present local maxima in the vicinity of the boundary. So, both

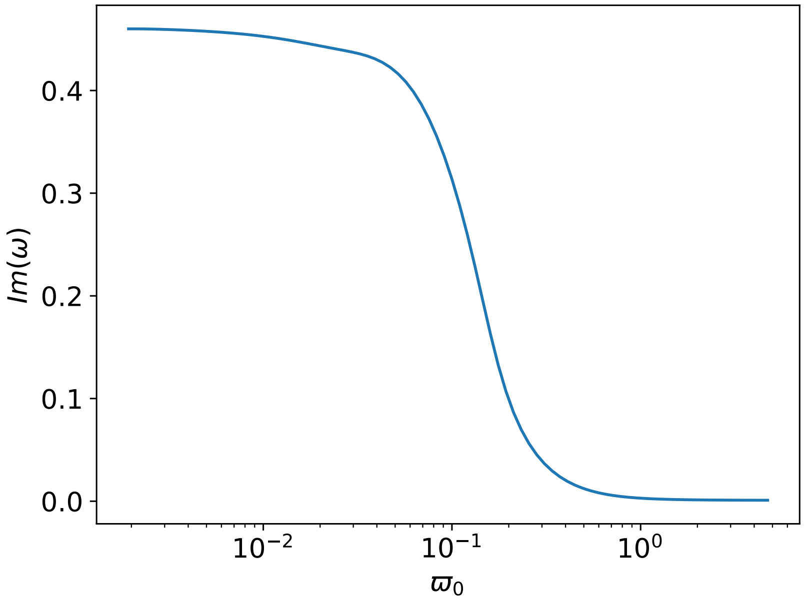

Figure 5.22: Plot of Im(ω) versus magnetic field components ratio ϖ_0 for the alternative configuration F5. The environment is hydrodynamic.

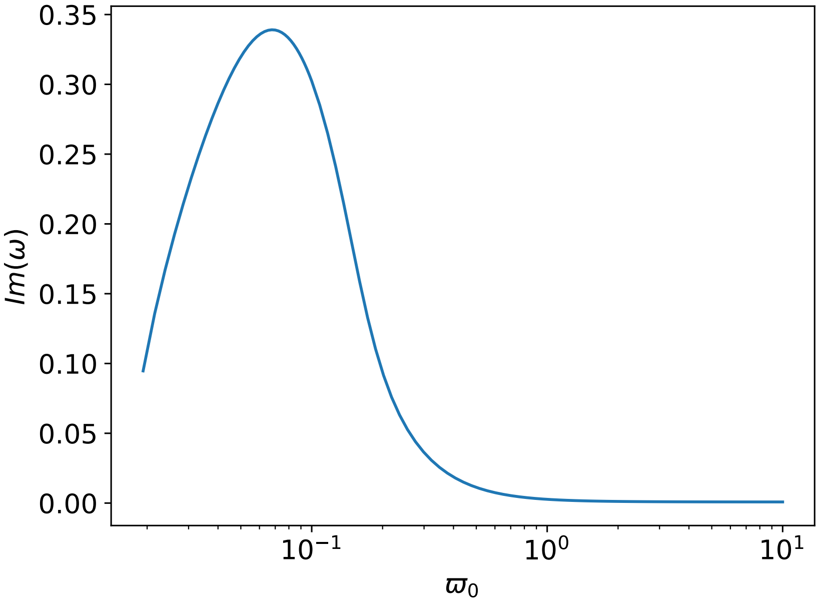

Figure 5.23: Similar to Fig. 5.22 for case F and a magnetized environment.

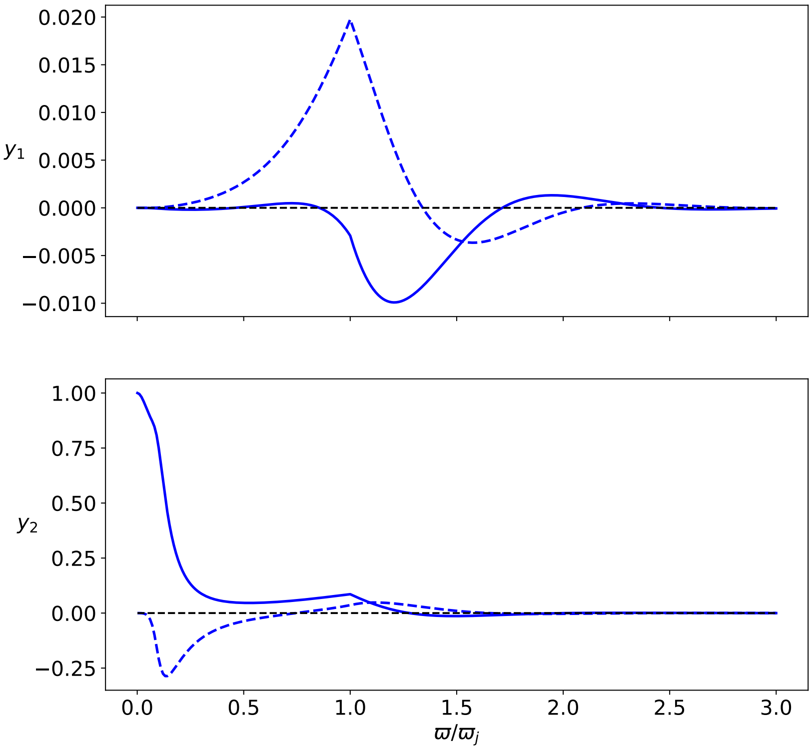

Figure 5.24: Plot of eigenfunctions of case F. Top plot show y_1 and bottom plot y_2 respectively. Solid and dashed lines represent the real and the imaginary part of the eigenfunctions.

eigenfunctions share the trend of localized activity at $\varpi \approx \varpi_j$. The heightened values of y_2 for $\varpi \to 0$, could be due to the reflection of waves on the axis of the jet. So, the main scenario is that the mode is mostly local, it is created on the boundary of the jet and propagates towards the axis and the ambient medium.

In order to provide clearer evidence for the previous statement, in Fig. 5.25 the eigenfunctions for fiducial case and for $k = 10$ are plotted. Evidently, both eigenfunctions are well established in the neighborhood of jet's boundary. They diminish rapidly propagating away from this surface, hence the mode's maximum intensity is expected to be at $\varpi \approx \varpi_j$.

Fig. 5.26 present the eigenfunctions for case F5. Both y_1 and y_2 present their maxima near the boundary of the jet. Total pressure perturbation showcases evidence of possible reflection similarly to Fig. 5.24. One important difference is that the mode does not decrease rapidly as the radius changes from ϖ_j. Especially for Im(y$_2$), the mode gradually decreases towards jet's axis while both eigenfunctions decrease smoothly as $\varpi \to \infty$. This result alongside the variation from the strict linear behavior in Fig. 5.17 could suggest that

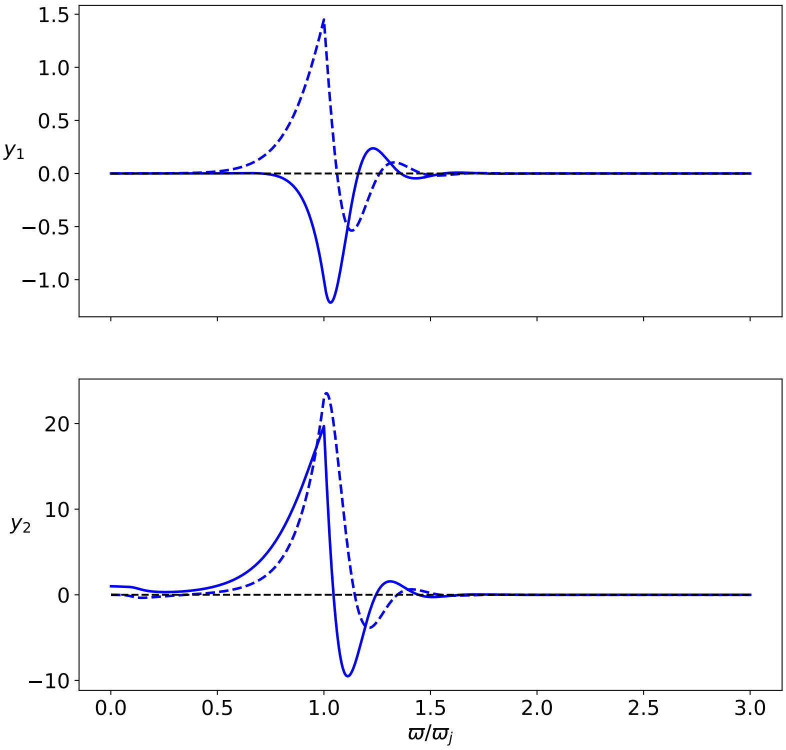

Figure 5.25: Similar to Fig. 5.24 for case F and $k = 10$.

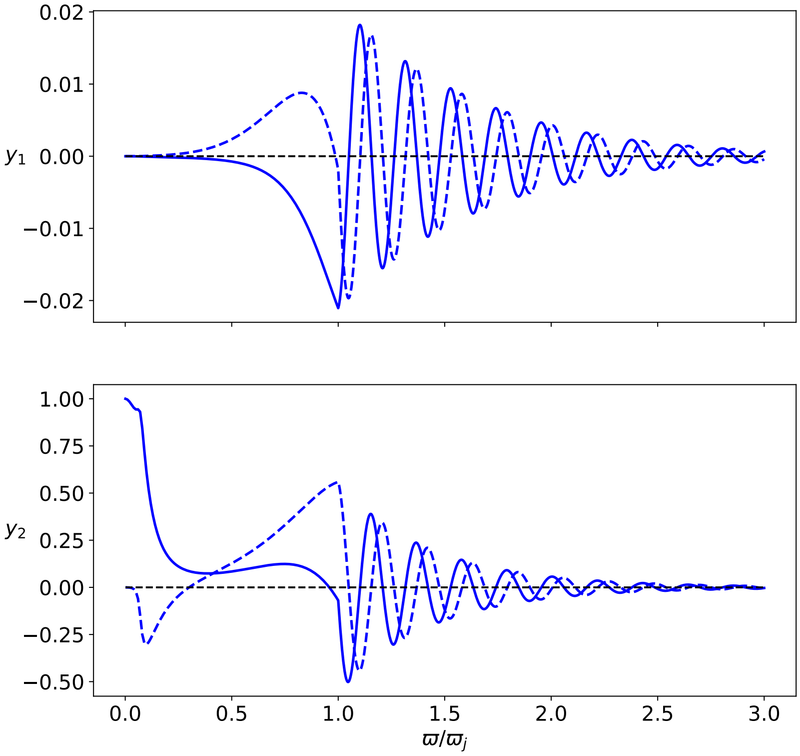

Figure 5.26: Plots of eigenfunctions for alternative configuration F5. Top and bottom plot correspond to y_1 and y_2 respectively. Solid and dashed lines represent the real and the imaginary part of the eigenfunctions.

as γ changes the solution progressively transforms to a different kind of instability which is related to a non-pure version of the KH mode.

5.2.5 WKBJ approximation

The analysis of the KH mode's eigenfunctions in section 5.2.4 supports the idea that the solution is localized, i.e. the mode emanates and affects mainly a specific portion of jet's cross-section and not the entirety of the configuration.

To further test this claim, the WKBJ approximation to zeroth order is applied on the fiducial configuration, case F. The methodology is applied on the system of equations at the jet's radius, $\varpi \approx \varpi_j$. The results are generated solely for a configuration with a hydrodynamic environment, but it has been confirmed that similar conclusions also apply to the magnetized counterpart. In Fig. 5.27-5.30 the Im(ω) versus η, σ, γ & ϖ_0 are presented respectively. Solid lines in figures represent the solution provided by the WKBJ

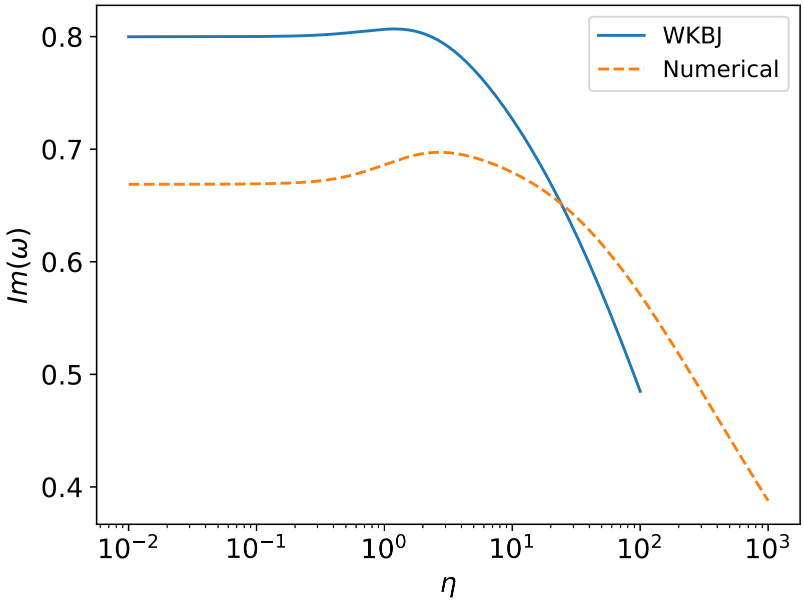

Figure 5.27: Plot of Im(ω) versus the density ratio η for the fiducial case F with hydrodynamic environment. This plot compares results from the WKBJ approximation and the full numerical methodology. WKBJ solution is depicted with blue solid lines and the numerical results are depicted with the orange dashed lines.

approximation, while the dashed lines are the fully numerical solution.

The main result is that the WKBJ predictions are in good agreement with the full numerical counterpart. The best fit can be seen in Fig. 5.29 which depicts the Im(ω) versus γ. Over the whole γ range the solid and dashed lines are close, especially for $\gamma \gtrsim 3$.

Regarding σ and ϖ_0 a good agreement between the two methods is noticed. The overall solutions' behavior is predicted correctly by the WKBJ approximation. It is really important that the transitions in both plots between the stabilized and the non-stabilized states is found to occur at the same parameter values. The least successful comparison between WKBJ and the full numerical treatise is noted for the density ratio in Fig. 5.27. The WKBJ methodology overestimates Im(ω) for the majority of η range, nonetheless the general behavior of Im(ω) versus η is predicted correctly and the error is not more than $\sim 20\%$.

It should be highlighted that the WKBJ prediction accuracy relies heavily on the value of k. As k increases, the results from the two methods tend to be even closer. Fig. 5.31 is similar to Fig. 5.27, but for $k = 10$. The convergence between the two solutions is quite good, and most importantly much better than the corresponding one for $k = \pi$. The solid line is able to follow the dashed counterpart more meticulously.

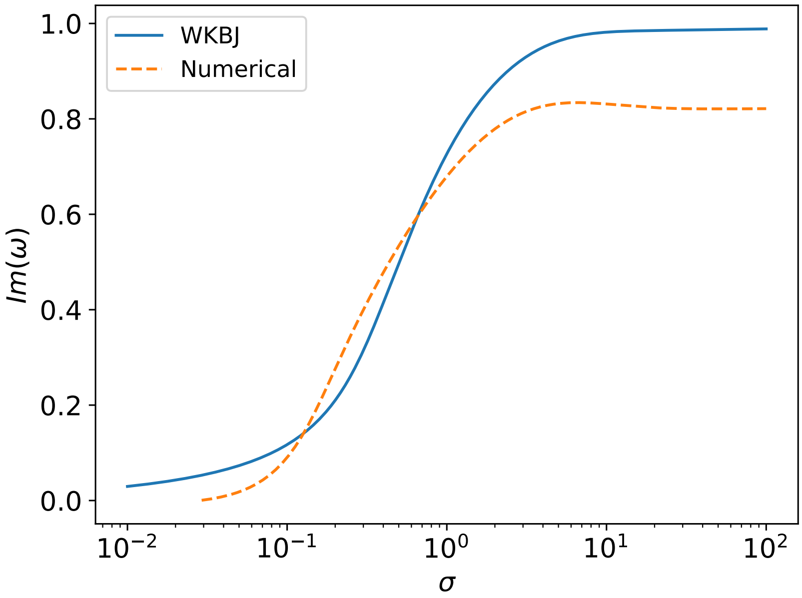

Figure 5.28: Similar to Fig. 5.27 (case F) but for Im(ω) versus magnetization σ.

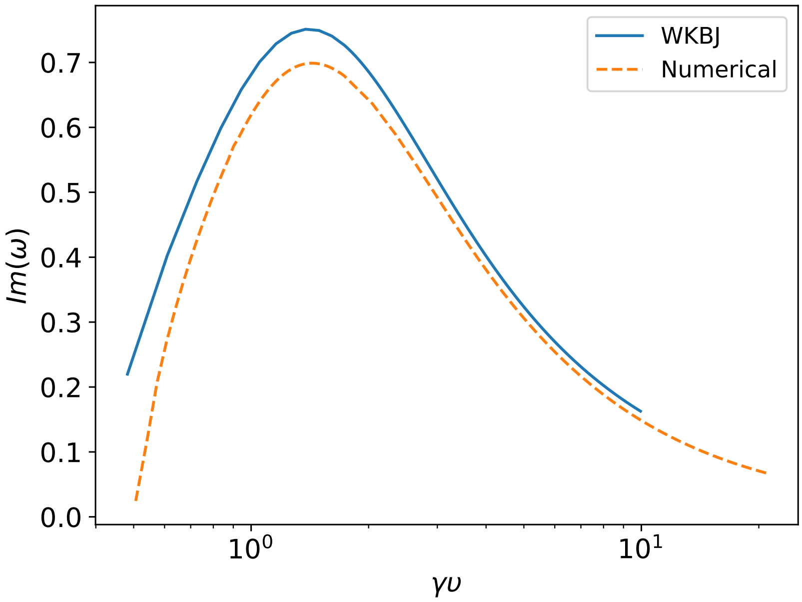

Figure 5.29: Similar to Fig. 5.27 (case F) but for Im(ω) versus proper velocity $\gamma\upsilon$.

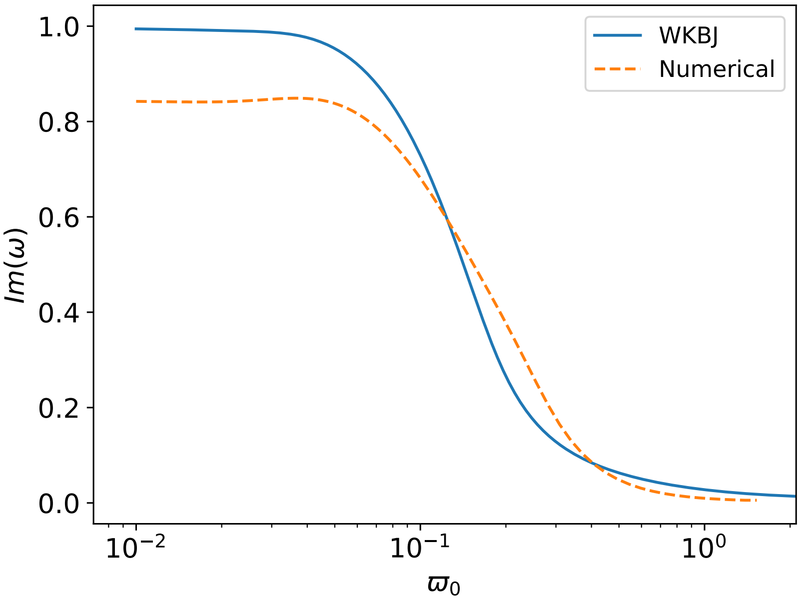

Figure 5.30: Similar to Fig. 5.27 (case F) but for $\mathrm{Im}(\omega)$ versus magnetic field components ratio ϖ_0.

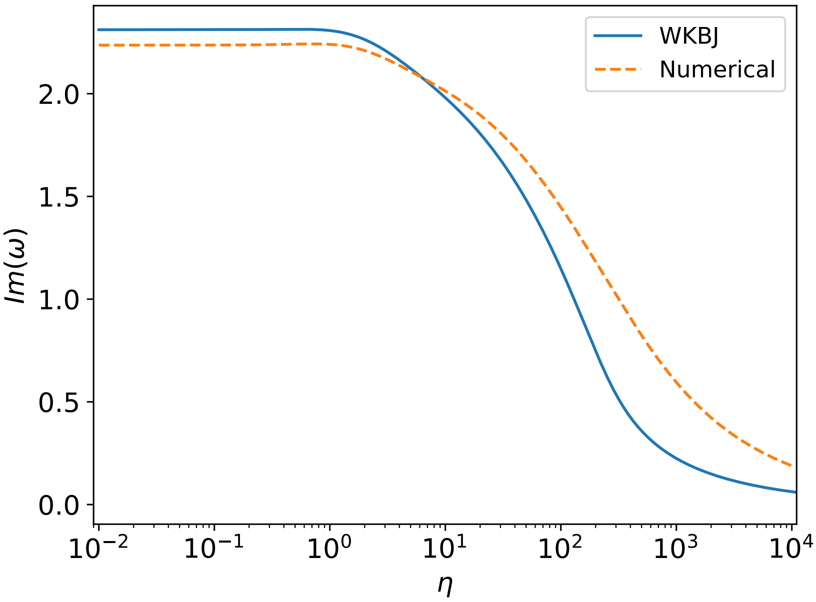

Figure 5.31: Similar to Fig. 5.27 for case F and $k = 10$.

5.2.6 Comparison with Kelvin–Helmholtz instability in Cartesian geometry

Relativistic Kelvin–Helmholtz has already been studied assuming Cartesian geometry for a variety of configurations (e.g. Bodo et al., 1994; Osmanov et al., 2008; Chow et al., 2022, 2023). Results from section 5.2.1 suggest a possible relation between the Kelvin-Helmholtz from the cylindrical jet and the Cartesian counterpart. As an example, the linear relation of $\mathrm{Im}(\omega)$ with k is such an indicating element, as in the Cartesian geometry the Kelvin-Helmholtz instability is characterized by $\mathrm{Im}(\omega) \propto k$ across the entire k value range. Hence, it is interesting to compare the results for the cylindrical jet with KH results generated for planar geometry.

For this purpose two planar flows in contact along the yz surface are assumed. The first one is the "jet" which has relativistic velocity along the z-direction while the second one is static and is considered to be the "environment". Essentially, the configuration of section 5.1 in Cartesian geometry is replicated. So, for the "jet" $\gamma = 2$, $\rho_0 = 1$, $P = 0$, and for the magnetic field equations (5.1), (5.2) at $\varpi = \varpi_j$ are adopted, i.e. $B_z|_{\text{cartesian}} = B_z(\varpi_j)$ and $B_y|_{\text{cartesian}} = B_\phi(\varpi_j)$. The "environment" is assumed non-magnetized, with constant pressure and density profiles. Below parametric plots of $\mathrm{Im}(\omega)$ versus η, σ & γ for different k values are presented.

The dispersion relation of the assumed configuration is presented in section 2.4.4. Alternatively, one is able to obtain the Cartesian dispersion relation by approximating the cylindrical system for $\varpi \ggg 1$. The cylindrical wavenumber components can be related to the Cartesian counterparts as $m/\varpi \to k_y$, $k \to k_z$. V23 discusses when the equations give the corresponding ones for the planar geometry and the radial wavenumber is given by $k_x = \tilde{\kappa}$ (equation 53 in V23). The $\mathcal{F}$ symbols are provided by equations (54)-(57) in V23, with the second term in $\mathcal{F}_{21}/\mathcal{D}$ omitted. The dispersion relation is given by equation (2.74).

In Fig. 5.32 $\mathrm{Im}(\omega)/k$ versus σ for case F and for $k = \pi,\ 10$ is plotted. The solid line represents the Cartesian solution while orange and green dashed lines represent the results from the cylindrical system for $k = \pi,\ 10$ respectively. The solid line indicates stabilization for the mode at $\sigma \approx 0.5$. As σ increases the value of $\mathrm{Im}(\omega)$ also increases. For $\sigma \gtrsim 10$ the rate of increase for $\mathrm{Im}(\omega)$ becomes smaller, and the $\mathrm{Im}(\omega)$ values form a plateau-like region. The solid line overestimates/underestimates the $\mathrm{Im}(\omega)$ values for $\sigma \gtreqless 2$ respectively. For $\sigma \lesssim 0.5$ both of the cylindrical results are not immediately stabilized like the Cartesian solution does. When $k = 10$ it is noticed that the blue line is much closer to the cylindrical counterpart, as the differences in $\mathrm{Im}(\omega)$ values of the two lines are much smaller. Briefly, as k increases the solid line tends to approximate the dashed lines quite successfully.

In Fig. 5.33 $\mathrm{Im}(\omega)/k$ versus η for case F is plotted. Similar to Fig. 5.32 the solid line is the result corresponding to the Cartesian geometry and the dashed lines correspond to the cylindrical jet for $k = \pi,\ 10$. The Cartesian mode has two cut-offs with values $\gamma v \sim 0.1$ and $\gamma v \sim 4$ respectively. The cylindrical solutions present cut-off at $\gamma v \sim 0.2 - 0.5$ while they diminish gradually for increasing Lorentz factor values beyond $\gamma v \sim 1$. As k becomes larger the blue solid line starts to converge with the cylindrical solution, as observed also in Fig. 5.32. For larger γv values the stabilization of the cylindrical mode becomes less

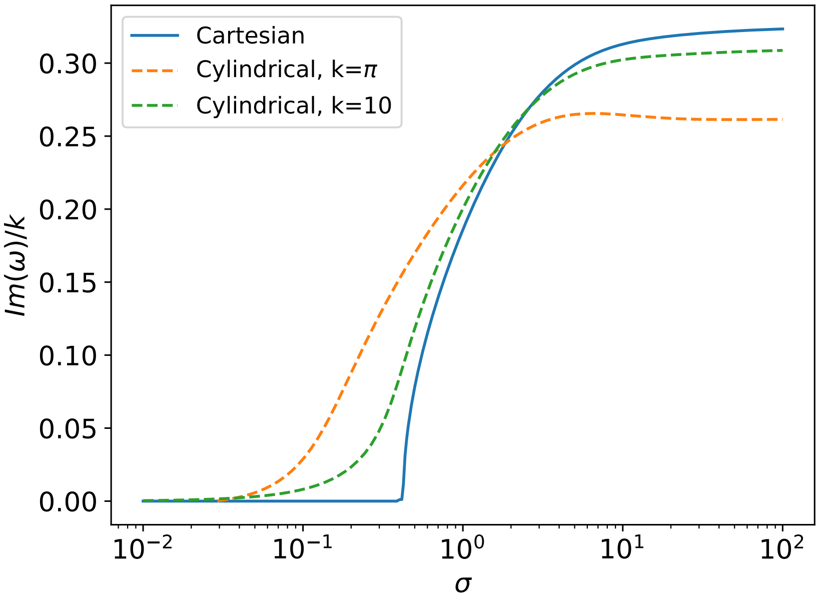

Figure 5.32: Plot of $\mathrm{Im}(\omega)/k$ versus σ for case F. The jet is surrounded by a hydrodynamic environment. Solid line represents solution in Cartesian geometry and dashed lines in cylindrical geometry for $k = \pi,\ 10$.

gradual, while the lower cut-off is closer to the Cartesian counterpart.

Similar to Fig. 5.32 and 5.33 $\mathrm{Im}(\omega)/k$ versus η is plotted in Fig. 5.34. This plot includes an extra wavelength value, $k = 15$, depicted with the red dashed line. The Cartesian solution forms a plateau for $\mathrm{Im}(\omega)$ values when $\eta \lesssim 1$. For $\eta \gtrsim 1$ the $\mathrm{Im}(\omega)$ values decrease until $\eta \sim 20$, where the KH mode fully stabilizes. The cylindrical solutions also form a plateau for $\eta \lesssim 1$ similar to the planar geometry. For $\eta \gtrsim 1$ the $\mathrm{Im}(\omega)$ decreases but does not fully stabilize for $\eta \sim 20$. Once more, it is observed that as k increases the Cartesian solution begins to approximate the cylindrical equivalent more precisely. In this plot an extra wavelength ($k = 15$) is included to emphasize on the fact that increasing k values further aids the Cartesian solution to follow the behavior of the cylindrical mode.

It is evident that the Cartesian geometry successfully predicts the KH mode of the cylindrical geometry, and the quality of the prediction is enhanced as k increases. More specifically, there are three length scales involved into the efficient approximation of the cylindrical geometry by the Cartesian counterpart. The first one is the wavenumber k, the second one is the $\tilde{\kappa}$ and the last one is the wavelength of the Hankel function's argument λ which are defined and analyzed in sections 5, 5.1 of V23. The analysis indicates that the cylindrical geometry can be omitted whenever $k \gg 1/\varpi_j$, $\tilde{\kappa} \gg 1/\varpi_j$ and $\lambda \gg 1/\varpi_j$. Hence, there are three length scale relations which need to be fulfilled simultaneously. Each one of them needs to be much larger compared to the radius of the jet, this way the curvature of the cylindrical jet can be discarded and the planar approximation is valid.

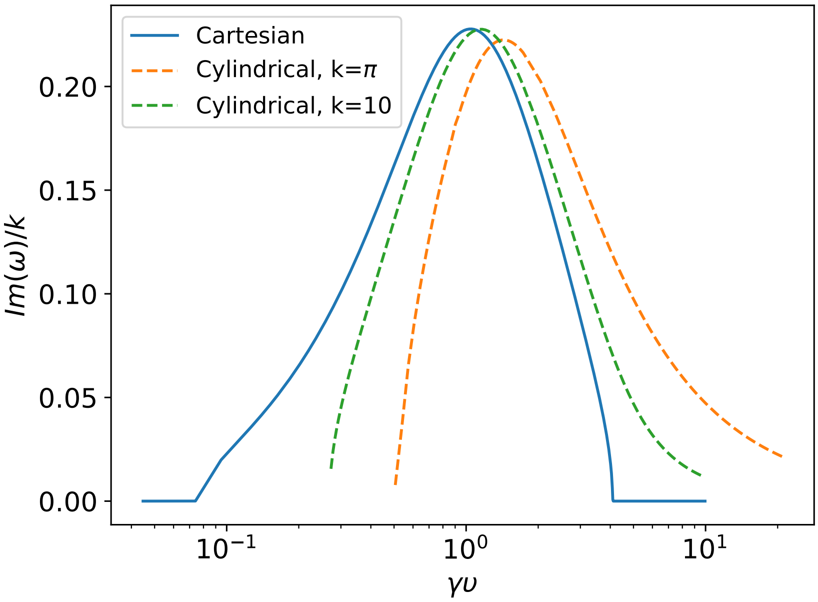

Figure 5.33: Plot of $\mathrm{Im}(\omega)/k$ versus σ for case F. The jet is surrounded by a hydrodynamic environment. Solid line represents solution in Cartesian geometry and dashed line in cylindrical geometry for $k = \pi,\ 10$.

5.3 Discussion and Conclusions

In this section a linear stability analysis was conducted on a cylindrical relativistic magnetized jet. The unperturbed outflow is in force balance with its environment, includes a helical magnetic field and does not have thermal pressure. It was opted to study axisymmetric solutions as they are found to be the most unstable. This model is a simplified version of the model developed in chapter 4. The analysis aimed to further study and understand the properties of specific solutions that were observed in section 4.3, and showcased instabilities' growth timescales comparable to the jet's radius light crossing time. Also, the solutions present a linear relation between $\mathrm{Im}(\omega)$ and k ($\mathrm{Im}(\omega) \propto k$) which is typical of Kelvin-Helmholtz mode in Cartesian geometry. As wavenumber decreases the solution vanishes via a cut-off at $k \sim 1$, thus the cylindrical counterpart does not extend to $k \to 0$. This is not the case for the Cartesian KH for which as $k \to 0 \Rightarrow \mathrm{Im}(\omega) \to 0$.

In order to fully understand the relation between this mode and the various outflow parameters a parametric study was utilized regarding the ratio of the jet's rest mass density over the rest mass density of the environment (η), the jet's Lorentz factor (γ), the magnetization (σ) and the ratio of the magnetic field's poloidal component over the toroidal component measured in the co-moving frame of reference (ϖ_0). Also, it was tested whether the mode is affected by the environment's pressure providing mechanism (thermal or magnetic pressure) or by the presence of a thermal pressure component inside the jet.

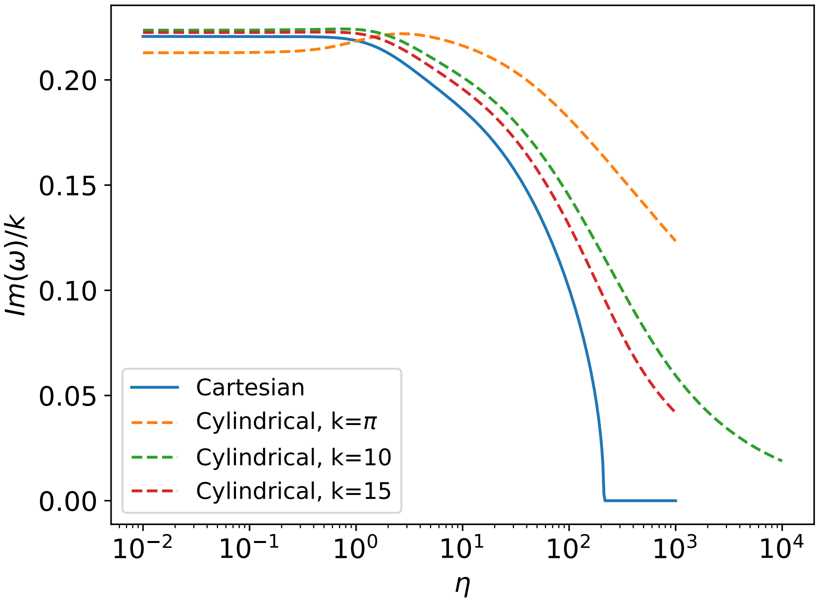

Figure 5.34: Plot of $\mathrm{Im}(\omega)/k$ versus η for case F. The jet is surrounded by a hydrodynamic environment. Solid line represents solution in Cartesian geometry and dashed line in cylindrical geometry for $k = \pi,\ 10,\ 15$.

The mode is favored by jets which are denser than their environment. $\mathrm{Im}(\omega)$ diminishes with increasing η, while it retains a constant high value for $\eta \ll 1$. When the environment becomes magnetized, the plateau for $\mathrm{Im}(\omega)$ disappears and the mode is stabilized for $\eta \lesssim 1$. For $\eta \gg 1$ the increased inertia of the environment is a prominent factor for the stabilization of the KH mode.

Next the relation of $\mathrm{Im}(\omega)$ on the magnetization value was examined. In general increasing σ leads to more unstable configurations. The instability hinders when the configuration becomes less magnetized. The change on σ was done by properly altering the amplitude of the magnetic field B_0. When the environment becomes magnetized, the mode terminates via a cut-off at $\sigma \approx 4$. The main element affecting this result is the presence of the magnetic field in the environment. As σ increases so does the external magnetic field, in order to provide adequate pressure to support the jet. When the instability emanates and starts displacing the field lines, the tension from the external magnetic field will be more intense for large σ values. Finally, for even higher σ the jet can not overcome the tension and the KH mode is stabilized.

The analysis continued by examining the dependence of $\mathrm{Im}(\omega)$ on the Lorentz factor value. This parameter also affects the KH mode, as for non-relativistic velocities the solution is stabilized. The same also happens for Lorentz factors $\gamma \gtrsim 8$, as the $\mathrm{Im}(\omega)$ gradually decreases with increasing Lorentz factor value for $\gamma \gtrsim 2$. The maximum growth rate for the KH mode is observed for $\gamma \simeq 2$. When the environment becomes magnetized the general behavior remains similar except for the small γ. The cut–off changes from $\gamma \sim 1$ to $\gamma \approx 1.4$, stabilizing a group of mildly relativistic configurations. In general, the magnetized environment hinders the mode. Similar result is provided by Fig.9 in Bodo et al. (2013), which is quite similar to both Figs. 5.9 & 5.10.

In Fig. 5.11 and 5.12 the relation of $\mathrm{Im}(\omega)$ versus ϖ_0 was analyzed. The physical quantity related to ϖ_0 is the ratio of the magnetic field components measured on the boundary of the jet in the co–moving frame, $B_z/|B_\phi|$. The most important result is the rapid stabilization of the mode when $B_z/|B_\phi| \sim 1$. The poloidal component of the magnetic field fully suppresses the mode. Technically, it was opted to fix the value of B_z and change B_ϕ. Alternatively, it could also be stated that when B_ϕ becomes negligible compared to B_z the mode is weakened. The toroidal component of the magnetic field seems to be an integral element of the KH solution's generating mechanism.

At this point it is insightful to notice that our results can also be characterized by the angle of the magnetic field with the wavevector $\boldsymbol{k}$. For $m = 0$ the wavevector is always parallel to the z-direction, essentially the angle measure is give by $\cos(\theta) = B_z/||\boldsymbol{B}_{co}||$, where $\theta = (\widehat{\boldsymbol{B}_{co}, \boldsymbol{k}})$. This angle can be related to the ϖ_0 parameter through $\cos(\theta) = \varpi_0/\sqrt{1+\varpi_0^2}$. For case F the angle between $\boldsymbol{B}_{co}$ and $\boldsymbol{k}$ is $\simeq \pi/2$.

In order to better understand the dependence on ϖ_0 it is noticed that by changing ϖ_0 the angle between the magnetic field and the z-direction is also changed (or equivalently the $\boldsymbol{k}$). When $\varpi_0 \gg 1 \Rightarrow \cos(\theta) \to 1$, which means that the magnetic field tends to align with the wavevector. In this scenario the instability needs to overcome the increased tension provided by the aligned magnetic field, leading to the inhibition of the KH mode. On the contrary, when $\boldsymbol{B}_{co} \perp \boldsymbol{k}$ the effect of the magnetic field's tension on the instability is minimized.

The magnetic tension effect also explains why the axisymmetric mode is the most unstable as seen in Fig. 5.4. As $|m|$ increases, the angle between the co-moving magnetic field and the wavenumber decreases, hence the instability needs to overcome the increased tension of the magnetic field. This leads to the instability inhibition and to smaller growth rates.

The mode's eigenfunctions present an exponential increase near the boundary of the jet. This trait is found in both the jet and the environment near their common interface. The mode fades out for $\varpi \to 0$ and $\varpi \to \infty$. The rate of descent for both directions is quite intense, implying that the rest of the jet remains unaffected. This result establishes the notion of the locality for the KH mode. The spatial range of the instability's effect on the configuration is local and exhibited mainly near the boundary surface of the jet. Also, the KH mode profile is shaped by the local jet configuration at $\varpi \approx \varpi_j$, while the rest of the jet/environment are disregarded.

In order to test the locality of the KH mode a WKBJ approximation on the system of equations (2.17) for $\varpi = \varpi_j$. It was noticed that the WKBJ serves as an efficient proxy for the mode's ω values. This behavior is enhanced when the k is increased. It is imperative to highlight the fact that the WKBJ approximation does not take into consideration the behavior of the solution near the jet's axis nor towards infinity. This means that the provided efficiency of the WKBJ method reinforces the conclusions provided by the analysis of the eigenfunctions.

Next, an alternative configuration was considered which has $\gamma = 5$ compared to the fiducial case which has $\gamma = 2$. The results of section 5.2.3 only consider a hydrodynamic environment surrounding the jet. In general, the parametric study reveals that the KH mode in the alternative configuration is related to the corresponding mode for the fiducial setup but they are not identical. It is evident that there are differences between the two cases. First of all, in Fig. 5.17 the mode is not linear with respect to k and the ω-plane is full of other modes that are not present in the fiducial setup with $\gamma = 2$. In Fig. 5.26 the eigenfunctions are not concentrated around $\varpi \approx \varpi_j$. y_1, y_2 extend with non-zero values for $\varpi < \varpi_j$ while for $\varpi > \varpi_j$ the eigenfunctions diminish gradually as ϖ increases. On the other hand, the WKBJ predicts correctly the growth rate of the instability. Moreover, the parametric study suggests that the behavior of the alternative configuration's KH mode on the various parameters is in accordance with the corresponding results of the fiducial case, besides the fact that the growth rates are in general smaller.

These results could indicate that the KH mode fuses with other type of instabilities, such as the current-driven modes. This way the instability retains its traits even if they are mildly modified compared to the fiducial case results. This phenomenon is also noted in Bodo et al. (2013) where the KH and current-driven instabilities can not be distinguished for a relativistic jet with a helical magnetic field.

Finally, a comparison was conducted between the KH mode in cylindrical and Cartesian geometry respectively. This was based on the existence of various common traits of the KH mode in both geometries which are $\mathrm{Im}(\omega) \propto k$, mode's locality, the effect of the angle between $\boldsymbol{B}_{co}$ and $\boldsymbol{k}$ has on the instability and finally the decrease of the $\mathrm{Im}(\omega)$ while M_{fast} increases. The analysis established a definite criterion regarding the characteristic length scales of the system. This criterion demands simultaneously λ, $\tilde{\kappa}$, $k \gg 1/\varpi_j$. Whenever this is fulfilled the cylindrical geometry can be discarded and the results can be approximated by the Cartesian Kelvin-Helmholtz instability.

Various traits of the KH mode can be identified in publications studying the Cartesian KH instability. For example the dependence of the mode's intensity on the angle between $\boldsymbol{B}_{co}$ and $\boldsymbol{k}$ is also observed to be crucial in Osmanov et al. (2008); Chow et al. (2022, 2023). The cut-off for small M_{fast} values is also discussed in Chow et al. (2022), where the "jet" velocities need to be super-Alfvénic. High density contrasts between the two fluids lead to stabilization of the KH mode Ferrari et al. (1980). Nonetheless, it has been shown in section (5.2.6) that the cylindrical KH mode is not identical to the Cartesian counterpart and the properties of the Kelvin-Helmholtz instability emanating in a jet are considerably modified.

Furthermore, the Kelvin-Helmholtz instability could have substantial implication on the phenomenology of the astrophysical jets. This is related to the non-linear evolution of the modes. Most notably, the Kelvin-Helmholtz mode creates vortices on the boundary layer of the jet and its environment. This layer is characterized by the velocity shear between the two media. The vortices distort the field lines and twist them in such a way that a variety of phenomena may be risen, such as turbulence. Moreover, this alteration of the magnetic field topology may create sites where field lines of opposite polarity may become adjacent, triggering magnetic reconnection and subsequently for non-thermal particle acceleration, as discussed in Sironi et al. (2021).

The non-linear evolution of the Kelvin-Helmholtz instability in astrophysical environments can be studied only numerically, through MHD simulations as e.g. Millas et al. (2017); Berlok &Pfrommer (2019a,b), or particle in cell (PIC) simulations as in Sironi et al. (2021). The plethora of phenomena regarding the non-linear phase of the Kelvin-Helmholtz mode is of great importance. In the next chapter a series of simulations expand the results of the linear stability analysis and the non-linear evolution of the KH mode is studied.

Chapter 6

Numerical simulations of the Kelvin-Helmholtz mode

The linear stability analysis results are valid for timescales up to $1/\mathrm{Im}(\omega)$. When the amplitude of the instabilities become comparable to the unperturbed quantities the analysis ceases to predict effectively the jet evolution. Complementary to the linear stability analysis (chapter 5), in this chapter the configuration that produces the KH mode is numerically evolved. The results from the simulations can be compared to the corresponding results of the linear stability analysis and they can be also utilized to study the non–linear evolution of the solution.

The unperturbed initial state of the outflow is presented in section 5.1. The main task is to utilize the simulations to study the non–linear evolution of the KH instability. For the simulations the relativistic magnetohydrodynamic code PLUTO (Mignone et al., 2007) is employed. The simulations are 2D and their geometry is cylindrical. For every case considered a static grid of 512×256 points is incorporated unless stated otherwise. The length of the box is set to $0 \leq \varpi/\varpi_j \leq 4$ and for the height to $0 \leq z \leq \lambda$, where λ is the wavelength of the instability. The modes are simulated for a fixed wavenumber $k = \pi \rightarrow \lambda = 2$ unless another value is referred, hence $z \in [0, 2]$. This choice for the grid setup ensures that the grid cells are squares with an acme length of ~ 0.008. The boundary conditions are axisymmetric and open (outflow) for the inner and outer cylindrical boundary surfaces, while along z periodic conditions are used. The choice of k and the parameter values leads to a growth timescale for the mode which is $\tau \sim 10$ crossing times (a crossing time is the required time interval a photon needs to travel a distance equal to the jet's radius, ϖ_j/c). The simulations are run for $t = 500$ crossing times, which is roughly $\times 45 - 50$ the instability growth timescale. This way the simulations explore the jet evolution deeply into the non-linear regime.

The selection of solvers depends on the jet configuration. For jets which include a thermal pressure component the hlld solver is chosen, as it is the least diffusive. On the contrary, for the cold jets due to technical issues the gforce solver is employed, which is the second best in terms of numerical diffusion. In order to simulate a perfectly cold jet the code requires to introduce significant levels of diffusion. In order to minimize the effects of numerical diffusion a constant thermal pressure component which is much smaller to the magnetic counterpart is added, i.e. the initial plasma beta ($\beta = P/P_{mag}$) is small. The constant pressure profile does not have any dynamic effect on the jet configuration. This way the gforce solver can be employed and the effects of the diffusion on the jet evolution can be contained as much as possible.

To destabilize the jet an initial perturbation is introduced in the radial component of the velocity field through the relation

$$\delta V_{\varpi} = C \exp\left(-\frac{(r-r_c)^2}{2L^2}\right) \cos\left(kz\right) \ , \tag{6.1}$$

which is a Gaussian centered on the boundary of the jet. The parameters of the perturbation are set to $C = 0.01$, $r_c = 1$, $L = 0.07$. The value of C ensures that the initial perturbation is in general small, and the value of L that the curve fades rapidly as $\varpi \to 0$ and $\varpi \to \infty$. Equation (6.1) is not an eigenfunction of the system, but is located near the boundary of the jet. This resembles the general behavior of the eigenfunctions, thus even if the initial perturbation is not an exact eigenfunction, in general it approximates the exact solutions.

The environment of the jet is assumed to be static with constant density and pressure profile, while the pressure providing mechanism is considered to be purely hydrodynamic.

6.1 Cold jet

The first configuration to be investigated is the cold jet, the model is presented in section 5.1. In figure 6.1 the contour plots for the initial jet state are presented. The quantities plotted on the top row and from left to right are the proper density and V_{ϖ}. In the second row there are V_z and the thermal pressure. In the same order in the third row B_{ϕ} and B_z are plotted respectively. In the bottom row the toroidal component of the vorticity is shown. As a reminder the initial parameter space for the jet configuration is $\eta = 10$, $\varpi_0 = 0.1$, $\sigma = 1$ on the jet's boundary, $\gamma = 2$ and finally $P = 0.05$ which corresponds to $\beta = 0.1$ at $\varpi = \varpi_j$.

In the plot of V_{ϖ} the Gaussian perturbation located on the surface of the jet is noticed. Also, at the bottom row the plot depicts the ϕ-component of the vorticity. The quantity is defined as $(\nabla \times \boldsymbol{V})_{\phi} = (\nabla \times \boldsymbol{V}) \cdot \hat{\phi}$. The configuration has a non-zero vorticity layer coinciding with the boundary of the jet. In figure 6.2 the jet quantities are plotted for $t = 30$. This time instance is close to the transition from the linear to the non-linear phase. The effect of this transition on the jet structure can be observed.

On the boundary of the jet a vortex is formed. Its rotation is clockwise, as the plots for V_{ϖ} and V_z indicate. V_{ϖ} shows a dipole-like formation of positive/negative radial velocity near the center of the plot box. At this same spot the V_z also presents a transition from

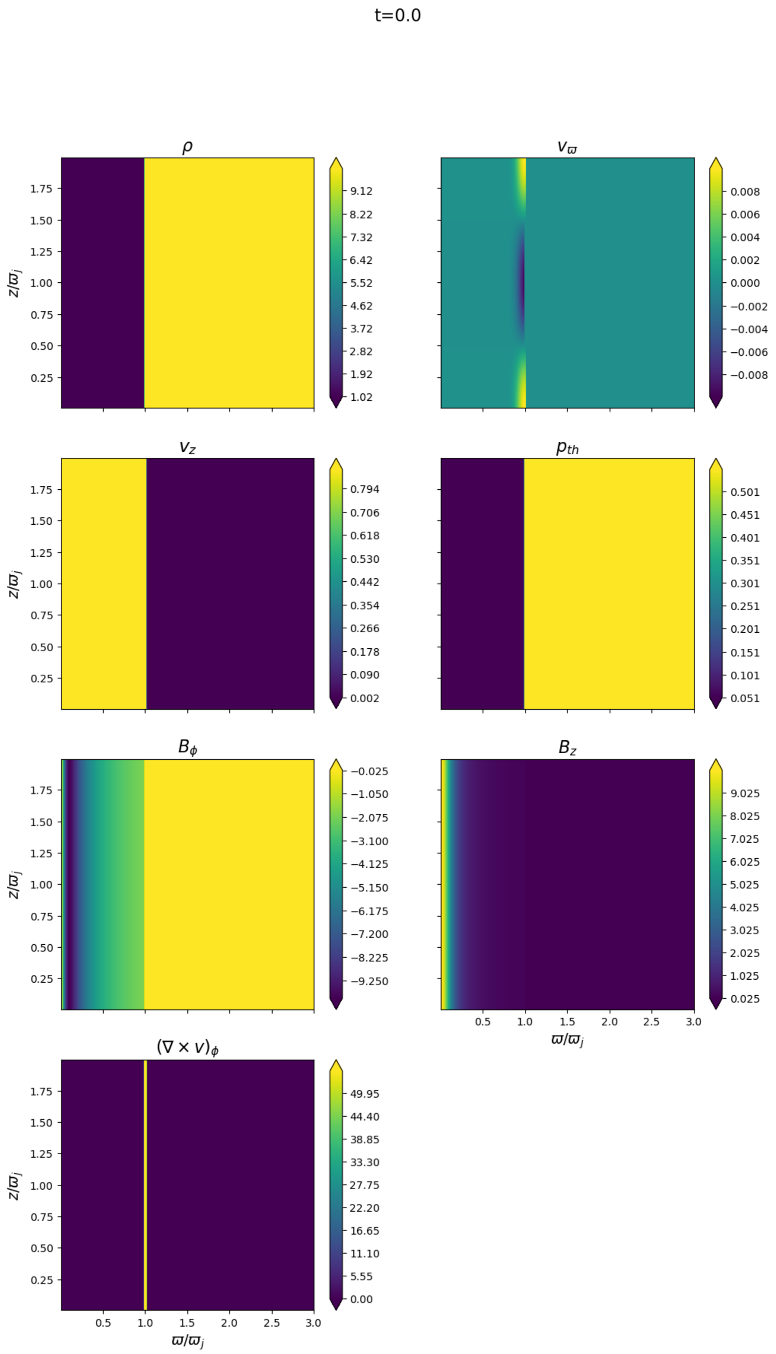

Figure 6.1: Contour plots of the initial jet configuration. From left to right on the first row the proper density and the radial component of the velocity are plotted. On the second row is the z-component of the velocity and the thermal pressure. In the third row B_ϕ and B_z are plotted. Finally, on the bottom row the ϕ-component of the vorticity is shown.

positive to negative values. The vorticity value calculated at this jet region is positive, these observations suggest that the flow rotates locally. The density at the center of the rotation presents a local minimum which is sparser than the initial density value. Apart from the vicinity of the vortex the jet is,in general, not affected by the instability.

Both components of the magnetic fields retain their large scale configuration. B_ϕ possibly is moderately disrupted near its minimum, overall the profiles for the magnetic field components are similar to their initial counterparts. The density profile remains mostly unaffected, while the jet bulk velocity remains relativistic. Near the flow axis the velocity decreases and the thermal pressure increases, specifically near the bottom of the plot a high-pressure spot has emerged. Moreover, the jet has expanded from $\varpi_j = 1$ to $\varpi_j \approx 1.5$. Overall, the vortex which is a dynamic component of the flow mixes the two media but does not disrupts the entirety of the outflow.

Figure 6.3 presents the state of the jet halfway through the simulation. The jet boundary has expanded to $\varpi_j \approx 2$, the initial radius is almost doubled. The jet quantity profiles are featureless and quite smooth. The density profile is constant apart from a low-density feature which does not coincide with any rotational movement. Near this feature V_ϖ and the vorticity profiles indicate local rotation, it is not clear if this motion is associated to the minimum density feature. Except for these two quantities there are none other which deviate from their respective constant background values. The existence of a vortex at this region is not likely, a probable scenario is that this rotation is an echo of the former vortex that resided at this flow neighborhood.

The V_z profile is also constant for the jet's interior and its value has decreased down to $V_z \approx 0.6$. Both of the magnetic field components have preserved their large scale configuration. The only difference compared to their initial conditions is that the absolute value of their amplitude has decreased, the jet halfway through the simulation is less magnetized. It should be noted that the B_ϕ has regained its initial radial configuration along the entire jet and the perturbation near the axis of the jet observed in figure 6.2 has vanished. The thermal pressure remains constant with small values apart from the vicinity of the axis, where an increase in its value is noticed. The jet remains non-turbulent and the outflow has been modified from its initial state but remains well-ordered regarding every quantity.

In figure 6.4 the contour plots for the final jet state are presented. The important element is that the outflow is still ordered and there is no presence of turbulence. The boundary of the jet has not expanded noticeably from $\varpi_j \approx 2$. The density in the jet seems to be constant and close to its initial value while for the environment and near the jet boundary the density has decreased from $\rho_0 = 10$ down to $\rho_0 \approx 8$.

The radial component of the velocity presents a small scale pattern with interchanging regions of positive and negative velocity. The z-component of the velocity presents a quite smooth profile along $\hat{z}$ and $\hat{\varpi}$ directions. The velocity has decreased down to $V_z \approx 0.6 \rightarrow \gamma = 1.25$ while the environment remains static. At this point if the simulation box is observed thoroughly, it could be noted that a new vortex starts to form at $(\varpi, z) \approx (2.3, 1.3)$. This is evident in the two velocity plots where for V_ϖ there is a dipole of positive/negative radial velocity suggesting a clockwise local rotation. At the same spot

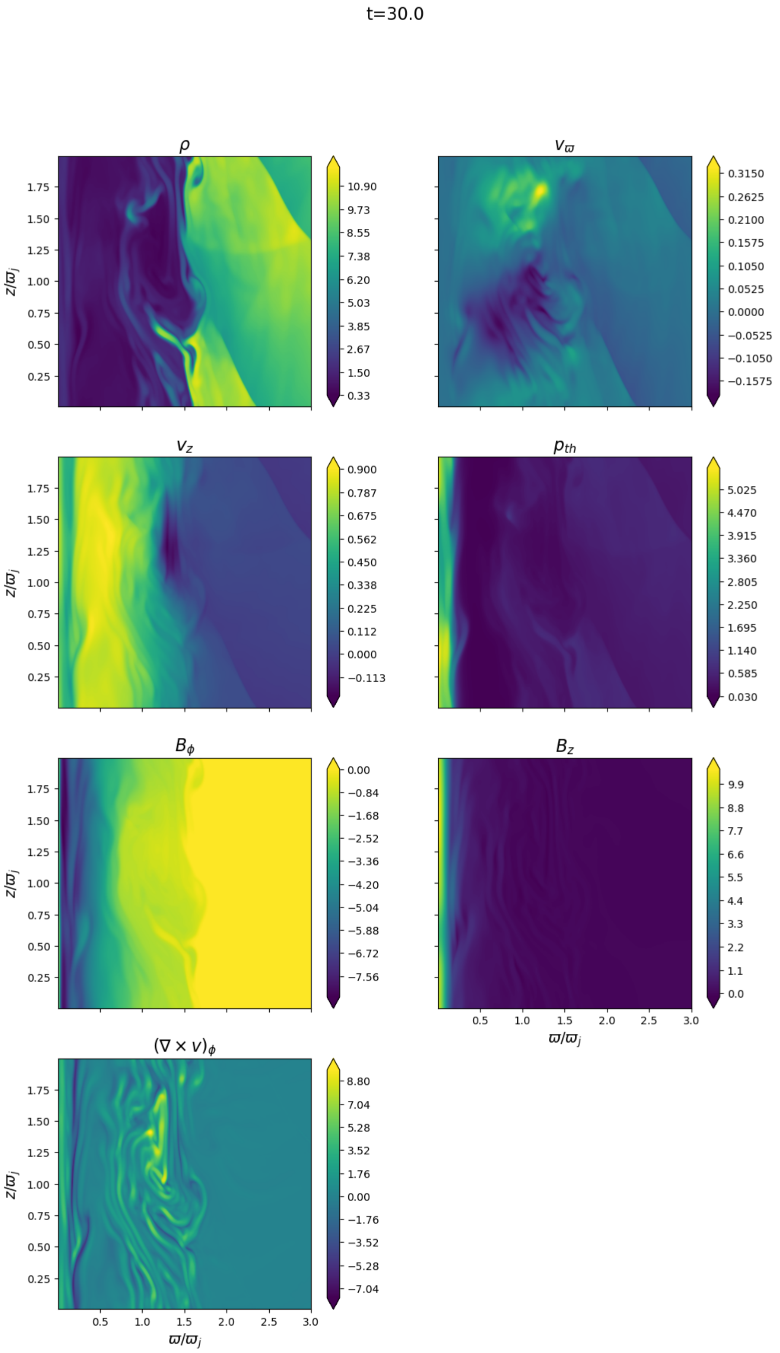

Figure 6.2: Similar to figure 6.1 for $t = 30$ crossing times.

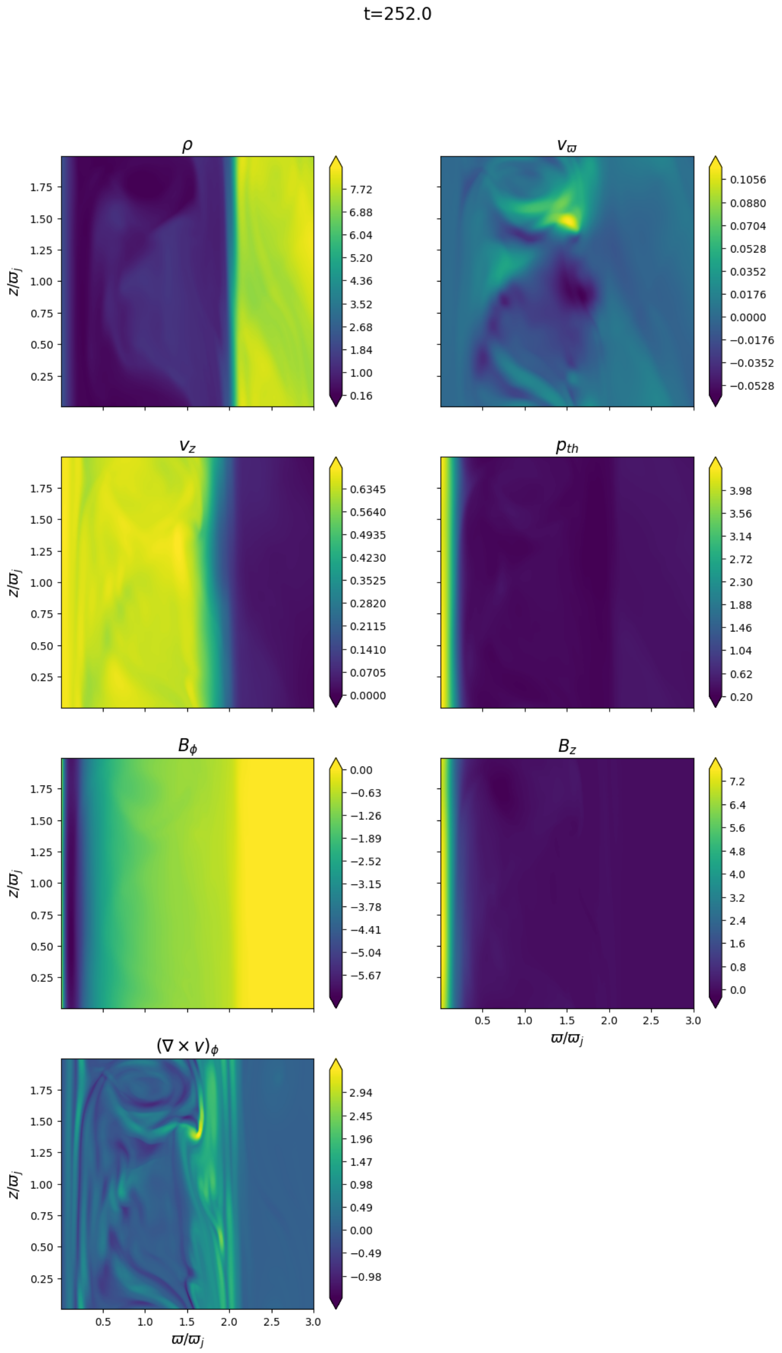

Figure 6.3: Similar to figure 6.1 for $t = 252$ crossing times.

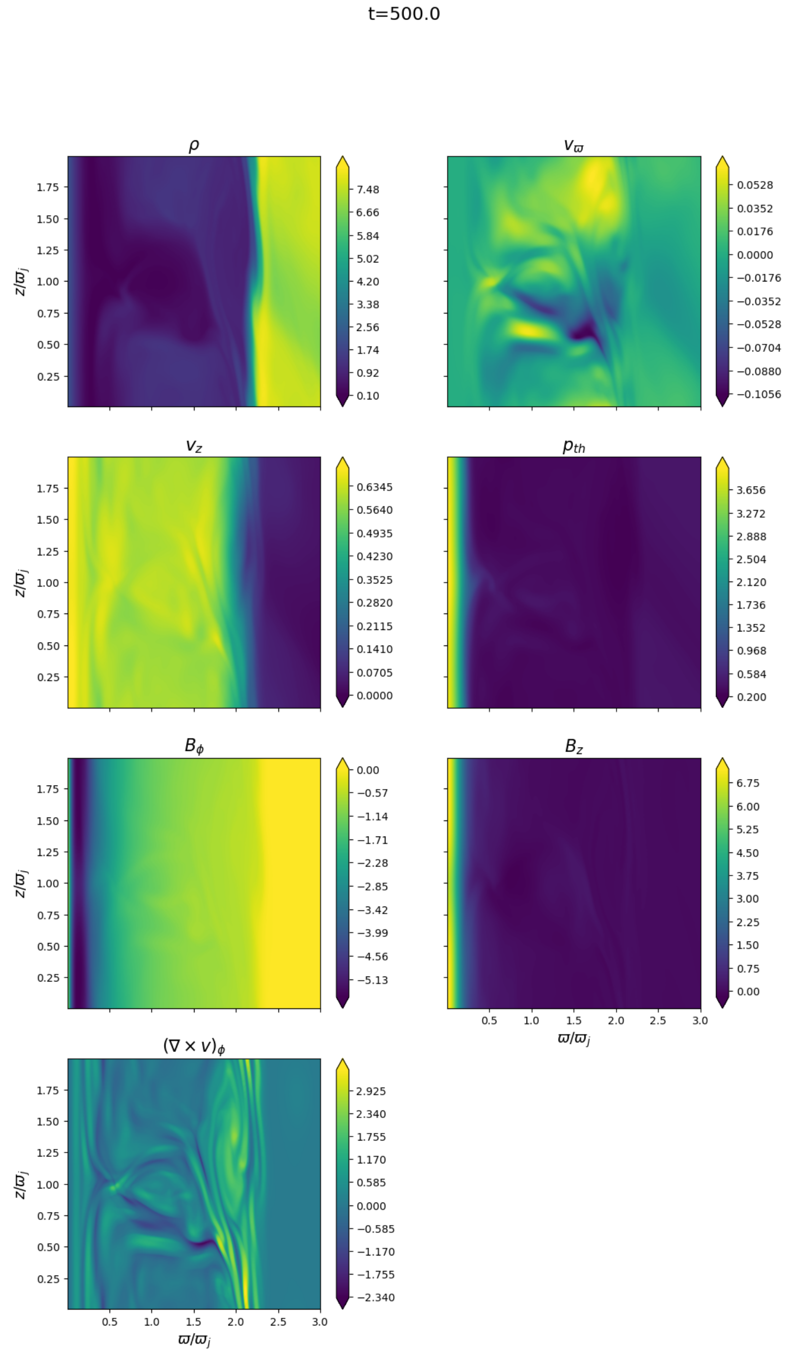

Figure 6.4: Similar to figure 6.1 for the final jet state, $t = 500$ crossing times.

the z-component of the velocity presents a higher/lower velocity interchange that agrees with the local rotation pattern. The density at this same spot also has a local minimum and the vorticity also suggests local rotational movement.

This vortex arises at $t \sim 500$, while the first one was active from $t \sim 30$ up to $t \sim 100$ hence the two vortices are not likely to be associated directly. The main reason behind this new vortex is probably the onset of a new KH instability on the boundary of the jet. Similar to the first vortex also this one will affect locally the outflow near $\varpi \approx 2$ and will change the local properties leaving the rest of the jet mostly unaffected.

In figure 6.5 plots for various jet quantities are presented. Top row has proper density and V_ϖ. Middle row depicts V_z and thermal pressure, while bottom row shows B_ϕ and B_z respectively. Dots with different color represent cross-sections for various z values of the simulation box. The jet has been divided into 9 slices at $z \approx 0,\ 0.26,\ 0.5,\ 0.75,\ 1,\ 1.25,\ 1.5,\ 1.75,\ 1.99$. These plots provide an enhanced overview over the jets quantity behavior across the simulation box in both directions. Whenever the slices coincide the jet has reached the same state along its axis and the quantities only depend on the radius. In order to further support this claim the mean value of the slices is plotted with a black solid line, which also fits the already coinciding slices. This implies that the outflow has evolved to a new quasi-steady state with the quantities being functions of ϖ similarly to the initial unperturbed state of the jet.

In figure 6.6 the mean profiles for the various jet quantities are presented. This mean profile is calculated for the slices along the z direction which were discussed previously and presented in figure 6.5. Essentially, the black line of figure 6.5 is plotted against the respective line for the initial jet configuration. The blue line corresponds to $t = 0$ and the orange line to $t = 500$. This plot eases the comparison between the initial and final jet state and points out the important differences. Also, this plot is trustworthy due to the fact that in figure 6.5 the slices coincide with each other, hence the mean profile represents effectively the distribution of its respective quantity.

For every quantity, apart from V_ϖ, the different slices and their respective mean agree with each other almost perfectly. The density of the jet present a local minimum at ~ 0.3 and slightly increases towards the axis and the boundary of the jet. For $0.4 \lesssim \varpi \lesssim 2$ the mean deviates from the slices. This occurs mainly due to the density profile for the red, brown and purple dots ($z \simeq 0.75,\ 1,\ \&1.25$) which correspond to the low density feature in the jet. In general, the mean density value of the jet at $t = 500$ is approximately the same with the initial respective value, $\rho_0 \simeq 1$. Right after this region the jet is connected to the environment through a zone in which the density increases rapidly. The environment's density value has decreased to $\rho_0 \approx 8$ and its slices are not overlapping each other consistently, instead the slices present an outgoing wave-like form.

The V_ϖ profile does not suggest a specific pattern for the radial movement of the plasma for the jet or the environment. It should be noted that $|V_\varpi| \leq 0.08$ which is significantly less than the respective values for the z component, while it changes sign rapidly across the jets radius thus its mean value is practically zero. This way the radial movement is not a crucial factor at this point for the jet evolution. The V_z profile is approximately constant for the interior of the jet. The value is ≈ 0.6 meaning that the jet

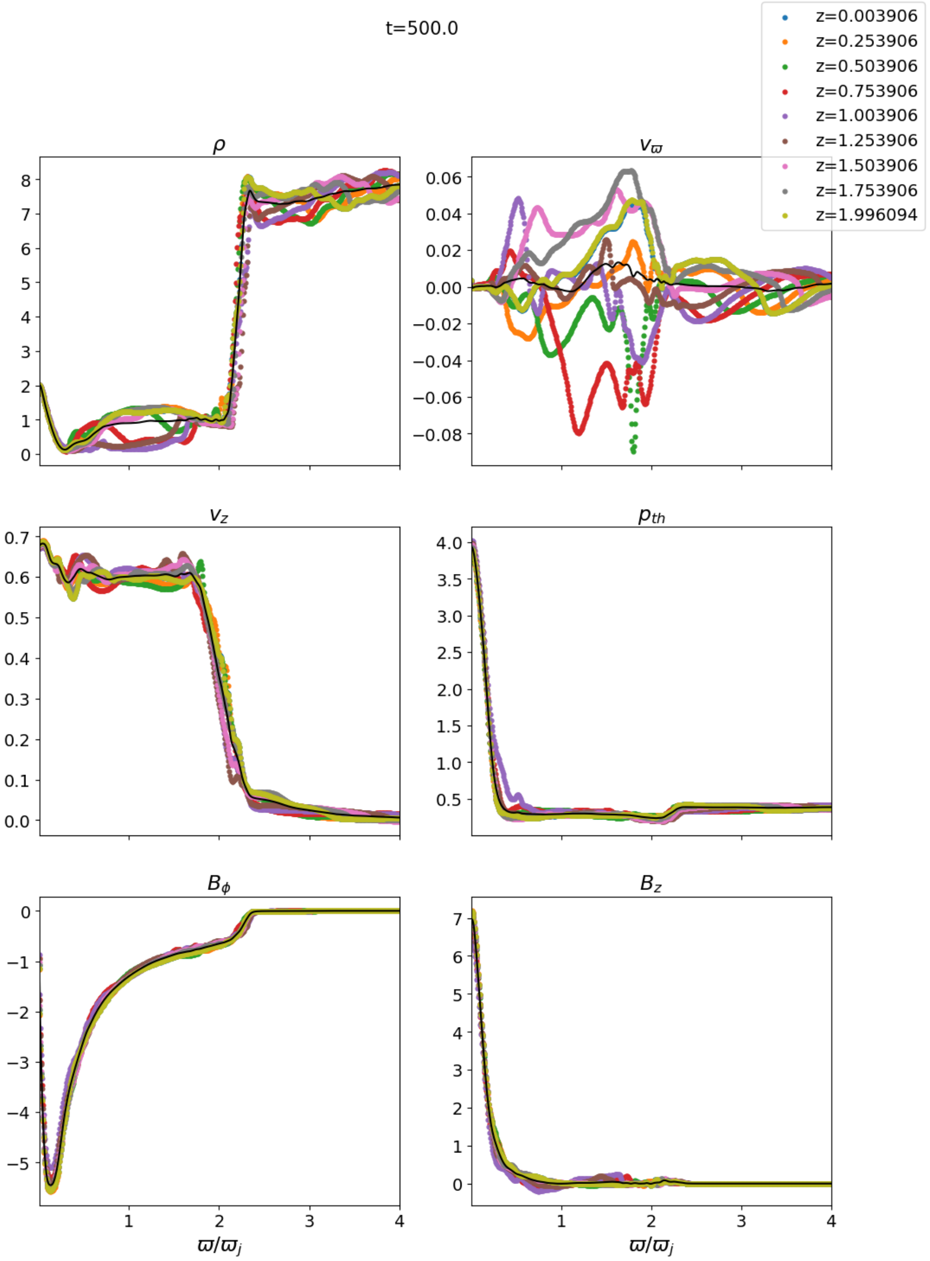

Figure 6.5: Cross section plots for various jet quantities for t=500. Black solid lines represent the mean of the slices shown. Different dots color represents different z value slice.

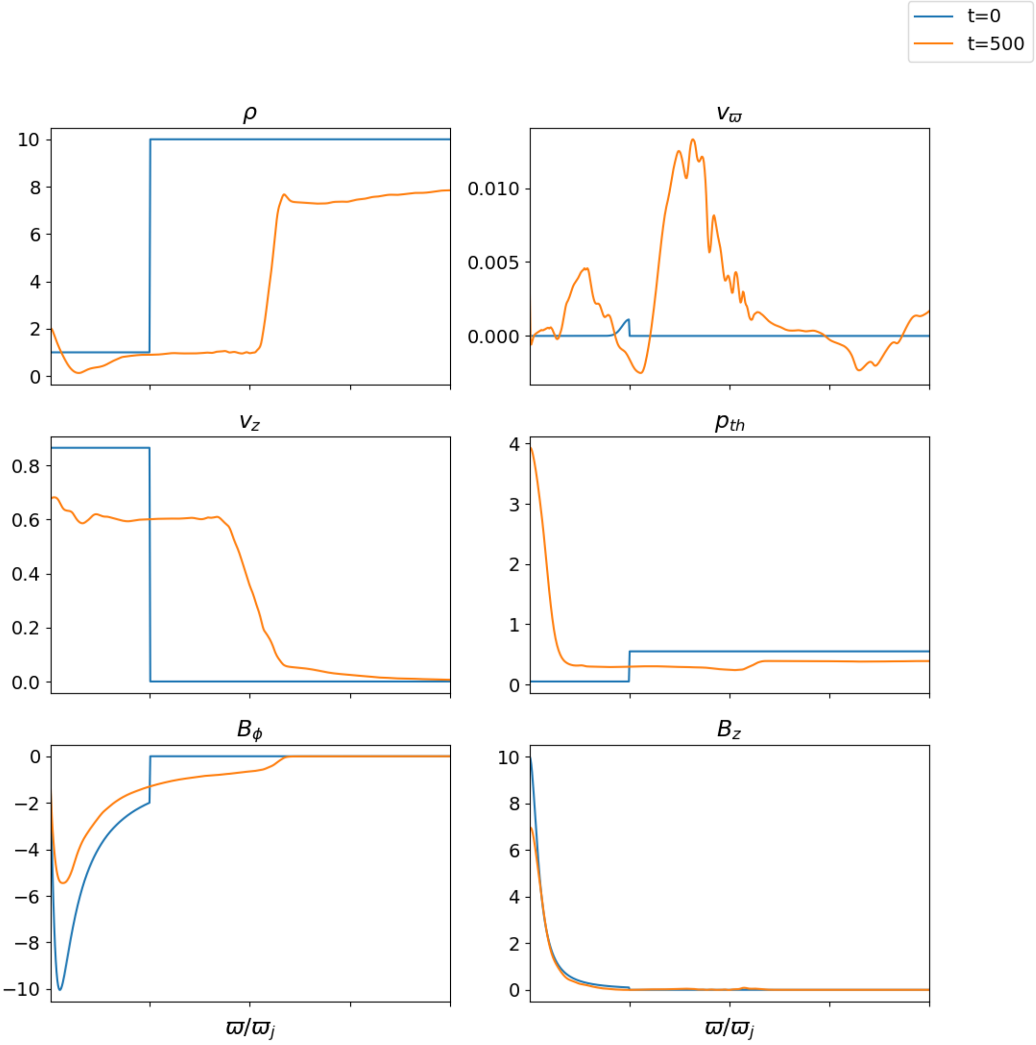

Figure 6.6: Mean profiles for the jet physical quantities with respect to the slices along the jet for the z values presented in figure 6.5. The blue and orange lines correspond to $t = 0$ and $t = 500$ respectively.

has decelerated significantly compared to the initial profile. The environment has achieved a non-zero velocity which is non-relativistic $V_z \lesssim 0.1$, while $V_z \to 0$ as $\varpi \to \infty$. The two components are connected through a high velocity gradient zone similarly to the density profile. The respective gradient zones for the density and the V_z profile coexist at $\varpi \sim 2$. The mean value curve efficiently overlaps the slices regarding the V_z profile.

The thermal pressure profile slices are coincident with their mean value. The quantity profile peaks towards the axis of the jet. The quantity remains constant for $0.3 \lesssim \varpi \lesssim 2$ and the jet's exterior. The pressure has increased for the jet interior whereas for the environment its value has decreased.

Both components of the magnetic field are represented by their mean value across the jet. Interestingly the magnetic field maintains its large scale structure up to $t = 500$. It is observed that B_ϕ and B_z expand radially to $\varpi = 2$ accordingly to the jet expansion. At this distance the magnetic field vanishes, the environment remains hydrodynamic. Most interestingly both components maintain their initial radial distribution apart from their respective amplitude value. The overall magnetic field structure of the jet is preserved.

In order to properly monitor the jet expansion versus time in figure 6.7 the position of the jet's boundary is plotted against the time. The boundary position is defined as the most outward cell of the mean density profile in the grid having $\rho_0 \leq 1.5$. At the first stages of the simulation the boundary seems to move inwards which is not accurate. The reason behind this is the existence and evolution of the vortex at its early stages, where the density profile fluctuates intensively, thus affecting this result. The jet boundary is not displaced inwards at this extend.

The jet expands in three phases. The first one is during the instability's linear phase for $t \lesssim 10$. Then there is a second phase for $20 \lesssim t \lesssim 100$ and finally the final phase is observed for $t \gtrsim 100$. The first phase is characterized by an almost instant expansion from $\varpi_j \simeq 1$ to $\varpi_j \sim 1.4$. Then there are two constant rate expansion stages, the transition from the second to the final phase occurs at $t \sim 100$. At $t \sim 100$ the vortex is assimilated by the rest of the flow and is not located on the jet boundary anymore. The jet expands from $\varpi_j = 1$ to $\varpi_j \approx 2.2$.

In figures 6.8 and 6.9 the proper fast magnetosonic Mach number is plotted for $t = 0$ and $t = 500$ respectively. The initial unperturbed configuration is sub-fast for $\varpi \lesssim 0.5$ and $\varpi > 1$, while the flow is super-fast for $0.5 \lesssim \varpi \leq 1$. At $t = 500$ the entire jet has become sub-fast magnetosonic apart from 2 hotspots near the new jet boundary which are marginally super-fast. Even though both the magnetic field and the z-component of the velocity decrease, the V_z has a higher rate of decrease and the flow eventually becomes sub-fast.

In figure 6.10 the energy is calculated and plotted as a function of time. The energies are calculated along the z direction, the mass and electromagnetic energy fluxes are given by $\xi\rho_0\gamma^2 V_z$, $\boldsymbol{E} \times \boldsymbol{B}$ respectively. The electromagnetic energy flux or as commonly known Poynting flux can be expressed only in terms of magnetic and velocity fields if the previous definition is combined with the ideal Ohm's law

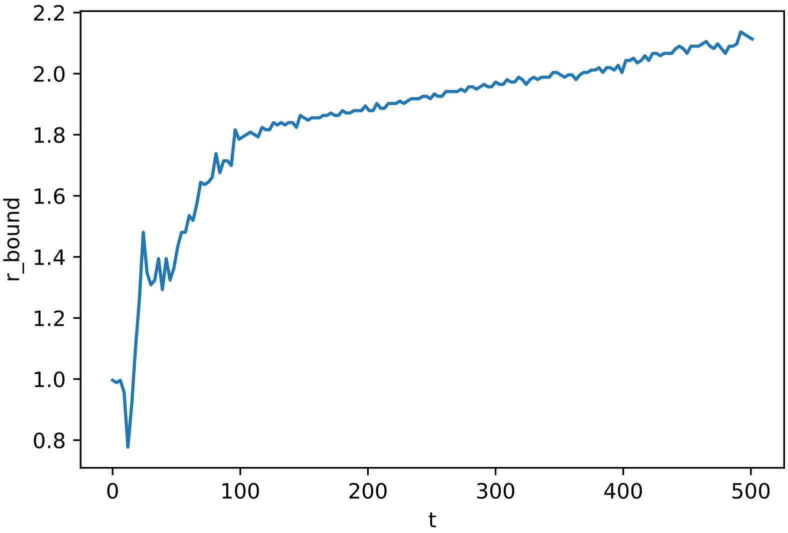

Figure 6.7: Jet boundary evolution versus time. The boundary is defined as the most outward cell of the mean density profile having $\rho_0 \leq 1.5$.

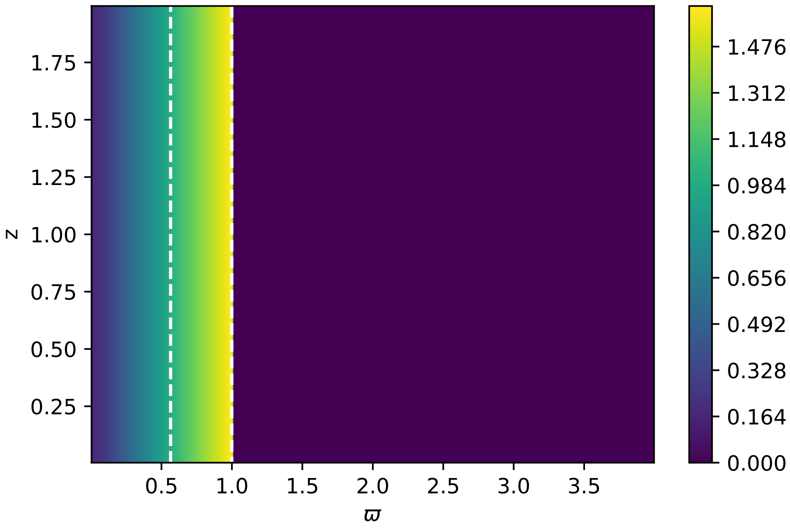

Figure 6.8: Proper fast magnetosonic Mach number contour plot for the initial jet state.

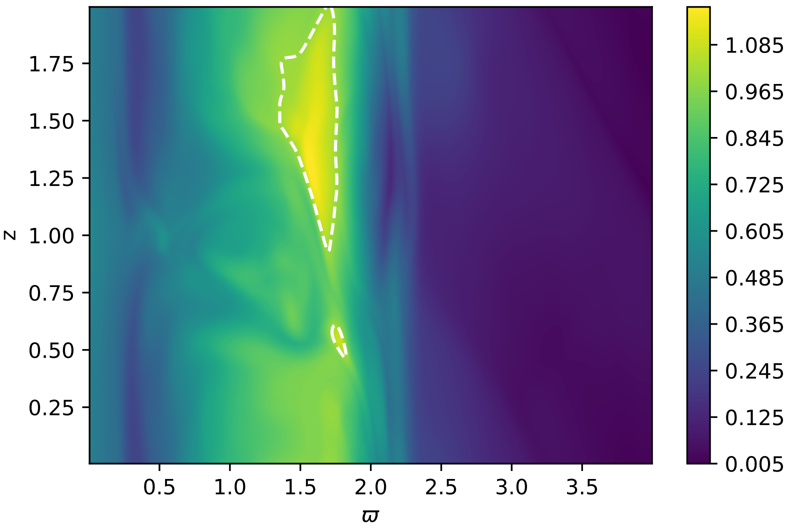

Figure 6.9: Similar to figure 6.8 for $t = 500$.

$$\begin{aligned}\text{Poynting flux} &= \boldsymbol{E} \times \boldsymbol{B}\,, \\ &= \boldsymbol{B} \times (\boldsymbol{V} \times \boldsymbol{B})\ , \\ &= B^2\boldsymbol{V} - (\boldsymbol{V}\cdot\boldsymbol{B})\,\boldsymbol{B}\,.\end{aligned}$$

Finally, if the flux is considered along the z-direction the above relation yields $B^2V_z - (\boldsymbol{V}\cdot\boldsymbol{B})B_z$. So, in figure 6.10 the orange and blue colored lines represent the mass and magnetic energy flux respectively. The green colored line is their sum and corresponds to the total energy flux carried by the outflow. Specifically the energies are computed by multiplying the related flux expression with the radius in order to ensure that the flux near the axis is not overestimated compared to the outer jet vicinity. Then this quantity is summed over the $\varpi \leq 2$ region. Thus, the quantities depicted have units of power (energy per time), as this summation is equivalent to integrating the energy flux in the cross-section of the jet.

Initially, the jet is Poynting dominated and for the first few crossing times the total energy of the system is constant. The steep increase in the mass energy per time is accompanied with a steep decrease in the electromagnetic energy per time and this indicates the onset and the rapid evolution of the Kelvin-Helmholtz instability. The loss of the electromagnetic power becomes more gradual for $t \gtrsim 30$ while the gain of mass energy also eases. The third phase begins at $t \approx 80$ at which the jet reaches equipartition and then becomes matter dominated. The jet seems to almost maximize its mass energy per time right after the shift in the energies. The electromagnetic power continues to decrease while the mass energy per time remains almost constant, it starts to decrease after $t \sim 300$ crossing times with a much smaller rate in comparison with the electromagnetic energy per time.

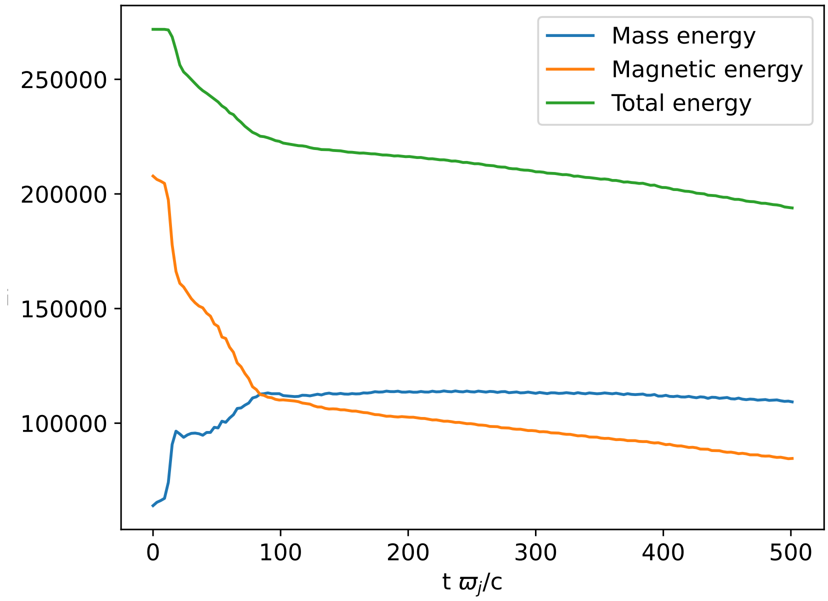

Figure 6.10: Time dependence of jet's energy per unit time. Blue, orange and green colored lines represent the mass, magnetic and total energy per time.

In figure 6.11 the energies per time are presented for $t \leq 100$ with an adopted time step of $\delta t = 1$, this provides a more detailed evolution of the quantities, especially for $t \leq 20$. This specific time interval includes the onset and the linear stage of the Kelvin-Helmholtz mode. The total energy per time remains constant for $t \lesssim 10$ and then decreases in value for the rest of the simulation. The energies per time change smoothly following an exponential-like pattern which indicates the linear phase of the instability. As predicted from the linear stability analysis the mode initiates almost at the beginning of the simulation and proceeds to the non-linear phase at $t \simeq 16$.

The rate of change for the energies per time has two distinct regimes. The first one is from $t \sim 20$ up to $t \approx 100$ where the change is steep for both quantities. Then for $t \gtrsim 100$ and until the end of the simulation the rate of change for both energies per time becomes smaller. These regimes can be associated with the morphological and dynamic processes occurring in the outflow at these specific time periods. During the steep rate of change the vortex is active in the jet and is located on the boundary of the jet. The mixing of the two media is at its maximum intensity during this stage, which affects accordingly the two powers. The vortex drags into the jet dense unmagnetized matter and pushes out to the environment magnetized relativistic plasma. This exchange is of local nature and involves parts of the outflow around the jet boundary.

For $t \gtrsim 100$ both $dE_{\rm mass}/dt$ and $dE_{\rm mag}/dt$ become less steep and the jet preserves these rates until the end of the simulation. As was observed in figures 6.3 and 6.4 the vortex has been dissolved, thus the interchange of matter between the two media has weakened.

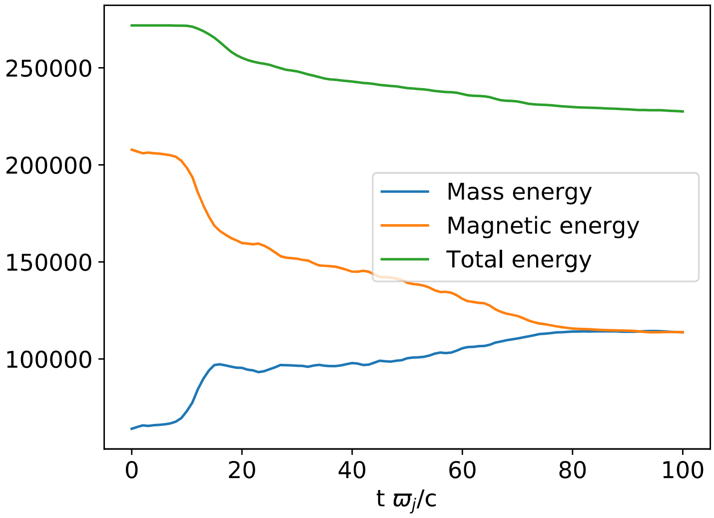

Figure 6.11: Similar to figure 6.10 with final simulation time being $t = 100$.

In general, the two distinct phases for the rates of change are associated to the vortex feature. This claim is further supported by the analysis on the energies per time for the jet which includes thermal pressure in the place of B_z in section 6.2.

The total energy per time, which is reminded that is calculated for the $\varpi \leq 2$ part of the plane, decreases with time. This means that the box for which the power is calculated emits power into the $\varpi > 2$ component. To verify this claim in figure 6.12 the energy fluxes are plotted across the jet at specific z values. Both quantities have non-zero components for $\varpi > 2$, which indicates energy emission from the interior of the jet towards its environment. Both energy fluxes for the environment and at $t = 0$ are zero, as $\boldsymbol{V} = 0$. The prominent component for the environment is the mass flux and up to $\varpi = 4$ the values of the quantity are non-negligible. On the contrary, the Poynting flux is mostly contained inside the outflow ($\varpi \lesssim 2$) while beyond this distance its value drops rapidly and becomes negligible almost instantly near $\varpi \gtrsim 2$.

The Poynting flux is contained inside the jet. This fact leads to the conclusion that the Poynting flux converts into mass energy flux while the jet transports portion of the mass energy into the environment.

6.2 Thermal case

This section includes the simulations of the jet which incorporates a thermal pressure component as was introduced in 5.2.2. It is reminded that the thermal pressure takes the place of the magnetic pressure generated by the B_z by replacing $P = B_z^2/2$ and then setting $B_z = 0$. This way the total pressure profile of the cold jet is also preserved to this

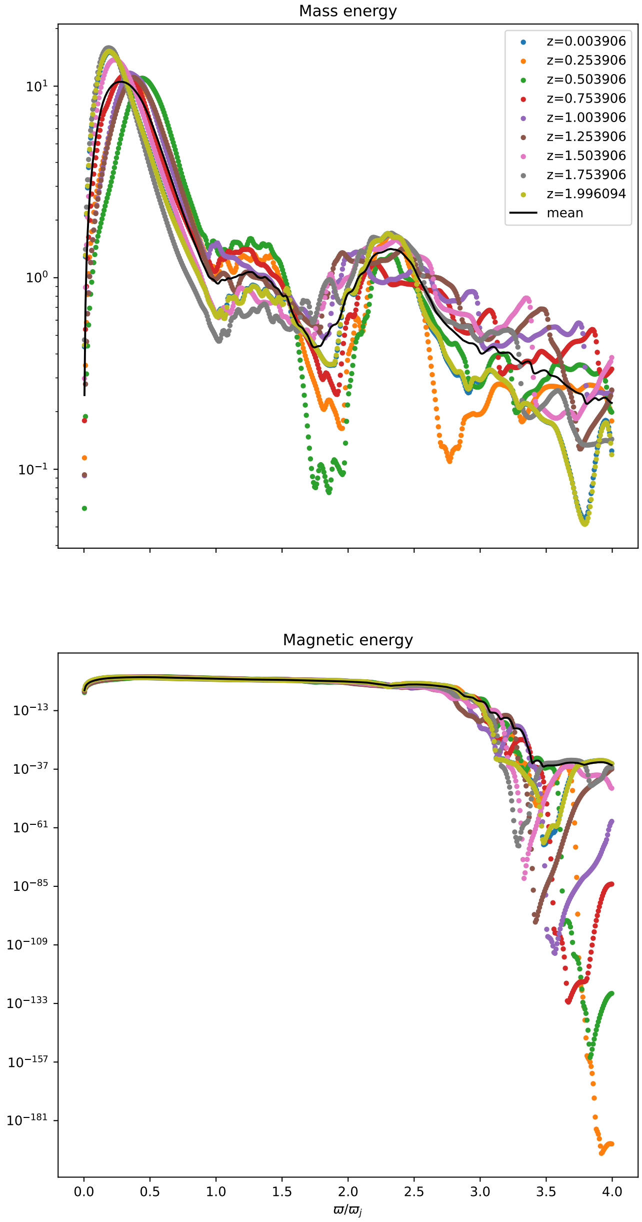

Figure 6.12: Cross section plots of energy fluxes for the final simulation instance. The slices height used in order to plot the quantity across the jet are shown in the figure legend with different color per z value. Black line represents the mean value of each flux for the presented slices. Top panel shows the mass energy flux and bottom panel the Poynting flux.

modified equilibrium and the jet has B_ϕ and P. The simulation setup is identical to the setup of section 6.1. For brevity's sake this specific simulation setup is referred as thermal jet/case throughout this chapter.

In figure 6.13 contour plots of the initial state of the simulation is shown. Top row from left to right shows the proper density, V_ϖ and V_z, while in the bottom row in the same order the thermal pressure, B_ϕ and the ϕ-component of the vorticity are depicted. The thermal pressure value maximizes in the region of the axis and drops rapidly towards the jet boundary. Apart from this quantity, the rest of the plots are identical to their counterparts in figure 6.1.

Figure 6.14 is similar to figure 6.13 but for $t = 30$ which is early in the non-linear evolution phase of the outflow. The jet has expanded to $\varpi \approx 1.5$ and the proper density does not showcase a smooth profile in both directions. On the axis there are a few spots of high density, specifically at $z \approx 1.5$ there is a bright spot indicating high density value.

V_ϖ profile presents a dipole formation of negative/positive value on the new jet boundary, the velocity value is $V_\varpi \approx -0.27$ and $V_\varpi \approx 0.3$ which indicate strong local plasma movement in opposite directions. For V_z the maximum value is located inside the jet with a value of $V_z \approx 0.85$. Moving towards the environment the velocity decreases, until it meets the part of the environment which is still static. At the point where the V_ϖ presents this dipole feature, the V_z profile also presents a similar local pattern. There is a positive/negative value interchange, combined with the V_ϖ profile a clock-wise rotation at this spot is indicated. Moreover, the proper density presents a local minimum, if this minimum is combined with the rotational movement then the feature at this spot is probably a vortex.

The density still has its maximum value near the jet's axis and decreases rapidly as the radius increases. The toroidal component of the magnetic field is substantially perturbed compared to its initial configuration. The minimum value in not effectively displaced regarding its prior position, nonetheless the area of the minimum presents a wiggling shape and increases near the upper box boundary. The magnetic field still increases towards the new jet boundary and finally diminishes in the jet environment. Regarding the vorticity a bright spot is noted at the vortex position, indicating strong rotational movement. This observation further supports the rotating vortex scenario. Additionally, the quantity plot reveals a number of secondary bright spots, smaller in size compared to the main vortex. If these spots are also traced in ρ_0 and V_z, V_ϖ plots it can be deduced that these are a number of smaller, secondary vortices which are mainly manifested near the outflow boundary. Due to their smaller size their impact on the evolution of the jet could be milder juxtaposed to the impact of the main feature.

In Fig. 6.15 the jet state is presented halfway through the simulation. The proper density plot indicates that the jet boundary is located at $\varpi \approx 1.5$. The vortex is clearly observed and its size has increased in comparison with its former state in Fig. 6.14. At $\varpi \approx 2.3 - 2.4$ and $z \approx 0$ a new smaller vortex has been formed.

The V_ϖ distribution also indicates the position of the vortex, the velocity value due to the rotation is $V_\varpi \sim 0.3$. It should be noted that near the axis ($\varpi \approx 0.1$) there is the emergence of interchanging positive/negative value pattern in the z-direction. This

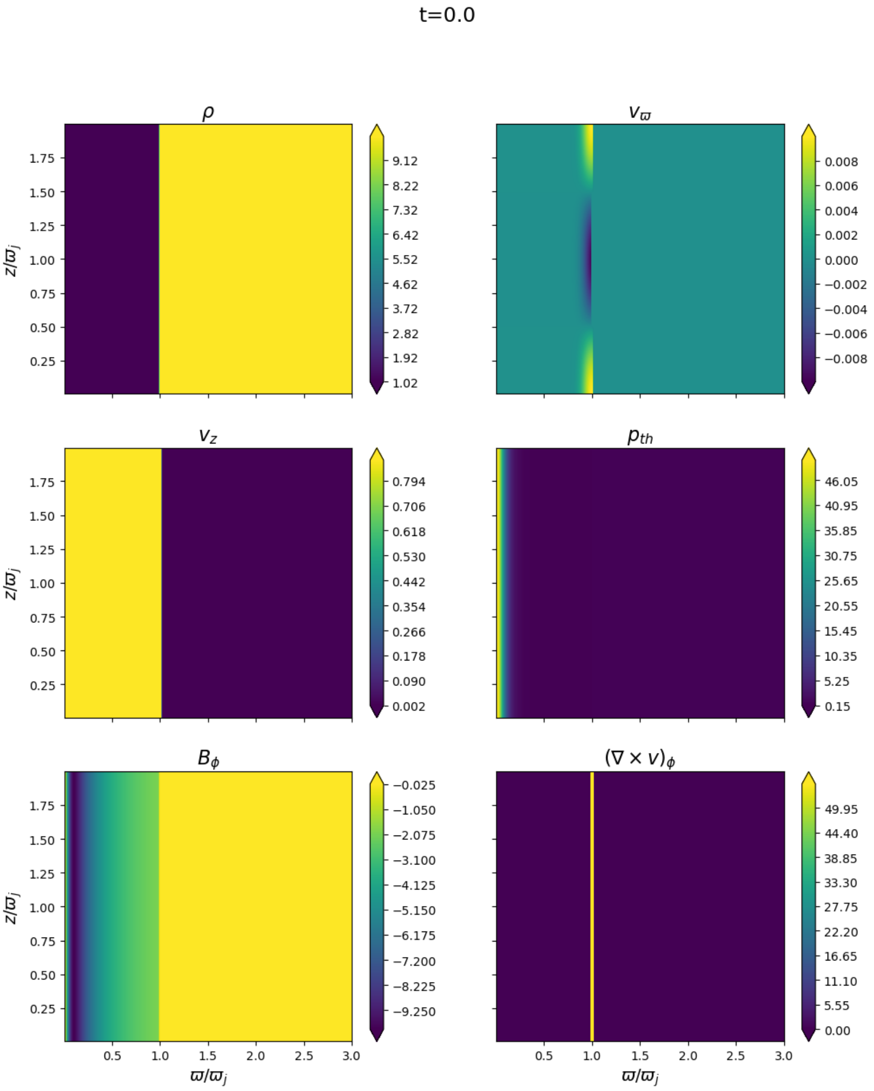

Figure 6.13: Contour plots of the initial jet configuration in the case of a thermal pressure component included appropriately in the configuration. Top row and from left to right the proper density, V_ϖ are depicted. Middle row in the same order V_z and the thermal pressure, and on the bottom row B_ϕ and the ϕ-component of the vorticity are depicted respectively.

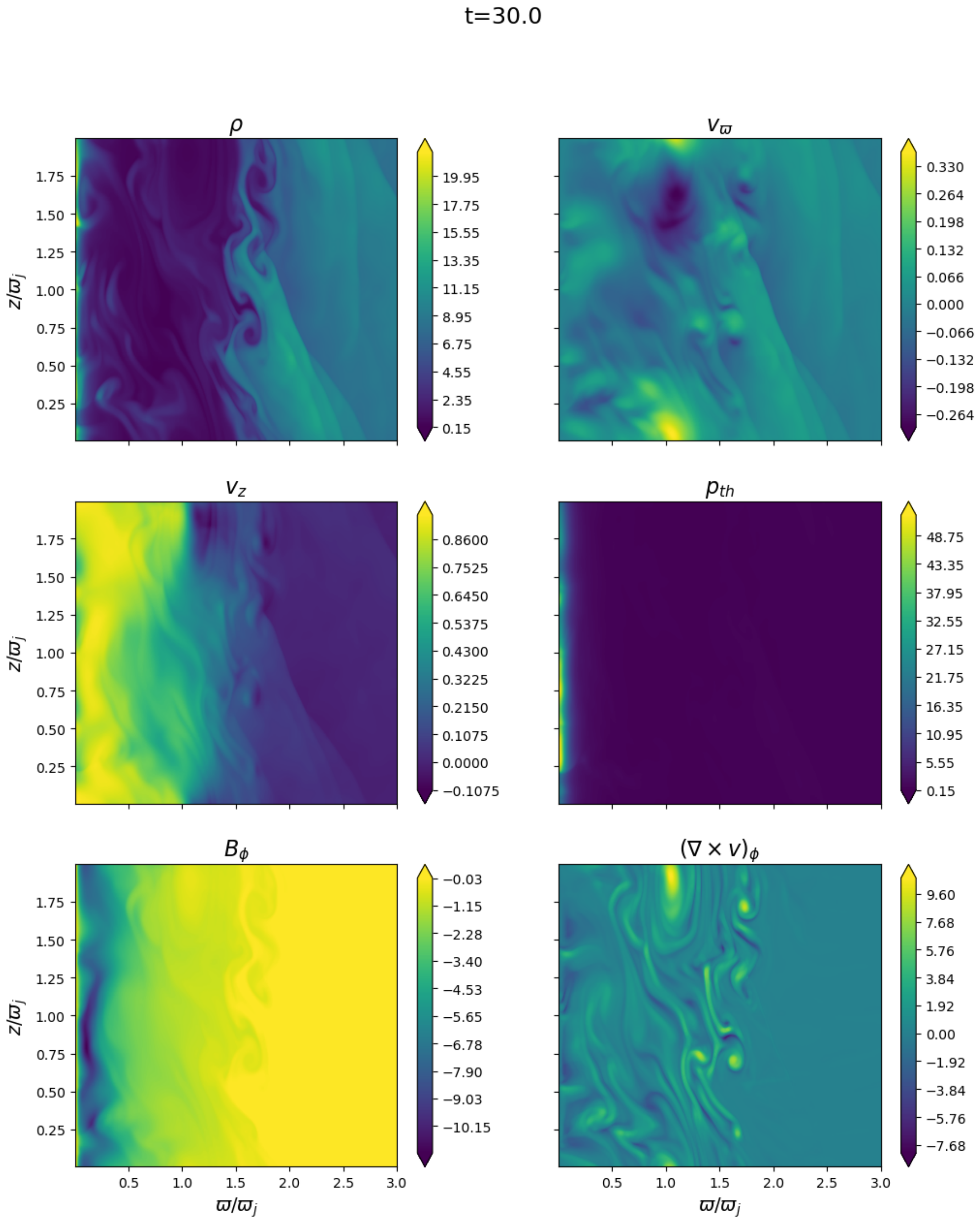

Figure 6.14: Similar to figure 6.13 for $t = 30$.

pattern has an equivalent "wavelength" of exactly 2× the box length. At the coordinates of the vortex the V_z presents a positive/zero value interchange, hence the vortex rotates clockwise. At the position of the secondary vortex the same pattern is noticed, consequently this feature also seems to rotate clockwise. Near the jet axis there is a core of high V_z value, which has a wave-like form. This pattern alongside the pattern in the V_ϖ profile could indicate a possible new local rotation, this time with an anti-clockwise direction.

The thermal pressure profile is effectively not differentiated compared to the respective plots in Figures 6.13 and 6.14. The maximum value of the quantity is located on the axis of the jet and decreases rapidly as the radius increases. The B_ϕ plot is similar to the V_z plot, i.e. presents the same wave-like disposition near its minimum. The quantity decays as the radius increases, and in the eye of the vortex the magnetic field is zero, probably due to the very sparse matter at this position.

The vorticity at this stage reveals with increased accuracy the regions of the jet that rotate locally. First and most noticeable is the bright spot corresponding to the main vortex which rotates clockwise, followed by the secondary vortex on the boundary of the jet. The rotation on the boundary is also clockwise as $(\nabla \times \boldsymbol{B}) \cdot \hat{\phi} > 0$. Near the axis where the wave-like disposition of the flow happens the vorticity reveals two spots with negative value. The first one resides in the middle of the simulation box and the second one crosses the upper box boundary. These negative values reaffirm the anti-clockwise rotation.

Finally, in Fig. 6.16 the state of the jet is presented for $t = 500$. The jet in general has not evolved significantly since $t = 252$. The boundary of the jet has increased slightly while the two vortices are still present in the flow. The wavelike disposition of the flow lines near the axis of the jet is still present, while the patterns for the V_ϖ and the V_z are also still observable. The vorticity has four points of interest inside the flow, which correspond to the same two clockwise rotating vortices near the boundary of the jet and two anti-clockwise vortices in the neighborhood of the axis.

Even though this configuration showcases more formations and is dynamically more complex compared to the simulation of the cold jet, the outflow does not transcend into a turbulent state. The relativistic jet is clearly distinct from the environment while the magnetic field maintains its large scale structure. The vortices do not dissolve and are clearly distinguishable from the rest of the flow.

In figure 6.17 the dependence of the quantities on the radius is shown for various slices of the simulation box and for $t = 500$. The black lines represent the mean profile of the 6 slices. This Figure showcases a few important differences in contrast with Fig. 6.5. The mean profile does not coincide with the profiles from the slice near the axis of the jet. The same is also true when comparing the different slices between them. The reason behind this inconsistency is the wavelike disposition of the field lines at $\varpi \ll 1$. For the majority of the quantities as ϖ increases the profiles for different z values converge, therefore the mean eventually overlaps the colored lines.

Nonetheless, the mean field generally acts as an efficient proxy in order to grasp the evolution of the various quantities. The quantity mean profiles at $t = 0$ and $t = 500$ are presented in Fig. 6.18. The jet expansion from $\varpi_j = 1 \to \varpi_j \approx 2$ is indicated especially

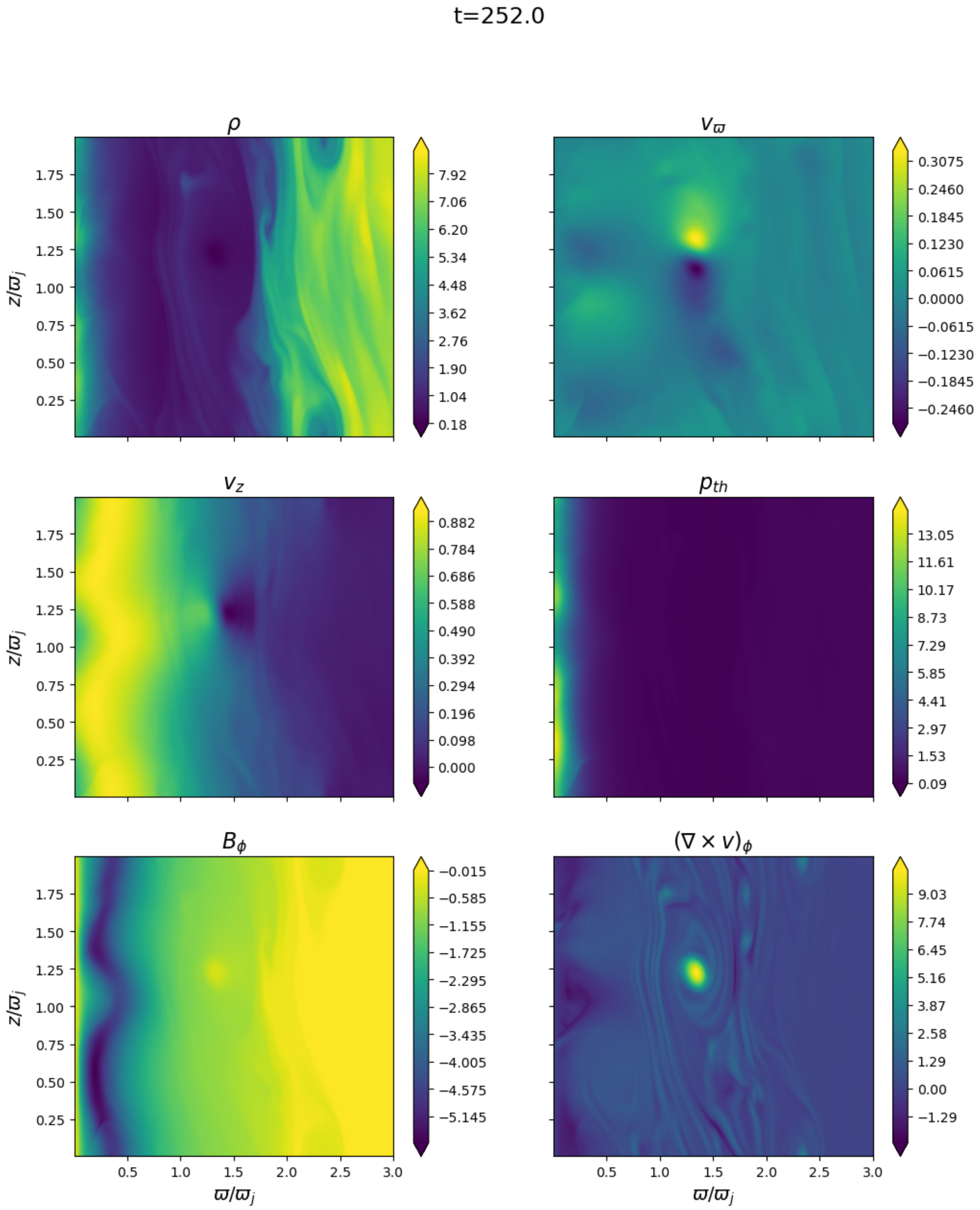

Figure 6.15: Similar to figure 6.13 for $t = 252$.

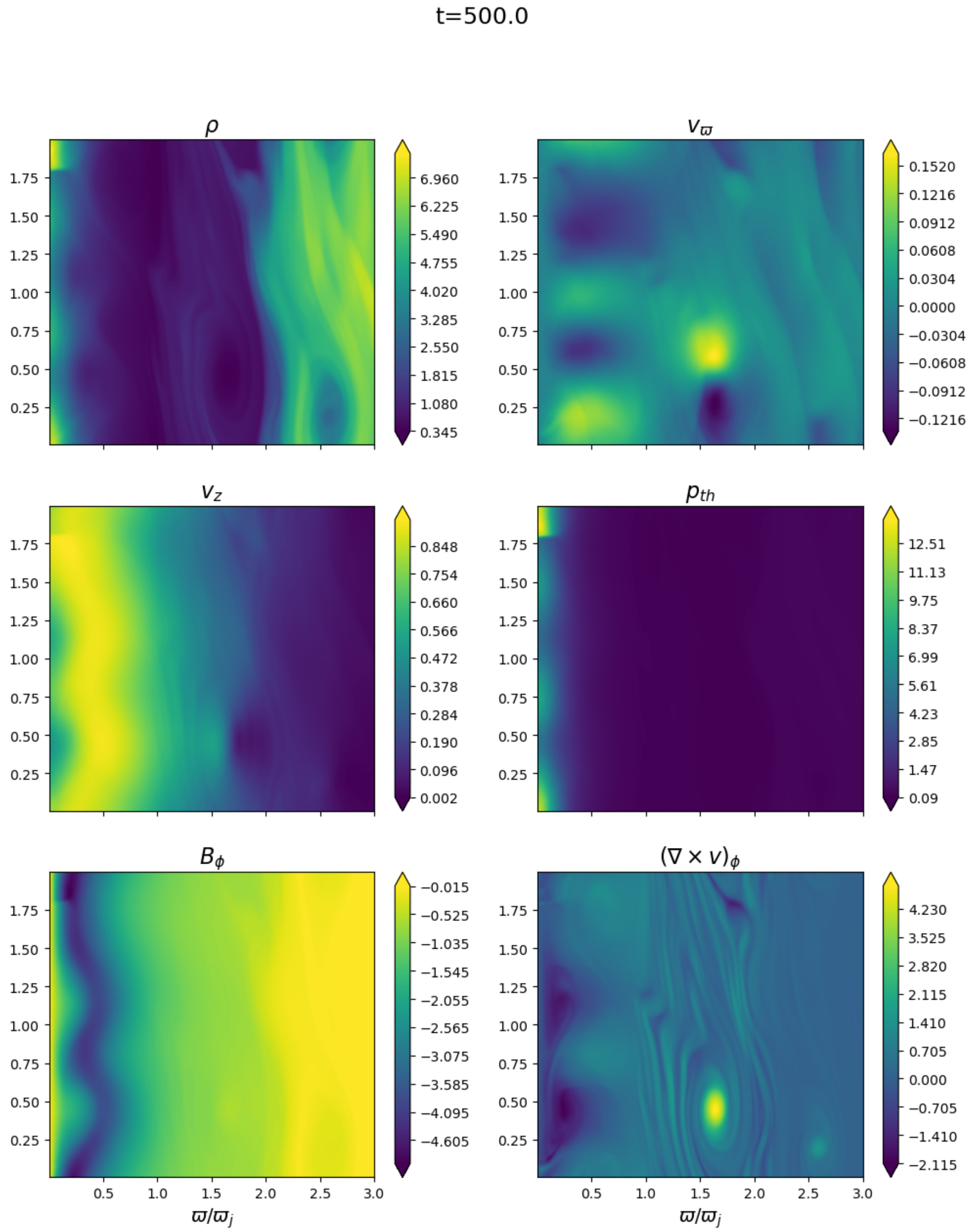

Figure 6.16: Similar to figure 6.13 for $t = 500$.

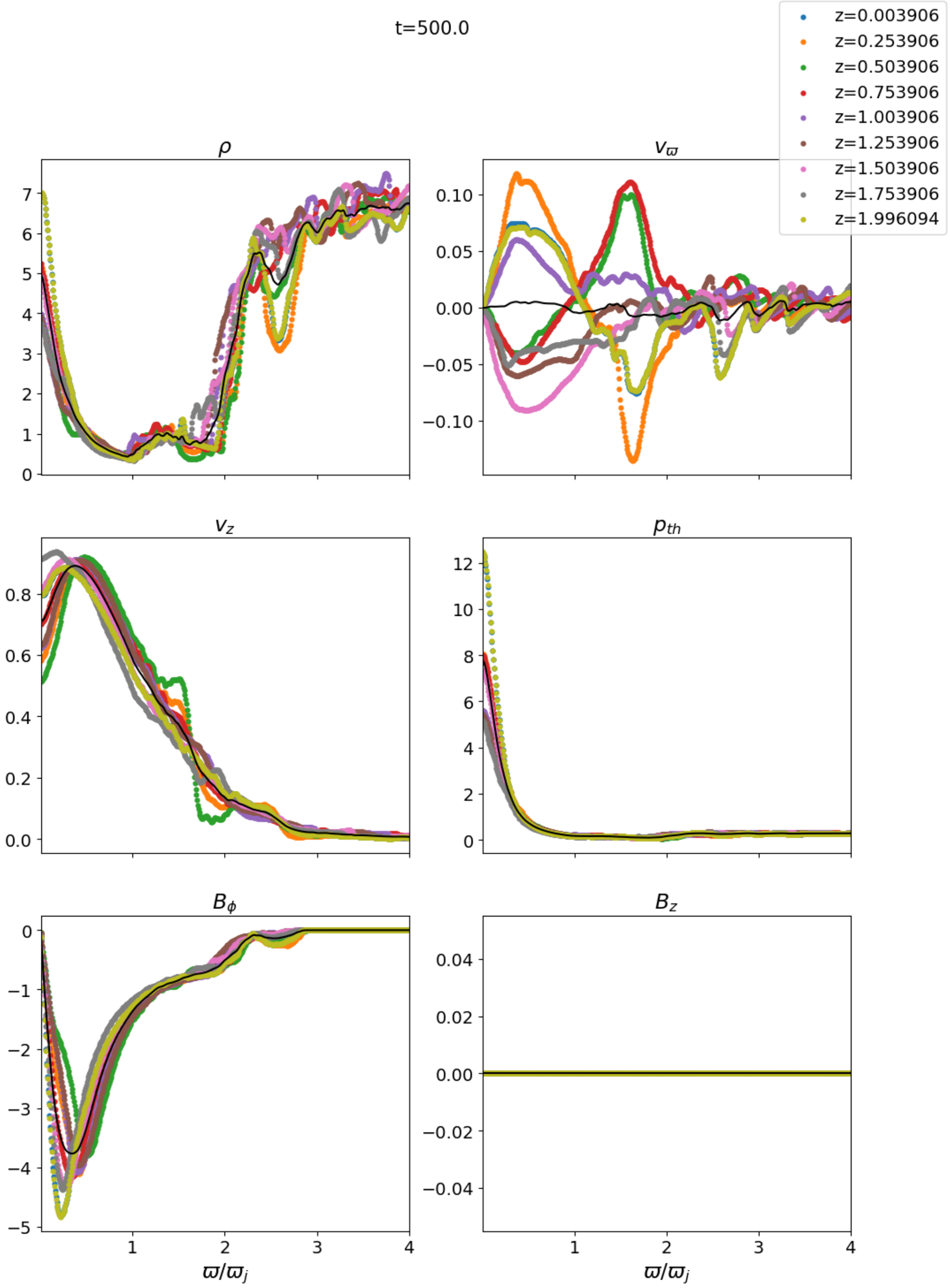

Figure 6.17: Cross section plots for various jet quantities in the case of $P = B_z^2/2$ for t=500. Black solid lines represent the mean of the slices shown. Different dots color represents different z value slice.

by observing the proper density profile. The density peaks towards the axis similarly to Fig. 6.6. Then the main body of the jet ($\varpi \lesssim 2$) retains approximately the initial density value, $\rho_0 \approx 1$. When the radius increases further more there is a zone where the density increases until it matches the corresponding value for the environment. The density of the environment continues to increase in a significantly more gradual rate as ϖ further increases.

The V_ϖ mean profile is irregular but it is more appropriate to analyze this quantity using Fig. 6.5, as the mean field is not representative. The slices reveal the complex structure of the outflow, for $\varpi \lesssim 2$ there are two radii values $\varpi \approx 0.2,\ 2$ for which the different z levels have different V_ϖ values. The reason for this is the rotational movement of the small scale vortices near the axis, and the main vortex at $\varpi \sim 2$. The same applies also for the local minimum in V_ϖ at $\varpi \approx 2.5$ which corresponds to the position of the small scale vortex in the environment. The radial component of the velocity is non-relativistic as $\left|V_\varpi\right| \lessapprox 0.1$.

The V_z mean profile is representative of the quantity behavior apart from $\varpi \approx 2$ where the main vortex resides and a fluctuation around the mean value is observed. The jet in general has decelerated except for a narrow lane at $\varpi \approx 0.5$ where the flow has accelerated slightly in comparison with its initial state. From this point outwards the velocity decreases with a constant rate, at the vicinity of the boundary $V_z \sim 0.1$. The environment is not static anymore and propagates with non-relativistic velocities $V_z \lesssim 0.1$, the velocity profile keeps decreasing as the radius further increases.

The maximum of the thermal pressure decreases with time, while the peak is always fixed on the axis of the jet. The toroidal component of the magnetic field is weakened and has expanded following the jet expansion. The minimum seems to have become wider compared to the initial state, this originates in the wavelike disposition of the flow lines. If one looks carefully the B_ϕ plot in Fig. 6.17, it can see that the maximum B_ϕ for each z level has not widened with respect to ϖ, hence this is an effect of the averaging over the different slices. Most importantly the magnetic field retains its large scale structure similarly to the cold jet in section 6.1.

In figure 6.19 the position of the boundary of the jet versus the time is presented. The expansion profile is different when compared to the corresponding profile in figure 6.7. Initially, the minimum of $\varpi_j \approx 0.25$ is due to the same reason as in the cold case, in reality the boundary of the jet never decreased so dramatically. The expansion consists of two phases, the first one for $t \lesssim 80 - 90$ and the second one for the rest of the simulation. The two phases are correlated with the existence and formation of the vortex on the boundary of the jet.

Figures 6.20 and 6.21 present the fast magnetosonic Mach number for $t = 0$ and $t = 500$ respectively. The jet initially is super-fast near the axis and for $0.5 \lesssim \varpi \leq 1$. At the final time instance the $0 \lesssim \varpi \lesssim 0.7$ portion of the jet remains super-fast. This happens as the jet in this region does not decelerate intensively while the magnetic field weakens significantly. The rest of the outflow (jet and environment) becomes or remains sub-fast.

In figure 6.22 the outflow energies per time are presented similarly to Fig. 6.10. Blue,

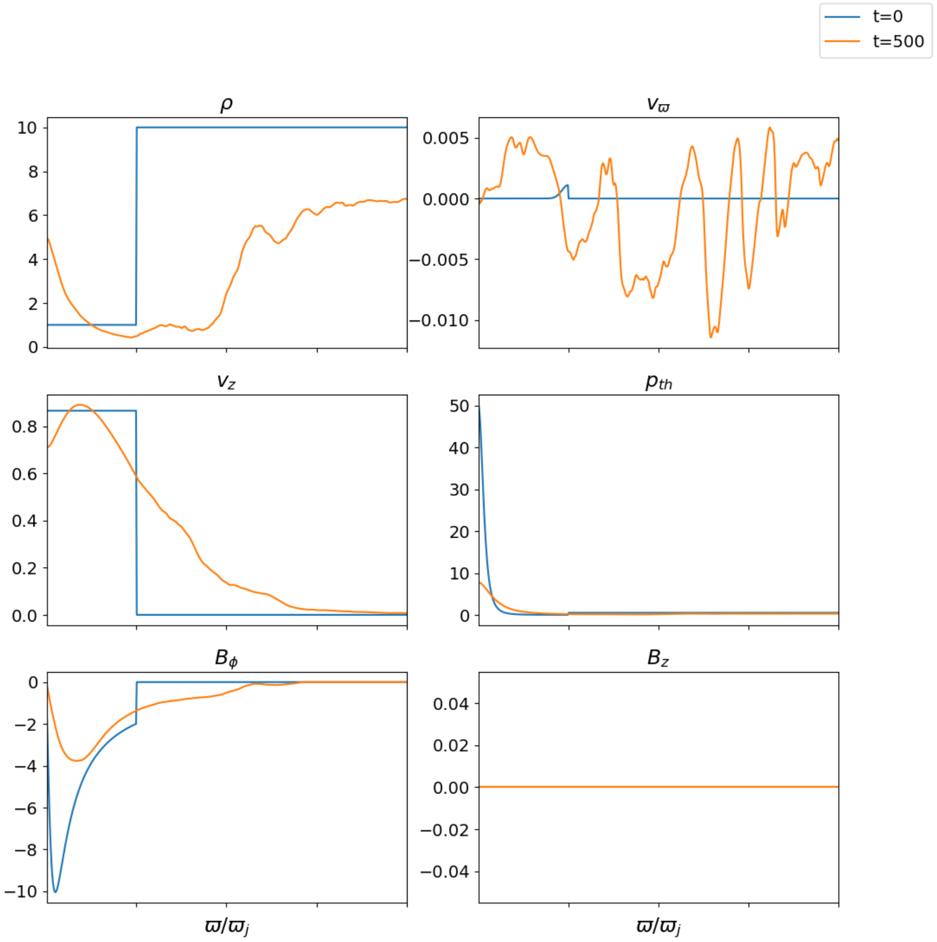

Figure 6.18: Mean profiles for the thermal jet physical quantities with respect to the slices along the jet for the z values presented in figure 6.17. The blue and orange lines correspond to $t = 0$ and $t = 500$ respectively.

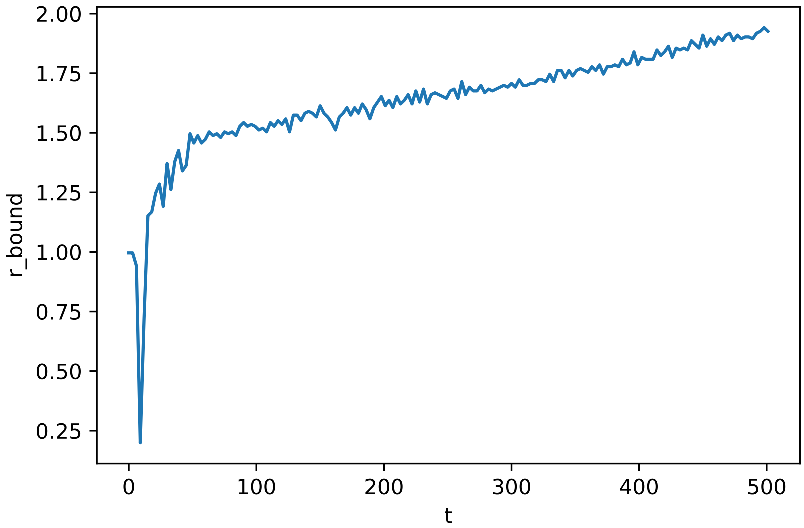

Figure 6.19: Jet boundary evolution versus time for the jet having a thermal pressure component. The boundary is defined as the most outward cell of the mean density profile having $\rho_0 \leq 1.5$.

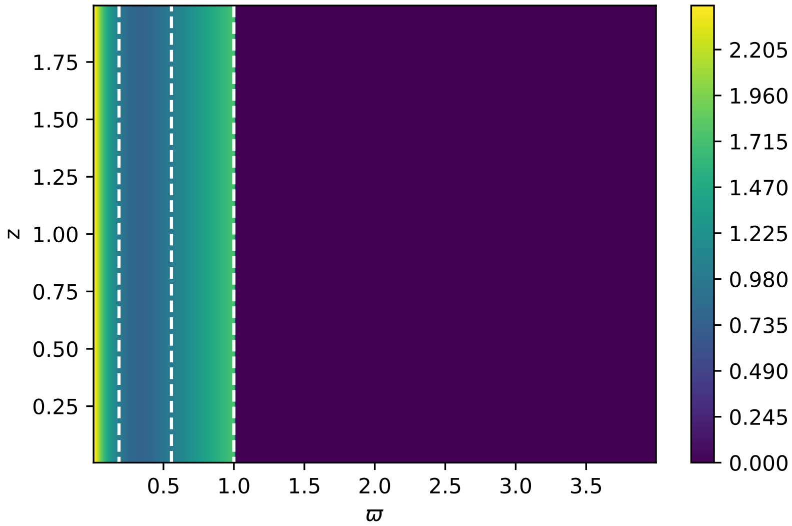

Figure 6.20: Fast magnetosonic Mach number for jet with thermal pressure for $t = 0$.

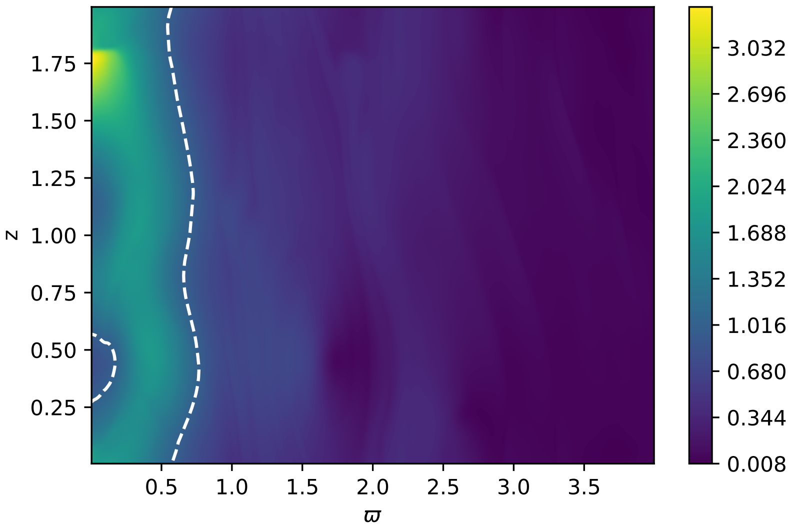

Figure 6.21: Similar to figure 6.20 for $t = 500$.

orange and green lines represent the mass, electromagnetic and total energies per time. In order to clearly depict the linear phase and the transition from linear to non-linear regime figure 6.23 focuses on the $t \leq 100$ part of the simulation.

The linear regime and the transition to the non-linear phase is pinpointed for $t \lesssim 12$ which is in accordance with the linear stability analysis and comparable to the value for the cold configuration. The mass energy per time overtakes the electromagnetic energy per time early in the simulation, for $t \lesssim 10$ which is during the transition between the two outflow states. Then the mass energy per time still increases in expense of the electromagnetic counterpart. The total energy per time after the transition to the non-linear regime decreases. Beyond $t = 100$ every power component decreases in value. The jet remains matter dominated until the end of the simulation and most importantly the jet transfers power into its environment.

An important element is that the power evolution consists of two phases contrary to figure 6.10 which consists of three phases. The dissimilarity emanates from the different evolution of the two configurations. The vortices for the jet having a thermal pressure component are present throughout the simulation run. The cold jet vortex is assimilated by the rest of the jet, thus the third phase recorded in Fig.6.10 is not present in Fig.6.22.

Fig. 6.24 showcases the energy fluxes across the jet for slices with different z values for $t = 500$. Different colored dots correspond to different levels and the black solid line represents their mean profile. The amplitude of the Poynting flux is almost constant for $\varpi \lesssim 2.5$, the flux value is $\approx 10^{-5}$. Immediately after $\varpi \approx 2.5$ the flux drops substantially and becomes essentially negligible as its value decreases to $\sim 10^{-30}$.

The mass energy flux is many orders of magnitude greater than the electromagnetic

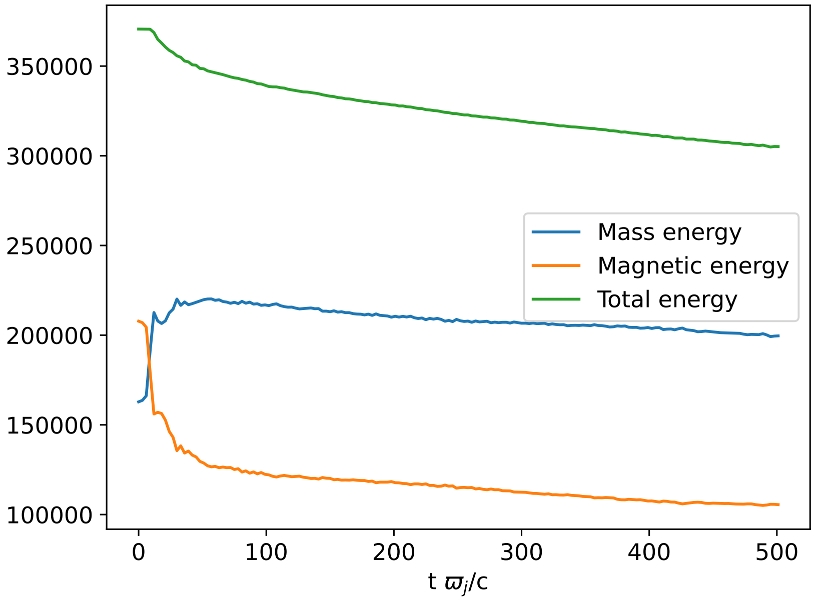

Figure 6.22: Time dependence of jet's energies per time for thermal jet. Blue, orange and green colored lines represent the mass, magnetic and total energy per time.

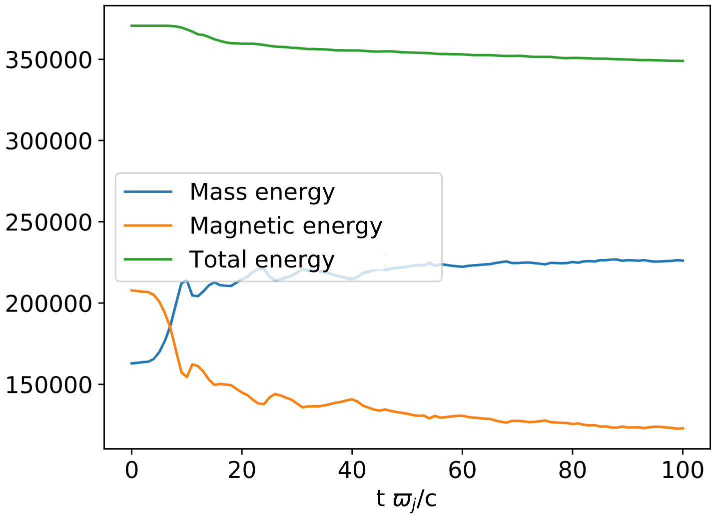

Figure 6.23: Similar to figure 6.22 while zooming into the $t \leq 100$ range.

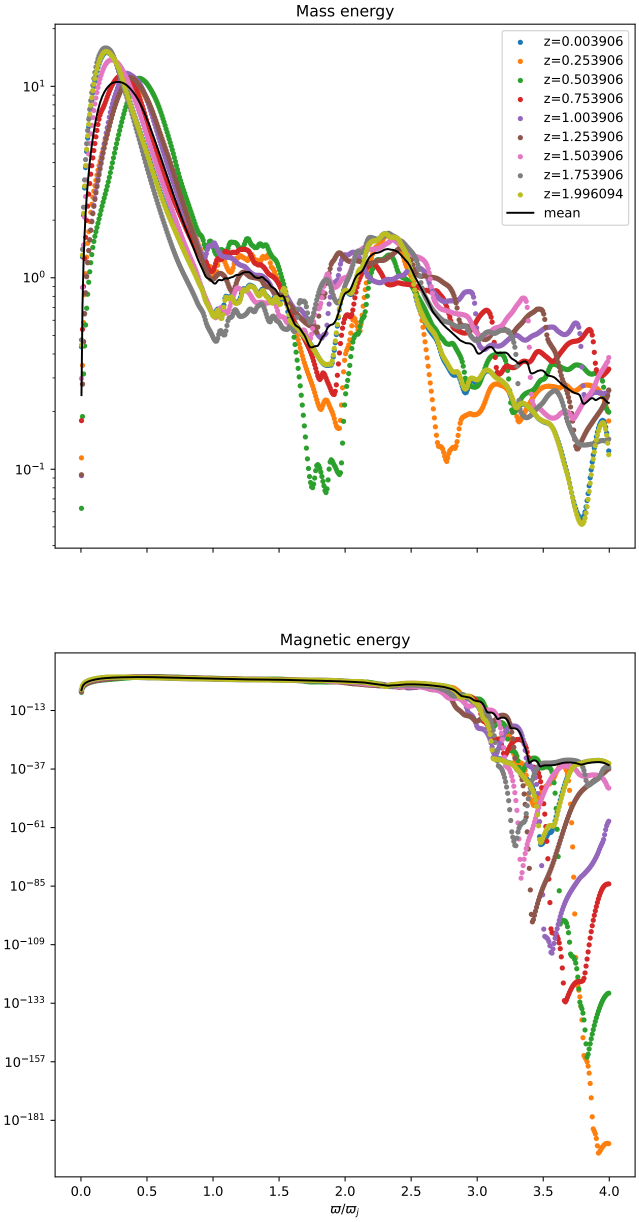

Figure 6.24: Cross section plot for the mass and Poynting energy fluxes. Top plot and bottom plot shows mass and Poynting energy flux. Colored dots represent different z level slices while the black line is their mean value profile.

counterpart. The flux is concentrated near the axis of the outflow having a value of $\sim 10^2$. As radius increases the flux diminishes and near the new jet boundary the value is ~ 1. The environment has a non-zero value of $0.1 \lesssim E_{mass} \lesssim 1$. The mass energy flux is transferred towards the environment. This could be the mechanism for the jet's energy loss, i.e. the instability transforms Poynting flux to mass energy flux and consequently this flux is propagated towards the environment.

6.3 Thermal case, $k = 10$

The final simulation examines the non-linear evolution of the Kelvin-Helmholtz mode for a jet with a thermal pressure component without B_z. The setup is identical to the setup of 6.2 except for the wavenumber which is $k = 10$. This choice is based on the dependence of the Kelvin-Helmholtz instability on k. In chapter 5 it was shown that as k increases the Cartesian solution tends to behave similarly to the cylindrical counterpart. The mode becomes more localized, meaning that the solution vanishes rapidly as $\varpi \to 0$ and $\varpi \to \infty$. Also, the $\mathrm{Im}(\omega)$ becomes larger, as a result the instability growth timescale further decreases.

Therefore it is natural to investigate the non-linear behavior of the instability as the wavenumber increases, and explore if there are important differences from the evolution of the mode when $k = \pi$. As a consequence of the change of the k value the box length along the z-direction is decreased as the new wavelength is $2\pi/10 \approx 0.628$, thus $z \in [0, 2\pi/10]$. The number of cells along the same direction is also decreased as it is preferred to preserve the cell shape and size throughout the various simulations. This leads to a grid of 512×80 grid points, retaining a cell acme length of ~ 0.008.

The initial jet state is identical to the corresponding state in section 6.2 and is depicted in Fig. 6.13. In Fig. 6.25 contour plots depicting the jet state at $t = 30$ are shown. There is no evidence of a vortex on the jet boundary while inside the jet there are two spots of low density. V_ϖ has two large regions of almost opposite value which cover a considerate area of the jet. V_z values have not changed considerably compared to its initial value. Nonetheless the distribution of the V_z inside the jet is not uniform, there are patches and areas of the jet which have decelerated noticeably.

The thermal pressure peaks near the jet axis and decreases rapidly with increasing radius. The toroidal component of the magnetic field has not evolved dramatically. The vorticity presents two points of interest, one on the jet boundary and the second near the axis. The first one reveal a clockwise rotating spot while the second one rotates counter-clockwise. Interestingly, only the spot near the axis is associated with a low density feature. The V_ϖ pattern is associated with the two non-zero vorticity regions, as both spots border with the area where the transition from positive to negative or negative to positive V_ϖ occurs.

In Fig. 6.26 the jet evolution is shown halfway through the simulation run. Most noticeably a feature of low density has developed which covers a considerable area of the jet and is not located on the jet boundary. At the vicinity of the low density feature the two

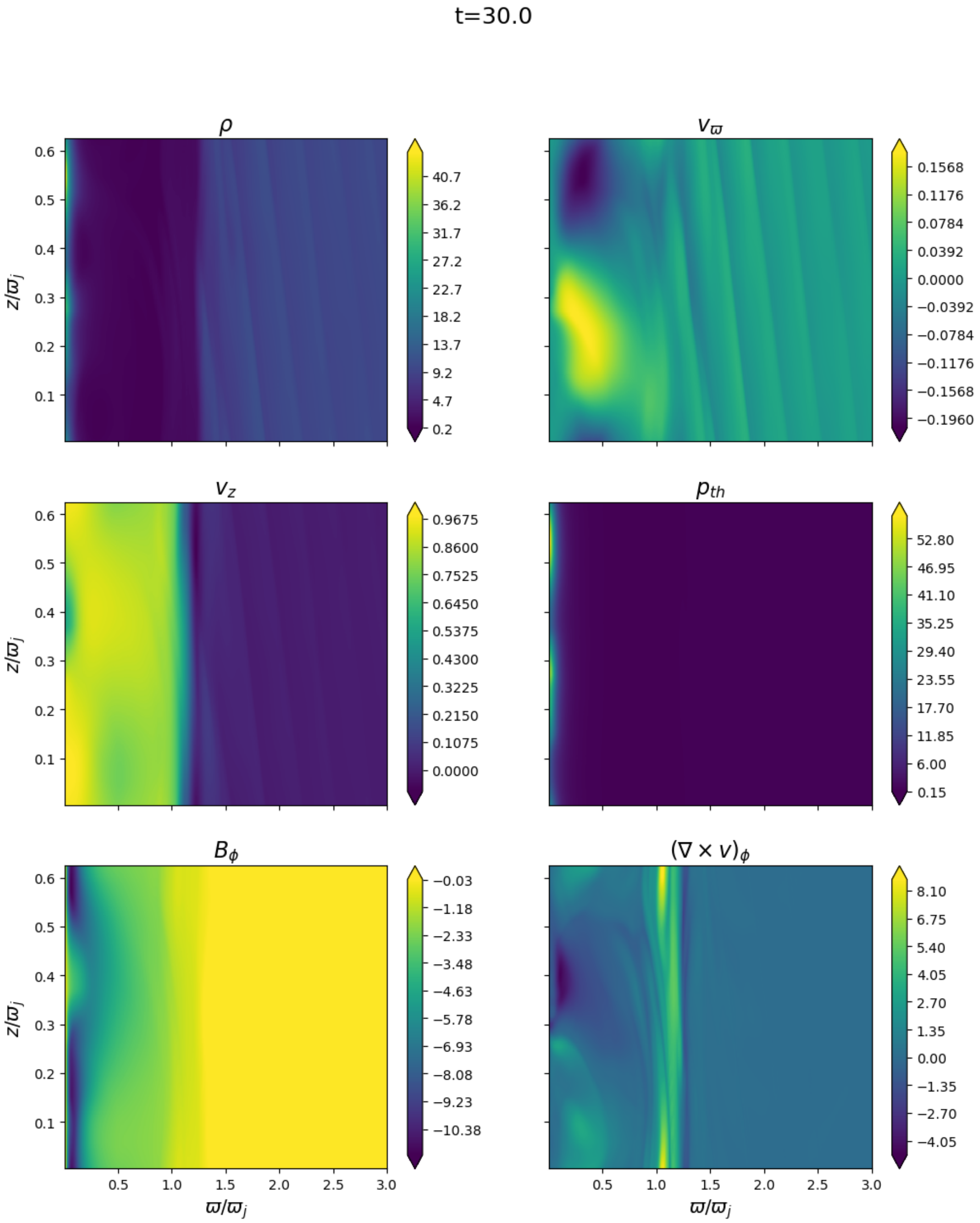

Figure 6.25: Contour plots for jet including a thermal pressure component when $k = 10$. Top row and from left to right proper density and V_ϖ are shown. In middle row V_z and thermal pressure are shown. Bottom row in the same order B_ϕ and the ϕ-component of the vorticity are shown respectively.

velocity components present a transition from positive to negative V_ϖ value and from high to small value for V_z. This is indicative of local rotational movement. If this is combined with the density profile, then the emergence of a rotating vortex is noted. The V_z also remains relativistic and shows a smooth profile for the entirety of the jet if the region of the vortex is excluded.

The magnetic field preserves its large scale, the minimum is located near its initial position. Near the start/end of the box the minimum B_ϕ (purple colored strip) bends outwards and shows sign of diffusion. The near zero-valued magnetic field oval shaped spot at $\varpi \approx 0.5$, coincides with the center of the vortex. This region has emptied of matter, thus the magnetic field also diminishes. Finally, the vorticity in the vicinity of the vortex indicates strong clockwise rotation. On the boundary of the jet there is a positive vorticity strip, probably created by the intense gradient of V_z, $\partial_\varpi V_z$.

Finally, in Fig. 6.27 the final jet state is presented. The jet has not evolved considerably in comparison to the jet state at $t = 252$. The vortex and the effect it has on the outflow are apparent (V_ϖ and V_z characteristic patterns, zero B_ϕ spot, vorticity pattern). The jet seems to have entered a new quasi-steady state at least since $t = 252$.

Figure 6.28 shows cross section plots for the quantities of interest for different z valued levels. The black solid lines represents the mean quantity profile of these slices. For most quantities the mean profile is a good proxy for the quantities' distribution across the jet. Figure 6.29 depicts the mean quantity profiles for $t = 0$ and $t = 500$. The jet has not expanded at the same rate as the configurations in sections 6.1 and 6.2. The jet is separated by the environment by a steep change in both the density and V_z profiles. The density also peaks near the jet axis, while its value is comparable to the respective initial value for the rest of the jet. The minimum in the mean profile at $\varpi \sim 0.3$ indicates the size of the vortex.

For the V_ϖ it is more appropriate to focus solely on the corresponding plot in figure 6.28 as the mean profile can not properly indicate the rotation of the vortex. This local movement is grasped appropriately by the range of the maximum values in V_ϖ profiles observed for the different z levels. In the region $\varpi > \varpi_j$ the pattern implies outgoing waves of diminishing amplitude as radius increases. The jet has accelerated slightly near its axis and has decelerated in a similar fashion for the rest of its radius. The environment has accelerated to a non-relativistic velocity near the interface of the two media and remains static for larger radii.

The thermal pressure profile for both time instances preserves its maximum on the axis of the outflow, while the value of the maximum has decreased. The magnetic field retains its large scale configuration, the quantity's amplitude has decreased (the absolute value) and the magnetic field has expanded following the jet's expansion.

Figure 6.30 provides the expansion of the jet's boundary versus the time, similarly to Figs. 6.7 and 6.19. There are two expansion phases, the first one which includes the linear phase, the transition to the non-linear phase and the early non-linear regime for $t \lesssim 100$. The rest of the simulation is characterized by a single expansion phase for which the jet radius does not change significantly. In total the jet radius increases from $\varpi_j = 1$

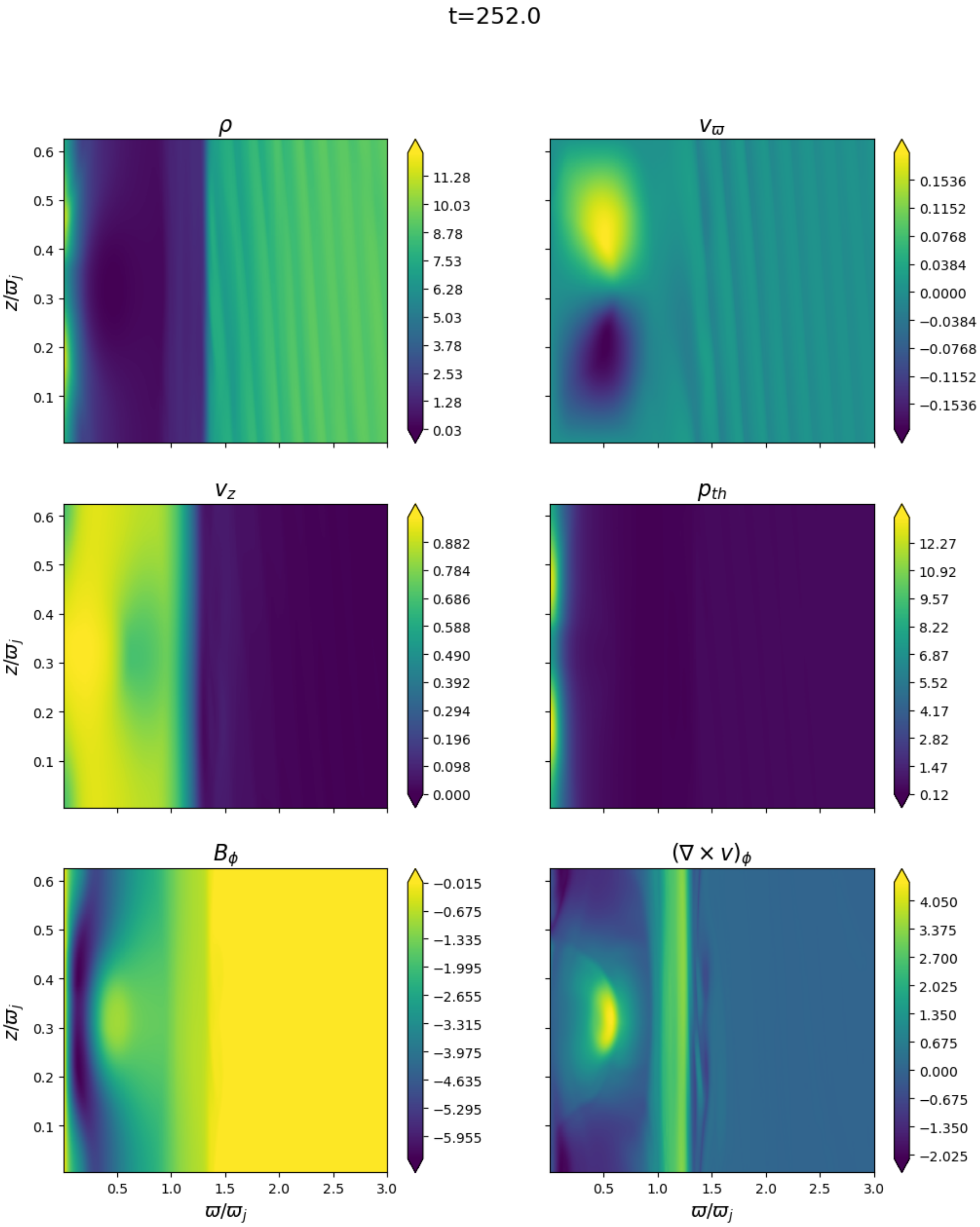

Figure 6.26: Similar to figure 6.25 for $t = 252$.

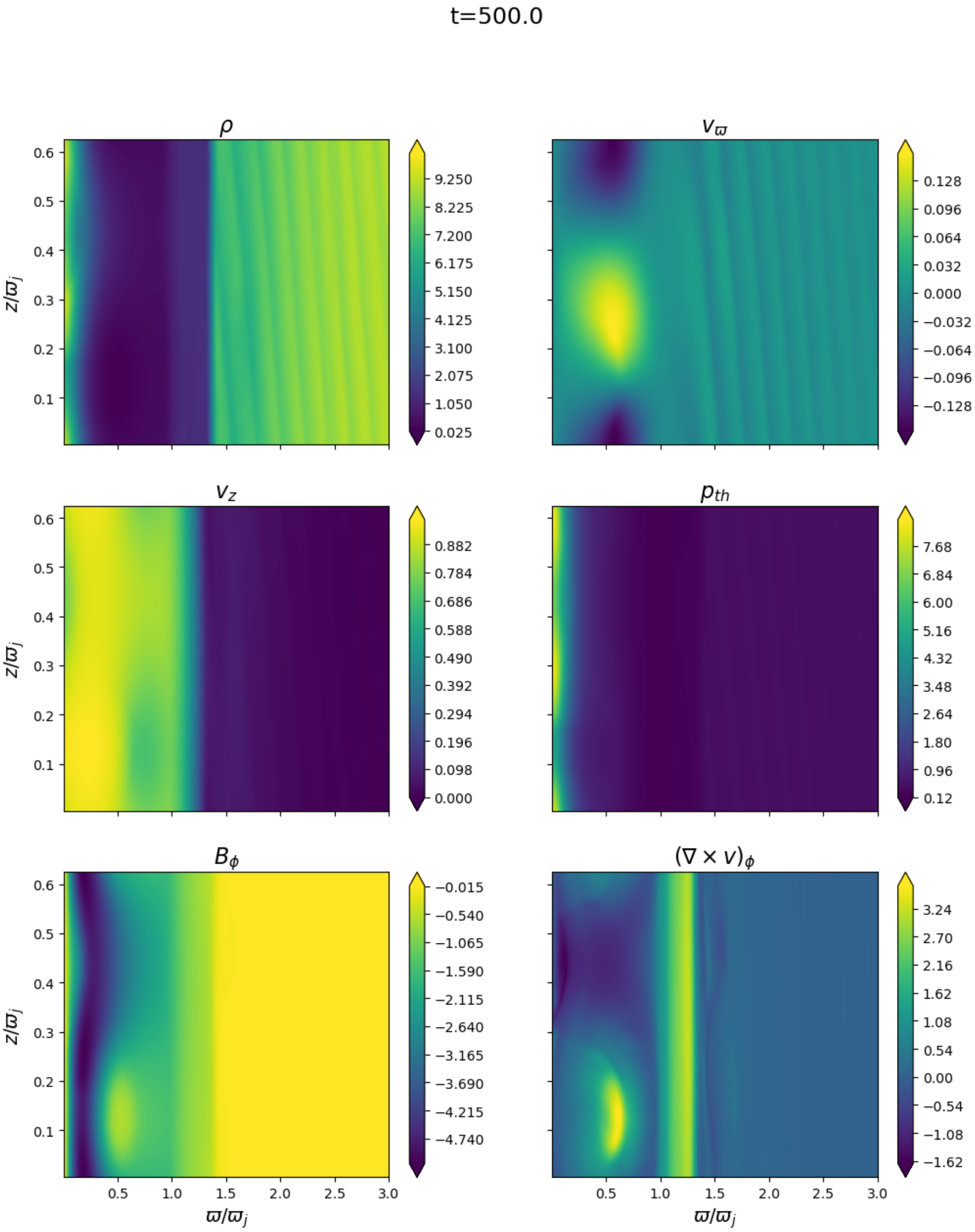

Figure 6.27: Similar to figure 6.25 for $t = 500$.

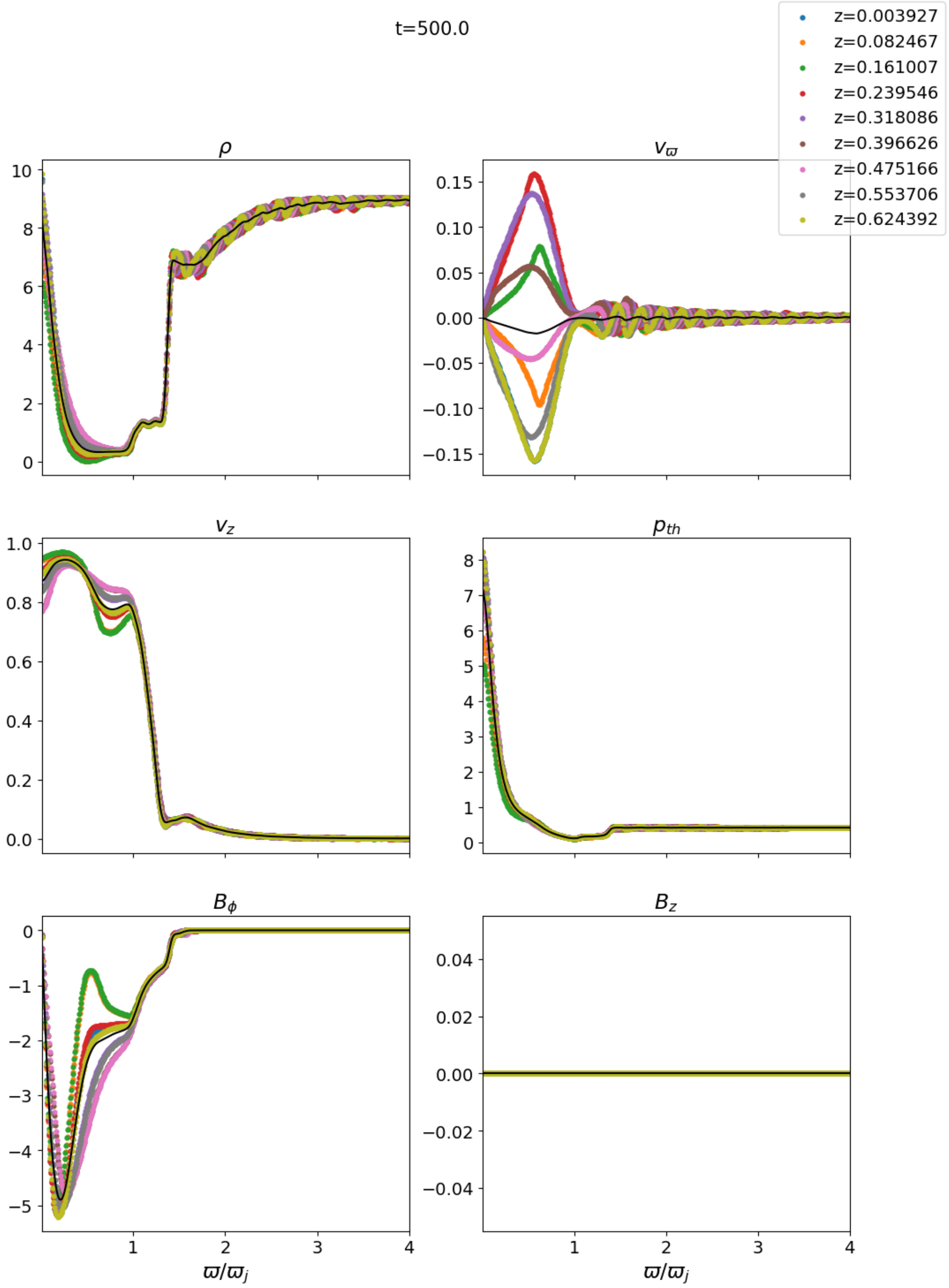

Figure 6.28: Cross section plot for jet physical quantities for different z value slices. Top row and from left to right there is the proper density and V_ϖ. Middle row V_z and the thermal pressure are depicted. Bottom row in the same order there is B_ϕ and B_z. Black line represents the mean quantity value of the jet slices.

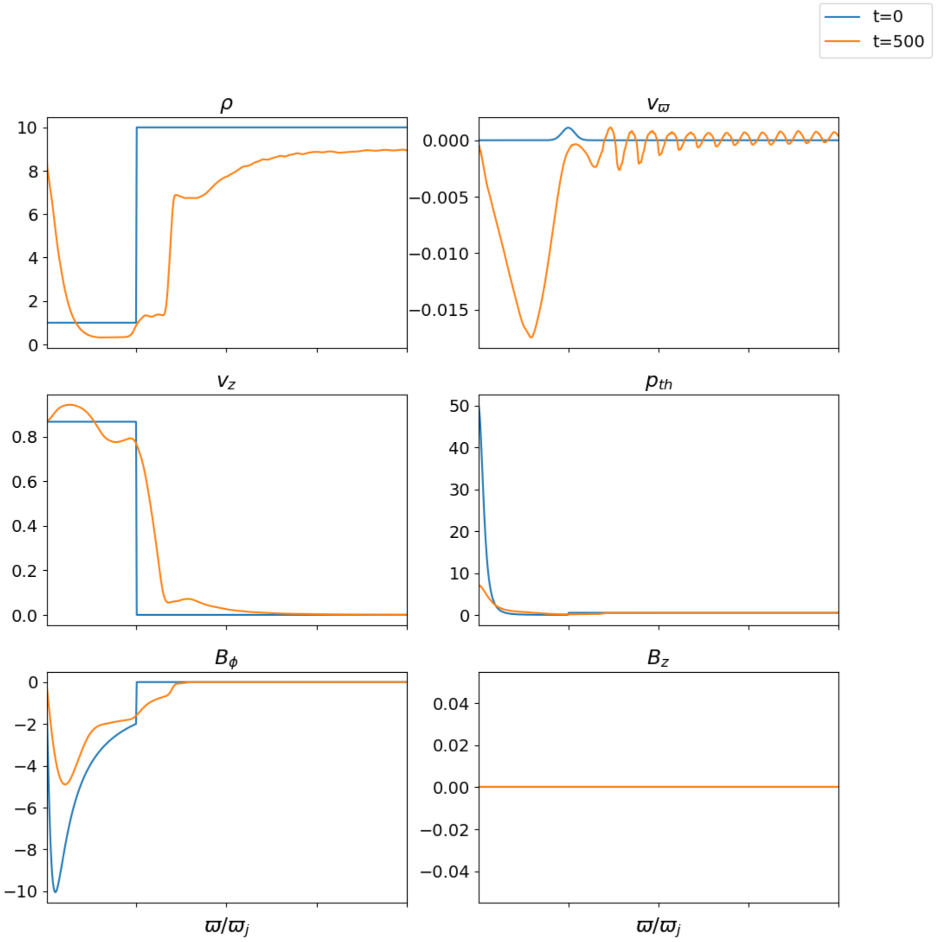

Figure 6.29: Mean profiles for the thermal jet physical quantities when $k = 10$ with respect to the slices along the jet for the z values presented in figure 6.28. The blue and orange lines correspond to $t = 0$ and $t = 500$ respectively.

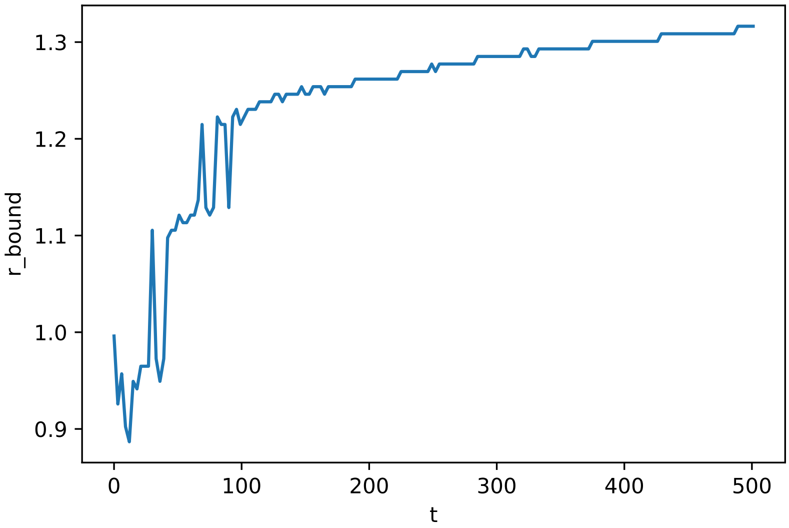

Figure 6.30: Jet boundary evolution versus time for the jet having a thermal pressure component and $k = 10$. The boundary is defined as the most outward cell of the mean density profile having $\rho_0 \leq 1.5$.

to $\varpi_j \approx 1.3$. It should be noted that up until $t \approx 100$ the inner vortex of the jet is forming, while for $t \gtrsim 100$ the vortex has settled to a state similar to the state that is observed for $t = 500$.

The expansion of the boundary versus the time could be translated into expansion of the boundary versus the distance traveled by the jet after the onset of the instability. This calculation comes with two caveats. The first one roots in the way the instability is triggered. The perturbed equations are analyzed into Fourier parts with respect to ϕ, z and t. This means that the entirety of the jet is perturbed, so strictly talking the jet expands uniformly due to the evolution of the various instabilities. The second caveat is the final magnetosonic Mach number (essentially the jet velocity is c), as the translation of the time into the distance traveled requires the jet to be super-fast magnetosonic. In this case the frozen pulse approximation is valid and the flow evolution is time-independent. The super-fast magnetosonic criterion is valid only for the configuration of section 6.3 until $t = 500$. For the two other simulations the jet eventually becomes sub-fast.

Nonetheless, if the simulation box is assumed to be an initial local perturbation which follows the jet flow, then the expansion of the jet boundary can be expressed in terms of the propagation distance. This distance is calculated by assuming that the velocity does not change substantially between two consecutive time instances, which is $\Delta t = 3$ crossing times. In Fig. 6.31 the jet boundary expansion is plotted against the distance traveled by the flow since the initiation of the instability. The plot also includes the symmetrical counterpart of the boundary with respect to the jet axis, so the plot resembles the evolution of the jet's entire cross section.

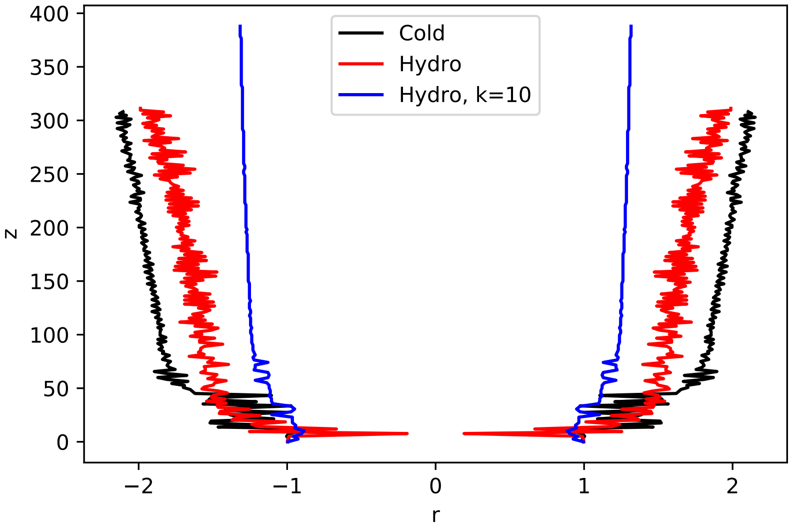

Figure 6.31: Jet boundary evolution versus distance traveled for the flow. Black, red and blue lines represent the results for cold jet, jet with thermal pressure component included and finally jet with thermal pressure component and $k = 10$.

The plot reveals different jet profiles for the different jet configurations. The cold jet widens the most, followed by the jet with the thermal pressure component and the configuration that remains most focused is the jet with the thermal pressure component and $k = 10$. This plot clearly indicates that the non-linear evolution of the Kelvin-Helmholtz instability can alter the jet's ridge line profiles, while preserving a large scale magnetized relativistic outflow.

Figure 6.32 shows the fast magnetosonic Mach number for $t = 500$. The plot for $t = 0$ is identical to Fig. 6.20. The jet presents a sub-fast region near the outflow boundary. The rest of the jet is super-fast, this result is similar to the corresponding result of section 6.2. We remind that the entire jet at $t = 500$ had become sub-fast, a significant difference between the cold jet and a jet with a thermal pressure component.

Figure 6.33 presents the evolution of the jet energy with time, similarly to figures 6.10 and 6.22. In figure 6.34 the plot focuses on the $t \leq 20$ range, hence the linear phase and the transition into the non-linear regime is resolved. The linear phase has already ended for $t = 5$ and the transition into the non-linear phase takes place. The equipartition between mass and electromagnetic energies per time occurs at $t \approx 10$. The total energy per time for the whole range of figure 6.34 remains constant.

The plots in figure 6.33 seem to consist of two phases. One until $t = 100$ and the other for $t > 100$ until the end of the simulation. This transition once more correlates with the formation of the large scale vortex inside the flow. Around $t \approx 100$ the phase of the vortex formation ends, the flow feature takes its form and settles at the position at which it is observed until the end of the simulation. The mass energy per time increases at

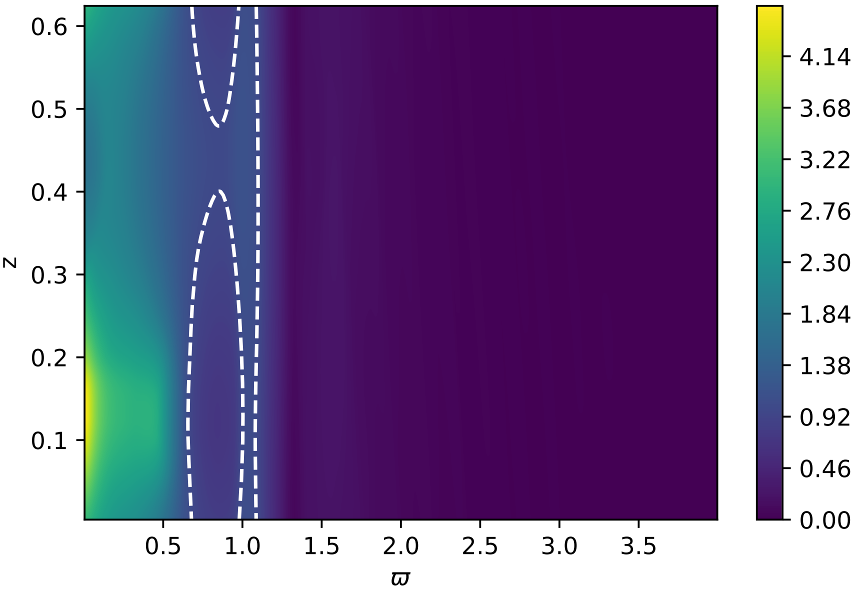

Figure 6.32: Contour plot of fast magnetosonic Mach number for jet with thermal pressure and $k = 10$. White dashed line represent the $M_{\text{fast}} = 1$.

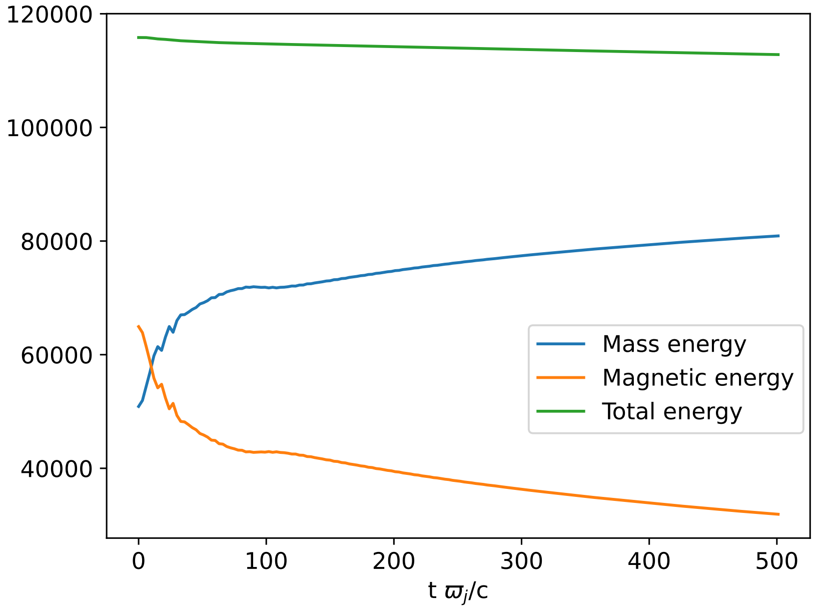

Figure 6.33: Time dependence of jet's energies per time for thermal jet when $k = 10$. Blue, orange and green colored lines represent the mass, magnetic and total energy per time.

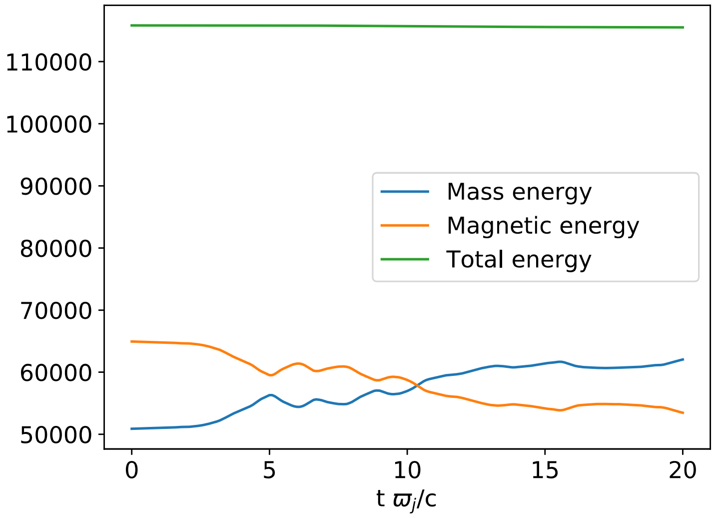

Figure 6.34: Similar to figure 6.33 for $t \leq 20$.

the expense of the electromagnetic counterpart. This energy transformation seems to be perfect and no substantial power losses towards the environment are noticed. This could be verified from the total energy per time, which decreases over time, the loss rate is subtle and the quantity is almost preserved.

Figure 6.35 shows cross sections of the jet for various z values regarding the energy fluxes. Both type of fluxes present their maxima in the vicinity of the axis. The Poynting flux essentially diminishes at $\varpi \approx 1.5$. The local minimum inside the jet for the green and orange dots is caused by the vortex as $B_\phi \to 0$ at its center. The mass flux energy drops towards the jet boundary. In the immediate vicinity of the boundary surface the flux decreases rapidly. The environment has non-zero flux near the jet boundary. This flux is transferred from the jet, but it does not propagate towards greater distances.

6.4 Summary and Discussion

A series of numerical simulations were conducted in order to study the non-linear evolution of the Kelvin-Helmholtz mode. The simulations assumed initial jet configurations that are identical to the unperturbed jet configurations from chapter 5. Thus, there are simulations for both a cold jet and a jet with a thermal pressure component. The radial component of the velocity field is perturbed using a localized Gaussian centered on the boundary of the jet (6.1). The wavevector of the initial perturbation is $k = \pi$, meaning that the corresponding wavelength is equal to the jet's diameter. Finally, an extra case is considered for the jet with a thermal pressure component and wavenumber value of $k = 10$.

The first key result is that all the simulations preserve well-defined and structured

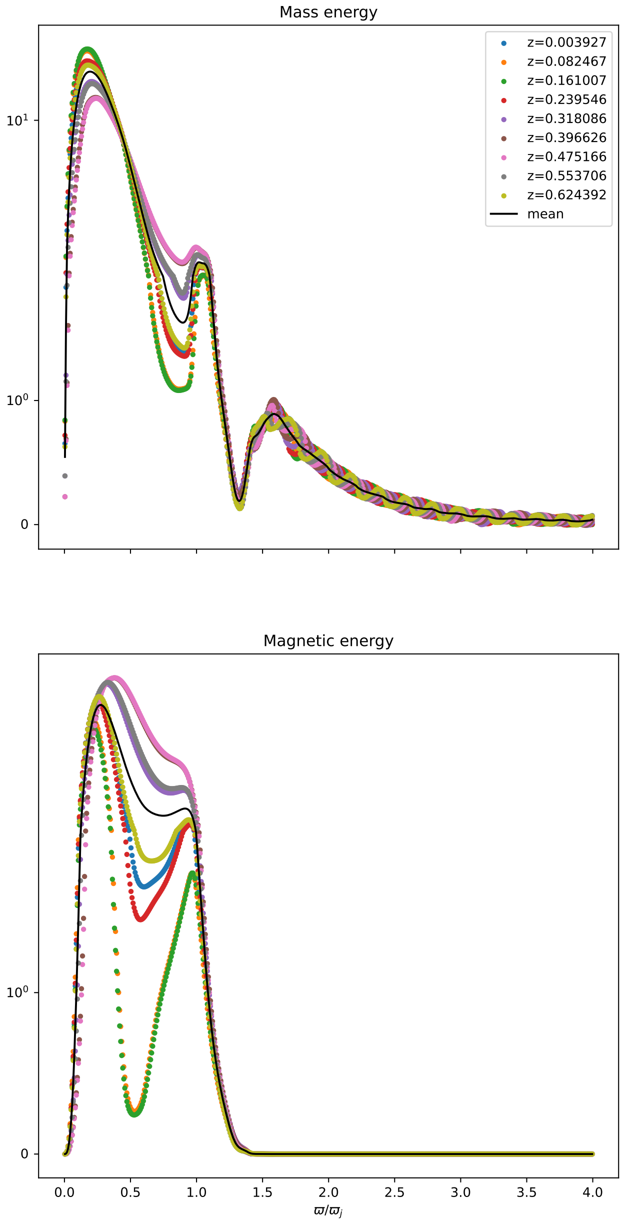

Figure 6.35: Cross section plot for the mass and Poynting energy fluxes when $k = 10$. Top and bottom plot shows mass and Poynting energy flux respectively. Colored dots represent different z level slices while the black line is their mean value profile.

outflows until the end of their run. The stopping time $t = 500$ crossing times is well within the non-linear regime of the mode for every case considered. As a reminder, the growth time of the Kelvin-Helmholtz mode for these configurations is ≈ 6.8 crossing times for both the cold and the thermal jet. This means that the simulation stopping time is approximately $\times 70$ the growth rate. For the thermal jet when $k = 10$ the $\mathrm{Im}(\omega) \approx 2$, the growth timescale is ≈ 2.3 crossing times. The simulation stopping time over the growth timescale is even greater, approximately $\times 217$. Thus, for every simulation considered in this chapter there is provided enough time to ensure that the non-linear regime is established and evolved properly. It should be noted that the simulations verify the growth timescales provided by the linear stability analysis.

In terms of jet morphology the simulations suggest that the the initial configurations transform into two component outflows. There is a core followed by a layer which ensures that the quantities are connected via a continuous and smooth transition layer from the core towards the environment. These layers are characterized by gradients for the various physical quantities, hence the initial step discontinuities on the boundary of the jet are replaced by these smooth transitioning layers. Similar results have also emerged from kinetic type simulations, such as in Sironi et al. (2021). These models are widely known in the literature as spine-sheath jets.

The simulations phenomenology is associated with the existence of vortices in the flow, which are verified for all three simulations. These flow features in the case of the cold configuration are present until $t \approx 100$, while for the thermal jets are active until the end of the simulation. They are created near the boundary of the jet and they can remain there or transition to other parts of the outflow. Primarily they mix matter in the region in which they are active. On the jet boundary they mix or at least initiate the mixing of the environment with the jet. Their number can vary and there can be more than one at the same time present in the outflow.

The cold configuration decelerates and eventually becomes sub-fast, while the velocity is ≈ 0.6. The environment near the boundary has been accelerated to a non-relativistic velocity of ~ 0.1. The thermal jet showcases a narrow strip where the jet preserves the initial V_z value. Then for the rest of the outflow until the transition layer the velocity profile decreases gradually, the sheath shows a slightly different rate of change for V_z compared to the spine. The portion of the environment that is adjacent to the boundary of the jet is also accelerated to a non-relativistic velocity, similarly to the cold jet. Finally, the results of the thermal jet with $k = 10$ are substantially differentiated compared to the fiducial thermal configuration counterparts. The spine-sheath components are clearly distinguished regarding every physical quantity. The rate of transition between the two media (spine-environment) is high. The velocity for the jet core remains highly relativistic, portion of the core has even accelerated. The majority of the jet is super-fast magnetosonic, contrary to the other two simulations.

The magnetic fields for every simulation preserve their large scale, and for the cold case preserve their spiral geometry. In general the intensity of the magnetic field diminishes over time. This means that the jets become less magnetized. Also, the magnetic fields follow the expansion of the jet (the magnetic field lines are frozen to the plasma), which explains a portion of the fields' intensity decrease. Nonetheless, the survival of large scale magnetic fields to such distances (300-500 pc) is something that can be verified by observations such as polarization surveys on jets (e.g. see Gabuzda et al., 2014a; Lisakov et al., 2021).

The simulations also provide how the jet expansion rate depends on time. The three simulations show different number of expansion stages and different expansion rates per stage. The rate seems to depend on the jet configuration (cold/thermal) and the wavenumber value. The smallest expansion is noted for the thermal jet with $k = 10$. Next is the thermal jet followed by the cold counterpart. Most interestingly, when the secular dependence is translated to distance measured from the point of the instability's onset, then the profile of the jet's boundary surface with distance is provided, $\varpi(z)$. All of the simulations yield change in the profile of the jet, yet the outflows still remain collimated. This transition in the profile of $\varpi(z)$ is crucial, as it is observed for a number of outflows. Possible mechanisms are the transition of jets through media of different physical traits, for example such transition can occur at the Bondi radius of the host galaxy, as in M87 (e.g. see Nakamura et al., 2018). Also, a sudden change in the intrinsic configuration of the jet is also proposed, the existence of shocks in the flow could cause this kind of modulation in jets physical quantities. These simulations indicate that Kelvin-Helmholtz instability could also be a probable mechanism for this kind of transition regarding the jet's profile.

The evolution of the energy against the time were calculated. All three simulations show conversion of electromagnetic to mass energy per time. The rate of conversion seems to be associated with the existence of vortices in the outflow. Especially for the cold jet the conversion rate, which consists of three phases, is mainly affected by the vortex of the flow. When the vortex is assimilated by the flow the rate changes significantly, while for the configurations for which the vortices do not dissipate the conversion consist of two phases. The first phase is always related to the linear phase of the instability and the transition to the non-linear regime. The next phases dwell in the non-linear regime and they also depend on the existence of these vortices.

Chapter 7

Generalizing the Kelvin-Helmholtz instability

The aim of this chapter is to study the behavior of the Kelvin-Helmholtz mode in a cylindrical jet when the jump in the velocity value is not situated on the boundary of the jet. In addition to the position of the velocity transition, the width of this transition can also be studied as an extra parameter. This transition can be translated to a specific width in which the velocity profile changes, thus the effect of this width on the Kelvin-Helmholtz mode can be probed.

In order to modify the velocity profile, a generalized logistic function for the Lorentz factor is introduced:

$$\gamma(\varpi) = \gamma_b + \frac{\gamma_a - \gamma_b}{1 + e^{\mu(\varpi - \varpi_1)}} \, . \tag{7.1}$$

This function generates a sigmoid curve, which can be manipulated by four parameters. γ_a, γ_b are the Lorentz factor values on the axis and the boundary of the jet. Throughout this chapter the values for these two parameters are fixed to $\gamma_a = 2$ and $\gamma_b = 1$. Essentially, the velocity discontinuity is transferred from the boundary to the interior of the jet. This creates a portion of the jet moving with $\gamma = 2$ followed by a static jet component which is followed by a static environment. ϖ_1 is the radius at which the transition occurs, this sigmoid is centered around this point. Finally, μ controls the rate of transition. As the value of μ increases the transition becomes steeper, this is showcased in Fig. 7.1.

The width of the transition region can be approximately calculated. The derivative of the Lorentz factor is given by:

$$\frac{d\gamma}{d\varpi} = -(\gamma_a - \gamma_b) \frac{\mu e^{\mu(\varpi - \varpi_1)}}{\left[1 + e^{\mu(\varpi - \varpi_1)}\right]^2} \, . \tag{7.2}$$

The derivative is negative due to the decrease in the velocity profile. $-C$ is an arbitrary

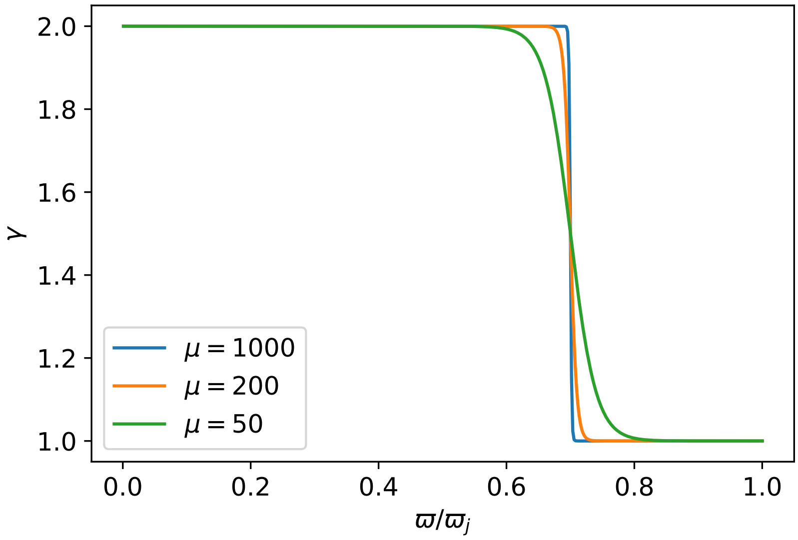

Figure 7.1: Lorentz factor profile when equation (7.1) is adopted. The parameters are set to $\gamma_a = 2,\ \gamma_b = 1,\ \varpi_1 = 0.7$. The blue, orange and green line represent $\mu = 1000,\ 200,\ 50$ respectively.

threshold, such that any point of the derivative with value below this threshold belongs to the transition layer, $d\gamma/d\varpi \le -C$. If $y \equiv e^{\mu(\varpi-\varpi_1)}$ then the layer boundaries are provided by:

$$\begin{aligned} \frac{y}{1+y^2} &= \frac{C}{\mu(\gamma_a-\gamma_b)} \Rightarrow \\ \nu y^2 + (2\nu-1)y + \nu &= 0\,, \end{aligned} \tag{7.3}$$

where $\nu = C/(\mu(\gamma_a - \gamma_b))$. The solutions of equation (7.3) are:

$$y = \frac{1-2\nu \pm \sqrt{1-4\nu}}{2\nu}\,. \tag{7.4}$$

In general $\nu \ll 1$ as $\gamma_a - \gamma_b \sim 1$ and $C \ll \mu$. The last inequality holds as the threshold is chosen to be a small portion of the μ parameter, thus $\sqrt{1-4\nu} \approx 1 - 2\nu - 2\nu^2$ if terms up to second order are kept. Then the solutions are:

$$y \approx \nu, \text{ positive root,} \tag{7.5}$$

$$y \approx \frac{1-2\nu}{\nu}, \text{ negative root} \tag{7.6}$$

If equations (7.5) & (7.6) are combined with the definitions of y and ν:

$$\varpi_+ \approx \varpi_1 + \frac{1}{\mu}\ln\left(\frac{C}{\mu(\gamma_a-\gamma_b)}\right), \text{ positive root,} \tag{7.7}$$

$$\varpi_- \approx \varpi_1 - \frac{1}{\mu}\left[\ln\left(\frac{C}{\mu(\gamma_a-\gamma_b)}\right) - 2\frac{C}{\mu(\gamma_a-\gamma_b)}\right], \text{ negative root}\,. \tag{7.8}$$

The negative root takes this form as $\ln(1-2\nu) \approx -2\nu$. From equations (7.7) and (7.8) the width of the transition layer can be calculated as $\left|\Delta\varpi\right| = \left|\varpi_+ - \varpi_-\right|$. The relation is given by:

$$\Delta\varpi = \frac{2}{\mu}\left(\ln C + \frac{C}{\mu(\gamma_a-\gamma_b)}\right)\,. \tag{7.9}$$

Equation (7.9) indicates that as $\mu \to \infty \Rightarrow \Delta\varpi \to 0$, thus when the Lorentz factor profile tends to become a step function then the width becomes zero. Also, when $\mu \to 0$ there is no transition and $\Delta\varpi \to \infty$. Throughout this chapter the value of C equals to 1% of the minimum value of the derivative, $C = 0.01\left|(d\gamma/d\varpi)_{max} - (d\gamma/d\varpi)_{min}\right| \approx 0.01\left|(d\gamma/d\varpi)_{min}\right|$.

The configurations used for the linear stability analysis are the same as those used in chapter 5. There are two configurations, the first one is a cold jet with both poloidal and toroidal components for the magnetic field and the second one , the thermal jet, has $B_z = 0$ and a thermal pressure component included. As was discussed above the main task is to study and observe if and in what degree the results are affected when the discontinuity in the velocity profile is not located on the boundary of the jet but at some radius $\varpi_1 < \varpi_j$. Also, it is tested whether the profile of the transition, or equivalently the value of μ, affects the instability profile. Finally, the profile of the jet's density is also altered. A sigmoid function is also adopted:

$$\rho_0(\varpi) = \rho_{0,b} + \frac{\rho_{0,a} - \rho_{0,b}}{1 + e^{\mu_\rho(\varpi-\varpi_1)}} \tag{7.10}$$

where $\rho_{0,a}$, $\rho_{0,b}$ are the density values on the axis and boundary of the jet and μ_ρ is the parameter controlling the rate of transition for the density profile.

The parametric study that follows assumes a fiducial configuration with $\mu = 1000$, $\varpi_1 = 0.7$, $\gamma_a = 2$, $\gamma_b = 1$ and constant density $\rho_0 = 1$. The rest of the parameters are identical to the configuration of the jet in chapter 5. Essentially, the jet configuration is identical to the respective configuration in section 5.1, apart from the Lorentz factor profile. As a reminder, both a hydrodynamic and a magnetized environment are considered and the ratio of the environment's density value over the jet's density value is $\eta = 10$. In the case of varying density profile $\rho_e = \eta\rho_{0,b}$.

7.1 Cold jet

The first configuration to be examined is the cold outflow, which was studied in 5.2.1. The results presented from this point on wards are numerical, as the WKBJ approximation requires the Lorentz factor to be constant. In figure 7.2 dispersion plots of the Kelvin-Helmholtz mode are shown for various values of the μ parameter. The solid and dashed lines represent the real and the imaginary part of ω respectively. For the fiducial setup (red solution) the $\mathrm{Im}(\omega)$ showcases linear relation with k for both $k \ll 1$ and $k \gg 1$ regimes respectively. For the high k values the Kelvin-Helmholtz behavior observed in chapter 5 is also present here. The solution does not terminate via cut-off at $k \sim 1$ but continues towards smaller wavenumbers.

As μ decreases the solution loses the linear dependence of $\mathrm{Im}(\omega)$ on k. For the high k range the $\mathrm{Im}(\omega)$ line becomes concave, thus there is the emergence of a maximum $\mathrm{Im}(\omega)$ at some specific k and then the quantity decreases as the wavenumber further increases. The linear dependence for $k \ll 1$ still exists, while a local minimum in the vicinity of $k \approx 0.45$ is enhanced as μ decreases. For $\mu = 100,\ 50$ the instability exists for $0.5 \lesssim k \lesssim 20$, the small wavenumbers have been stabilized. This is also observed for the high values of k, for which there is an upper valued cut-off. The Kelvin-Helmholtz mode is stabilized for a wide range of the wavevector values as the transition layer widens. It should be noted that for $\mu = 10^3 \Rightarrow \Delta\varpi = 0.014$ and for $\mu = 50 \Rightarrow \Delta\varpi = 0.21$. This means that for $\mu = 10^3$ the transition is effectively behaving as a step function due to the fact that $\Delta\varpi/\varpi_j \sim 1\%$. The $\mathrm{Im}(\omega)$ is $\gtrsim 1$ when $k \gtrsim 10 - 15$ for the same μ value. For $\mu = 50$ the maximum $\mathrm{Im}(\omega)$ is ≈ 1 for $k \approx 9$, thus the instability still has growth timescales compared to the jet's radius light crossing time.

In figure 7.3 the transition is transferred towards a smaller radius, $\varpi_1 = 0.3$. This way the effect of the transition's position inside the outflow is examined. The general behavior of the KH mode regarding the value of μ is similar to figure 7.2. For high μ values the solutions span over the whole k range, the linearity holds for $k \gg 10$ and $k \ll 1$. When μ decreases the instability for the high wavenumber values alter and the $\mathrm{Im}(\omega)$ line becomes concave, i.e. for $\mu = 50$ there is a cutoff at $k \approx 20$. At $k \approx 0.6$ there is a local minimum which is enhanced as μ decreases, meaning that the solutions probably are stabilized for $k \lesssim 0.6$ for even smaller μ values. In order to verify this, an extra value for μ is added. With brown color the solution represents the configuration with $\mu = 35$. For this parameter value the solution has also a cutoff at $k \approx 1$.

The $\mathrm{Im}(\omega)$ observed in Figures 7.2 and 7.3 are comparable. For high μ and $k \gtrsim 10$ the $\mathrm{Im}(\omega) \gtrsim 1$. As μ decreases the respective maximum values also decrease, thus for $\mu = 50$ the mode has been stabilized for $k \gtrsim 20$ and the maximum $\mathrm{Im}(\omega) \approx 0.66$ at $k \approx 10$. Obviously, for $\mu = 50$ the maximum $\mathrm{Im}(\omega)$ is smaller for the configuration with $\varpi_1 = 0.3$ than the value corresponding to the fiducial counterpart.

In Figure 7.4 the dependence of the Kelvin-Helmholtz mode on the different η values is assessed. The blue line corresponds to the fiducial case. First of all, the dispersion relations for $\eta = 0.1,\ 1$ almost coincide. Both modes are stabilized through a cut-off at $k \approx 0.6$, while the $\mathrm{Im}(\omega) \propto k$ when $k \gtrsim 3$. The blue colored mode extends over the whole

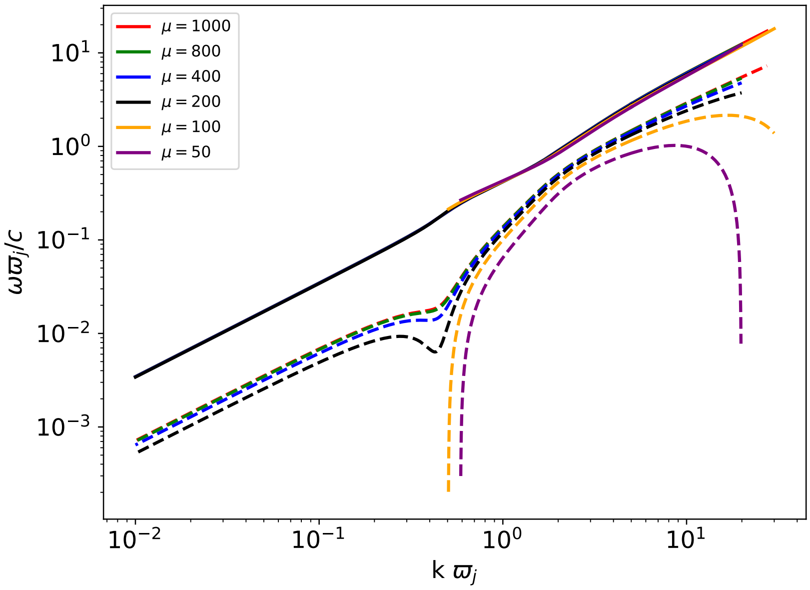

Figure 7.2: Dispersion relation plot for configurations with different μ values. Solid and dashed lines represent real and imaginary part of ω respectively.

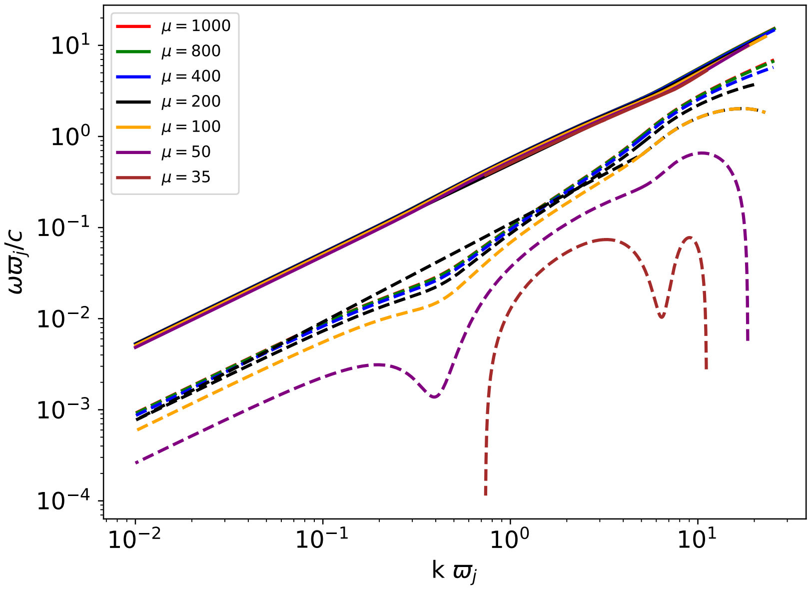

Figure 7.3: Dispersion relation plot for configurations with different μ values and $\varpi_1 = 0.3$. Solid and dashed lines represent real and imaginary part of ω respectively.

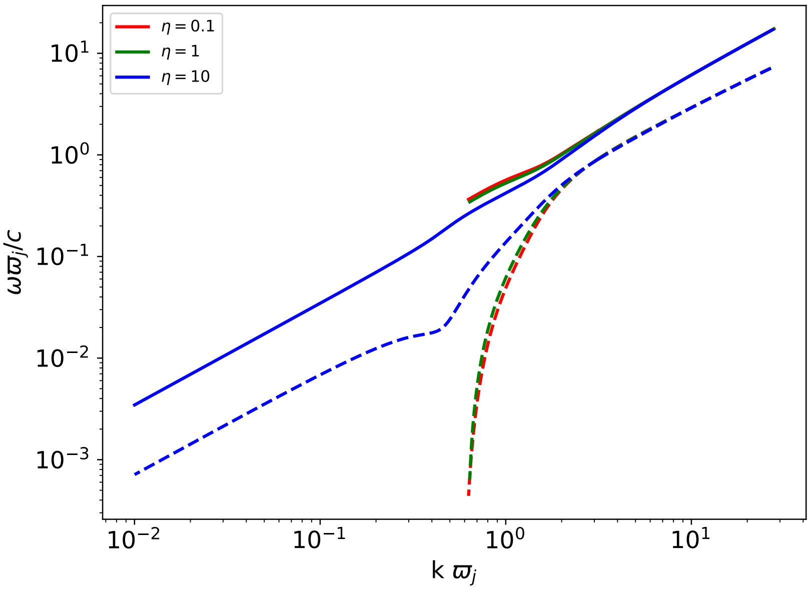

Figure 7.4: Dispersion relation plot for different environment density values. Blue line correspond to the fiducial case, while red and green line correspond to $\eta = 0.1,\ 1$ respectively.

k range, and converges with the other two solutions for $k \gtrsim 3$. This indicates that the Kelvin-Helmholtz mode is not affected by the value of the η parameter for large enough wavenumbers, this conclusion does not hold as k decreases.

Next, the profile of the jet's density is taken into consideration in Fig. 7.5. The fiducial configuration is still used, the only alteration is introduced to the density profile by adopting equation (7.10). The parameters are chosen to be equal to $\rho_{0,a} = 1$, $\rho_{0,b} = 10$ and $\mu_\rho \in \{50, 100, 200, 400, 800, 1000\}$. The density ratio parameter still remains $\eta = 10$, thus $\rho_e/\rho_{0,a} = 100$. Both the Lorentz factor and the density profile change in the vicinity of ϖ_1.

The solutions, in general, are stabilized via a cutoff at $k \sim 1$. The linear profile for $\mathrm{Im}(\omega)$ holds for $\mu_\rho = 10^3$, as the parameter value decreases the dashed lines become concave, thus the instability is resolved. Nonetheless, the modes with small μ_ρ do not present a cutoff at high k values, at least for $k \lesssim 30$. The change in μ_ρ value does not affect the instability behavior with the same severity as the change in the Lorentz factor profile does. The different solutions of Fig. 7.5 behave similarly despite the broad range of the μ_ρ parameter.

It is worth mentioning that the most unstable mode is provided for the constant density profile. In figure 7.6 the $\mathrm{Im}(\omega)$ versus the wavenumber is plotted for two different density profiles. The constant profile with $\mu = 10^3$ is drawn with black dashed lines and the varying profile is plotted in red dashed lines, the latter mode has $\mu = 10^3,\ \mu_\rho = 10^3$. The constant profile provides the most unstable mode, even though the two solutions become

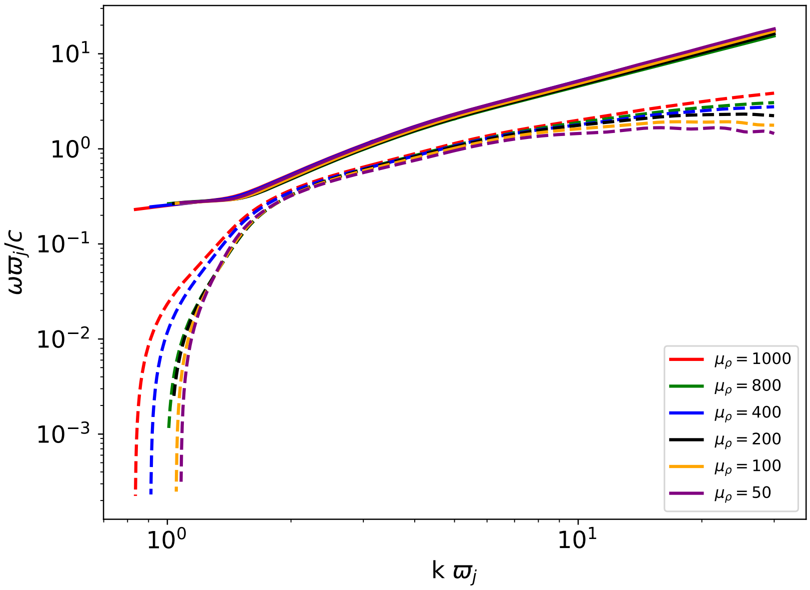

Figure 7.5: Dispersion relation plot for different values of μ_ρ density profiles. Solid lines represent Re(ω) while dashed lines represent Im(ω).

similar for $k \gtrsim 3$. This observed convergence for the modes loosens as μ_ρ decreases as it is observed in figure 7.5, hence the modes with varying density and wider transition layers regarding the density profile are farther distanced from the black solution.

In figure 7.7 the two extreme cases in terms of the μ and μ_ρ parameters are compared. The first configuration has in both the Lorentz factor and the density profile a steep transition with $\mu = 10^3$, $\mu_\rho = 10^3$. The second one has $\mu = 50$, $\mu_\rho = 50$, hence this configuration has the widest possible transition layers. The red colored solution clearly is a more unstable mode compared to the green colored counterpart. The first solution exists for $k \gtrsim 0.8$ and the other for $1.5 \lesssim k \lesssim 13$, therefore the span of the red colored mode is much wider than the green colored counterpart. Also, the Im(ω) of the red solution is greater compared to the corresponding values of the green mode for the wavelengths that both solutions co-exist.

In figure 7.8 the effect of the pressure providing mechanism of the environment on the stability profile is probed. The red colored mode represents a jet with a hydrodynamic environment, while the green colored counterpart represents a jet with a magnetized environment. The two solutions are comparable they essentially differ for $0.2 \lesssim k \lesssim 2$. For the rest of the wavenumber range these modes coincide and their Im(ω) is linearly dependent on k. The nature of the environment's pressure providing mechanism does not affect the behavior of the instability.

Figure 7.9 showcases dispersion relation plots for multiple values of parameter ϖ_0. The red colored solution corresponds to the fiducial configuration with $\mu = 10^3$ and $\varpi_0 = 0.1$.

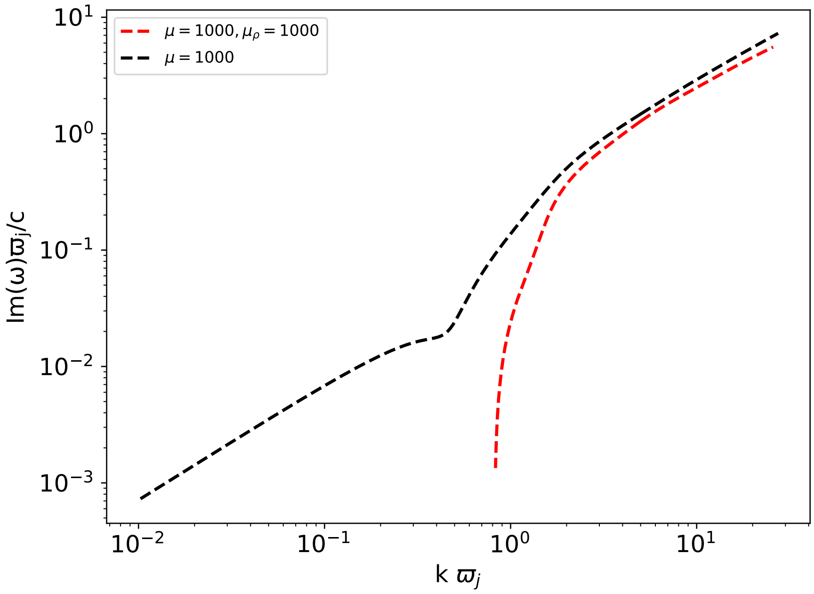

Figure 7.6: Im(ω) versus the wavenumber k for outflow configuration with constant density profile plotted in black dashed line and non constant profile in red dashed lines.

As ϖ_0 increases the $k \gg 1$ part of the solution is not heavily affected. The Im(ω) for these wavenumbers slightly decreases, while the linear dependence of Im(ω) on k is not substantially modified. Most importantly, the mode is affected when $k \ll 1$. The solutions for $\varpi_0 \geq 0.2$ are stabilized for $k \lesssim 1$ through the formation of a cutoff. The exact wavenumber for which the stabilization occurs depends on the ϖ_0 value, in general this threshold is of the order of $k \sim 1$.

Similarly to figure 7.9, figure 7.10 showcases dispersion relation plots of the cold configuration for varying value of parameter ϖ_0 when $\mu = 100$. The red colored solution corresponds to $\mu = 100$ and $\varpi_0 = 0.1$ case. The variation in the value of ϖ_0 affects the wavenumber at which the cutoff is observed. An increase in ϖ_0 also increases the threshold value. In particular, for $\varpi_0 = 0.1 \rightarrow k \approx 0.5$ while for $\varpi_0 = 0.5 \rightarrow k \approx 4$. Moreover, the respective cutoff at large k shifts towards smaller wavenumbers. This leads to a single unstable region for $\varpi_0 = 0.5$ which is limited to $3.5 \lesssim k \lesssim 25$.

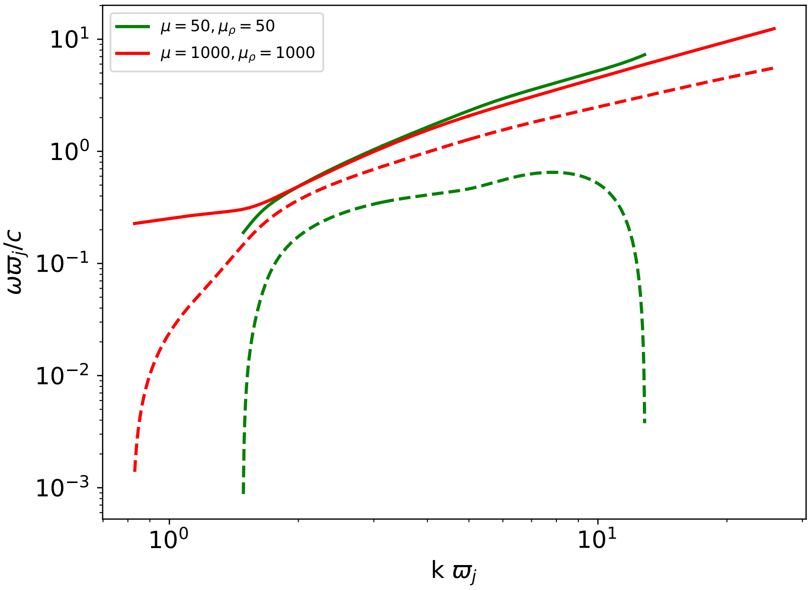

Figure 7.7: Dispersion relation plot for the two extreme cases with $(\mu, \mu_\rho) = (10^3, 10^3)$, $(50, 50)$. The first set of parameters impose steep change on the profiles for the Lorentz factor and the density and is represented by the red colored dispersion line. The second one has the widest transition layers considered for both quantities and is represented by the green colored counterpart.

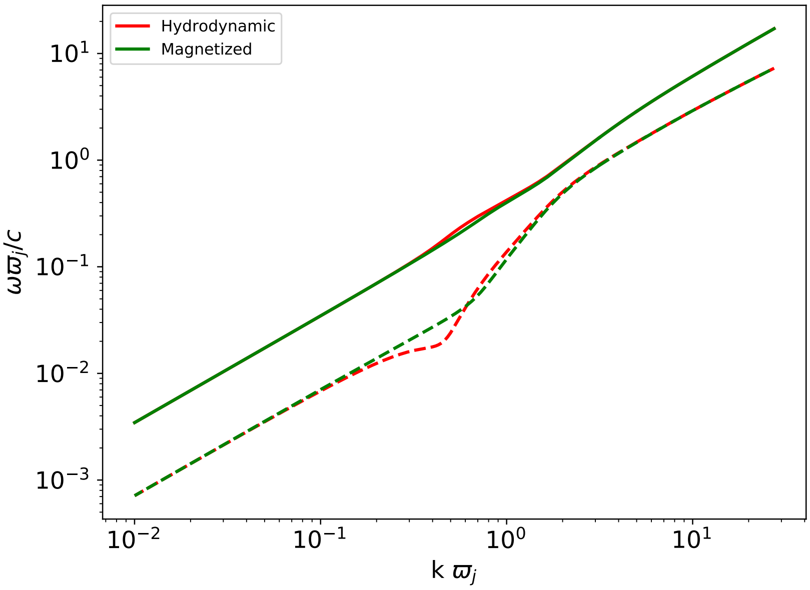

Figure 7.8: Dispersion relation plot for the fiducial case for a hydrodynamic and a magnetized environment. Hydrodynamic environment is denoted by the red colored solution while the magnetized counterpart is green colored.

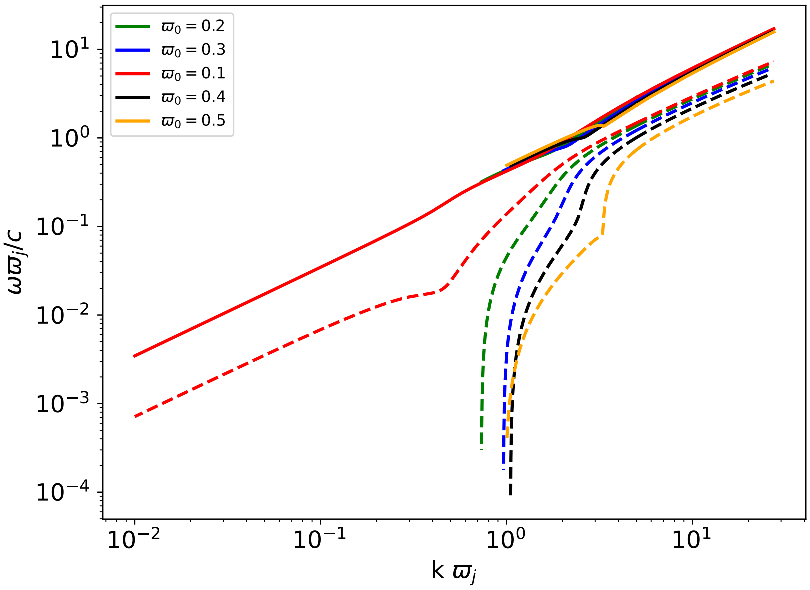

Figure 7.9: Dispersion relation plots for the cold configuration versus multiple ϖ_0 values. Solid lines represent $\mathrm{Re}(\omega)$ and dashed lines represent $\mathrm{Im}(\omega)$. Red colored solution represents the $\mu = 10^3$ and $\varpi_0 = 0.1$ fiducial case.

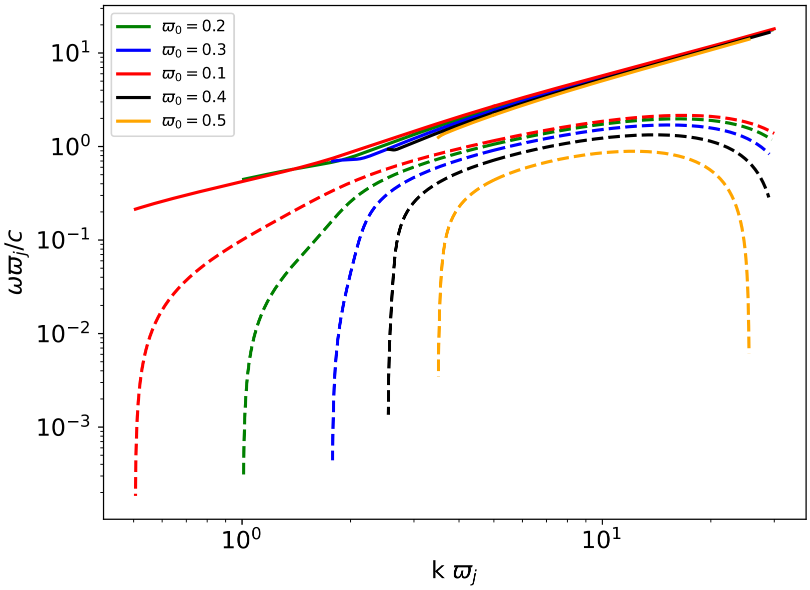

Figure 7.10: Dispersion relation plots for the cold configuration versus multiple ϖ_0 values for $\mu = 100$. Solid lines represent $\mathrm{Re}(\omega)$ and dashed lines represent $\mathrm{Im}(\omega)$. Red colored solution is represents the $\mu = 100$ and $\varpi_0 = 0.1$ case.

7.2 Thermal jet

The second configuration is a jet where a thermal pressure component is introduced assuming $P = B_z^2/2$ and then setting $B_z = 0$, similarly to section 5.2.2. The aim is to investigate if the results of section 7.1 are modified by the existence of a thermal pressure component in the outflow. The fiducial configuration assumes a steep transition at $\varpi_1 = 0.7$ with $\mu = 10^3$, constant density profile $\rho_0 = 1$ and $\eta = 10$, similarly to the fiducial case of the cold jet. The configuration of this section is referred to as "thermal" for the rest of this section.

Figure 7.11 shows dispersion relation for various values of the μ parameter, similarly to figure 7.2 for the cold jet. The solid and dashed lines represent $\mathrm{Re}(\omega)$ and $\mathrm{Im}(\omega)$ respectively. For $k \lesssim 0.3$ the $\mathrm{Im}(\omega)$ showcases a linear dependence on k. This trait also exists for $k \gtrsim 10$ only for the configurations with $\mu = 10^3, 800$. As μ decreases the $\mathrm{Im}(\omega)$ lines become concave and the instability is resolved and the maximum of $\mathrm{Im}(\omega)$ shifts towards smaller wavenumbers. For small enough μ values the mode is stabilized via a cutoff for the large k, as indicated by the yellow and purple colored modes, i.e. for $\mu = 100, 50$ respectively. The maximum $\mathrm{Im}(\omega)$ for the $\mu = 50$ case is ≈ 1, thus the mode's growth time remain comparable to the jet's radius light crossing time.

Figure 7.12 shows the dispersion relation when $\varpi_1 = 0.3$. The differences between this figure and figure 7.11 are small. The linearity for $k \gg 1$ does not hold as μ decreases.

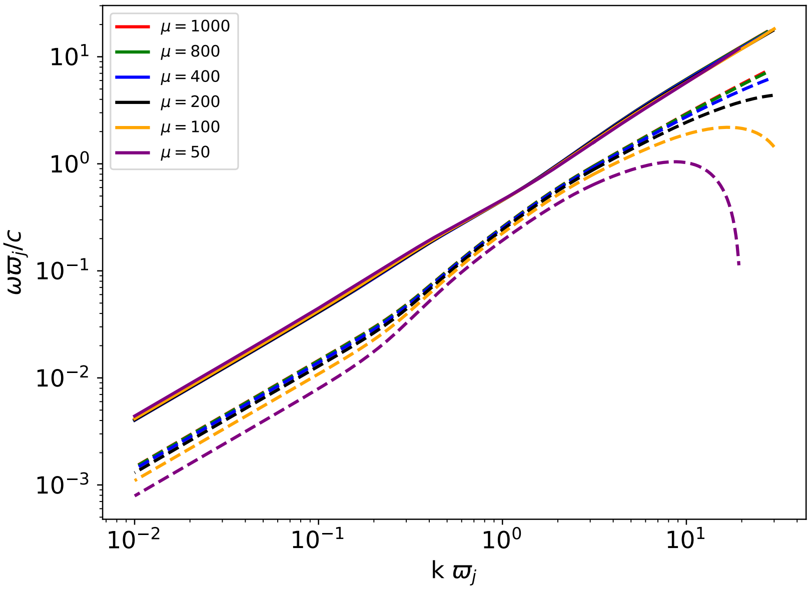

Figure 7.11: Dispersion relation plot for configurations with different μ values for thermal jet. Solid and dashed lines represent real and imaginary part of ω respectively.

The dashed lines become concave for bigger $\Delta\varpi$ and the maximum $\mathrm{Im}(\omega)$ shifts towards smaller k as μ lessens. The values of the $\mathrm{Im}(\omega)$ for each μ value between figures 7.11 & 7.12 are comparable. Essentially, for the thermal jet the value of ϖ_1 does not seem to affect the Kelvin-Helmholtz mode.

In order to emphasize on this conclusion in figure 7.13 the $\mathrm{Im}(\omega)$ versus the wavenumber are displayed. Red and blue solutions depict jets with $\mu = 10^3, 50$ respectively. The dashed lines represent modes linked to $\varpi_1 = 0.3$ configurations and dash-dotted lines to $\varpi_1 = 0.7$ counterparts. The proximity of the $\mathrm{Im}(\omega)$ lines for each μ case is obvious. The lines converge even more as the wavenumber increases. This plot clearly displays that in the case of the thermal jet the ϖ_1 value affects weakly the mode's behavior.

Figure 7.14 displays the dispersion relation for multiple η values. This figure indicates that neither the density ratio affects the behavior of the Kelvin-Helmholtz instability. The change in η mostly differentiates the solution in the range of $k \sim 1$. For $k \lesssim 0.2$ and $k \gtrsim 2$ the solutions coincide and they are linearly dependent on the wavenumber. Thus, the mode is weakly associated to the value of η.

Next, the density profile is modified, an increase is introduced at $\varpi_1 = 0.7$. The density function is given by equation (7.10). The parameters are set to $\rho_{0,a} = 1$, $\rho_{0,b} = 10$, while $\mu_\rho \in \{50, 100, 200, 400, 800, 1000\}$. The rest of the configuration is the same as the fiducial setup. Figure 7.15 shows the dispersion relation for multiple μ_ρ values. Most interestingly, the whole set of solutions are nearly identical. Slight differentiation among the modes is noticed for $k \ll 1$ and $k \gg 1$. Nonetheless, the effect is minimal and the

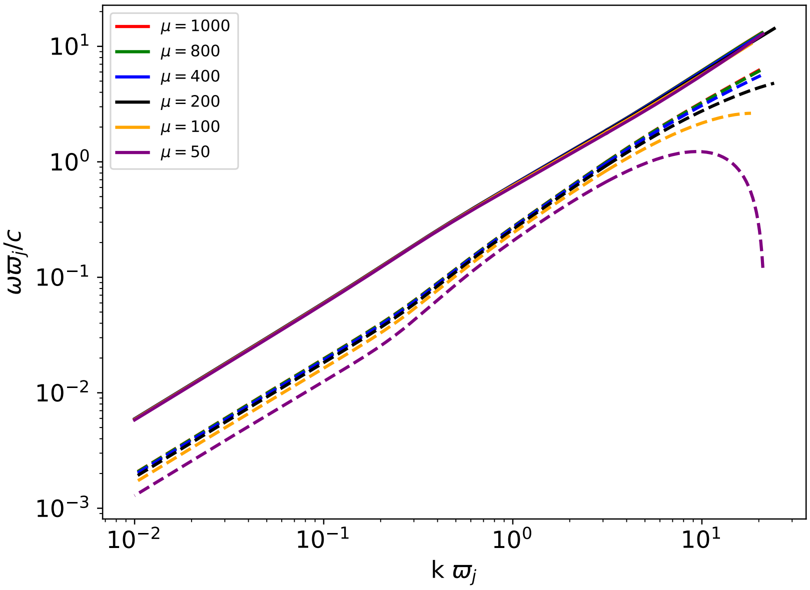

Figure 7.12: Dispersion relation plot for configurations with different μ values and $\varpi_1 = 0.3$ for a thermal jet. Solid and dashed lines represent real and imaginary part of ω respectively.

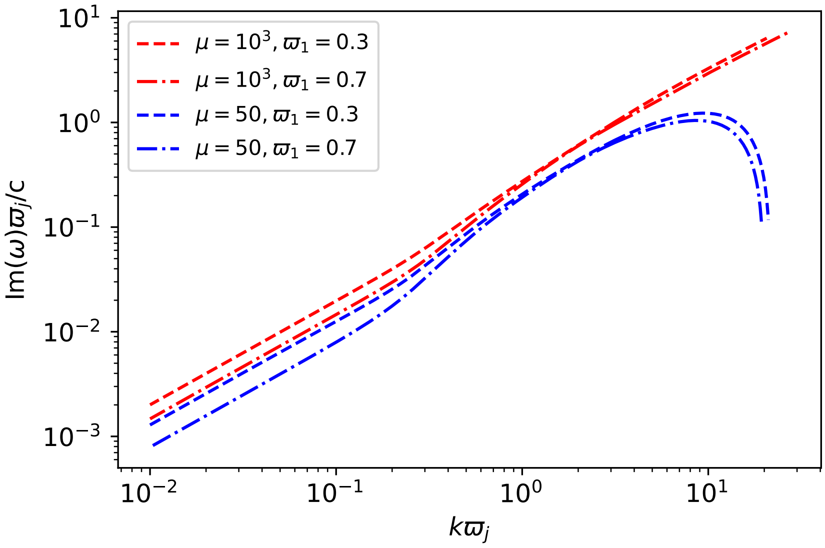

Figure 7.13: Imaginary part of ω versus the wavenumber. Red lines represent modes for configurations with $\mu = 10^3$ and blue lines represent the counterparts with $\mu = 50$. Dashed and dash-dotted lines display configurations with $\varpi_1 = 0.3,\ 0.7$ respectively.

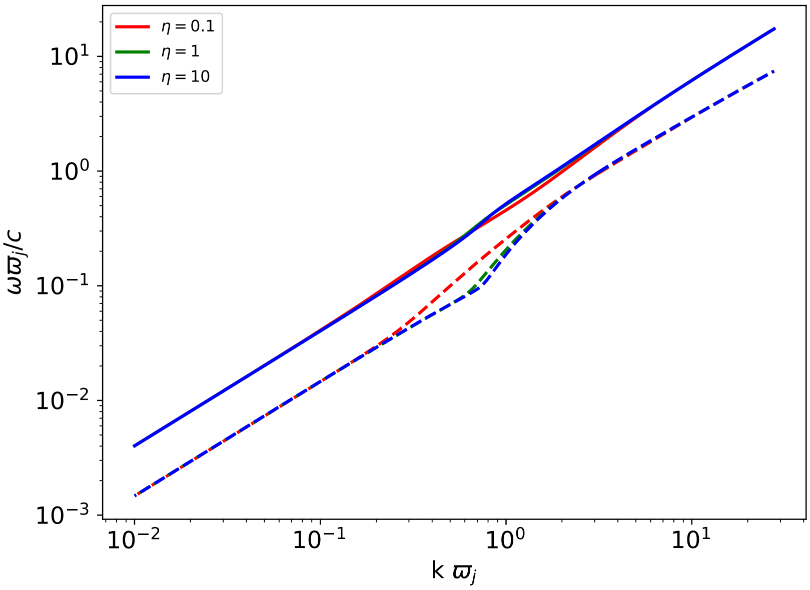

Figure 7.14: Dispersion relation plot for different environment density values for a thermal jet. Blue line correspond to the fiducial case, while red and green line correspond to $\eta = 0.1,\ 1$ respectively.

variation of μ_ρ is insignificant to the Kelvin-Helmholtz mode.

Figure 7.16 depicts the $\mathrm{Im}(\omega)$ versus the wavenumber for two solutions. The first one has constant density profile and it is plotted with black dashed line while the configuration with varied density profile with red dashed line. The result is similar to the corresponding result of figure 7.6. The jet with constant density profile is more unstable than the non-constant counterpart. Even though the two solutions converge for $k \gtrsim 0.2$, the constant density model for the whole k range has greater $\mathrm{Im}(\omega)$ values.

Figure 7.17, similar to figure 7.7, depicts the two extreme cases with $(\mu, \mu_\rho) = (10^3, 10^3)$ (red colored mode) and $(\mu, \mu_\rho) = (50, 50)$ (green colored mode). The green colored mode is terminated via a cutoff at $k \approx 10$ while the red colored counterpart exhibits the linear relation $\mathrm{Im}(\omega) \propto k$. Both solutions are comparable for $0.04 \lesssim k \lesssim 1$ and they are moderately differentiated for $k \lesssim 0.04$. The maximum value of the imaginary part for the ω is ≈ 0.66 at $k \approx 7.8$. The solution still has $\mathrm{Im}(\omega) \sim 1$, thus the mode grows rapidly with the resulting timescale to be analogous to the jet's radius light crossing time. If the plots from figures 7.11 and 7.15 are also considered, then the difference in the value of μ is the main contributor for the change in the mode's behavior, rather than the change in μ_ρ.

Next, the effect of the pressure providing mechanism of the environment on the Kelvin-Helmholtz mode is explored. Figure 7.18 shows the fiducial configuration for a hydrodynamic and a megnetized environment colored in red and green respectively. The two solu-

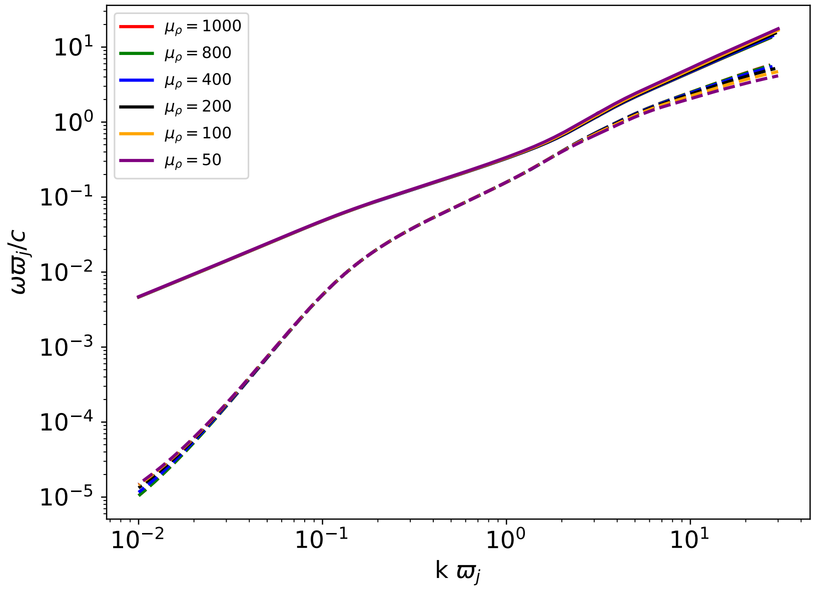

Figure 7.15: Dispersion relation plot for different values of μ_ρ for a thermal jet. Solid lines represent Re(ω) while dashed lines represent Im(ω).

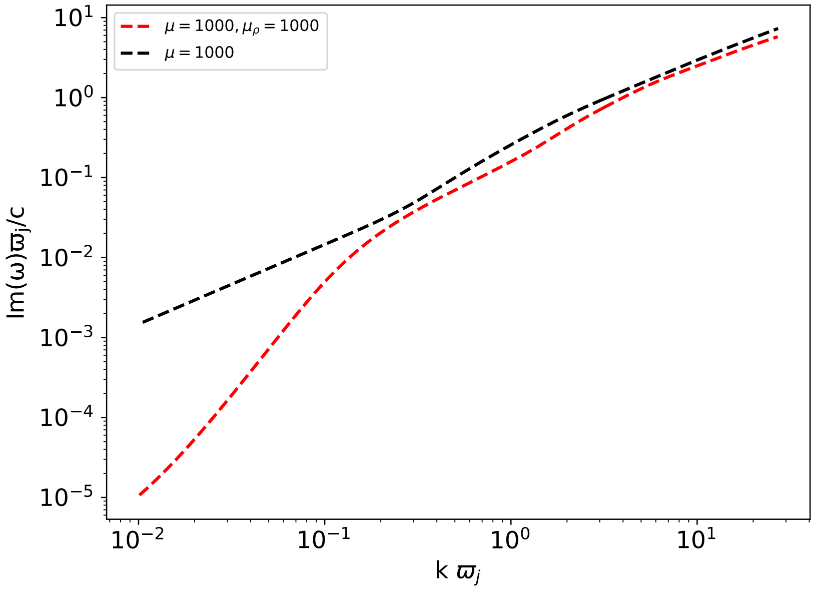

Figure 7.16: Im(ω) versus the wavenumber k for thermal outflow configuration with constant density profile plotted in black dashed line and non constant profile in red dashed lines.

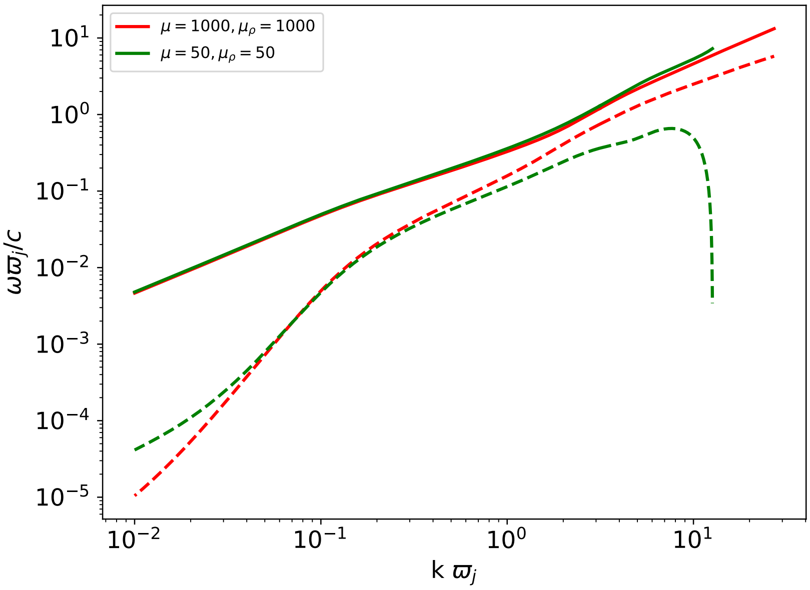

Figure 7.17: Similar to figure 7.7, dispersion relation plot for the two extreme cases with $(\mu, \mu_\rho) = (10^3, 10^3)$, $(50, 50)$ are drawn. The first set of parameters impose steep change on the profiles for the Lorentz factor and the density and is represented by the red colored dispersion line. The second one has the widest transition layers considered for both quantities and is represented by the green colored counterpart.

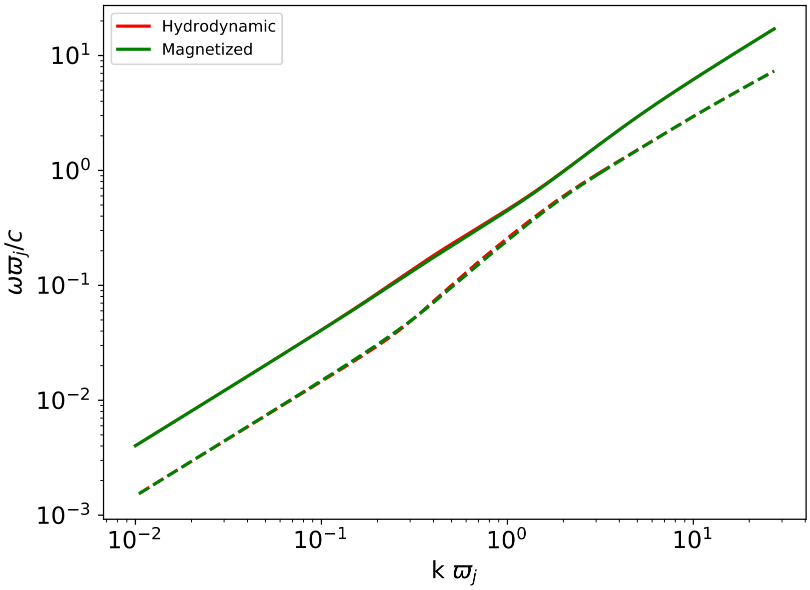

Figure 7.18: Dispersion relation plot for the fiducial case regarding a hydrodynamic and a magnetized environment for the thermal jet. Hydrodynamic environment is denoted by the red colored solution while the magnetized counterpart is green colored.

tions coincide perfectly across the whole k range. The last result indicates that the thermal jet's Kelvin-Helmholtz instability totally disregards if the environment is hydrodynamic or magnetized.

Figures 7.19 and 7.20 display dispersion relations regarding the change in the value of ϖ_0 for the thermal jet. The fiducial case in Figure 7.19 is depicted with red colored lines and has $\mu = 10^3$. Most noticeably, all the solutions converge and behave almost identically for $k \gtrsim 4$, showcasing linear dependence between $\mathrm{Im}(\omega)$ and k. As ϖ_0 increases ($\varpi_0 = 0.2,\ 0.3$) the $\mathrm{Im}(\omega)$ decreases, especially for $k \lesssim 4$. Further increase in ϖ_0 ($\varpi_0 = 0.4,\ 0.5$) creates a cutoff at $k \sim 10^{-2}$ for both solutions. Nonetheless, the value of ϖ_0 affects the small wavenumbers. It should be noticed that the separation of the $\mathrm{Im}(\omega)$ among the different modes becomes significant for $k \lesssim 1$.

Similar traits can also be observed for the solutions depicted in figure 7.20. The configuration is similar to the fiducial case apart from the value of μ, $\mu = 100$. The solutions behave similarly for $k \gtrsim 4$ and the modes are resolved as it is expected from the value assigned to μ. The modes behave differently for the small wavenumber regime as the value of ϖ_0 increases. For $k \lesssim 4$ the solutions become less unstable, as the $\mathrm{Im}(\omega)$ value decreases. The modes corresponding to $\varpi_0 = 0.2,\ 0.3$ cover the whole wavenumber range of the plot. The two modes with $\varpi_0 = 0.4,\ 0.5$ are stabilized through a cutoff at $k \approx 0.04,\ 0.06$ respectively.

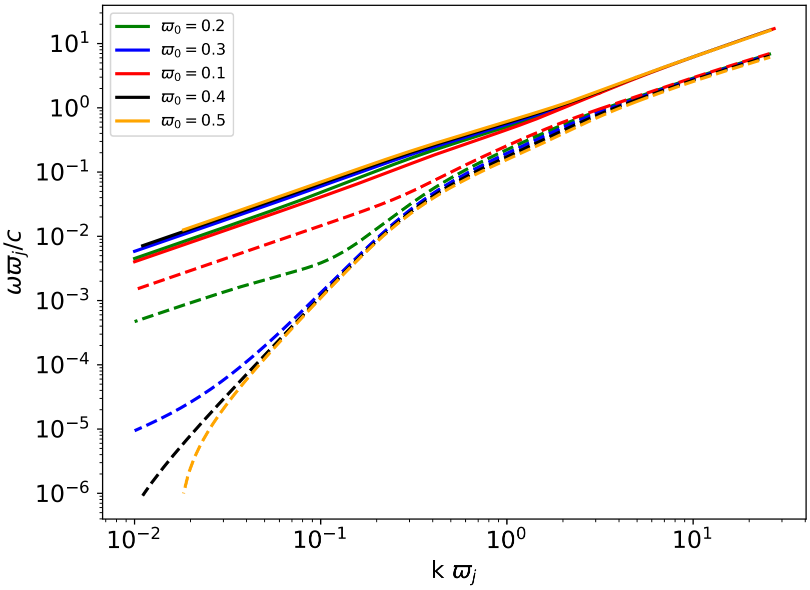

Figure 7.19: Dispersion relation plots for the cold configuration versus multiple ϖ_0 values for a thermal jet. Solid lines represent Re(ω) and dashed lines represent Im(ω). The red colored solution has $\mu = 10^3$ and $\varpi_0 = 0.1$.

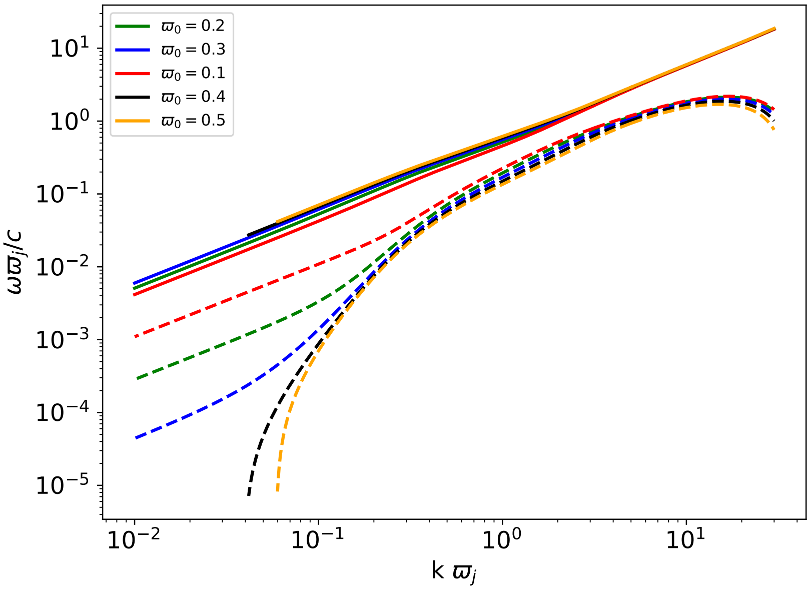

Figure 7.20: Dispersion relation plots for the cold configuration versus multiple ϖ_0 values for $\mu = 100$ and for a thermal jet. Solid lines represent Re(ω) and dashed lines represent Im(ω). The red colored solution has $\mu = 100$ and $\varpi_0 = 0.1$.

7.3 Discussion and Summary

This chapter focuses on the generalization of the Kelvin-Helmholtz mode. The task is to study the stability behavior of the mode when the velocity discontinuity is not located on the boundary of the jet, but it is repositioned at its interior at some specific radius ϖ_1. The new Lorentz factor profile is provided by a logistic equation (7.1), which smoothly transitions from the value of the Lorentz factor on the axis of the jet to the value the quantity has on the boundary. The width of the transition layer is controlled by the parameter μ in equation (7.1), thus by controlling μ it can be tested whether the rate of the transition affects the behavior of the Kelvin-Helmholtz instability.

The width of the transition layer is possibly the most important parameter as it is indicated from figures 7.2 and 7.11. The $\mu = 10^3$ is almost a discontinuous transition, as $\mu \to \infty$ is needed to formally achieve a true discontinuity. For this μ value the mode resembles the corresponding solutions observed in chapter 5, the imaginary part of ω is noted to be analogous to the wavenumber. This means that the Kelvin-Helmholtz mode does not necessarily emanates on the boundary of the outflows. The main prerequisite is for the outflow to present a velocity shear at some distance across its radius.

When the width of the layer increases the instability becomes resolved, i.e. the $\mathrm{Im}(\omega)$ ceases to be proportional to k. This means that the $\mathrm{Im}(\omega)$ values do not diverge as $k \to \infty$ and the instability affects the outflow for a specific wavenumber range. The two configurations respond differently to the decrease of μ. For the cold jet the instability initially becomes resolved for $k \gg 1$, while as μ further decreases the mode also stabilizes for the small values of the wavenumber. The mode survives for a definite range of k. In the case of the thermal jet the instability is also resolved for $k \gg 1$. Contrary to the cold counterpart, the mode is not stabilized for the small k. Thus, the existence of the B_z affects the wavelengths that are stabilized when the width of the velocity's shear layer changes. Berlok &Pfrommer (2019a) have also observed for both a 2D Cartesian configuration and a 3D cylindrical counterpart in the non-relativistic regime that the Kelvin-Helmholtz instability is resolved when $k \gg 1$ if the velocity fields of the two media are connected via a smooth transition of finite width. In their work this result is noted for a hydrodynamic outflow or a magnetized counterpart for which $\boldsymbol{B} \parallel \boldsymbol{V}$.

The radius ϖ_1 for which the transition layer is centered around affects mainly the cold configuration. The stabilized wavenumbers are mainly $k \lesssim 1$ as μ decreases noted for both figures 7.2, 7.3. The value of μ required to stabilize these wavenumbers is ~ 100 when $\varpi_1 = 0.7$. For the configuration with $\varpi_1 = 0.3$ the respective value is $\mu \sim 35$. The change in ϖ_1 does not essentially affect the results regarding the thermal jet. This result is clearly depicted in figure 7.13, where the $\mathrm{Im}(\omega)$ versus k is plotted. Dispersion relations for both configurations indicate that the value of ϖ_1 does not modify the instability behavior radically.

The value of η is vital for the cold configuration's stability properties, as it was analyzed in section 7.1. The wavenumbers $k \lesssim 0.6$ of the fiducial case are stabilized when $\eta = 0.1,\ 1$. All three solutions converge for every η value when $k \gg 1$. This result is also observed in figure 7.14, where all three solutions have converged and coincide perfectly.

The solutions of the thermal jet also coincide for $k \ll 1$, contrary to the results of the cold counterpart.

The profile of the density is examined in figures 7.5, 7.15 assuming that ρ_0 is defined by equation 7.10. For both configurations the value of the μ_ρ parameter does not affect the behavior of the mode. It could be stated that among the two outflow setups the thermal jet is the least affected. Also, for both configurations the jets with constant density profile are more unstable than their varying density counterparts. This result is also noticed for the non-relativistic configurations in Berlok &Pfrommer (2019a) where the constant density profiles are more unstable than the non-constant counterparts.

If both the velocity and the density profiles are allowed to vary, then two cases are compared. The first one incorporates step-like discontinuities with $\mu = 10^3$, $\mu_\rho = 10^3$, while the second one smooth transitions for both quantities with $\mu = 50$, $\mu_\rho = 50$. Once more, the cold configuration is mostly affected, where as the corresponding $\Delta\varpi$ increases for both quantities the mode becomes less unstable. High and small wavenumbers are stabilized and $\text{Im}(\omega)$ values decrease. B_z seems to be the decisive factor for the differences in the results of the two configurations.

The pressure providing mechanism for both jet models is not an important elements for the instability's properties. The interchange between hydrodynamic or magnetized environment does not differentiate the dispersion relations as it can be noted in figures 7.8 and 7.18. This result indicates that the existence of the magnetic field in the environment is relevant to the Kelvin-Helmholtz mode only when the transition in the velocity profile or ideally the discontinuity is situated on the jet boundary. This is evident by comparing these results with the respective results in section 5.2.

Finally, the dependence of the Kelvin-Helmholtz mode on the value of ϖ_0 is examined. For this task two values for μ are used, $\mu = 50,\ 10^3$. When $\mu = 10^3$ the $k \gg 1$ part of the solution is not greatly affected by the change in the value of ϖ_0. For the thermal jet the solutions retain their linear relation with k and tend to the same asymptotic $\text{Im}(\omega)$ value regardless of the ϖ_0 value. For the cold counterpart the different ϖ_0 solutions tend to similar values of $\text{Im}(\omega) \sim 5$. The $k \ll 1$ part of the solutions becomes more stable as ϖ_0 increases for both configurations. This result is more evident for the cold jet, as for $k \lesssim 1$ the solutions are stabilized when $\varpi_0 \geq 0.2$. The thermal counterpart becomes less unstable but not fully stabilized regarding $k \ll 1$.

When $\mu = 100$ the change in ϖ_0 value modifies both the $k \ll 1$ and $k \gg 1$ portions of the solution regarding the cold configuration. Due to the value of μ the $\text{Im}(\omega) \propto k$ property is invalid, the resolved part of the solution is affected by the value of the ϖ_0 parameter. The thermal counterpart is not being affected at the same rate, the $k \gg 1$ cutoff stays unaffected by the value of ϖ_0. The $k \ll 1$ part of the solutions is affected by the alteration in the value of ϖ_0, nonetheless the thermal jet is not substantially dependent on ϖ_0. Once again, the importance of B_z for the Kelvin-Helmholtz instability's properties when the velocity transition is located inside the jet is shown.

In general, the results indicate that the important parameters are μ, ϖ_0 and the existence of the B_z component. The cold jet, which includes B_z, is affected by changes in the values of these parameters. ϖ_0 controls the value of $B_z/\left|B_{\phi,co}\right|$ and eventually the value of $(\widehat{\boldsymbol{k},\boldsymbol{B}_{co}})$. As it was discussed in section 5.3 this angle value is crucial for the properties of Kelvin-Helmholtz mode. This is also verified from figures 7.9 and 7.10. As ϖ_0 increases the magnetic field becomes aligned with $\boldsymbol{k}$, the tension of the magnetic field increases in the direction of the mode's propagation and the instability is weakened. Also, this could partially explain the smaller $\mathrm{Im}(\omega)$ values when $\varpi_1 = 0.3$ in comparison with the results from the fiducial setup. As ϖ_1 decreases the $B_z/\left|B_{\phi,co}\right|$ ratio increases, thus the tension is also increased in the direction of $\boldsymbol{k}$. The weak dependence of the thermal jet's mode on the ϖ_0 value further validates the importance of B_z, and subsequently the $(\widehat{\boldsymbol{k},\boldsymbol{B}_{co}})$ respective value. When $B_z = 0 \rightarrow \boldsymbol{B} \perp \boldsymbol{k}$, thus the Kelvin-Helmholtz mode is not affected by the magnetic tension in the direction of $\boldsymbol{k}$. The change in ϖ_0 value is linked to the plasma β (see equation 5.6) and it seems to mainly affect the $k \ll 1$ part of the solutions.

Chapter 8

Thesis Summary

This thesis examines the stability properties of relativistic astrophysical jets. These jets are assumed to be cylindrical and they carry magnetic fields which have both a poloidal and a toroidal component in general. The dynamics of the jets are described by the RMHD system of equations. The stability properties of the outflows are examined by utilizing the linear stability analysis methodology throughout the thesis, which requires to insert small perturbative terms for every physical quantity of the RMHD set of equations, linearize with respect to these perturbative terms and solve the emerged linear system. Only unstable solutions are important for this kind of study, as these can disrupt and destabilize the initial outflow. Apart from the linear stability analysis, numerical simulations of cylindrical jets can be used to verify the results of the linear counterpart and also examine the non-linear evolution of the system.

The first model that was analyzed is a two component jet, consisting of a fast and low density spine, surrounded by a slower and denser sheath. The jet stability is examined for a variety of values for the magnetization of the outflow. It is shown that for $\sigma \leq 1$ the instabilities that prevail are of kinetic nature, while for more magnetized configurations the instabilities are enhanced (higher values for the growth rate) and are affected by the strengthened magnetic field. For every considered value for the magnetization these modes mainly manifest at the inner boundary surface between the spine and the sheath or the boundary surface of the entire jet.

In the context of $m = 1$ solutions for the most unstable modes, numerical simulations have been conducted for varying magnetization values. Both methodologies demonstrate strong consistency, as growth rates from stability analysis align with simulation results. Additionally, the linear stability analysis accurately predicts the primary destabilized regions of the jet across all considered cases, further validating its reliability.

The next model that was examined is a jet whose physical quantities are shaped by the acceleration and collimation processes occurring at the base of the outflow. Among the solutions that emerged during the stability analysis, there is one solution that exhibits growth timescales proportional to the radius light crossing time and a linear relation is observed between $\mathrm{Im}(\omega)$ and the wavenumber k. Also, this mode is found for both axisymmetric and non-axisymmetric solutions.

To study this specific mode, it is opted to use a simplified model of the previous case. The instability is also verified for this configuration and shows the $\mathrm{Im}(\omega) \geq 1$ and $\mathrm{Im}(\omega) \propto k$ traits. Further analysis indicates that the most unstable solutions are the axisymmetric, $m = 0$, thus the parametric study of the model focuses on configurations with $m = 0$.

The stability analysis examines the behavior of the solution with respect to the value of the jet's velocity, magnetization, the ratio of the density values of the jet over the environment and the ratio of the poloidal magnetic field component over the toroidal counterpart. All these quantities are measured on the boundary of the jet. Furthermore, the pressure-providing mechanism from the environment towards the jet is examined, interchanging between a purely hydrodynamic or magnetized medium.

The parametric analysis reveals two crucial factors controlling the mode's behavior. Firstly, the fast magneto-sonic Mach number: for super-fast outflows, the instability is suppressed. Additionally, when the flow velocity approaches non-relativistic values, the solution stabilizes. Secondly, the magnetic field's tension, parallel to the $\boldsymbol{k}$ direction, plays a role. As the projection of $\boldsymbol{k}$ onto the magnetic field increases, so does the tension and the instability weakens. Finally, when the environment is magnetized the instability is weakened with regards to the corresponding cases with hydrodynamic environments.

The parametric study results indicate that the analyzed solution represents the Kelvin-Helmholtz instability in cylindrical, magnetized, and relativistic outflows. Furthermore, the eigenfunctions of the system imply that the instability is confined near the jet's boundary. This characteristic is also confirmed by employing the WKBJ approach at an appropriate radius ($\varpi \approx \varpi_j$), where the method's results align well with those from the fully numerical counterpart.

The agreement of the results between the local and global solutions led to the comparison of the cylindrical Kelvin-Helmholtz instability with its Cartesian counterpart. It was shown that the Cartesian Kelvin-Helmholtz can reproduce the results of the cylindrical case as long as specific wavelengths of the system are much larger than the radius of the jet. The equivalence of the two geometries further validates the observed locality of the Kelvin-Helmholtz instability.

Simulations were used to validate the results of the linear stability analysis and examine the evolution of the instability in the non-linear regime. Initially, the growth timescales predicted by the linear analysis are also confirmed by the simulations. The part of the jet in which the instability mainly evolves is near the boundary of the jet, which is also predicted by the linear analysis of the mode. More noticeably, the Kelvin-Helmholtz mode does not entirely disrupt the outflow but reshapes it into a modified state that seems to be stable until the end of the simulation runs.

An important observation is the creation of vortices on the boundary of the jet during the initial evolution phase of the instability. These vortices initiate the mixing of the two media in contact and results to energy export from the jet towards its surroundings.

Ultimately, the environment near the separating surface is accelerated to non-relativistic velocities.

The simulated jets typically decelerate and expand radially, preserving their large scale magnetic field structure. In cases with an initially helicoid magnetic field, the final structure maintains a similar topology. Notably, shearing layers develop for velocity and density profiles near the jet's radius, resembling sheaths around the inner components. This leads to a spine-sheath structure for the jet.

The expansion of the jet's boundary indicates a change in the width of the outflow and subsequently to its profile. The rate of this change can be associated with the existence of an active vortex on the boundary of the jet. Energy-wise the Poynting flux of the is transformed into mass energy flux. It should be emphasized that as k increases, the evolution of the instability may be contained in a narrow layer near the boundary of the jet. The enhanced locality of the mode due to the higher value of k can also affect the non-linear evolution of the outflow.

Finally, the discontinuity in the velocity profile was moved from the boundary of the jet to some specific distance inside the outflow. Moreover, it was examined which is the effect on the stability profile if shear is introduced in the velocity and density profiles. Due to the shearing of the velocity profile the Kelvin-Helmholtz mode was resolved, leading to a modified $\mathrm{Im}(\omega) \propto k$ and a fading instability for large k. The density shear had a less prominent stabilizing impact. The key factor controlling the solution's behavior remains the angle between $\boldsymbol{k}$ and $\boldsymbol{B}$, and the setup of the environment does not essentially affect the instability's properties.

Bibliography

Appl S., Lery T., Baty H., 2000, A&A, 355, 818

Barniol Duran R., Tchekhovskoy A., Giannios D., 2017, MNRAS, 469, 4957

Begelman M. C., 1998, ApJ, 493, 291

Berlok T., Pfrommer C., 2019a, MNRAS, 485, 908

Berlok T., Pfrommer C., 2019b, MNRAS, 489, 3368

Blandford R. D., Payne D. G., 1982, MNRAS, 199, 883

Blandford R. D., Znajek R. L., 1977, MNRAS, 179, 433

Boccardi B., et al., 2021, A&A, 647, A67

Bodo G., Massaglia S., Ferrari A., Trussoni E., 1994, A&A, 283, 655

Bodo G., Mignone A., Rosner R., 2004, Phys. Rev. E, 70, 036304

Bodo G., Mamatsashvili G., Rossi P., Mignone A., 2013, MNRAS, 434, 3030

Bodo G., Mamatsashvili G., Rossi P., Mignone A., 2019, MNRAS, 485, 2909

Bodo G., Mamatsashvili G., Rossi P., Mignone A., 2022, MNRAS, 510, 2391

Borse N., Acharya S., Vaidya B., Mukherjee D., Bodo G., Rossi P., Mignone A., 2021, A&A, 649, A150

Bromberg O., Tchekhovskoy A., 2016, MNRAS, 456, 1739

Bromberg O., Singh C. B., Davelaar J., Philippov A. A., 2019, ApJ, 884, 39

Casadio C., et al., 2021, A&A, 649, A153

Chantry L., Cayatte V., Sauty C., Vlahakis N., Tsinganos K., 2018, A&A, 612, A63

Chashkina A., Bromberg O., Levinson A., 2021, MNRAS, 508, 1241

Chatterjee K., Liska M., Tchekhovskoy A., Markoff S. B., 2019, MNRAS, 490, 2200

Chow A., Davelaar J., Rowan M., Sironi L., 2022, arXiv e-prints, p. arXiv:2209.13699

Chow A., Rowan M. E., Sironi L., Davelaar J., Bodo G., Narayan R., 2023, MNRAS, 524, 90

Christodoulou D. M., Gabuzda D. C., Knuettel S., Contopoulos I., Kazanas D., Coughlan C. P., 2016, A&A, 591, A61

Cohn H., 1983, ApJ, 269, 500

Contopoulos J., 1994, ApJ, 432, 508

Contopoulos I., Kazanas D., 1998, ApJ, 508, 859

Contopoulos I., Christodoulou D. M., Kazanas D., Gabuzda D. C., 2009, ApJL, 702, L148

Curd B., Narayan R., 2023, MNRAS, 518, 3441

Curtis H. D., 1918, Publications of Lick Observatory, 13, 9

Das U., Begelman M. C., 2019, MNRAS, 482, 2107

Dihingia I. K., Vaidya B., Fendt C., 2021, MNRAS, 505, 3596

Fanaroff B. L., Riley J. M., 1974, MNRAS, 167, 31P

Ferrari A., Trussoni E., Zaninetti L., 1978, A&A, 64, 43

Ferrari A., Trussoni E., Zaninetti L., 1980, MNRAS, 193, 469

Ferrari A., Trussoni E., Zaninetti L., 1981, MNRAS, 196, 1051

Fromm C. M., Perucho M., Porth O., Younsi Z., Ros E., Mizuno Y., Zensus J. A., Rezzolla L., 2018, A&A, 609, A80

Gabuzda D. C., Christodoulou D. M., Contopoulos I., Kazanas D., 2012, in Journal of Physics Conference Series. p. 012019, doi:10.1088/1742-6596/355/1/012019

Gabuzda D. C., Cantwell T. M., Cawthorne T. V., 2014a, MNRAS, 438, L1

Gabuzda D. C., Reichstein A. R., O'Neill E. L., 2014b, MNRAS, 444, 172

García-García L., López-Cámara D., Lazzati D., 2023, MNRAS, 519, 4454

Gottlieb O., Levinson A., Nakar E., 2020, MNRAS, 495, 570

Gottlieb O., Nakar E., Bromberg O., 2021a, MNRAS, 500, 3511

Gottlieb O., Bromberg O., Levinson A., Nakar E., 2021b, MNRAS, 504, 3947

Hardee P. E., 2007, ApJ, 664, 26

Huang L., Pan Z., Yu C., 2020, ApJ, 894, 45

Kim J., Balsara D. S., Lyutikov M., Komissarov S. S., George D., Siddireddy P. K., 2015, MNRAS, 450, 982

Kim J., Balsara D. S., Lyutikov M., Komissarov S. S., 2016, MNRAS, 461, 728

Kim J., Balsara D. S., Lyutikov M., Komissarov S. S., 2017, MNRAS, 467, 4647

Kim J., Balsara D. S., Lyutikov M., Komissarov S. S., 2018, MNRAS, 474, 3954

Kin K., Kisaka S., Toma K., Kimura S. S., Levinson A., 2023, arXiv e-prints, p. arXiv:2310.12532

Komissarov S. S., Vlahakis N., Königl A., Barkov M. V., 2009, MNRAS, 394, 1182

Kovalev Y. Y., Pushkarev A. B., Nokhrina E. E., Plavin A. V., Beskin V. S., Chernoglazov A. V., Lister M. L., Savolainen T., 2020, MNRAS, 495, 3576

Kravchenko E. V., Kovalev Y. Y., Sokolovsky K. V., 2017, MNRAS, 467, 83

Laing R., 2015, in Advancing Astrophysics with the Square Kilometre Array (AASKA14). p. 107 (`arXiv:1501.00452`), doi:10.22323/1.215.0107

Lalakos A., et al., 2022, ApJL, 936, L5

Li Z.-Y., Chiueh T., Begelman M. C., 1992, ApJ, 394, 459

Lisakov M. M., Kravchenko E. V., Pushkarev A. B., Kovalev Y. Y., Savolainen T. K., Lister M. L., 2021, ApJ, 910, 35

Lister M. L., Homan D. C., Kellermann K. I., Kovalev Y. Y., Pushkarev A. B., Ros E., Savolainen T., 2021, ApJ, 923, 30

Mandal S., Duffell P. C., Li Y., 2022, ApJ, 935, 42

Massaglia S., Bodo G., Rossi P., Capetti S., Mignone A., 2016, A&A, 596, A12

Massaglia S., Bodo G., Rossi P., Capetti S., Mignone A., 2019, A&A, 621, A132

Massaglia S., Bodo G., Rossi P., Capetti A., Mignone A., 2022, A&A, 659, A139

Matsumoto J., Komissarov S. S., Gourgouliatos K. N., 2021, MNRAS, 503, 4918

Meliani Z., Keppens R., 2009, ApJ, 705, 1594

Mertens F., Lobanov A. P., 2016, A&A, 587, A52

Mignone A., McKinney J. C., 2007, MNRAS, 378, 1118

Mignone A., Bodo G., Massaglia S., Matsakos T., Tesileanu O., Zanni C., Ferrari A., 2007, ApJS, 170, 228

Mignone A., Zanni C., Tzeferacos P., van Straalen B., Colella P., Bodo G., 2012, ApJS, 198, 7

Millas D., Keppens R., Meliani Z., 2017, MNRAS, 470, 592

Mizuno Y., Hardee P. E., Nishikawa K.-I., 2011, ApJ, 734, 19

Mizuno Y., Lyubarsky Y., Nishikawa K.-I., Hardee P. E., 2012, ApJ, 757, 16

Mościbrodzka M., Falcke H., Noble S., 2016, A&A, 596, A13

Mukherjee D., Bodo G., Mignone A., Rossi P., Vaidya B., 2020, MNRAS, 499, 681

Nakahara S., Doi A., Murata Y., Hada K., Nakamura M., Asada K., 2018, ApJ, 854, 148

Nakahara S., Doi A., Murata Y., Nakamura M., Hada K., Asada K., Sawada-Satoh S., Kameno S., 2020, AJ, 159, 14

Nakamura M., et al., 2018, ApJ, 868, 146

O'Neill S. M., Beckwith K., Begelman M. C., 2012, MNRAS, 422, 1436

Okino H., et al., 2022, ApJ, 940, 65

Osmanov Z., Mignone A., Massaglia S., Bodo G., Ferrari A., 2008, A&A, 490, 493

Paraschos G. F., et al., 2022, A&A, 665, A1

Parfrey K., Philippov A., Cerutti B., 2019, PRL, 122, 035101

Park J., et al., 2019, ApJ, 887, 147

Park J., Hada K., Nakamura M., Asada K., Zhao G., Kino M., 2021, ApJ, 909, 76

Pasetto A., et al., 2021, ApJL, 923, L5

Pavan A., Ciolfi R., Kalinani J. V., Mignone A., 2023, MNRAS, 524, 260

Payne D. G., Cohn H., 1985, ApJ, 291, 655

Perucho M., Martí J.-M., Quilis V., 2019, MNRAS, 482, 3718

Perucho M., Martí J.-M., Quilis V., 2022, MNRAS, 510, 2084

Porth O., 2013, MNRAS, 429, 2482

Pushkarev A. B., Gabuzda D. C., Vetukhnovskaya Y. N., Yakimov V. E., 2005, MNRAS, 356, 859

Pushkarev A. B., Kovalev Y. Y., Lister M. L., Savolainen T., 2017, MNRAS, 468, 4992

Pushkarev A. B., et al., 2023, MNRAS, 520, 6053

Ricci L., et al., 2022, A&A, 664, A166

Rossi P., Bodo G., Massaglia S., Capetti A., 2020, A&A, 642, A69

Sauty C., Tsinganos K., 1994, A&A, 287, 893

Singh C. B., Mizuno Y., de Gouveia Dal Pino E. M., 2016, ApJ, 824, 48

Sinnis C., 2016, Stability analysis of astrophysical magnetized jets without current sheets

Sinnis C., Millas D., Vlahakis N., 2023, MNRAS, 523, 6294

Sironi L., Rowan M. E., Narayan R., 2021, ApJL, 907, L44

Soares G., Bosch P., Lazzati D., Mösta P., 2023, ApJ, 953, 73

Sobacchi E., Lyubarsky Y. E., 2018, MNRAS, 473, 2813

Sobacchi E., Lyubarsky Y. E., Sormani M. C., 2017, MNRAS, 468, 4635

Synge J. L., 1957, The relativistic gas. North-Holland Publishing Company, Amsterdam; Interscience Publishers Inc., New York

Tchekhovskoy A., Bromberg O., 2016, MNRAS, 461, L46

Tchekhovskoy A., McKinney J. C., Narayan R., 2009, ApJ, 699, 1789

Tchekhovskoy A., Narayan R., McKinney J. C., 2010, ApJ, 711, 50

Tchekhovskoy A., Narayan R., McKinney J. C., 2011, MNRAS, 418, L79

Urrutia G., De Colle F., López-Cámara D., 2023, MNRAS, 518, 5145

Velović V., et al., 2022, MNRAS, 516, 1865

Vlahakis N., 2004, ApJ, 600, 324

Vlahakis N., 2023, Universe, 9, 386

Vlahakis N., Königl A., 2001, ApJL, 563, L129

Vlahakis N., Königl A., 2003a, ApJ, 596, 1080

Vlahakis N., Königl A., 2003b, ApJ, 596, 1104

Yates-Jones P. M., Shabala S. S., Krause M. G. H., 2021, MNRAS, 508, 5239

Čada M., Torrilhon M., 2009, Journal of Computational Physics, 228, 4118

Appendix A

Details on the linearized equations

In chapter 2, equation 2.17 provides the linearized differential system of equations. The following derivation has been published in Vlahakis (2023), an open access article distributed under the terms and conditions of the Creative Commons Attribution (CC BY) license (`https://creativecommons.org/licenses/by/4.0/`). The unknowns are y_1 and y_2 respectively, the total pressure perturbation which is involved in the equation of y_2 and the perturbation of the electric field are given by:

$$\Pi_1 = \boldsymbol{B}_0 \cdot \boldsymbol{B}_1 - \boldsymbol{E}_0 \cdot \boldsymbol{E}_1 + P_1 \tag{A.1}$$

$$\boldsymbol{E}_1 = -\left(\boldsymbol{V}_1 \times \boldsymbol{B}_0 + \boldsymbol{V}_0 \times \boldsymbol{B}_1\right) \tag{A.2}$$

The linearized system results from properly perturbing equations 2.1-2.8 alongside the equation providing the relation for the specific enthalpy (e.g. equation 2.10 or 2.12). The linearized system is provided by equation A.4, where the perturbation of the Lorentz factor is given by:

$$\gamma_1 = \gamma_0^3 \boldsymbol{V}_0 \cdot \boldsymbol{V}_1 \, . \tag{A.3}$$

The differential system A.4 can be transformed into the system 2.17 if the quantities $[\gamma_1, \rho_{01}, B_{1z}, B_{1\phi}, iB_{1\varpi}, \xi_1, V_{1z}, V_{1\phi}, d\left(i\varpi V_{1\varpi}\right)/d\varpi, d\Pi_1/d\varpi]$ are expressed as functions of $V_{1\varpi}$, Π_1, and ϖ. The first eight equations give γ_1, ρ_{01}, B_{1z}, $B_{1\phi}$, $B_{1\varpi}$, ξ_1, V_{1z}, $V_{1\phi}$. The remaining two consist of the 2.17 system.

$$\begin{pmatrix} D_{11} & 0 & 0 & 0 & 0 & 0 & D_{17} & D_{18} & 0 & 0 & 0 & 0 \\ D_{21} & D_{22} & 0 & 0 & 0 & 0 & D_{27} & D_{28} & D_{29} & 0 & D_{211} & 0 \\ 0 & 0 & D_{33} & 0 & D_{35} & 0 & D_{37} & D_{38} & D_{39} & 0 & D_{311} & 0 \\ 0 & 0 & 0 & D_{44} & D_{45} & 0 & D_{47} & D_{48} & D_{49} & 0 & D_{411} & 0 \\ 0 & 0 & 0 & 0 & D_{55} & 0 & 0 & 0 & 0 & 0 & D_{511} & 0 \\ 0 & D_{62} & 0 & 0 & 0 & D_{66} & 0 & 0 & 0 & 0 & D_{611} & 0 \\ D_{71} & 0 & D_{73} & D_{74} & D_{75} & D_{76} & D_{77} & D_{78} & 0 & 0 & D_{711} & D_{712} \\ D_{81} & 0 & D_{83} & D_{84} & D_{85} & D_{86} & D_{87} & D_{88} & 0 & 0 & D_{811} & D_{812} \\ 0 & D_{92} & D_{93} & D_{94} & 0 & D_{96} & D_{97} & D_{98} & 0 & 0 & 0 & D_{912} \\ D_{101} & D_{102} & D_{103} & D_{104} & D_{105} & D_{106} & D_{107} & D_{108} & 0 & D_{1010} & D_{1011} & 0 \end{pmatrix} \begin{pmatrix} \gamma_1 \\ \rho_{01} \\ B_{1z} \\ B_{1\phi} \\ iB_{1\varpi} \\ \xi_1 \\ V_{1z} \\ V_{1\phi} \\ d\left(i\varpi V_{1\varpi}\right)/d\varpi \\ d\Pi_1/d\varpi \\ i\varpi V_{1\varpi} \\ \Pi_1 \end{pmatrix} = 0\,. \quad \text{(A.4)}$$

$$\omega_0 = \omega - \frac{m}{\varpi}V_{0\phi} - kV_{0z}\,, \quad D_{11} = 1\,, \quad D_{17} = -\gamma_0^3 V_{0z}\,, \quad D_{18} = -\gamma_0^3 V_{0\phi}\,,$$

$$D_{21} = \omega_0\rho_{00}\,, \quad D_{22} = \omega_0\gamma_0\,, \quad D_{27} = -k\gamma_0\rho_{00}\,, \quad D_{28} = -\frac{m}{\varpi}\gamma_0\rho_{00}\,, \quad D_{29} = \frac{\gamma_0\rho_{00}}{\varpi}\,, \quad D_{211} = \frac{1}{\varpi}\frac{d\left(\gamma_0\rho_{00}\right)}{d\varpi}\,,$$

$$D_{33} = \omega_0\,, \quad D_{35} = -\frac{dV_{0z}}{d\varpi}\,, \quad D_{37} = \frac{m}{\varpi}B_{0\phi}\,, \quad D_{38} = -\frac{m}{\varpi}B_{0z}\,, \quad D_{39} = \frac{B_{0z}}{\varpi}\,, \quad D_{311} = \frac{1}{\varpi}\frac{dB_{0z}}{d\varpi}\,,$$

$$D_{44} = \omega_0\,, \quad D_{45} = -\varpi\frac{d\left(V_{0\phi}/\varpi\right)}{d\varpi}\,, \quad D_{47} = -kB_{0\phi}\,, \quad D_{48} = kB_{0z}\,, \quad D_{49} = \frac{B_{0\phi}}{\varpi}\,, \quad D_{411} = \frac{d\left(B_{0\phi}/\varpi\right)}{d\varpi}\,,$$

$$D_{55} = \omega_0\,, \quad D_{511} = \frac{1}{\varpi}\left(kB_{0z} + \frac{m}{\varpi}B_{0\phi}\right)\,,$$

$$D_{62} = -\frac{\xi_0 c_s^2}{\rho_{00}}\omega_0\,, \quad D_{66} = \omega_0\,, \quad D_{611} = \frac{1}{\varpi}\frac{dxi_0}{d\varpi} - \frac{\xi_0 c_s^2}{\varpi\rho_0}\frac{d\rho_{00}}{d\varpi}\,,$$

$$D_{71} = \omega_0\xi_0\gamma_0\rho_{00}V_{0z}\,, \quad D_{73} = kB_{0z} + \frac{m}{\varpi}B_{0\phi} - \omega V_{0\phi}B_{0\phi} + kE_0V_{0\phi}\,, \quad D_{74} = V_{0z}\left(\omega B_{0\phi} - kE_0\right)\,,$$

$$D_{75} = -\frac{dB_{0z}}{d\varpi} - \frac{V_{0\phi}}{\varpi}\frac{d\left(\varpi E_0\right)}{d\varpi}\,, \quad D_{76} = \omega_0\gamma_0^2\rho_{00}V_{0z}\,, \quad D_{77} = \omega_0\xi_0\gamma_0^2\rho_{00} + \omega B_{0\phi}^2 - kE_0B_{0\phi}\,,$$

$$D_{78} = B_{0z}\left(kE_0 - \omega B_{0\phi}\right)\,, \quad D_{711} = \frac{\gamma_0\rho_{00}}{\varpi}\frac{d\left(\xi_0\gamma_0V_{0z}\right)}{d\varpi} + \frac{B_{0\phi}}{\varpi^2}\frac{d\left(\varpi E_0\right)}{d\varpi}\,, \quad D_{712} = -k\,,$$

$$D_{81} = \omega_0\xi_0\gamma_0\rho_{00}V_{0\phi}\,, \quad D_{83} = V_{0\phi}\left(\omega B_{0z} + \frac{m}{\varpi}E_0\right)\,, \quad D_{84} = kB_{0z} + \frac{m}{\varpi}B_{0\phi} - \omega V_{0z}B_{0z} - \frac{m}{\varpi}E_0V_{0z}\,,$$

$$D_{85} = \frac{V_{0z}}{\varpi}\frac{d\left(\varpi E_0\right)}{d\varpi} - \frac{1}{\varpi}\frac{d\left(\varpi B_{0\phi}\right)}{d\varpi}\,, \quad D_{86} = \omega_0\gamma_0^2\rho_{00}V_{0\phi}\,, \quad D_{87} = -B_{0\phi}\left(\frac{m}{\varpi}E_0 + \omega B_{0z}\right)\,,$$

$$D_{88} = \omega_0\xi_0\gamma_0^2\rho_{00} + \omega B_{0z}^2 + \frac{m}{\varpi}E_0B_{0z}\,, \quad D_{811} = \frac{\gamma_0\rho_{00}}{\varpi^2}\frac{d\left(\xi_0\gamma_0\varpi V_{0\phi}\right)}{d\varpi} - \frac{B_{0z}}{\varpi^2}\frac{d\left(\varpi E_0\right)}{d\varpi}\,, \quad D_{812} = -\frac{m}{\varpi}\,,$$

$$D_{92} = -\Theta_0\,, \quad D_{93} = -E_0V_{0\phi} - B_{0z}\,, \quad D_{94} = E_0V_{0z} - B_{0\phi}\,, \quad D_{96} = \rho_{00}\left(\frac{\Theta_0}{\xi_0 c_s^2} - 1\right)\,,$$

$$D_{97} = E_0B_{0\phi}\,, \quad D_{98} = -E_0B_{0z}\,, \quad D_{912} = 1\,,$$

$$D_{101} = 2\xi_0\gamma_0\rho_{00}\frac{V_{0\phi}^2}{\varpi}\,, \quad D_{102} = \xi_0\gamma_0^2\frac{V_{0\phi}^2}{\varpi}\,, \quad D_{103} = -2\frac{V_{0\phi}}{\varpi}E_0\,, \quad D_{104} = -2\frac{B_{0\phi}}{\varpi} + 2\frac{V_{0z}E_0}{\varpi}\,,$$

$$D_{105} = kB_{0z} + \frac{m}{\varpi}B_{0\phi} - \omega\left(V_{0z}B_{0z} + V_{0\phi}B_{0\phi}\right) + E_0\left(kV_{0\phi} - \frac{m}{\varpi}V_{0z}\right)\,,$$

$$D_{106} = \rho_{00}\gamma_0^2\frac{V_{0\phi}^2}{\varpi}\,, \quad D_{107} = 2E_0\frac{B_{0\phi}}{\varpi}\,, \quad D_{108} = 2\xi_0\gamma_0^2\rho_{00}\frac{V_{0\phi}}{\varpi} - 2\frac{B_{0z}E_0}{\varpi}\,, \quad D_{1010} = -1\,,$$

$$D_{1011} = \omega_0\frac{\xi_0\gamma_0^2\rho_{00}}{\varpi} + \omega\frac{B_{0z}^2 + B_{0\phi}^2}{\varpi} + \frac{E_0}{\varpi}\left(\frac{m}{\varpi}B_{0z} - kB_{0\phi}\right)\,.$$

In equation 2.17 the coefficients $\mathcal{F}$ are provided by:

$$\mathcal{F}_{11} = \mathcal{C}_{11} + \frac{1}{\omega_0}\frac{d\omega_0}{d\varpi}\mathcal{D} - \frac{1}{\varpi}\frac{d\Pi_0}{d\varpi}\frac{1}{\omega_0}\mathcal{C}_{12}\,, \tag{A.5}$$

$$\mathcal{F}_{12} = \frac{1}{\omega_0}\mathcal{C}_{12}\,, \tag{A.6}$$

$$\mathcal{F}_{21} = \omega_0\mathcal{C}_{21} - \frac{d}{d\varpi}\left(\frac{1}{\varpi}\frac{d\Pi_0}{d\varpi}\right)\mathcal{D} + \frac{1}{\varpi}\frac{d\Pi_0}{d\varpi}\left(\mathcal{F}_{11} - \mathcal{C}_{22}\right)\,, \tag{A.7}$$

$$\mathcal{F}_{22} = \mathcal{C}_{22} + \frac{1}{\varpi}\frac{d\Pi_0}{d\varpi}\mathcal{F}_{12}\,. \tag{A.8}$$

The $\mathcal{C}_{ij}$ and $\mathcal{D}$ symbols represent determinants which are provided by:

$$\mathcal{C}_{11} = \begin{vmatrix}
D_{11} & 0 & 0 & 0 & 0 & 0 & D_{17} & D_{18} & 0 & 0 \\
D_{21} & D_{22} & 0 & 0 & 0 & 0 & D_{27} & D_{28} & D_{211} & 0 \\
0 & 0 & D_{33} & 0 & D_{35} & 0 & D_{37} & D_{38} & D_{311} & 0 \\
0 & 0 & 0 & D_{44} & D_{45} & 0 & D_{47} & D_{48} & D_{411} & 0 \\
0 & 0 & 0 & 0 & D_{55} & 0 & 0 & 0 & D_{511} & 0 \\
0 & D_{62} & 0 & 0 & 0 & D_{66} & 0 & 0 & D_{611} & 0 \\
D_{71} & 0 & D_{73} & D_{74} & D_{75} & D_{76} & D_{77} & D_{78} & D_{711} & 0 \\
D_{81} & 0 & D_{83} & D_{84} & D_{85} & D_{86} & D_{87} & D_{88} & D_{811} & 0 \\
0 & D_{92} & D_{93} & D_{94} & 0 & D_{96} & D_{97} & D_{98} & 0 & 0 \\
D_{101} & D_{102} & D_{103} & D_{104} & D_{105} & D_{106} & D_{107} & D_{108} & D_{1011} & D_{1010}
\end{vmatrix}\,,$$

$$\mathcal{C}_{12} = \begin{vmatrix}
D_{11} & 0 & 0 & 0 & 0 & 0 & D_{17} & D_{18} & 0 & 0 \\
D_{21} & D_{22} & 0 & 0 & 0 & 0 & D_{27} & D_{28} & 0 & 0 \\
0 & 0 & D_{33} & 0 & D_{35} & 0 & D_{37} & D_{38} & 0 & 0 \\
0 & 0 & 0 & D_{44} & D_{45} & 0 & D_{47} & D_{48} & 0 & 0 \\
0 & 0 & 0 & 0 & D_{55} & 0 & 0 & 0 & 0 & 0 \\
0 & D_{62} & 0 & 0 & 0 & D_{66} & 0 & 0 & 0 & 0 \\
D_{71} & 0 & D_{73} & D_{74} & D_{75} & D_{76} & D_{77} & D_{78} & D_{712} & 0 \\
D_{81} & 0 & D_{83} & D_{84} & D_{85} & D_{86} & D_{87} & D_{88} & D_{812} & 0 \\
0 & D_{92} & D_{93} & D_{94} & 0 & D_{96} & D_{97} & D_{98} & D_{912} & 0 \\
D_{101} & D_{102} & D_{103} & D_{104} & D_{105} & D_{106} & D_{107} & D_{108} & 0 & D_{1010}
\end{vmatrix}\,,$$

$$\mathcal{C}_{21} = \begin{vmatrix} D_{11} & 0 & 0 & 0 & 0 & 0 & D_{17} & D_{18} & 0 & 0 \\ D_{21} & D_{22} & 0 & 0 & 0 & 0 & D_{27} & D_{28} & D_{29} & D_{211} \\ 0 & 0 & D_{33} & 0 & D_{35} & 0 & D_{37} & D_{38} & D_{39} & D_{311} \\ 0 & 0 & 0 & D_{44} & D_{45} & 0 & D_{47} & D_{48} & D_{49} & D_{411} \\ 0 & 0 & 0 & 0 & D_{55} & 0 & 0 & 0 & 0 & D_{511} \\ 0 & D_{62} & 0 & 0 & 0 & D_{66} & 0 & 0 & 0 & D_{611} \\ D_{71} & 0 & D_{73} & D_{74} & D_{75} & D_{76} & D_{77} & D_{78} & 0 & D_{711} \\ D_{81} & 0 & D_{83} & D_{84} & D_{85} & D_{86} & D_{87} & D_{88} & 0 & D_{811} \\ 0 & D_{92} & D_{93} & D_{94} & 0 & D_{96} & D_{97} & D_{98} & 0 & 0 \\ D_{101} & D_{102} & D_{103} & D_{104} & D_{105} & D_{106} & D_{107} & D_{108} & 0 & D_{1011} \end{vmatrix},$$

$$\mathcal{C}_{22} = \begin{vmatrix} D_{11} & 0 & 0 & 0 & 0 & 0 & D_{17} & D_{18} & 0 & 0 \\ D_{21} & D_{22} & 0 & 0 & 0 & 0 & D_{27} & D_{28} & D_{29} & 0 \\ 0 & 0 & D_{33} & 0 & D_{35} & 0 & D_{37} & D_{38} & D_{39} & 0 \\ 0 & 0 & 0 & D_{44} & D_{45} & 0 & D_{47} & D_{48} & D_{49} & 0 \\ 0 & 0 & 0 & 0 & D_{55} & 0 & 0 & 0 & 0 & 0 \\ 0 & D_{62} & 0 & 0 & 0 & D_{66} & 0 & 0 & 0 & 0 \\ D_{71} & 0 & D_{73} & D_{74} & D_{75} & D_{76} & D_{77} & D_{78} & 0 & D_{712} \\ D_{81} & 0 & D_{83} & D_{84} & D_{85} & D_{86} & D_{87} & D_{88} & 0 & D_{812} \\ 0 & D_{92} & D_{93} & D_{94} & 0 & D_{96} & D_{97} & D_{98} & 0 & D_{912} \\ D_{101} & D_{102} & D_{103} & D_{104} & D_{105} & D_{106} & D_{107} & D_{108} & 0 & 0 \end{vmatrix},$$

$$\mathcal{D} = \begin{vmatrix} D_{11} & 0 & 0 & 0 & 0 & 0 & D_{17} & D_{18} & 0 & 0 \\ D_{21} & D_{22} & 0 & 0 & 0 & 0 & D_{27} & D_{28} & D_{29} & 0 \\ 0 & 0 & D_{33} & 0 & D_{35} & 0 & D_{37} & D_{38} & D_{39} & 0 \\ 0 & 0 & 0 & D_{44} & D_{45} & 0 & D_{47} & D_{48} & D_{49} & 0 \\ 0 & 0 & 0 & 0 & D_{55} & 0 & 0 & 0 & 0 & 0 \\ 0 & D_{62} & 0 & 0 & 0 & D_{66} & 0 & 0 & 0 & 0 \\ D_{71} & 0 & D_{73} & D_{74} & D_{75} & D_{76} & D_{77} & D_{78} & 0 & 0 \\ D_{81} & 0 & D_{83} & D_{84} & D_{85} & D_{86} & D_{87} & D_{88} & 0 & 0 \\ 0 & D_{92} & D_{93} & D_{94} & 0 & D_{96} & D_{97} & D_{98} & 0 & 0 \\ D_{101} & D_{102} & D_{103} & D_{104} & D_{105} & D_{106} & D_{107} & D_{108} & 0 & D_{1010} \end{vmatrix}.$$

The final determinant $\mathcal{D}$ can also be written:

$$\mathcal{D} = -\frac{\gamma_0 \xi_0^3 \rho_{00}^3}{\varpi} \left(1 + U_{\mathrm{A}}^2\right) \left(c_s^2 + U_{\mathrm{A}}^2\right) \omega_{\mathrm{co}}^2 \left[\omega_{\mathrm{co}}^2 - \frac{\left(\boldsymbol{k}_{\mathrm{co}} \cdot \boldsymbol{U}_{\mathrm{A}}\right)^2}{1 + U_{\mathrm{A}}^2}\right] \left[\omega_{\mathrm{co}}^2 - \frac{c_s^2 \left(\boldsymbol{k}_{\mathrm{co}} \cdot \boldsymbol{U}_{\mathrm{A}}\right)^2}{c_s^2 + U_{\mathrm{A}}^2}\right]. \tag{A.9}$$